UNICA

UNIVERSITÀ
DEGLI STUDI
DI CAGLIARI

Ph.D. DEGREE IN

Industrial Engineering

Cycle XXXV

TITLE OF THE Ph.D. THESIS

Development of algorithms to support the plasma control in disruptive scenario in DEMO relevant machines

Scientific Disciplinary Sector(s)

Fusion Engineering

Ph.D. Student:	Massimiliano Lacquaniti
Supervisor	Giuliana Sias
Co-Supervisor	Giuseppe Calabrò

Final exam. Academic Year 2021/2022
Thesis defence: January 2024 Session

Abstract

The lessons learned from disruptions in current tokamaks play a crucial role in the EU-DEMO Research & Design (R&D) strategies. The data sharing among tokamak experiments is crucial in advancing our understanding and mitigation capabilities of disruptions in future fusion devices. In this context, this thesis aims to support the EU-DEMO R&D activities with inter-machine studies on the several disruption implications. The chapter 3 present a machine learning algorithm application for the real-time automatic tracking of the Multifaceted Asymmetric Radiation From the Edge (MARFE) evolution at AUG, which is a precursor of H-mode density limit disruptions disruption. This study represent the first step of a cross-machine algorithm, which will consider also JET and WEST data, to be scaled for the MARFE detection in EU-DEMO and ITER. In the chapter 2 an inter-machine database is presented. The database collects EU-DEMO relevant plasma perturbations causing both Vertical Displacement Events, Major Disruption in Single Null and Quasi-Double Null configurations both from JET and AUG. These experimental perturbations, properly scaled to EU-DEMO, are the starting point for the predictive analyses to foreseen the plasma position and the EM loads during VDEs. Disrupted experiments with tungsten (W) accumulation in the plasma both from AUG and JET have been collected in the database to study the effect of W accumulation in the core on the plasma performance and to quantify the mechanisms that determine the W concentration in the plasma. In addition, flux pumping eligible experiments have been collected from hybrid scenarios JET experiments. The hybrid scenario is a good candidate for ITER and EU-DEMO scenarios thanks to its robustness and high performances. The chapter 4 present the procedure conducted to characterize the inverse boundary reconstruction errors due to the white noise effect on in-vessel pick-up coils. Finally, in the conclusions, the results discussed in three chapter are summarized and next steps of the work are presented.

Contents

Chapter 1

Introduction

1.1 An overview on global energetic scenario

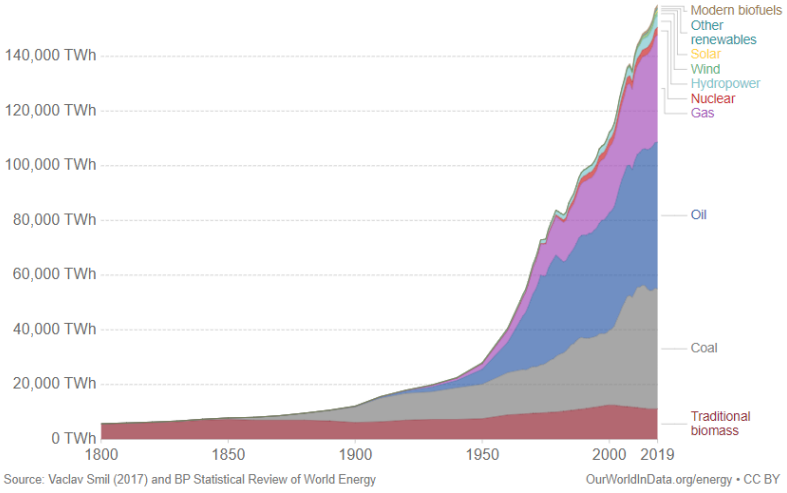

FIGURE 1.1: Global direct primary energy consumption: inefficiencies in fossil fuel production have not been taken into account [1]

Population growth rate along with urbanization trend leads to an increasing energy demand in the past century, and in the last decades. Figure 1.1 [1] shows the primary energy consumption from the 17^{th} up to 2019. A fast increase of the energy consumption is clearly visible from the 50's. Due to these and various other factors, the CO_2 concentration in the atmosphere almost doubled the pre-industrial level, from 280 ppm to 417 ppm (see Figure 1.2[2]). The Intergovernmental Panel for Climate Change (IPCC) states that an average increase of

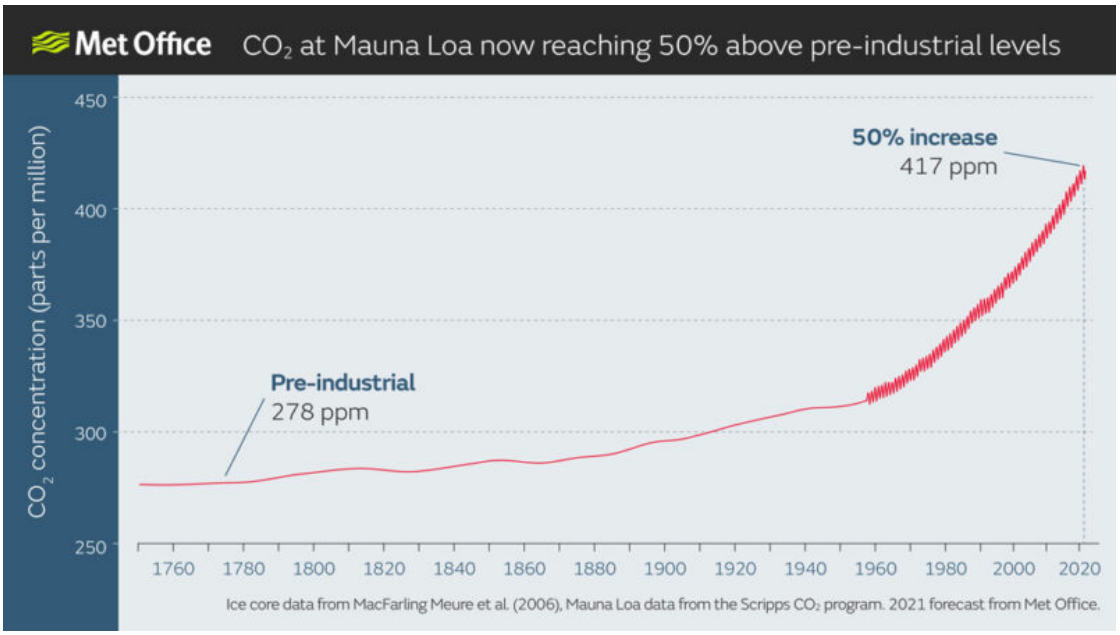

FIGURE 1.2: CO_2 concentrations in the atmosphere from the pre-industrial period until 2020 [2].

temperature of 1 °C has been already reached and a value of 1.5 °C will be reached between 2030-2050 years [3]. The target presented in this report is to reach zero global CO_2 emission within 2050 through an intermediate target of 45% CO_2 emission reduction in 2030 with the respect to the 2010 level; more realistic goal could be reached with zero CO_2 emission in 2075. In absence of this emissions reduction the increase of average temperature would be difficult to contain leading to a value from 2 °C up to 5.5 °C. 40% of the CO_2 emission related to the energy production systems is due to electric energy production. In Figure 1.3 [3] the CO_2 emission from different primary energy sources is reported, the plot highlights how the most traditional primary sources (i.e. coal) present the highest CO_2 production rate, in terms of grams of CO_2 equivalent per kWh produced. Instead, renewable energy and nuclear energy present the lowest values of grams of CO_2 equivalent per kWh.

Thus, a decoupling of the CO_2 emission from the electric energy production systems is necessary to satisfy the goal defined by the IPCC. However, producing enough energy for the world population is essential. These two needs can be satisfied by fusion energy, in particular by controlled fusion.

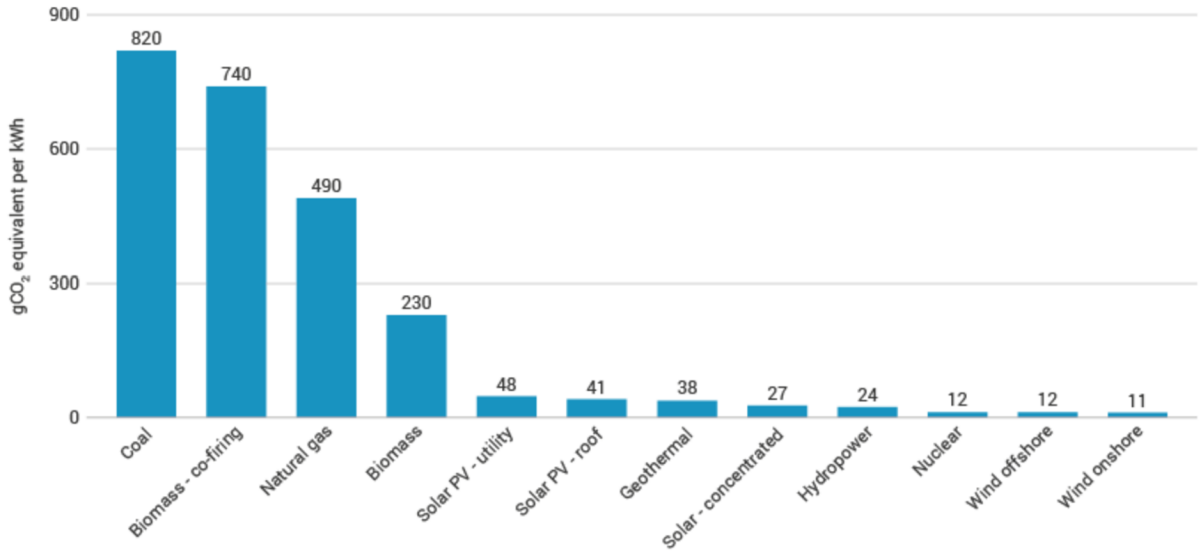

FIGURE 1.3: CO_2 grams produced per kWh from different primary energy forms [3].

1.2 Nuclear fusion

A nuclear fusion reaction occurs when two (or more) different nuclei merge to form a single nucleus. The fusion reaction is one of the most promising mechanisms among sustainable energy sources, mostly the only viable option to replace fossil fuel in the future decades. After a fusion reaction, the nuclei mass of the product is lower than the reagents one and the missing mass is converted into energy, as quantified by the well know mass energy equivalence (1.1)

$$E = (m_r - m_p)c^2 \tag{1.1}$$

where E is the energy resulting from the fusion reaction, m_r is the reagents mass, m_p is the products mass and c is the speed of light.

The challenge in nuclear fusion is to develop a device that can heat the fuel to the high temperatures needed and then confine it for a time long enough to let the fuel release more energy than the one used for heating. To make the fusion happen, since nuclei have a positive charge and they repel each other, the Coulomb barrier must be overcome increasing the kinetic energy of the nuclei by heating them. The fuel must be heated to temperatures around 100 million degrees, becoming a plasma. There are three known ways to accomplish this:

- Gravitational confinement: this is how the fusion occurs in the stars. The star core is

so massive that it presents such a density that its gravitational field provides a natural mechanism for plasma confinement. Energy in the stars is produced by different fusion reactions between protons. In small stars, like the sun, the fusion of hydrogen protons is the most source of energy, while in bigger stars fusion reactions between heavier protons are also possible (e.g. carbon protons and oxygen protons).

- Inertial confinement (IC): a solid capsule pellet of fuel, such as hydrogen isotopes, is compressed to reach very high density (from 1000 to 10 000 times the density of typical solids) and temperature. The compression is accomplished by focusing an intense laser beam on the pellet so that fusion power is produced in the few nanoseconds before the pellet blows apart.

- Magnetic confinement: since a plasma is made of charged particles (electrons and nuclei) if a magnetic field is present, the dynamics of the charged particle is governed by the Lorentz force. The interaction between charges and magnetic field enables the plasma confinement in a well-defined region.

The most promising among these approaches is the magnetic confinement [4], which is the one used in tokamak and stellarator machines. The most feasible fusion reaction on a human-built device is the fusion of two heavy nuclei of hydrogen, the lightest element in nature, so the easiest to accelerate in order to obtain enough energy to trigger the reaction. Among the different hydrogen isotopes the ones identified as the best couple are deuterium (D) and tritium (T). The reaction 1.2 is the most promising one to realize the controlled fusion on the earth:

$$D + T \rightarrow {}^4He + n + 17.6\,\mathrm{MeV} \tag{1.2}$$

The deuterium may be easily extracted from water, with a rate of 1 atom of deuterium each 3250 molecules of water. From 100 mg of deuterium (available from 3 L of sea water) and 150 mg of tritium, potentially it is possible to obtain an amount of energy approximately equivalent to 7 barrels of oil. Instead, the tritium is very rare but it can be produced from the lithium, using neutrons from reaction 1.2 itself, by the reaction 1.3

$${}^6Li + n \rightarrow {}^4He + T + 4.8\,\mathrm{MeV} \tag{1.3}$$

Figure 1.4 reports the reactivity for D-T fusion reaction in function of the temperature, showing that the ideal temperature for this reaction is around 15 keV, which corresponds to about 175 million °C. No existing material material can be faced to this temperature.
The most promising solution for magnetic confinement is the tokamak. The tokamak concept was invented by Soviet Union researchers in the late 1950s. Tokamak is an acronym developed from the Russian words TOroidalnaya KAmera e MAgnitaya Katushka which means "toroidal chamber with magnetic coils". As the name suggests, it is a magnetic confinement device with toroidal geometry. Figure 1.5 shows the tokamak's magnetic field coils, the magnetic field lines, the plasma region and the plasma current:

- Poloidal Field Coils (PFC): the toroidal currents flowing in these coils generate a poloidal magnetic field
- Toroidal Field Coils (TFC): the poloidal currents flowing in these coils generate a toroidal magnetic field
- Central Solenoid (CS): the coils at the center of the machine acts as the transformer primary winding, where the plasma is the transformer secondary winding, so that a toroidal current is induced in the plasma, called the plasma current.

Twisted magnetic field lines are created by the combination of the toroidal magnetic field and the poloidal magnetic field, the most part of the poloidal magnetic field is due to the plasma toroidal

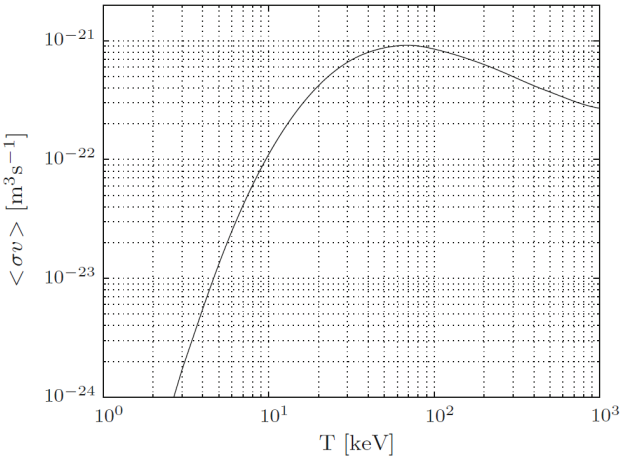

FIGURE 1.4: The reactivity $< \sigma v >$ as a function of the plasma temperature for the D-T reaction

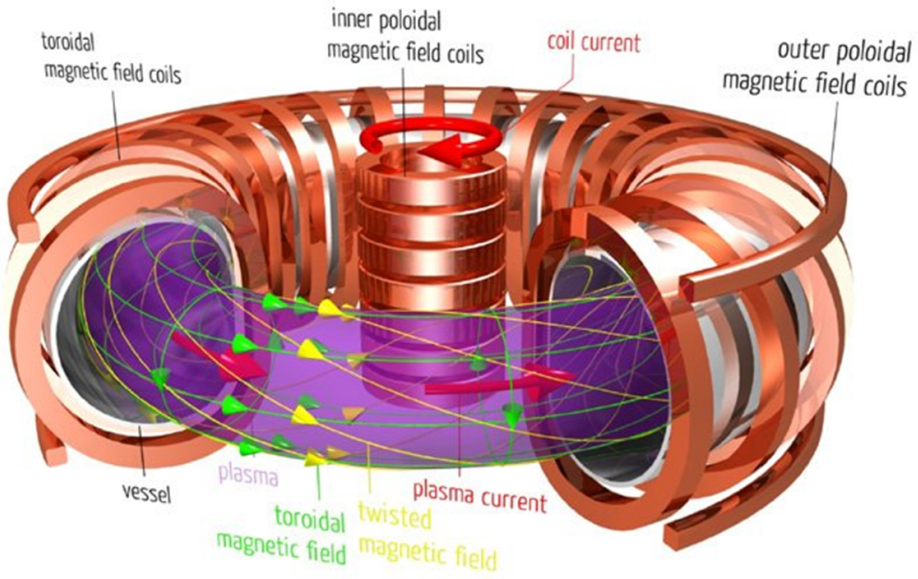

FIGURE 1.5: Tokamak view. Toroidal field (TFC) and poloidal field (PFC) coils, central solenoid (CS), magnetic field lines and plasma current I_p

current obtained with the transformer principal mentioned above. Therefore, the plasma current is induced by a current ramp in the solenoid, due to plasma resistivity the plasma current flow results in Ohmic heating of the plasma. Moreover, the current ramp set a limit to the operation time of tokamak, making it a pulsed device.
In addition to the tokamak, the stellarator is another human-built device to realize controlled nuclear fusion with magnetic confinement. Stellarators grants some advantages compared to tokamaks, since they do not require plasma current so that they are inherently steady-state capable and un-afflicted by some classes of instability.

1.3 European Fusion Roadmap

The European Fusion Roadmap has the role to indicate the short, medium and long term requirements to provide the basis for an electricity-generating fusion power plant. At the present day there are almost 30 nuclear fusion device world-wide, among these there are:

- 12 operative toroidal tokamaks, 2 spherical tokamaks and 3 foreseen tokamaks (DTT, ITER and EU-DEMO)
- 2 main IC devices: Laser Megajoule (France) and National Ignition Facility (USA)

- 3 main Stellarator devices: Wendelstein 7-X (Germayny, most advanced), Helically Symmetric Experiments (USA) and Large Helical Devis (Japan)

In the short to medium term, the main project is the International Thermonuclear Experimental Reactor (ITER), a worldwide collaboration which aims to demonstrate the scientific and technological feasibility of nuclear fusion as energetic source on Earth. ITER will generate ten times more fusion power than the power injected to sustain the fusion process. Meanwhile, the design, research and development for the EUropean DEMOnstration Power Plant (EU-DEMO), the construction and first exploitation of fusion materials testing facility (i.e. Divertor Tokamak Test, DTT), the exploitation of the stellarator concept, will take place among the other activities. Therefore, in the long term, high performance and advanced technology results of ITER will be an important input to optimize the EU-DEMO design. Thus, EU-DEMO will be able to demonstrate first electricity production to the grid by fusion. In 2012, European Fusion Development Agreement (EFDA) published a document on the European Fusion Roadmap [5], revised by EUROfusion in 2018 [6]. A strategic vision to achieve the generation of electrical power by a Demonstration Fusion Power Plant (EU-DEMO) by 2050 has been proposed in these documents. This roadmap identifies eighth critical strategic missions that need to be fulfilled to achieve this ambitious goal:

1. **Magnetic plasma confinement**: plasmas must be confined at temperatures 20 times higher than the core temperature of the sun. Energy losses due to turbulence minimization and active control of plasma instabilities are required for magnetic confinement. Plasma regimes of operation will be developed and qualified to be used on ITER, considering both experiments and theory-based models. Advancement will be required for EU-DEMO and commercial power plants, respect to ITER minimum needs.

2. **Heat exhaust systems**: the power injected in the plasma to sustain its high temperatures have to be exhausted. This is done through the main chamber wall and the divertor region. The heat flux in the divertor region can be extremely high, in the order of magnitude of tens of MW per square-meter, which is about ten times the heat-flux at 1 meter of distance from the Sun. Plasma facing components and materials and exhaust systems suitable for ITER have been already developed, however their operation needs to be developed and qualified. The development of a proper heat exhaust solution for EU-DEMO

is still in the experimental and theoretical phase being very challenging and requiring very technologically advanced Plasma Facing Components and strategies to spread to the power over a divertor area as large as possible.

3. **Neutron tolerant materials**: Plasma Facing Components must withstand the flux of neutrons up to 14 MeV and properly maintain their structural and physical properties for long periods. This is not a significant issue for ITER, but it represent a crucial point for EU-DEMO and commercial devices since long period activities are a crucial requirement to ensure efficient electricity production and adequate plant availability. In this field, the goal of the researcher is to produce suitable structural and high-heat flux materials also characterized by a reduced activation to avoid permanent waste and allow recycling.

4. **Tritium self-sufficiency**: is a must for EU-DEMO and commercial power plants. Tritium self-sufficiency requires efficient breeding and extraction system to minimize the tritium inventory management. The choices of the materials and the coolant of the breeding blanket will have to be made consistently with the choice of the components for the transformation of the high-grade heat into electricity (in the so-called Balance of Plant). In this contest ITER will be the perfect environment for a successful Test Blanket Module program as validation stage for the EU-DEMO design.

5. **Intrinsic Safety**: the implementation of the intrinsic safety features of fusion is a key goal for any EU-DEMO and commercial power plants to grant their inborn passive resistance to any incidents and to avoid the need of evacuation in the worst incident case. The main requirements are effective methods for reducing the presence of tritium in the components extracted for disposal and the identification of appropriate disposal and recycling steps.

6. **Integrated EU-DEMO design**: ITER and DTT construction will carry several benefits in combining the fusion technologies, materials and plasma knowledge into an integrated EU-DEMO design. EU-DEMO, with respect to ITER, will add the self-sufficient tritium producing blanket and more efficient technical solutions for the remote maintenance. A proper level of reliability and availability is one of the primary key goals for the nuclear fusion economic attractiveness. Moreover, EU-DEMO will be provided with a complete Balance of Plant, including the heat transfer and the associated electrical generation systems.

7. **Economical electricity production**: fusion power plants have to be cost-attractive to play a significant role in the future energy production scenery. Although this is not a primary goal for EU-DEMO, the perspective of economical electricity production from fusion has to be set as a target minimising the EU-DEMO capital and operational costs as a first step. To aim at a credible basis for commercial energy production and transfer to industries, design solutions that demonstrate a reliable plant with a high availability are pursued.

8. **Stellarator maturity**: a specific mission has been defined to bring the stellarator line to maturity as a possible long-term alternative to tokamaks. Nevertheless, their physics knowledge level doesn't meet the requirement of electricity production in the second half of the century. Meanwhile, they are providing scientific and technology information useful also for the tokamaks.

1.4 Disruptions

The tokamaks are promising device for achieving controlled nuclear fusion. Despite significant progress achieved in tokamak research and development, still several open issues need to be addressed to make fusion power a reality. Some of the key challenges that the tokamaks must face are: plasma confinement and stability, plasma heating and current drive, power plant engineering and economics, material for high neutron flux environment, nuclear waste decommissioning and fusion power demonstration (economic feasibility).
The operating scenarios foreseen for future tokamaks require to control with enough precision and reliability highly unstable and strongly shaped plasmas. Nevertheless, accessible operative conditions of tokamaks are highly restricted by disruptive events. The grow of plasma instabilities and uncontrolled transient can sometimes cause the loss of plasma confinement leading to a sudden energy ejection with a premature termination of the discharge resulting in a fast quench of the plasma current. During a disruption, in a short-time interval, first wall materials have to withstand a large heat load, then the quench of the plasma current induces eddy currents on the surrounding metallic structures, leading to high electromagnetic (EM) forces. As summarized in [7], the main factors triggering disruptions are known to be: 1) mode lock; 2) density limit; 3) high radiated power; 4) H/L mode transition; 5) internal transport barrier; 6) vertical plasma

column displacement. When disruptions are studied in terms of precursor and/or thermal and electromagnetic loads it is important to distinguish between vertical displacement events (VDEs) and Major Disruptions (MD).

- **VDE**. VDEs are one of the most common disruptions in tokamaks triggered by a loss of the electromagnetic control. They are characterized by a rapid downward movement of the plasma column, caused by instabilities in the plasma [8]. The movement of the plasma can lead to a collision between it and the divertor or other components, potentially causing several damage since VDE occurs with an high plasma current value. To mitigate the effects of VDEs, researchers are investigating advanced magnetic control techniques and developing real-time control systems to respond quickly and stabilize the plasma column.
- **MD**. MD are triggered by various factors such as mode locking, density limit, H/L mode transition, internal transport barrier and interaction with impurities [8]. During a MD, the released energy can lead to intense heat on the limiter and first wall, potentially causing severe damage. The challenge in dealing with MD lies in predicting and avoiding them. Researchers are exploring advance diagnostics and machine learning techniques to detect pre-disruptions signals, enabling timely measures to prevent or mitigate major disruptions.

Despite the MDs are commonly considered the most severe plasma perturbations, VDEs produce the highest electromagnetic loads occur since a vertical plasma displacement occurs while the plasma current value is still high. The knowledge of these thermal and electromagnetic loads due to the disruptions is a requirement to project future machine as ITER or EU-DEMO. Disruptions may lead also to deconditioning and therefore long periods of time may be necessary for recovering the optimal operational conditions. Thus, in future tokamaks, disruptions pose significant threat to reliability (due to the production failure) and to the capital return (caused the reduced device lifetime) of the tokamak reactor. EU-DEMO must prevent the disruptive process to a much greater extent than any tokamak.

1.4.1 Disruptions studies in view of EU-DEMO

EU-DEMO is an important step in the roadmap towards commercial fusion power. As a fusion demonstration power plant, EU-DEMO is expected to operate at higher power and longer

pulses than previous tokamaks, like ITER. During disruptions, especially during VDE, strong eddy currents are induced on the conductive materials surrounding the plasma. These currents generate strong EM loads that need to be predicted to support the EU-DEMO Research & Development (R&D) activities. Indeed, the design activities of the EU-DEMO limiter structures require a deep understanding of the effects induced by plasma perturbations. Thus, experimental plasma perturbations from present days tokamak have to be properly scaled to EU-DEMO to be simulated to predict EM loads on EU-DEMO limiter and to conduct a good design strategy. Lessons learned from disruptions in current tokamaks play a crucial role in informing the design and operational strategies for EU-DEMO limiter design. International collaboration and data sharing among tokamak experiments is crucial in advancing our understanding and mitigation of disruptions in future fusion devices. In this thesis an inter-machine database of EU-DEMO relevant plasma perturbations and scenarios has been built in order to support EU-DEMO R&D activities. The database contains VDE, MD, minor disruption (mD), QDN configuration, experiments with tungsten accumulation in the core, both from AUG and JET and Flux Pumping eligible experiments from JET. The methodology and the algorithms developed to populate the database are explained in the chapter 2 and discussed in [9].

Therefore, disruptions are a greater concern for the overall integrity of EU-DEMO. In the last years it has become evident that to optimise the mitigation strategy it would be important also to predict the type and not only the imminence of a disruption [10]. However, disruption present several difficulties in theoretical modeling. A surveying picture of the causes generating disruptions in JET [11] showed that they are structured in highly complex patterns of chain events. Automatic machine learning techniques have proved to be able to tackle with this complexity [10]. These methods extract the useful information from complex combinations of several plasma diagnostic parameters related to several destabilizing factors. In these approaches, the disruptions can be considered to be triggered by an initiating event with subsequent precursors. For example, the Multifaced Asymmetric Radiation From the Edge (MARFE) is a plasma instabilities that have to be suppressed to avoid the disruptions, thus predicting the MARFE evolution enables to develop a mitigation strategy allowing the disruption prevention. Indeed, in this thesis a machine learning approach has been trained at AUG to provide automatic real-time tracking of the MARFE evolution able to trigger MARFE mitigation strategy. This work is presented in chapter 3 and discussed in [12] and [13].

In addition, the long and safe operations foreseen for EU-DEMO require also a good feedback control of the plasma shape and position. Commonly, the plasma boundary is defined as the Last Closed Magnetic Surface and its the determination is a crucial point for the feedback control. In this thesis, a characterization of the error on the plasma boundary inverse reconstruction, from in-vessel pick-up coils magnetic measurement, in presence of white noise effect has been conducted. This work aim to optimize the inverse boundary reconstruction required for the feedback control of plasma shape and position. The work has been conducted on DTT, who will play a key role in the data extrapolation to EU-DEMO, since no actual device can operate with an heat-load comparable with the one foreseen for EU-DEMO. This activity is described in chapter 4 and also discussed in [14]

Chapter 2

Inter-machine experimental database of EU-DEMO relevant scenarios

According to the Roadmap to Fusion Electricity [15], a Pre-Conceptual Phase (PrCP) of the Research & Development (R&D) activities has been defined for the period 2014–2020 in order to investigate several alternative plant architectures to be analyzed in parallel for the definition of a set of possible EU-DEMO plant solutions. Only in the conceptual phase (from 2021 to 2027), a down selection at plant level will be done arriving at the end of 2027 with the conceptual design of one reference EU-DEMO plant. Finally, an engineering phase will follow up to the start of the EU-DEMO construction after 2040[16]. The EU-DEMO design is expected to benefit largely from the experience gained with ITER construction and operation [17]. Nevertheless, with ITER alone, the confidence level in achieving EU-DEMO operating goals has been quantified in [18] and is unacceptably low (¡ 1 %). Indeed, fusion technologies, materials, plasma conditions and scenarios foreseen for EU-DEMO have to be tested in actual machines and scaled to EU-DEMO dimension, power and magnetic configurations. Thus, in this thesis an inter-machine database of EU-DEMO-relevant scenarios has been constructed to support the EU-DEMO design activity. This database has been constructed to support three different R&D activities:

- Design of the EU-DEMO limiter structures: a deep understanding of the effects induced by

transient plasma perturbations (TPP), such us Edge Localized Mode (ELMs) [19], transitions from high to low confinement modes and vice versa (H-L/L-H transitions) [20] and minor disruptions (mDs)[21], is needed. Indeed, TPPs often cause variations of the plasma internal parameters and, consequently, to a plasma displacement [22] which may lead to high control efforts by the vertical stability (VS) system. Moreover, in EU-DEMO, PF coils are expected to be at large distance from the plasma implying a less effective passive stabilization of the VV and a more needed power for the plasma vertical position control, especially during such off-normal condition. The natural vertical instability of the plasma coupled with the TPP could lead, ultimately, to a Vertical Displacement Event (VDE) with a collision between the plasma and the upper or lower part of the plasma facing components (PFCs), with subsequent currents induced into the VV conductive materials. The magnetic field of tokamaks, combined with these currents, generates strong Electro-Magnetic (EM) loads during the VDE that are crucial for the EU-DEMO limiters design. Thus, 2D/3D electromagnetic simulations [23–26] are essential to understand the implication of these transients on the plasma vertical stability. To this purpose, an inter-machine experimental database of TPP has been built considering JET and AUG experiments. In both these machines, several TPPs have been observed, such as (ELMs), H-L/L-H transitions and mDs. Thus, in section 2.1 the collected TPPs will be described among with the algorithms developed for their automatic detection and the conducted simulation to compute EM loads will be briefly presented.

- Study of tungsten (W) Plasma Facing Component effects on plasma performance: in a fusion reactor, a central W concentration of only $3 \cdot 10^5$ increases the minimum triple product for ignition nT_{τ_e} by 20% and at $1.9 \cdot 10^{-4}$ the ignition condition can not be reached [27]. Tungsten is used as a plasma facing component in today's experiments, e.g. ASDEX Upgrade [28] and JET [29], and one objective is to quantify the mechanisms that determine the W concentration in the plasma, when using W as a first wall material. While a stepwise transition at ASDEX Upgrade allowed to document the relative importance of various components for a full W device JET's ITER-like wall was implemented during one shut down allowing an easier comparison with the previous carbon plasma facing components (PFCs). Tungsten is foreseen as plasma facing material in next generation tokamaks (ITER/EU-DEMO) due to better properties: high melting point, capable of

sustaining high heat and particle fluxes from the core, low erosion rates and limits the fuel retention which is, in particular, relevant to prevent radioactive tritium accumulation in the wall components [27]. In view of these overall good qualities and the need to gather experience on tokamak operation with W plasma facing components, in AUG [28] and JET [29] have been already operated for several campaigns with a full W wall and a W divertor respectively, and WEST is recently operating with a W wall as well [30]. Experiments in AUG [28] and JET [29] have shown that the presence of W significantly affects plasma operation. Thus, in section 2.2 the methodology used to build a database of JET and AUG experiments with a tungsten accumulation in the plasma core will be described.

- Identification of the best scenarios: the appropriate and best performing plasma scenarios are under study. In particular the high performance advanced tokamak scenarios are very attractive for future burning plasmas. Among the scenarios running in the operative tokamaks, those having performances intermediate between the standard H-mode and the steady state advanced tokamak scenario, called "HyBrid" scenarios (HB), are candidate to as EU-DEMO one. HBs can be achieved stabilizing the sawtooth instability, which would reduce performance and trigger other deleterious modes [31, 32]. The sawtooth stabilization can be obtained by elevating the central q-profile to values around unity [33]. This flat and elevated central q-profile, due to MHD modes that modify the current profile [34, 35], can be observed in high-β_N plasmas. This self-regulating mechanisms, triggering anomalous evolution of the magnetic flux, can be referred to by the general term "magnetic flux pumping" or "flux pumping". The flux pumping has been observed in dedicated AUG and DIII-D experiments [34, 36]. In section 2.3, JET pulses in hybrid scenario have been investigated in order to obtain a set of scenarios for dedicated experimental campaigns and prove the existence of the flux pumping mechanism in the JET machine.

2.1 Plasma perturbations

For studying the TPP effect on VDEs, ELMs, L-H/H-L transitions, mDs and VDEs have been selected from JET and AUG experiments in standard SN and in QDN configurations, with the aim to characterize the plasma perturbations in terms of vertical position and internal

parameters variation [9]. The algorithms developed to support the realization of the datasets are presented in the following sections.

2.1.1 Vertical Displacement Event (VDE)

Elongated plasmas need a feedback control of the vertical position since the loss of the control causes hot VDEs. Even when the vertical instability is not the primary reason of the disruption itself, the fial loss of the plasma current is often assiocated to a VDE. Large vertical displacements are characterized by a sudden and large change of plasma parameters which, among others, affects the vertical feedback control. Plasma disruptions are usually classified, according to [20], considering the plasma position at the thermal quench (TQ) and they can be divided in two main categories, Major Disruption (MD) and Vertical Displacement Event (VDE):

- **MD**: when the thermal quench occurs with the plasma close to its neutral position (Central Disruptions) and a loss of position control is often experienced after the thermal quench (cold VDE).
- **VDE**: in Up and Down VDE (UVDE and DVDE), a loss of position control destabilizes the plasma before the TQ, occurring when the plasma touches the wall or at a given critical safety factor.

In [9] disruptions have been labelled from the perspective of the vertical displacement event occurrence and taking into account the Massive Gas Injection (MGI) system action, as follows:

- Type 1 VDE is the so-called hot VDE: a large plasma vertical displacement (several centimetres) induces a MD and the MGI (if any) follows the MD, as in the example reported in Figure 2.1 for an AUG pulse. The blue line reports the plasma current; the dashed red line indicates the time when the final collapse occurs, assumed as disruption time t_D, and the brown line reports the actual plasma vertical position Z_c. In this case no action is taken by the MGI system.

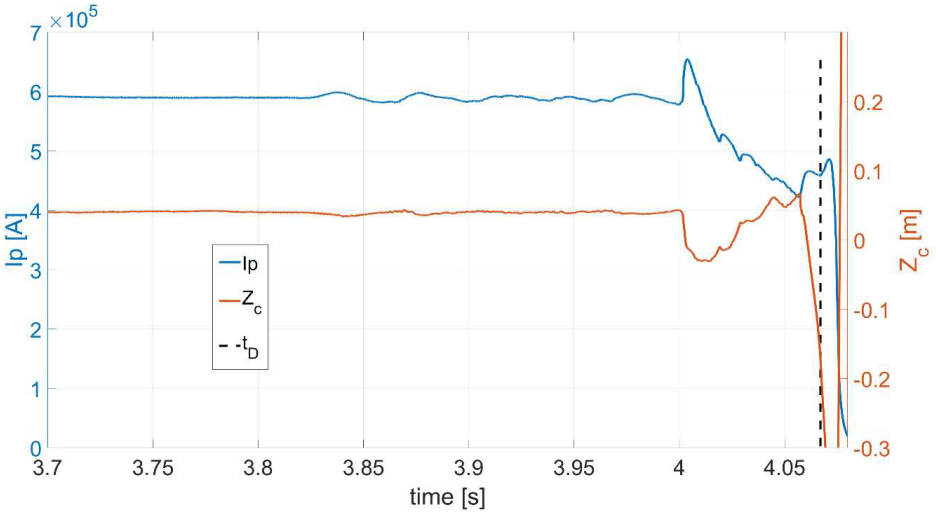

FIGURE 2.1: AUG pulse #29462, Type 1 VDE. A deviation larger than 15 cm of Z_c (brown line) is reached at the disruption time highlighted with a red dashed line on the plasma current (Ip) evolution (blue line). In Type 1 VDE, a large vertical displacement induces the disruption. No action is taken by MGI.

- Type 2 VDE: a large plasma vertical displacement activates the MGI that, in turn, induces a disruption. In Figure 2.2, an example of a disruption induced by the killer gas injection at AUG is shown. The potential consequences of a downwards movement of the plasma column are prevented by the MGI. The dashed green line in Figure 2.2 indicates the killer gas puffing onset (t_{kG}); in 3 ms, this results in a disruption (black dashed line).

- Type 3 VDE is the so-called cold VDE: a large vertical displacement follows a MD and the MGI (if any) is triggered in the late Current Quench (CQ). In Figure 2.3, a Type 3 VDE at JET is shown: the killer gas puffing onset (green dashed line) follows the large vertical displacement due to the disruption (black dashed line).

Another type of VDE (Type 4) can be defined when the MGI follows the disruption and precedes the VDE, but it is not interesting for the present study because the VDE is affected by the MGI. Referring to the ITER Physics classification [20], Type 1 and Type 2 fall into VDE category, whilst Type 3 and Type 4 fall into MD category. Note that, no distinction has been made between upward and downward displacement in [9].

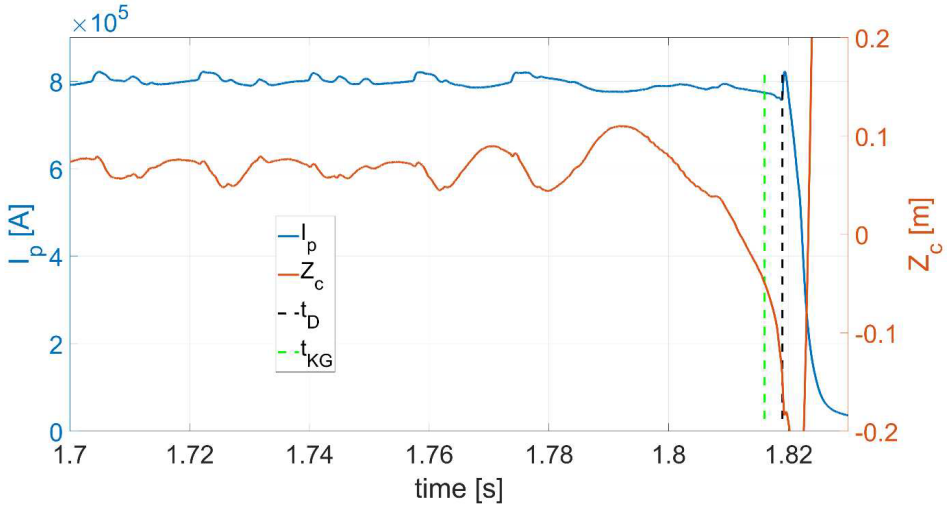

FIGURE 2.2: AUG pulse #29515, Type 2 VDE. A deviation of Z_c (brown line) of about 10 cm activates the MGI system (green dashed line), in turn inducing the disruption highlighted with a black dashed line on the plasma current (Ip) evolution (blue line). In a Type 2 VDE, the MGI interrupts a larger vertical displacement.

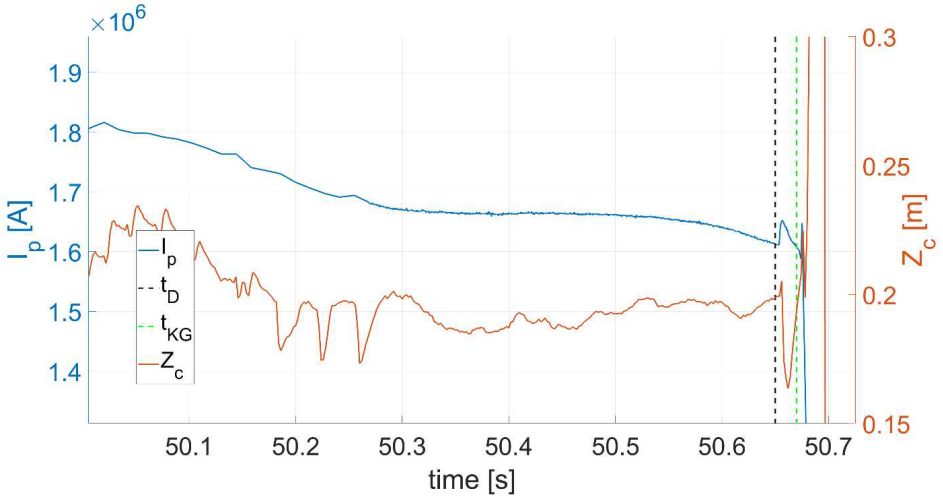

FIGURE 2.3: JET pulse #92100, Type 3 VDE. A large deviation in Z_c (brown line) is observed after the disruption time (black dashed line) during the CQ phase (blue line). The MGI is activated during the CQ. In a Type 3 VDE, a large vertical displacement is induced by a MD.

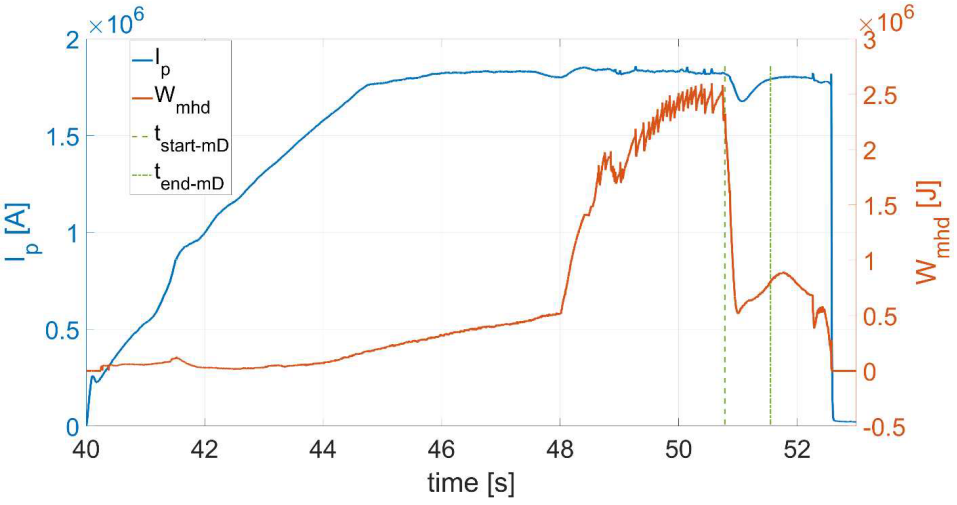

FIGURE 2.4: JET pulse # 89604: flat-top minor disruption.W_{mhd} in brown, I_p in blue, mD starting ($t_{start,mD}$) and ending ($t_{end,mD}$) times are indicated by the dashed and dot green vertical lines.

2.1.2 Minor Disruptions (mD)

A minor disruption (mD) is characterized by a temporary degradation of the plasma energy confinement, however the stored energy ($Wmhd$) is not completely released and an ohminc heating recovering of the discharge is observed [23]. In the Figure 2.4 a minor disruption occurring during the flat-top phase of a JET pulse is reported; it starts at 50.8 s ($t_{start,mD}$, dashed green vertical line), the energy is recovered at ($t_{start,mD}$), dashed green vertical line), and a MD follows it approximately 1 s later. Both $t_{start,mD}$ and $t_{start,mD}$ have been automatically detected by a developed algorithm. Similarly to the MDs, the starting of a mD results in a plasma current (Ip) drop corresponding to a sudden variation of the internal inductance (l_i) and a plasma energy drop ($Wmhd$). A mD is completely recovered when the realese of $Wmhd$ stops and the plasma current is resumed.

2.1.3 L-H/H-L transition and ELMs

A good confinement is crucial to achieve the high densities required for a sufficient production of energy and good fusion performance. The high confinement mode (H-mode) is the foreseen operational scenario for EU-DEMO, ITER and future fusion power plants. The H-mode is characterized by high density and pressure gradients at the plasma edge and by the presence

of Edge Localized Modes (ELMs). The ELMs are fast MHD instabilites (ms) during with a loss of energy and particles from the edge is observed [21]. In [9], both L-H/H-L transitions have been classified as slow or fast according to the methodology reported in [29, 37] and have been selected from dedicated experiments detailed in [29]. Figure 2.5 shows an example of slow L-H/H-L transitions for a JET pulse. The Figure 2.5 report, from top to bottom, the NBI power (P_{NBI}), the photon flux near the divertor target plates (D_α), the average electron density (n_e), and the diamagnetic energy (W_{DIA}) repelled by the plasma. The slow L-H transition is experimentally obtained by a slow increase of the additional power injected into the plasma, and it is characterized by a pronounced increase of n_e and W_{DIA}, followed by an increase of D_α [24]. On the other hand, a fast L-H transition is obtained by a fast increase of the additional power injected into the plasma and is characterized by a sharp increase of n_e and W_{DIA} and an increase of D_α [38]. The above mentioned increases are shown in Figure 2.6 in correspondence of the first vertical red dashed line. On the contrary, a fast H-L transition follows a decrease of the additional power injected into the plasma and is characterized by a sharp decrease of n_e and W_{DIA} and a decrease of D_α [38] (see the second vertical red dashed line). The ELM perturbation database has been populated with what reported in the reference experiments [29].

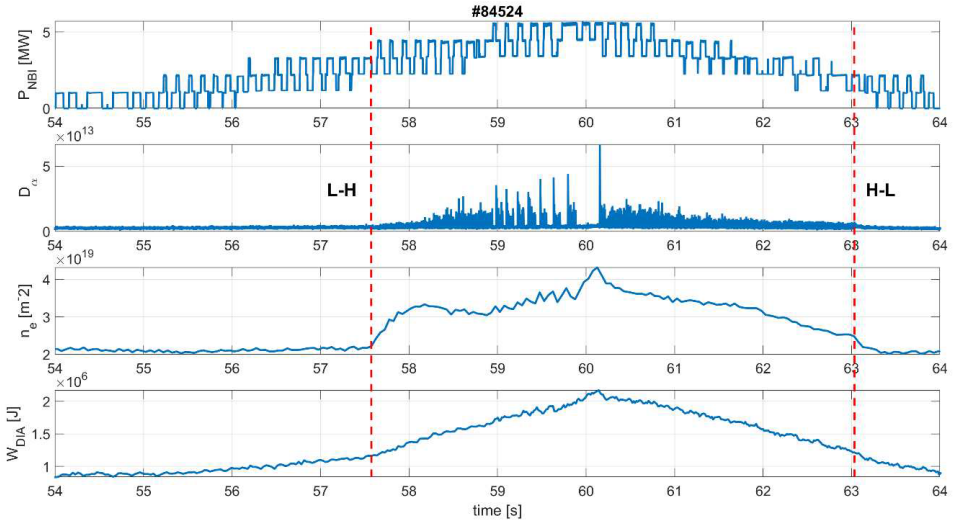

FIGURE 2.5: JET pulse # 84524: slow L-H and H-L transitions. Total heating power (top row), D_α (second row) in a.u., average electron density (third row) and diamagnetic energy repelled by the plasma (bottom row). The vertical dashed red lines indicate the slow L-H and H-L transitions.

Typically, the effect of the L-H/H-L transitions and ELMs on β_{pol} and Z_c parameters for the selected JET discharges can be summarized as in [9]:

- SLOW L–H/H–L: small variation of the poloidal beta ($\Delta\beta_{pol} \approx 5\%$)that leads to a small variation of the vertical position of the plasma centroid ($\Delta Z_c \approx 1$mm).
- FAST L–H/H–L: high variation of the poloidal beta ($\Delta\beta_{pol} \approx 50\%$) that leads to a small variation of the vertical position of the plasma centroid ($\Delta Z_c \approx 6$mm).
- ELM: moderate variation of the poloidal beta ($\Delta\beta_{pol} \approx 20\%$) that leads to a high variation of the vertical position of the plasma centroid ($\Delta Z_c \approx 40$mm).

The identification of end points of the H-mode time window (i.e.,the L–H transition start and the H–L transition end) for both slow and fast transitions has been performed by manually analysing the time traces of the parameters shown in Figures 2.5 and 2.6 following an approach similar to what discussed in [39]. The time instants are identified as those when a change in the slope of electron densities (n_e) and diamagnetic energy W_{DIA} (positive for L–H and negative for H–L transitions) occurs, together with a drop or a step up into D_α signal, for the L–H and the H–L transitions,respectively.

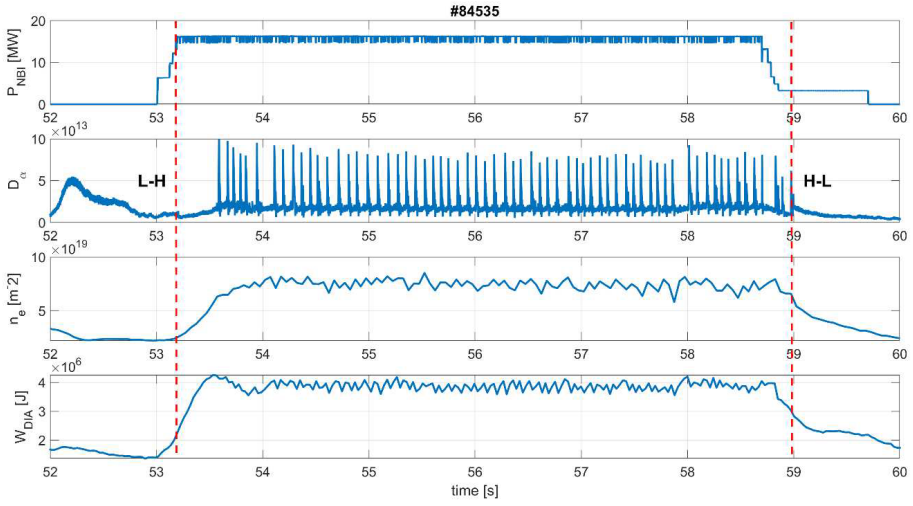

FIGURE 2.6: JET pulse # 84835: fast L-H and H-L transitions. Additional Power (top diagram), D_α (second top diagram) in a.u., average electron density (third top diagram), diamagnetic energy repelled by the plasma (bottom diagram) in a significant time window. ELMs have been observed during the H-mode phase. The vertical dashed red lines indicate the fast L-H and H-L transitions.

2.1.4 Algorithms for database construction

Several algorithms have been developed to support the construction of the inter-machine databases presented in this thesis. In this section the algorithms providing general information, such as characteristic times and phases (flat-top, thermal quench and current quench), the killer gas puffing onset and the plasma configuration, are presented. Moreover, the databases presented in this chapter collect information about the additional heating powers and the values of the main plasma parameters in prefixed time windows.

2.1.4.1 Characteristics times

To construct a database that collects plasma perturbations occurred in the plasma current flat-top phase, the first step is to identify the flat-top according to the discharge termination behaviour (regular or disrupted). If the pulse is regularly terminated, the plasma current flat top is defined by two time instants: the starting time t_0, which represents the end of the ramp up phase, and the ending time t_f, which represents the start of the ramp down phase. Differently, if the discharge disrupt, the flat top ending time is the disruption time t_D, which has been assumed within the Current Quench (CQ) phase.
Thus, an algorithm for the automatic flat top identification has been developed. The first step is the t_0 detection, this has been carried out optimizing a threshold on the time derivative value of the pre-programmed current, which defines the minimum slope for the ramp-up phase. In its second step the algorithm detects all the current spikes with a slope larger than an optimized threshold and presenting an absolute value of l_i time derivative larger than a certain threshold (in time window of the current rising phase). Finally, the disruption time t_D is defined as the starting time of the current spike presenting the largest percentage variation of l_i and I_p. Since not all the VDEs CQ are preceded by a plasma current spike, if no t_D is detected so far, a check is performed on the CQ rate. If the CQ slope is higher than an optimized threshold, the discharge is assumed to be a VDE, and the last time instant of the flat top is assigned as t_D. Otherwise, the discharge is regularly terminated, and the final point of the flat top is labelled as t_f. After detecting the flat-top phase, the starting and the ending time of CQ ($t_{start,CQ}$, $t_{end,CQ}$) are selected based on both the value of the I_p time derivative and the I_p fraction value, which is evaluated with respect to the I_p flat-top value.

To optimize the different thresholds used in the algorithm, the characteristic times in a set of discharges in the database have been manually identified, and the corresponding thresholds have been selected by minimizing the errors made using the automatic identification of the aforementioned times.

2.1.4.2 Massive Gas Injection Time

At JET and AUG, three valves are used for the killer gas puffing. In this thesis, an algorithm for the automatic detection of the time when the killer gas is injected into the vessel (t_{kG}) has been developed: t_{kG} is assumed as the time when a sudden change in the killer gas pressure occurs, shortly after the MGI trigger onset for AUG, and after the MGI power system shutdown for JET.

2.1.4.3 Plasma configuration

Double Null (DN) configurations seems to be promising in EU-DEMO [24] thanks to the up-down vertical symmetry of the plasma (and the structures) which reduce the vertical unstable mode from the plasma perturbations. Due to this, there is an interest in the evaluation this effect in realistic conditions in the present day tokamaks, where a certain up-down asymmetry of their passive structures is present [24, 40] making a DN configurations not available for JET and AUG experiments. However, a selection of mDs and VDEs occured in Quasi-Double-Null (QDN) configurations has been carried out. The QDN configuration is characterized by a main Lower or Upper Single Null (LSN and USN) and a second null which not generate an X_{point} but increase plasma elongation and triangularity up to value comparable with the DN scenarios. In the provided database all the discharge presents a dominant LSN and in this thesis the LSN and the second null position are indicated as $X_{p,l}$ and $X_{p,u}$. Labelling if the plasma is in SN or QDN configuration is another key information collected in the inter-machine database. Since the information about the QDN configuration, during the phase of interest, was not available at JET, an algorithm has been developed to automatically provide it by meaning of the projection of the $X_{p,l}$ and $X_{p,u}$ on the poloidal plane. The tracking of time variation of the $X_{p,l}$ and $X_{p,u}$ positions with respect to the wall boundary easily allow the detection of the time instant when the $X_{p,u}$ leaves the vessel. The monitoring of the plasma configuration and the automatic

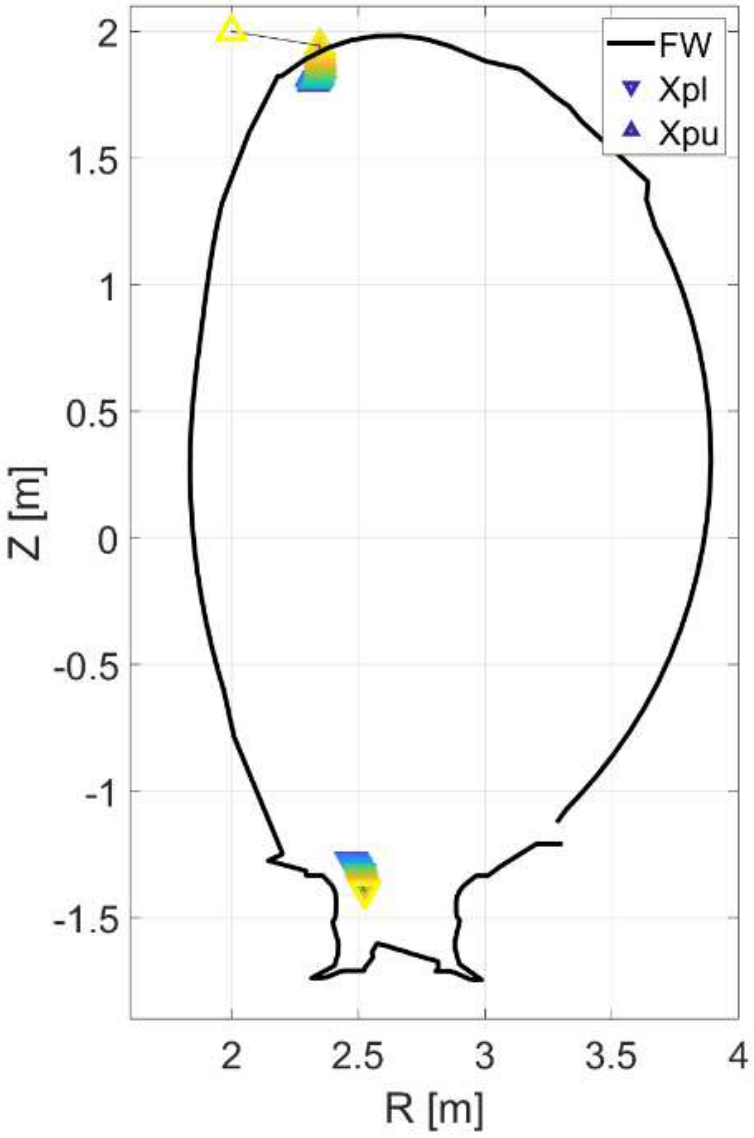

FIGURE 2.7: JET-CW pulse #68808: tracking of both the lower and upper X_{point} positions with respect to the JET-CW boundary on R-Z plane. The shade from blue to yellow tracks the upper and lower X_{point} positions during the minor disruption. The QDN configuration is lost at 47.02s when the upper X_{point} trajectory overcomes the first wall boundary.

detection of the time instant when the QDN configuration is achieved or lost can be easily performed by means of the control of this information together with the minimum value reached by the triangularities (upper and lower, δu and δ_l respectively) and by the elongation (k). The reference values needed for elongation and triangularities to achieve the QDN are reported in [40] for both JET and AUG. Figure 2.7 tracks the lower and upper null positions ($X_{p,l}$ and $X_{p,u}$ respectively), by a shade from blue to yellow, on the JET C-Wall boundary for pulse #68808,

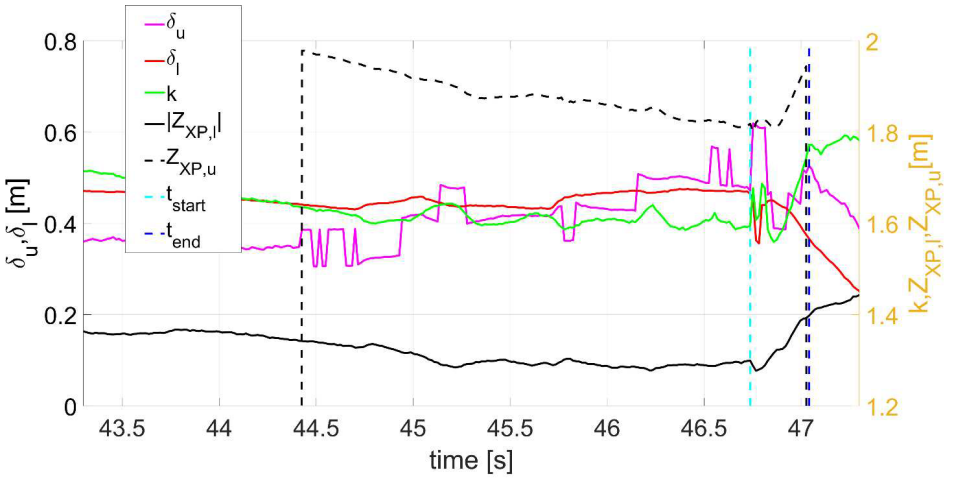

FIGURE 2.8: JET-CW pulse #68808: the behavior of triangularities (magenta and red lines for δu and δ_l respectively), elongation k (green line), $Z_{xp,u}$ and $Z_{xp,l}$ (solid and dashed black lines respectively), $t_{start,mD}$ and $t_{end,mD}$ (cyan and blue vertical line respectively) during the flat top phase. The QDN configuration is lost at 47.02s when Zxp,u falls down, δu, δ_l, and k deviate from the reference values and the upper X_{point} trajectory overcomes the first wall boundary.

during a mD occurring between 46.74 s and 47.04 s. Figure 2.8 shows the behavior of δu and δ_l (magenta and red lines respectively), k (green line), $Z_{xp,u}$ and $Z_{xp,l}$ (solid and dashed black lines respectively), $t_{start,mD}$ and $t_{end,mD}$ (cyan and blue vertical line, respectively). From 45.35s (QDN achieved) until $t_{start,mD}$, the triangularities and the elongation roughly fit the values indicated in [40]. During the minor disruption, elongation and triangularity values start to deviate from the reference values. At 46.83 s, $Z_{xp,u}$ starts to increase while the upper X_{point} ($X_{p,u}$) approaches the first wall. The QDN configuration is definitely lost at 47.02 s when $Z_{xp,u}$ falls down and the upper X_{point} trajectory goes outside the first wall boundary.
Instead, the information about the QDN configuration drawn from the elongation and triangularities is not supported by projection of the X_{point}s on the poloidal plane for AUG, but it is corroborated by the maximum variation of the distance between the two separatrices, defined by means of the proximity to DN configuration factor which must be lower than 10 mm [40].

2.1.4.4 VDEs detection

In [41], the automatic detection of VDEs at AUG was obtained by evaluating the deviation of the actual vertical position Z_c with respect to the reference vertical plasma position signal

(Z_{ref}). At JET, an algorithm based on the evaluation of the normalized vertical position is proposed in [42]. In [9], a simple approach is proposed to perform both the automatic detection and the classification of VDEs, following the types defined above, for both the considered machines. The algorithm evaluates the absolute deviation of Z_c (Z_c, DEV) from its own mean value in the last time window t_W, at each time. The t_W length and the threshold value discriminate if the VDE occurs before (Types 1 and 2) or after (Type 3) the disruption time and have been optimized for JET and AUG on VDE databases previously manually classified. Finally, the discrimination between Type 1 and Type 2 is performed considering the temporal consecution of t_{kG} and t_D. Note that, the proposed algorithm can be used even when the Z_{ref} signal is not available or if an offset is present.

2.1.4.5 mDs detection

The mD automatic detection is performed by computing the absolute deviation of I_p, l_i and W_{mhd} signals at each time with respect to their own mean values in a previous time window t_W. A minimum and a maximum threshold have been optimized for the deviation of each signal. The time when the three differences exceed their own maximum threshold is assumed as the minor disruption starting time. The energy confinement is totally recovered when the three deviations fall below the minimum values of their own thresholds.

2.1.5 Database structure

To populate the inter-machine database hundreds of discharges from both JET and AUG have been analyzed. Moreover, since QDN configuration is avoided in JET ITER-Like Wall (JET-ILW) due to the fragile ILW metals, both JET-ILW and JET Carbon Wall (JET-CW) experiments have been analyzed considering a set of discharges in QDN performed in 2006 [43]. In Table 2.1 the characteristic times provided in database are summarized. Table 2.1 summarizes the characteristic times provided in the databases. For each pulse affected by the considered perturbation, information to identify the flat top phase (t_0, t_f or t_D) are provided. In addition, the CQ times ($t_{start,CQ}$, $t_{end,CQ}$) and the intervention of MGI system time (t_{kG}) are also provided for VDEs. For mDs and ELMs, the starting and the ending time of the perturbation are reported. For L-H and H-L, the transition time is provided. Moreover, a reference time (t_{ref}) when the values of the plasma parameters are provided, is defined for each perturbation; in particular, VDEs reference time is defined based on the classification reported in section 2.1.1. In addition, for VDEs and mDs, the time of the last L-H or H-L transition preceding the perturbation (if any) is given.

TABLE 2.1: Characteristc times for puses containing VDEs, mDs, L-H, H-L and ELMs.

Time	**VDEs**	**mDs**	**L-H/H-L**	**ELMs**
Characteristic times	t_0; t_D; $t_{start,CQ}$; $t_{end,CQ}$; t_{kG} (if any)	t_0; t_f (or t_D); $t_{start,MD}$; $t_{end,MD}$	t_0; t_f (or t_D); t_{LH}; t_{HL}	t_0; t_f (or t_D); $t_{start,ELM}$; $t_{end,ELM}$
Reference time t_{ref}	Type 1: t_D Type 2: t_{KG} Type 3: t_D	$t_{start,mD}$	L-H: t_{LH} H-L: t_{HL}	$t_{start,ELM}$
Last H-L transition (if any)	$t_{start,HL}$	$t_{start,HL}$	-	-
Last L-H transition (if any)	$t_{start,LH}$	$t_{start,LH}$	-	-

The study presented in [9] and reported in section 2.1.6 aims to characterize the magnitude of the plasma vertical displacement with respect to the main plasma parameter variations and time derivatives during both L-H and H-L transition and ELMs. To this aim, the built database contains the maximum variation, within a prefixed time window (for each L-H/H-L transition and ELM), of the main plasma equilibrium parameters (l_i, β_{pol}, Ip and Z_c) as reported in Table 2.2. The considered time window depends on the perturbations considered. For both slow and fast L-H/H-L tranistion a time window lasting 200 ms around the transition time has been considered. Instead, for the ELMs, the time window has been considered as the ELM transientr ($t_{start,ELM} \div t_{end,ELM}$). More than 300 JET discharges have been analyzed to populate the

perturbation database, from specific experiments dedicated to L-H/H-L transition and H-mode scenario development in the presence/absence of impurities and in the presence/absence of pellets [37, 38]. Finally, about 60 discharges characterized by the following features have been selected:

- low and high triangularity.
- plasma current ranging between 1.8 and 3 MA.
- SN configurations.

TABLE 2.2: Plasma parameters provided in the experimental database for L-H, H-L transitions and ELMs.

Plasma parameters	**L-H,H-L**	**ELMs**
Maximum variation of I_p, l_i, β_{pol}, Z_c	in the time window $(t_{ref} - 0.1s \div t_{ref} + 0.1s)$	in the time window $(t_{start,ELM} \div t_{end,ELM})$
Plasma configuration	at t_{ref}	at t_{ref}

Since the study aims to extrapolate to EU-DEMO the transient evolution, both in terms of plasma perturbations and trajectory of the plasma column to evaluate electro-magnetic loads, EU-DEMO-relevant VDEs and mDs have been selected from the built database. First of all, ohmic discharges have been discarded and only mDs with a maximum plasma energy variation larger than 50% have been considered. The EU-DEMO-relevant constraints have been applied on the remaining perturbations considering a safety factor $q95 = 3 \div 4$ and a high value of the Greenwald fraction (f_{GRW}). As effect of the density peaking, the low collisionality and the fast particles in the turbulence stabilization, EU-DEMO aims at fGRW of about 1.2 [44]. However, present days reactor are not able to achieve such a value, thus the Greenwald fraction constrain has been set as $f_{GRW} > 0.7$. To apply the EU-DEMO-relevant constraints, the mean value of $q95$ evaluated in the last 500 ms before the perturbation has been considered to select the subset of EU-DEMO relevant perturbations. Regarding the Greenwald fraction constraint, an in-depth analysis showed that most of disruptions are characterized by high variability of the Greenwald fraction signal in the last 500 ms before t_D. For this reason, its average or its value at t_D are not representative of the signal behaviour before the perturbation and the maximum value of the f_{GRW} ($f_{GRW,max}$) has been considered as EU-DEMO relevant constraint, for both VDEs and mDs.

In the database provided in [9], the perturbations are featured by the values of I_p, l_i, β_{pol}, Z_c

and R_c at the reference time and/or their variations (in a prefixed time window). In addition, information about powers from each additional heating system is provided. Finally, the triangularities and the elongation, the upper and lower X_{point} poloidal position, and the maximum variation of the radial separation of the two separatrices are given for discriminating among the different plasma configurations, together with the configuration at the reference time, as detailed in Table 2.3. The resulting VDE databases contains six Type 1 and thirty Type 3 SN pulses

TABLE 2.3: Plasma parameters provided in the experimental database for VDEs and mDs.

Plasma parameters	**VDEs**	**mDs**
I_p, f_{GW}, ΔZ_c and ΔR_c	value at t_{ref}	value a t_{ref}
I_p, l_i, β_{pol}	maximum variation in the time window $[t_{ref} - 0.5s, t_{ref}]$	maximum variation in the time window $[t_{ref} - 0.5s, t_{ref}]$
q_{95}	mean value in the time window $[t_{ref} - 0.5s, t_{ref}]$	mean value in the time window $[t_{ref} - 0.5s, t_{ref}]$
f_{GW}	maximum and mean values in the time window $[t_{ref} - 0.5s, t_{ref}]$	maximum and mean values in the time window $[t_{start,mD}, t_{end,mD}]$
NBI, ECRH, and ICRH power	value at t_{ref}	maximum value in the time window $[t_{start,mD}, t_{end,mD}]$
Plasma configuration	at t_{ref}	at t_{ref}
δ_u, δ_l	mean value in the time window $[t_{ref} - 0.5s, t_{ref}]$	value at t_{ref} mean value in the time window $[t_{start,mD}, t_{end,mD}]$
Upper and lower X_{point} vertical and radial position	value at t_{ref}	value at t_{ref} maximum variation in the time window $[t_{start,mD}, t_{end,mD}]$
Radial separation of the two separatrices	maximum variation in the time window $[t_{ref} - 0.5s, t_{ref}]$	maximum variation in the time window $[t_{start,mD}, t_{end,mD}]$

for JET, where only 6 of them fulfil both the f_{GRW} and the $q95$ constrains; instead, six Type 1, thirty Type 2 and forty-five Type 3 VDEs are available for AUG: thirteen of them are EU-DEMO relevant, seven of which are in QDN configuration. The resulting mD database contains eighteen events for JET: five are EU-DEMO relevant, one of which is QDN configuration; the AUG database resulted in four SN mDs: none of them is EU-DEMO relevant because of the $q95$ constraint, which is always higher than the EU-DEMO relevant upper limit.

2.1.6 Vertical displacement characterization during plasma transients

In [9] the plasma centroid vertical displacement has been characterized by meaning of the database described in Table 2.2. At this purpose, the plasma centroid vertical displacement during perturbations has been correlated to the variation of its internal parameters for JET slow (red points) and fast (blue points) L-H/H-L transitions (red point and blue points in Figure 2.9 and Figure 2.11). Figure 2.9[9] shows a correlation behaviour in terms of β_{pol} and l_i variation

with respect to the variation of the plasma centroid similar to what discussed in [45].

Figure 2.10[9] shows a correlation behaviour in terms of variation of β_{pol} and l_i variation with respect to the variation of the plasma centroid similar to the one discussed in [46] for ELMs plasma perturbations, and discussed for the most recent JET VS system. However, although the correlation in Figure 2.9 and Figure 2.10 do seem to find corroboration in [45, 46], further work would be needed to investigate the explicit parametric dependence between the analysed variables. A similar behavior has been obtained also for H-L transitions, as shown in Figure 2.11. In Figure 2.12, the new discharges have been added to those in Figure 2.9 and marked with a square if an initial strong MHD activity is observed before the L-H transition and with a triangle if not. The VDEs marked with a triangle follow the same behavior shown in Figure 2.9 (remaining inside the region bordered by the orange dashed line ($|\Delta Z_C| \leq 10$ mm). For those marked with a square, a larger variation ($|\Delta Z_C| \geq 10$ mm) of the plasma position is present, falling outside the orange bordered region.

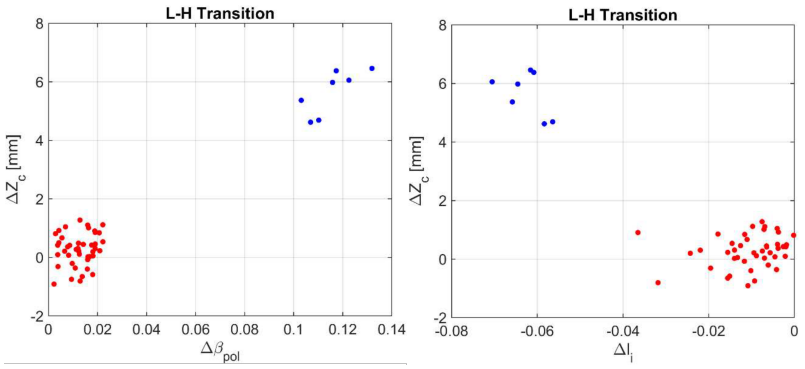

FIGURE 2.9: JET experimental data: Comparison between slow (red) and fast (blue) L-H transitions – plasma centroid vertical displacement versus β_{pol} variation (right plot) and l_i variation (left plot)[9].

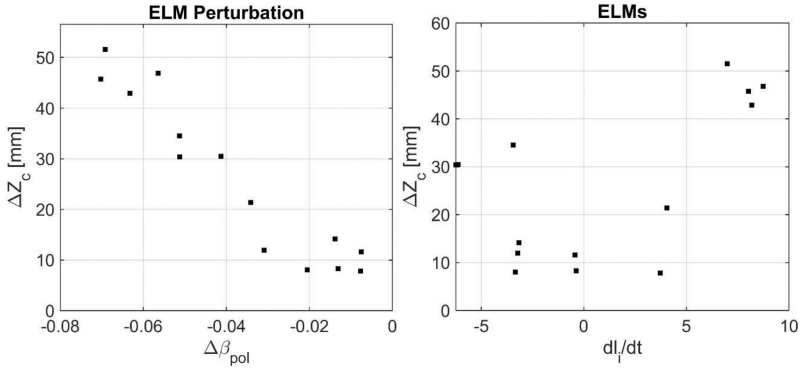

FIGURE 2.10: JET experimental data: ELMs effects on plasma centroid vertical displacement versus β_{pol} variation (right plot) and l_i variation (left plot) [9].

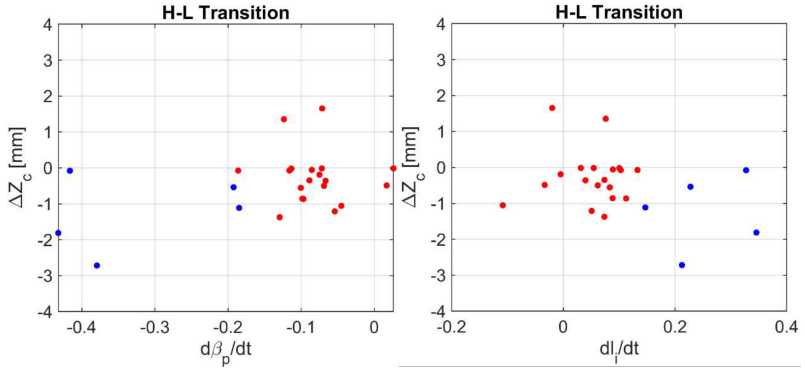

FIGURE 2.11: JET experimental data: Comparison between slow (red) and fast (blue) H-L transitions – plasma centroid vertical displacement versus β_pol time derivative (right plot) and l_i time derivative (left plot) [9].

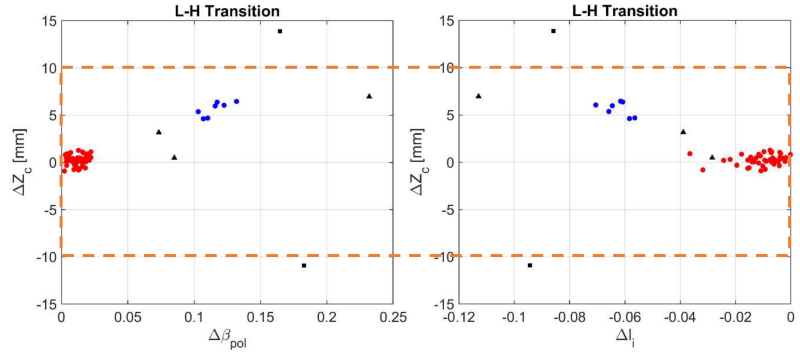

FIGURE 2.12: Comparison between the L-H transitions in Figure 2.9 (blue and red colored points) and VDEs (black colored points) selected from the experimental database detailed in Section 2.1.5: plasma centroid vertical displacement versus variation of a) β_{pol}, and b) l_i.[9]

2.1.7 MAXFEA reconstruction of plasma dynamic behaviour during plasma perturbation phases and scaling to EU-DEMO

MAXFEA has been used in [9] to perform 2D numerical simulations on designed discharges. Thus, a set of disruptions, coming from the provided database, following plasma perturbations adapted to EU-DEMO conditions has been simulated. Both MDs and hot VDEs can follow a plasma perturbation. Usually, MDs are more frequent but also hot VDEs can happen, often when the plasma is perturbated far from the neutral point or when the vertical position controller actuator is working near its limit. From the provided database the following simulations have been conducted through MAXFEA:

- A Type 1 VDE preceded by an H-L transition referring to JET pulse #91991.
- A Type 3 VDE preceded by a mD, referring to JET pulse #92132.

- Type 1 and Type 3 VDEs in SN EU-DEMO configuration, referring to JET pulse #92132.
- A Type 1 VDE preceded by a plasma mD in QDN configuration, referring to JET pulse #68805.
- A Type 1 VDE in QDN configuration preceded by a HL transition and mD, referring to AUG pulse #32120.
- A Type 3 VDE predictive simulation in DN and QDN in EU-DEMO2020 scenario, scaling from JET pulse #68805.

Due to the length of the full treatment, only the predictive simulation will be discussed in this thesis.

2.1.7.1 DN Type 3 VDE predictive simulations in EU-DEMO2020 scenario

A set of disruptions in DN and QDN configurations adapted to EU-DEMO conditions has been simulated by means of MAXFEA code using the recent EU-DEMO 2020 reference geometry [47]. The simulated configurations are a symmetric DN and two QDN, upper and lower (UQDN and LQDN), shown in Figure 40. The symmetric DN EU-DEMO configuration has been developed based on official WPPMI DN @ EOF, whilst the QDN have been modelled moving the secondary null at distance $\Delta_{EU-DEMO}$ from the separatrix. The distance has been scaled from JET (Δ_{JET} = 0.38 m obtained from the CREATE-NL equilibrium reconstruction at 46.6 s for the pulse #68805), and using the equation 2.1:

$$\Delta_{EU-DEMO} = \Delta_{JET} \cdot \frac{R_{0,EU-DEMO}}{R_{0,JET}} \tag{2.1}$$

where R_0 is the related machine major radius, $R_{0,JET}$ = 2.96 m and $R_{0,EU-DEMO}$ = 8.95 m. $\Delta_{EU-DEMO}$ results in 1.15 m.

For each EU-DEMO configuration shown in Figure 2.13, a destabilizing drop of β_{pol} occurring 10 ms after the start of simulation is applied to set up the MD, which is followed by the loss of position control (VDE phase). The CQ durations has been set to ∼78 ms (Fast MD). The halo and eddy currents and the EM loads on VV have been evaluated for a time window lasting 250 ms. The simulation results are shown in Figures 2.14–2.16 for DN, LQDN and UQDN respectively,

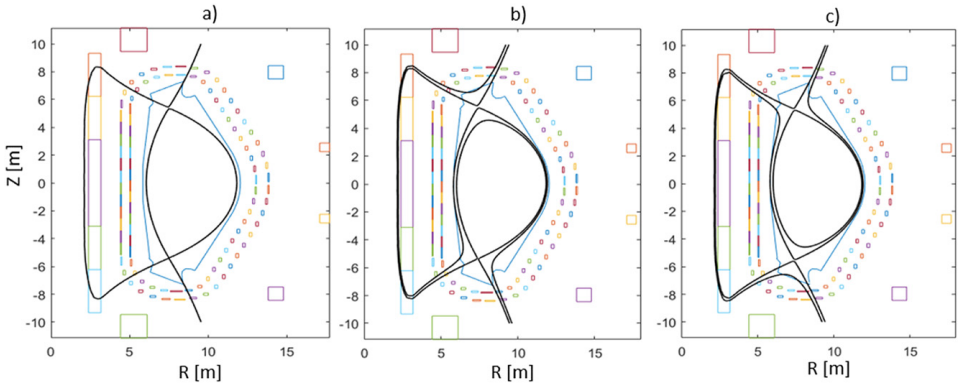

FIGURE 2.13: Simulated EU-DEMO configurations: a) official WPPMI – DN @ EOF symmetric DN, b) perturbed DN: LQDN; c) perturbed DN: UQDN. The perturbed ones have been modelled moving the secondary null at a distance from the separatrix of $\sim$ 1.15 m (from equation (1)).

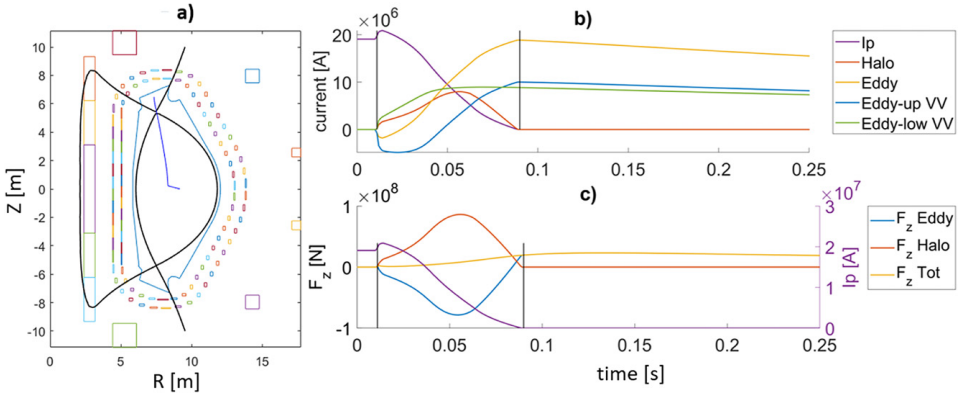

FIGURE 2.14: EU-DEMO DN MAXFEA simulation: a) plasma separatrix at VDE phase starting point (black solid line), plasma trajectory during VDE (solid blue line); b) plasma current (purple line), halo current (red line), overall eddy current (yellow line), upper VV eddy currents (blue line) and lower VV eddy currents (green line); c) EM loads on VV: eddy (blue), halo (red) and the total (yellow) vertical forces.

and summarized in Table 2.4. For each case: subplot a) reports the plasma separatrix at VDE starting point and the trajectory of the plasma centroid during the VDE phase (solid blue line); subplot b) reports the halo current (red), the eddy currents on the upper VV (blue), the eddy currents on the lower VV (green) and the total eddy currents (yellow); subplot c) reports the electromagnetic vertical forces on VV due to halo current (orange), eddy current (blue) and their sum (yellow). In both subplots b) and c), the purple line is the simulated plasma current. Table 2.4 summarizes the simulation results in terms of $I_{halo,max}$, maximum axisymmetric index and F_{z-max}. As expected, similar results have been found in terms of total vertical force. Furthermore, the three analyzed configurations resulted comparable in terms of halo currents.

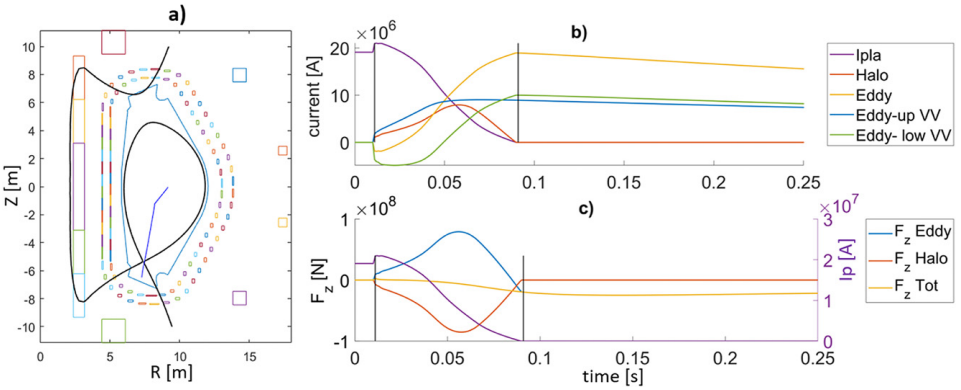

FIGURE 2.15: MAXFEA simulation of EU-DEMO perturbed DN (LQDN): a) plasma separatrix at VDE starting point (red solid line), plasma trajectory during VDE (solid blue line); b) plasma current (purple line), halo current (red line), overall eddy current (yellow line), upper VV eddy currents (blue line) and lower VV eddy currents (green line); c) EM loads on VV: simulated eddy (blue) halo (red) and total (yellow line) vertical forces.

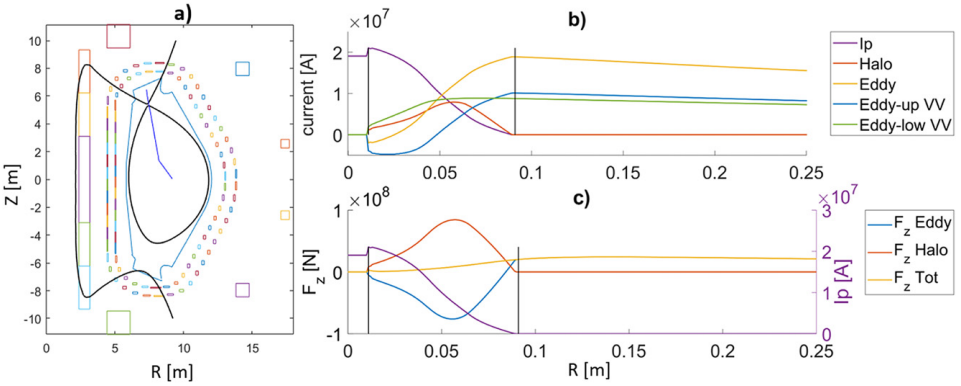

FIGURE 2.16: MAXFEA simulation of EU-DEMO perturbed DN (UQDN): a) plasma separatrix at VDE starting point (black solid line), plasma trajectory during VDE (solid blue line); b) plasma current (purple line), halo current (red line), overall eddy current (yellow line), upper VV eddy currents (blue line) and lower VV eddy currents (green line); c) EM loads on VV: Simulated eddy (blue), halo (red) and total (yellow) vertical forces.

TABLE 2.4: Characteristc times for puses containing VDEs, mDs, L-H, H-L and ELMs.

Configuration	Event	$I_{halo,max}$ [MA]	Axisym-max halo	F_{z-max} [MN]
DN	Fast Type 3 VDE	~ 8	~ 0.4	~ 23.5
LQDN	Fast Type 3 VDE	~ 7.9	~ 0.4	~ 24.9
UQDN	Fast Type 3 VDE	~ 7.9	~ 0.4	~ 24.4

2.2 Tungsten core accumulation detection in AUG and JET

To detect the W-accumulation at the plasma core in disruptive AUG experiments in EU-DEMO relevant scenario an algorithm for the automatic detection has been developed. In order to do this, a database of 143 flat-top disruptions and 87 HDL disruptions in the pulse range [28000÷34000] has been investigated, for a total of 230 pulses. Among the 143 flat-top disruption, 68 pulses were manually investigated to be used for optimizing the algorithm, and the remaining 75 flat-top disruptions and 87 HDL disruptions have been used as test set. Note that, even if only 60 pulses of the whole list respect the EU-DEMO-relevant constraints at the t_D, the whole list has been used to optimize and test the algorithm and to check if EU-DEMO-relevant constraints are satisfied during the W-accumulation phase.
For JET, it was not possible to develop an algorithm for the automatic detection of W-accumulation for the reasons that will be better described in Section 2.2.1.1. Thus, a list of 57 pulses has been manually analyzed in order to find pulses with W-accumulation in the plasma core.

2.2.1 W plasma core accumulation at AUG

In principle, a simple criterion could be set for the automatic detection of W plasma core accumulation at AUG: $c_{W,I} > 3c_W$ where c_W is the W concentration for plasma regions where $0.8 < Te < 1.8$ keV and $c_{W,I}$ is the W-ions W^{40+} to W^{45+} concentration for plasma regions where $2.2 < Te < 5.0$ keV (see blu and red dots respectively in Figure 2.17 right-bottom side). The factor 3 is required to distinguish the W-accumulation from less localized W-peaking and also to accommodate for systematical uncertainties of the measurement of the W concentration measurement. However, interpretation of the c_W signal is more challenging and it strongly depend on Te profile behavior. Indeed, if $Te < 2.2$ keV the $c_{W,I}$ measure is not reliable and no statement about the W-ions W^{40+} to W^{45+} can be made.In addition, in the Te range (2.2÷5.5 keV), the vicinity to the lower boundary increase the uncertainties ($\delta c_{W,I}$) on $c_{W,I}$ making more difficult to assert the W accumulation. Thus, the criterion based only on comparison between $c_{W,I}$ and c_W could not be exhaustive for detecting the W accumulation in the plasma core, the electron temperature at the core Te_{core} and also measures of the radiated power need to be considered. The Te_{core} is needed to verify the reliability of the $c_{W,I}$ signal, and the radiated power is needed to compare the radiation of different plasma regions. Thus, for supporting the

detection of W accumulation, radiated power measures from a set of bolometer lines of sight have been considered to compare the plasma radiation from the plasma core with respect to the external core (ex-core) region. In particular, the radiated power average of channels 28 and 29 looking at center of the plasma is considered to evaluate the radiated power behavior from the core region ($Prad_{core}$). While the average of the lines 20 and 34, below and above the center respectively, has been taken into account to evaluate the radiated power behavior from the ex-core region ($Prad_{ex-core}$). Indeed, for a discharge with W accumulation in the plasma core, $Prad_{core}$ starts increasing while $Prad_{ex-core}$ stays constant. Additionally, assuming a constant n_e and considering the W-cooling factor a weak function of the electron temperature, a W-accumulation of about a factor 10 is occurring ($c_{W,I} > 10c_W$) when $Prad_{core} > 2Prad_{ex-core}$. For the optimization of the algorithm for the automatic detection of the W accumulation, the W accumulation time (t_W) has been manually detected for 68 pulses. The t_W is assumed as the first time instant where $c_{W,I} - \delta c_{W,I} > 3c_W$, and both $Te > 2.2$ keV and $Prad_{core}$ ramps-up while $Prad_{ex-core}$ stays flat.
The algorithm for the automatic detection of the W-accumulation in the core implements the following steps:

1. $c_{W,I} - \delta c_{W,I} > 3c_W$ for 3 sequent samples (this correspond to a 30 ms time window). When this constrain is satisfied, the time of first sample is set as t_{ref}. Once the t_{ref} is defined the following condition has to be satisfied in order to proceed with the step 2, otherwise the pulse is discarded:

   - $Te_{core}(t_{ref}) > 2.2$ keV $\wedge$ $\delta c_{W,I}(t_{ref}) < c_{W,I}/10$

   Where Te_{core} is the average of the ECE radiometer core channels (magenta bold line in Figure 2.17 left-bottom plot). The core channels are defined as the channels placed in the major radius interval $1.2 \div 1.7$ m (colored thin lines in Figure 2.17 left-bottom plot). $\delta c_{W,I}$ is the uncertainty on $c_{W,I}$ and its order of magnitude have to be lower than the one of $c_{W,I}$. Both these constrain allow to establish the reliability of the $c_{W,I}$ measurement

2. Step 2 implements a logic *or* between the following conditions **a)** and **b)** applied on the radiated powers for $t > t_{ref}$. In particular, the two conditions are:

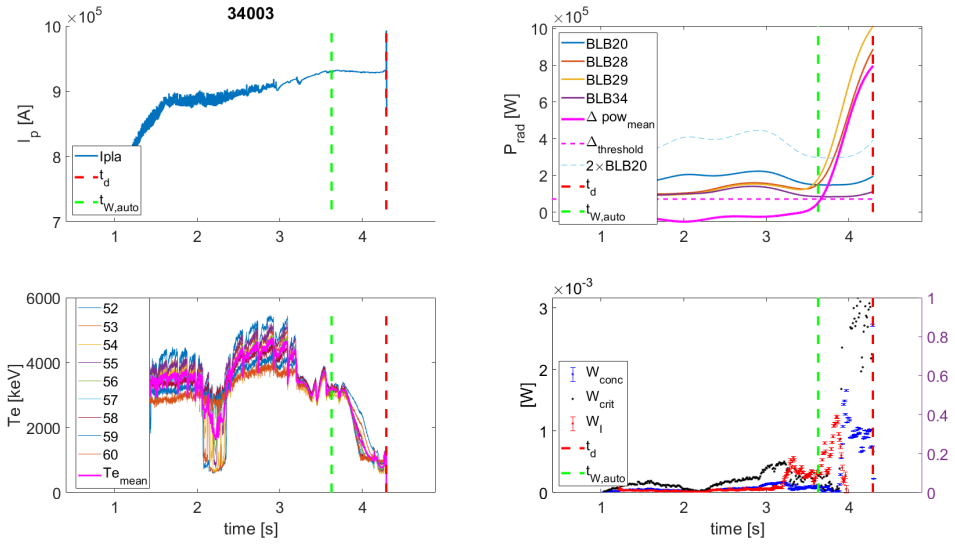

FIGURE 2.17: AUG #34003: left-upper plot I_p , right-upper plot bolometer core and ex-core channels, left-bottom plot Te, right-bottom plot W concentration. The red dashed line is t_D and the green dashed line is the automatically detected t_W.

- **a)** $\Delta Prad > 7.1 \cdot 10^4 \wedge \text{diff}(\Delta Prad) > 175$

  Where $\Delta Prad = Prad_{core} - Prad_{ex-core}$ (magenta line in Figure 2.17 upper-right plot), and the thresholds 7.1 · 104 (magenta dashed line in Figure 2.17, upper -right plot) and 175 have been set as the minimum value of $\Delta Prad$ and of diff($\Delta Prad$), respectively, in the optimization set (68 pulses) at the manually detected t_W. These constrains allow to determine when the plasma core is becoming more irradiating respect to the ex-core region and the $Prad_{ex-core}$ stays constant.

- **b)** $Prad_{core} > 2Prad_{ex-core}$ as previously discussed this condition is an evidence of W-accumulation in the plasma core. The blue dashed lines in Figure 2.17 (upper-right plot) represents $2Prad_{ex-core}$.

If either **a)** or **b)** conditions are verified the t_{ref} is assumed as the starting time (t_W) of the W-accumulation in the core, otherwise the pulse is discarded.

Among the 60 EU-DEMO relevant pulses, 10 pulses present W-accumulation in the plasma core. Moreover, 2 pulses respect the EU-DEMO relevant constraints at the t_W.

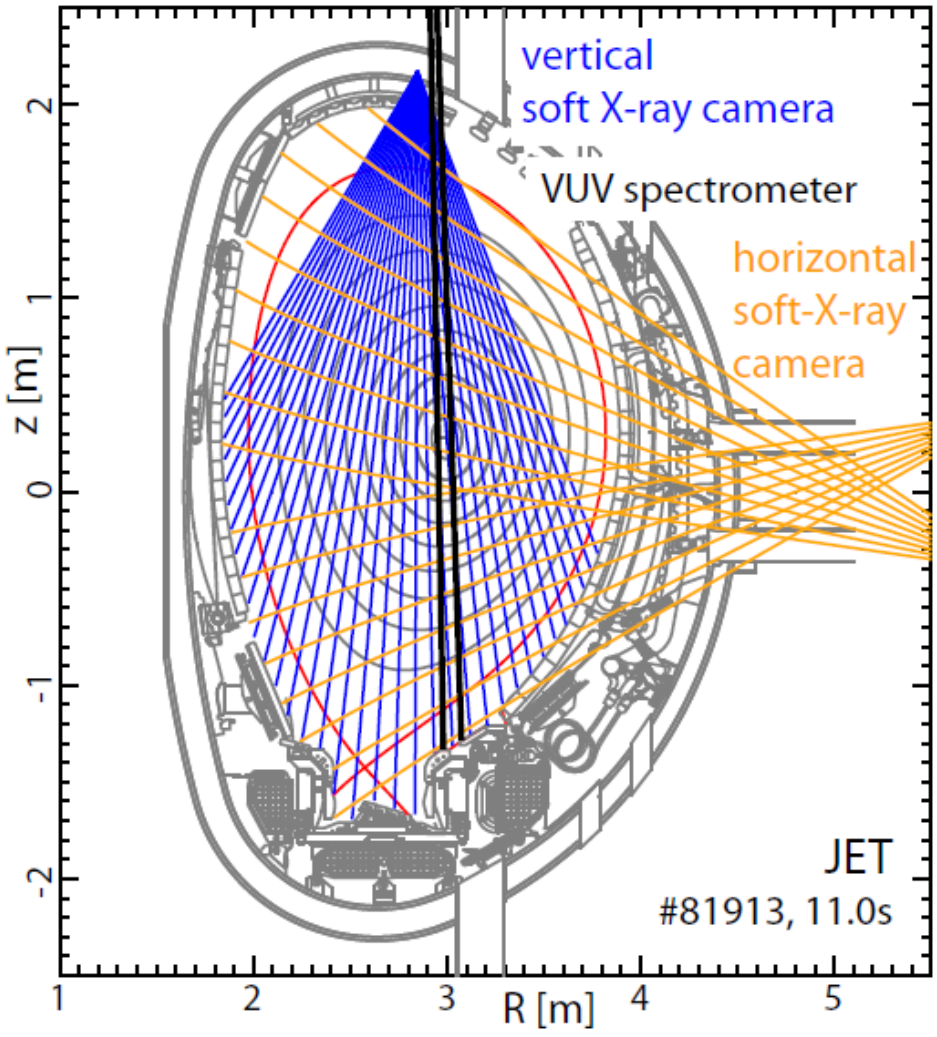

FIGURE 2.18: Diagnostic setup for determining the W concentration and its poloidal asymmetry. Sight lines of the Soft-X-ray cameras (blue and orange) and of the VUV spectrometer (black).

2.2.1.1 W plasma core accumulation at JET

In principle two approaches are available to provide a quantitative measure for the W concentration in the JET core plasma. The first approach makes use of density measure from the Divertor-viewing VUV spectrometer set on wavelength equal to 5 nm (KT7/3, black lines in Figure 2.18) where a strong spectral feature of the W-ions W^{27+} to W^{35+} is emitted. Nevertheless, due to the centrifugal asymmetries, the KT7/3 based analysis must be considered incomplete, which called for an alternative quantification not hampered by the centrifugal asymmetries. The second approach is to use the radiated power measured by the Soft-X-Ray (SXR) cameras to determine the W concentration. The large number of lines of sight allows for determining a

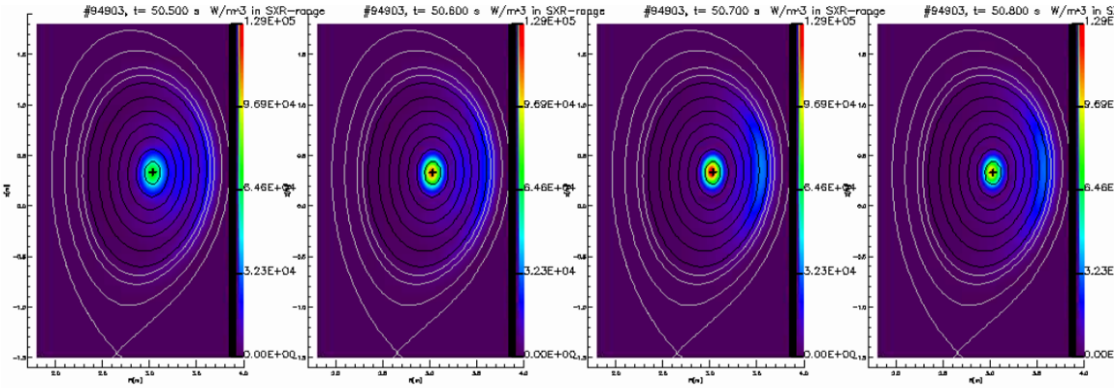

FIGURE 2.19: JET pulse #94903, 2D-profiles of derived total radiated power shows a W accumulation in the core from 50.5 to 50.8 with a time step $dt = 0.1$ s. The color shade from black to red represent the growing of the W-concentration from 0 to $1.29{\cdot}10^5$ W/m^3.

2D radiation profile and poloidal asymmetries can easily be handled. However, it is not unambiguous what species in the plasma are responsible for the radiation in the SXR range. Thus, a re-calibration procedure is needed to provide a robust measure for the W concentration to quantify the contribute of radiation caused by the only W.

At JET, a tool named *SXR W analyzer* has been developed, which define a procedure based on the radiated power measure from the SXR to compute the W concentration [48]. The procedure is divided in the following 3 steps:

1. Deconvolution of the radiation measured by the SXR cameras. To derive absolute W concentration from the SXR camera signals, the Bremsstrahlung contribution due to low Z-ions is subtracted and the excess radiation is attributed to W. This operation allows to take into account poloidal asymmetries and its results are consistent with the Wesson-formula [49]. The W density on a flux surface is thus described by the: 2.2:

$$n_W(r_{norm}, R) = n_{W,0}(r_{norm}) e^{\lambda(r_{norm})(R^2 - R_0^2(r_{norm}))} \tag{2.2}$$

where R is the major radius and $n_{W,0}(r_{norm})$ is the W-density on the flux surface labeled r_{norm} at the large radius $R_0(r_{norm})$, $\lambda(r_{norm})$ contains the dependence on the rotational frequency. Since the 2.2 only allows for in-out asymmetries, but no up-down asymmetries, it is possible to carry a good analysis only considering vertical cameras for deconvolution. However also tangential and horizontal cameras can be used at the same time.

This step is done twice, the second time using slightly different electron profiles in order to determine error bars.

2. Evaluation of the flux surface with averaged W concentration. This step converts the deconvolution results into 2D-profiles of derived total radiated power, showing only the W radiation, see Figure 2.19), where the color shade from black to red represent the growing of the W radiation from 0 to $1.29{\cdot}10^5$ W/m^3. A reference time t_{ref} and an interval dt can be chosen so that a time sequence of 2D profiles is printed starting from $t_{ref} - dt$ to $t_{ref} + 2dt$, with time step dt. The deconvolution result into W 2D-radiation profiles it is not reliable in the plasma regions where $Te < 1.5$ keV. Ence, in the 2D plots, the flux surfaces edges are colored depending on the electron temperature of the region, as reported in Figure 2.19 for the JET pulse #94903. The reliable region is indicated by black flux surfaces, while the not reliable region is defined by white flux surfaces.

3. Plot of the results. Once selected a reference time where a possible W core accumulation occurs, the tools allows plotting the Te, n_e and the W concentration time-traces at different normalized radius and their 1D profiles. For the pulse #94903, the left column plots in Figure 2.20) reports the Te (upper plot), n_e (mid plot) and the c_W (bottom plot) time-traces at different normalized radius (0 = core, 1 = edge), in a selected time range containing the reference time (black vertical line). In addition, the right column in Figure 2.20) reports in gray Te (upper plot), n_e (mid plot) and the W concentration (bottom plot) 1D profiles in shorter time range around the t_ref, while at the t_ref the profiles are plotted in black. The abscissa of the colored points on the black lines indicates the normalized radius of the corresponding time-trace colors on the left side.

The algorithm developed for the automatic detection of W-core accumulation at AUG cannot be applied because of the unavailability of the needed signals in batch mode. Thus, at JET, the SXR W-analyzer has been used to manually select the pulses with W accumulation in the plasma core.

On the considered JET database, the first point was to identify for each pulse a time window in a W-accumulation may occur, in order to perform the analysis available by the SXR W-analyzer tool. Since the W core accumulation cools down the plasma core, an increasing radiation from it should be observed, while the radiation from the ex-core region stays flat, as seen for AUG. Thus,

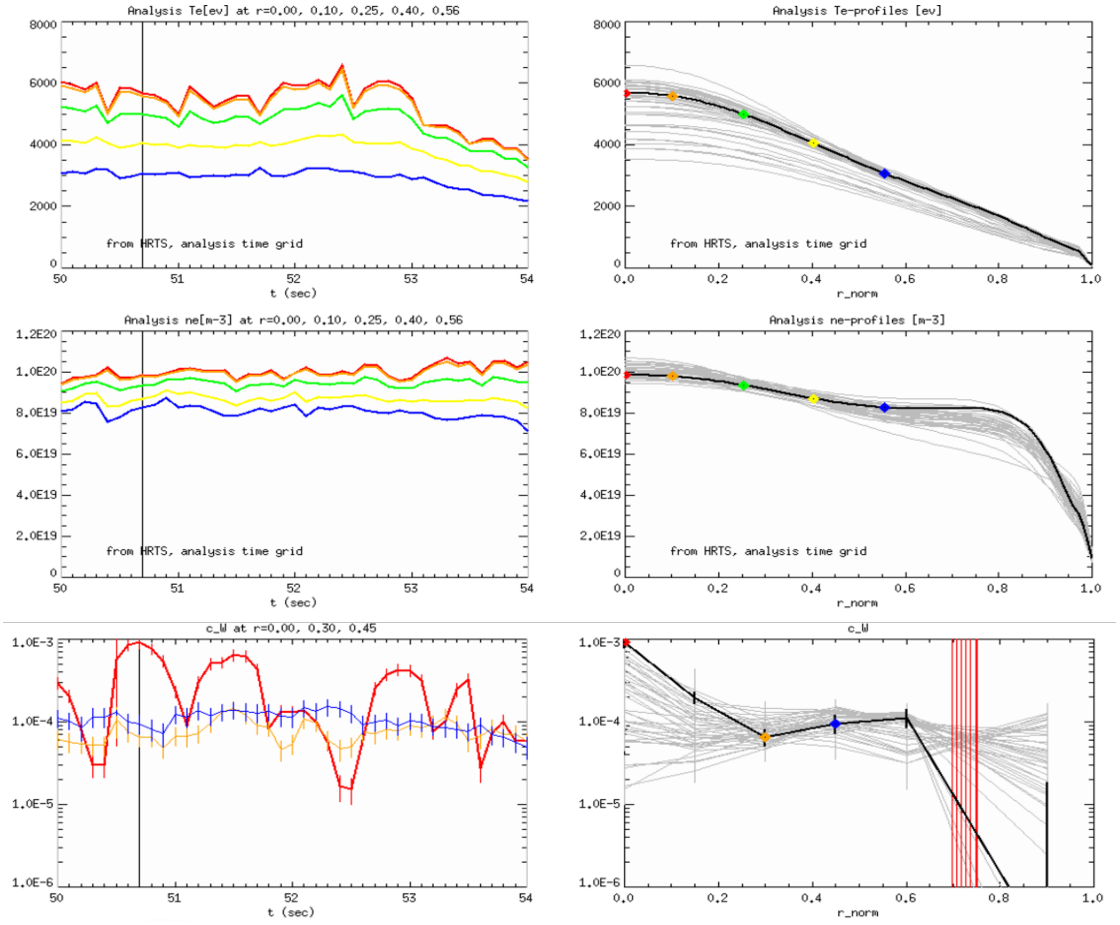

FIGURE 2.20: JET pulse #94903, Te, n_e and c_W time traces (left column) and 1-D profiles (right column). The abscissa of the colored points on the black lines indicates the normalized radius of the corresponding time-trace colors on the left side.

as first selection, the radiated power from the bolometer horizontal camera has been observed in order to detect a time window with possible W accumulation in the core. The Figure 2.21 shows the radiated power from the core region (chords 14 and 15, green and red lines respectively) and from the ex-core region (chords 12 and 17, blu and cyan lines respectively) for the JET pulse #94903. The analysis of the bolometer signals allows to choose the t_{ref} requested in the step 2 of the SXR W-analyzer procedure. The Figure 2.21 highlight a more irradiating core, with respect to the ex-core, in the time window from 50.5 s to 51 s, approximately. Thus, a W core accumulation is supposed between 50.5 s to 51 s and then the SXR W-analyzer procedure has been applied, assuming 50.6 s as t_{ref}. Indeed, the Figure 2.19 shows 2D-profiles of the derived total radiated power from 50.5 s to 50.8 s. Note that, the flux surfaces corresponding to the core region are black. In addition, it can be observed from Figure 2.20 upper plots, that during

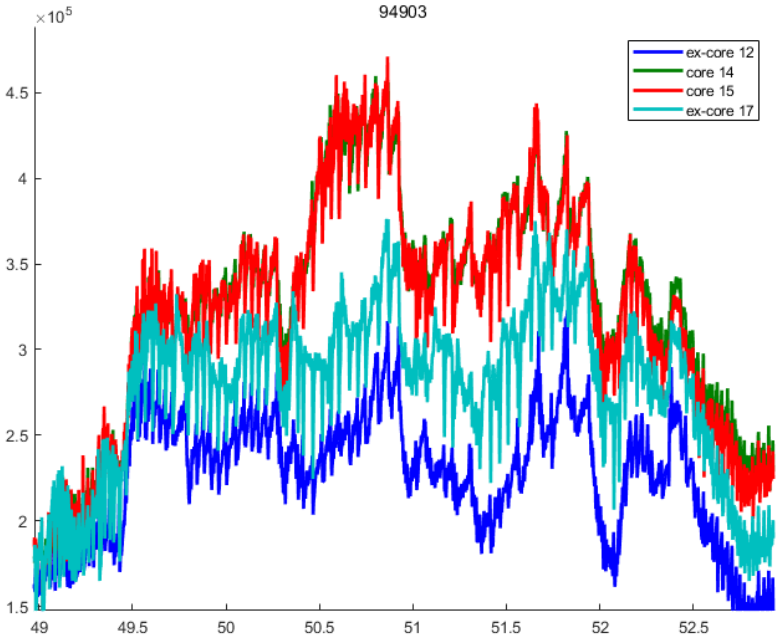

FIGURE 2.21: JET pulse #94903, bolometer horizontal chords 14 and 15 (green and red lines) defining the core region and chords 12 and 17 (cyan and blue lines) defining the ex-core region. A more irradiating core, with respect to the ex.core, is observed in the window from 50.5 s to 51 s.

the chosen time window the core temperature (red and orange lines) its higher than 1.5 keV. Moreover, in Figure 2.20, the red line, in bottom left plot, indicates that the W concentration at the core present a maximum at 50.7, approximately. Thus, a W accumulation in the core has been considered for the pulse #94903 in the time window 50.5 s to 51 s.

Through this analysis, from the starting list, 8 pulses have been selected, presenting W accumulation in the plasma core; starting time and ending time of the flat-top phase and W-accumulation time have been provided for each shot.

2.3 Flux Pumping investigation at JET

In high performance tokamak plasmas, the peaking of the central current density triggers sawtooth cycles that can provide seed islands for neoclassical tearing modes (NTMs). Measurements on several tokamaks suggest that sawtooth instability is caused by an internal kink instability with a $(m, n) = (1, 1)$ destabilized by a central peaking of the toroidal current density profile that corresponds to the central safety factor below the unit ($q_0 < 1$) [36]. A mode of tokamak operation that avoids sawtoothing is the Hybrid scenario. An important feature of the hybrid scenario is that the plasma current profile is broader than expected for resistive diffusion, which stabilizes the sawtooth instability by elevating the safety factor q everywhere above unity [34]. This eliminates a trigger for deleterious NTMs and allows the hybrid scenario plasmas to operate at high β. In several machines, the hybrid scenario has the attractive characteristic of a self-organized current profile by means of a physical mechanism, referred as flux pumping, in which poloidal flux is anomalously redistributed and the toroidal current broadened [50]. These mechanisms are potentially important for future non-inductive tokamaks, as they could provide a way to redistribute the current driven by electron cyclotron current drive (ECCD), which is most efficient in the plasma center. Flux pumping could redistribute current outward, helping to maintain a flat central q-profile around unity and maximizing both the current drive efficiency and plasma stability at high normalized beta (β_N). Thus, flux pumping mechanism results an interesting scenario for future tokamak device and his behavior has to be investigated on different machines.

Mechanisms responsible for the flux pumping have been simulated in [34, 36] with 3D non-linear MHD codes. Experimentally, the flux pumping mechanism has been observed in DIII-D [51] and ASDEX Upgrade [50] hybrid scenarios. Whereas, no evidence of the flux pumping mechanism has been proved detected in JET experiments yet. Therefore, in the context of developing an Inter-machine experimental database of EU-DEMO-relevant scenarios, a database of JET experiments potentially candidate for developing the flux pumping mechanism has been built. The aim is to identify pulses proving the presence of flux pumping mechanism at JET and to study the scenarios to design next experiments. In the section 2.3.1, the characteristics of flux pumping experiments at AUG will be shortly presented. Then, in the section 2.3.2 the selection analysis of past JET experimental campaigns, considering both Iter-Like-Wall (ILW) and

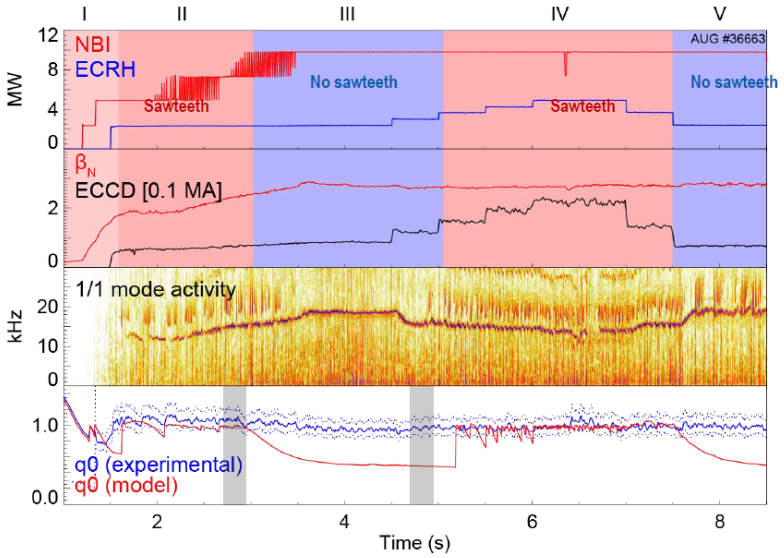

FIGURE 2.22: Time traces of the NBI and ECRH heating power, β_N, ECCD, (1,1) mode activity, experimental and modeled (without flux pumping) q_0.

Carbon-Wall (CW) discharges, and the analysis conducted to verify the presence of the flux pumping mechanism will be presented.

2.3.1 Flux pumping experiments at AUG

At AUG, the combination of the Integrated Data analysis Equilibrium solver (IDE) and the imaging motional stark effect diagnostic (IMSE) [52] allows to measure changes of q in the order of magnitude of 0.1 in the plasma center. Along with the current drive capabilities of the Upgraded Electron Cyclotron Resonance Heating (ECRH) systems [53], AUG is the ideal device to perform experiment tests of the theoretical flux pumping model. To this end, a high confinement plasma scenario with a central q around unity was developed such that a (1,1) mode forms. An example of such an experiment is the AUG discharge #36663, shown in Figure 2.22 [36]. Figure 2.22 reports, on the upper subplot the time traces of the NBI and ECRH heating power, red and blue lines respectively. Third subplot from the bottom reports β_N and ECCD time traces, red and blue lines respectively. The second subplot from the bottom reports the (1,1) mode activity. Finally, the bottom subplot reports the experimental and modeled (without flux pumping) q_0, blue and red lines respectively. Here, the NBI power was feed forward programmed to increase the plasma β_N during the discharge, which should act to increase the flux pumping effect generated by the (1,1) mode activity. This should result in the suppression of any sawtooth

instabilities as q_0 is raised toward unity. In AUG discharge #36663, see Figure 2.22, five distinct phases can be distinguished, the red shading ones indicates the presence of sawteeth, while the blue shading ones their absence. In the first phase, the q-profile and β_N are still evolving after the current ramp-up and transition to H-mode and classic sawteeth can be observed. The beginning of phase II is marked by the time of the last periodic sawtooth around 1.62 s. In this phase, clear (1,1) mode activity becomes visible in magnetic diagnostics and remains throughout the rest of the discharge (see subplot on the second row from the bottom). As the plasma β_N is increased via an NBI power ramp, those the sawteeth at first remain until β_N is increased above 2.5, then the sawteeth and all sawtooth-like core events disappear, as indicated by the blue shaded phase III in Figure 1.22. During phase III, at 3.5 s, β_N reaches its maximum value of 2.9 and stays roughly constant for the remainder of the discharge. After this, still in phase III, the central ECCD is increased, but complete sawtooth suppression is maintained. Only when the ECCD is increased above 150 kA (phase IV), sporadic sawteeth reappear. These become more frequent as more ECCD is added to the plasma. In the last phase, the ECCD driven current is reduced back to the values of phase II and the sawteeth disappear again. The behavior observed in this discharge is consistent with the idea of two competing current profile alteration mechanisms: one proportional to the plasma pressure holding the central q-value above one and thus preventing the sawtooth instability, and the second being the ECCD driven current, which reduces q_0, making the plasma vulnerable to sawteeth. To test this, the experimental and modeled central q-value observations can be compared. The bottom panel of Figure 2.22 shows the experimental q_0 in red and the modeled q_0 generated by IDE, a Grad-Shafranov solver coupled with a current diffusion equation solver. The modelled central current present an excellent agreement with the experimental one when no anomalous redistribution of magnetic flux is present. Indeed, in Phase 3 modeled q_0 drops below unity suggesting that an anomalous modification, compared to neoclassical current diffusion model, is occuring that holds central q value around unity. The Figure 2.23 is useful to confirm the flux pumping presence. Indeed, the flux-averaged current density profiles are shown in Figure 2.23(a) where the red line is the modelled profile and the blue one is the measured one. The subtraction of these two profiles, considering the plasma resistivity, provides the additional toroidal electric field necessary to obtain the experimental safety factor starting from the modelled one. This electric field, shown in Figure 2.23(b), can be considered as the electric field generated by the (1,1) mode which keeps the central q around

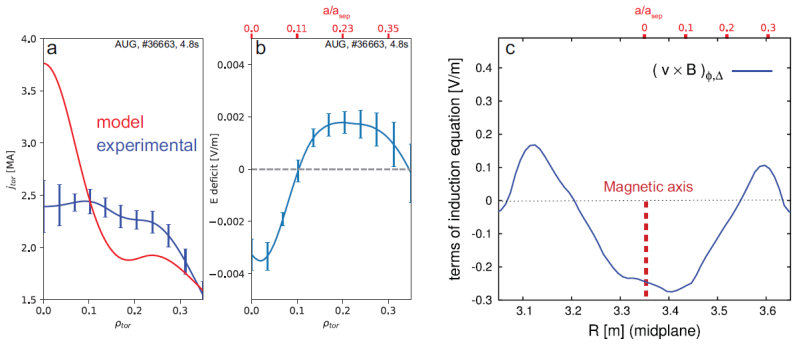

FIGURE 2.23: a) experimental (blue) and modeled (red) current density, b) corresponding electric field deficit, c) electric field generated by the (1,1) quasi-interchange mode in one of the flux pumping simulations in reference [8] (figure adapted from the reference).

unity. Indeed, this qualitatively similar to the field computed in the flux pumping simulations [54] reported in Figure 2.23(c).

2.3.2 Flux pumping investigation at JET

At JET, a flux pumping dedicated campaign has never been conducted and, moreover, this mechanism has never been proved by observing the discharges data. Thus, with the aim of investigate if the flux pumping has been attained also without focused experiments, 941 Iter-Like Wall (ILW) and 280 Carbon Wall (CW) JET discharges, both in hybrid scenario, have been analyzed in order to identify experiments presenting this mechanism. The analysis is divided in two main steps:

1. An automatic selection done for selecting EU-DEMO-relevant pulses in high β scenario
2. A detailed manual analysis conducted on the remaining pulses in order to identify the pulses candidate for flux pumping

This analysis has the aim to collect a dataset of JET experiments for which TRANSP simulations have to be conducted as last step to prove the flux pumping presence.

2.3.2.1 Automatic selection

As first step, an automatic selection has been conducted in order to select EU-DEMO relevant pulses at high β regime with a n_1 mode amplitude greater than the n_2 one. For this purpose three constraints (C1-C3) have been applied hierarchically:

- C1: $3.5 < q_{95,mean} < 5$, where $q_{95,mean}$ is the q_{95} mean value during the flat-top phase. This constraint is applied to select EU-DEMO-relevant scenarios;
- C2: $\beta_N > 2.4$ for $\Delta t^* > 0.8s$: as mentioned above flux pumping occurs at high-β_N. Indeed, this constrain allows us to select pulses with high β_N for a time window long enough to let flux pumping occurs, and to be observed. Different β_N signals have been investigated. Finally, the normalized β derived from the diamagnetic energy (BTND) and the one derived from equilibrium stored energy (BTNM) from the equilibrium code EFIT, were chosen because of their availability and reliability. Both signal were considered for this constraint, so to maintain, for the next constraint and the manual investigation, each pulses that satisfies it just with the greater measurement. The average time window for which C2 is satisfy on ILW pulses ($\Delta t_{mean,ILW}$) has been calculated, $\Delta t_{mean,ILW} = 1.5$ s, while for CW pulses $\Delta t_{mean,CW} = 3.8$ s
- C3: $n_{1,amp} > n_{2,amp}$: for a time window lasting 0.9 s for the ILW experiments and 1 s for the CW ones, where $n_{i,amp}$ is the amplitude of the $n = i$ mode as calculated from the fast magnetic acquisition system (KC1 - coil 16). The Time window is different for ILW and CW experiments because of the different $\Delta t_{mean,ILW}$ and $\Delta t_{mean,CW}$ length. This constraint is met even when $n_{1,amp}$ is slightly greater than $n_{2,amp}$ during the high-β_n time window.

Applying each constraints, at each step a subset of pulse has been selected as reported in Table 2.5.Thus, the automatic selection results in 74 ILW and 77 CW pulses, available for the manual analysis.

TABLE 2.5: Resulting subset of pulses applying the constraints C1, C2 and C3.

	Hybrid Scenario	$3.5 < q_{95,mean} < 5$	$\beta_N > 2.4$	$n_{1,amp} > n_{2,amp}$
ILW	941	800	80	74
CW	280	276	117	77

2.3.3 Manual investigation

The flux-pumping mechanism is characterized by having in the high-β_N time window $n_{1,amp}$ prevalent with respect to $n_{2,amp}$ and by the saw-teeth absence. Indeed, the flux pumping mechanism helps to avoid sawteeth. Nevertheless, when there is not enough flux pumping to avoid of periodic sawteeth, an isolated saw-tooth can occur. As described in section 2.3.1 to prove the presence of the flux pumping mechanism the modeled q_0 has to be compared with the experimental one. To this aim, affordable equilibrium reconstruction codes like EFTF and EFTM should be available since the uncertainty on the experimental q_0 computed with EFIT or EFTP is too much high. A manual analysis of the mode amplitudes and the sawteeth behavior in the high-β_N time window, conducted on the automatically selected pulses, allows us to label them as good and bad candidate for the flux pumping mechanism. Good candidates are pulses where the flux pumping may have occurred. Whereas, bad candidates are pulses where it is almost sure that flux pumping is not occurring. These pulses can't be considered a good scenario for the flux pumping.
The criterion to classify the pulse in good and bad candidates is reported in the following:

- Bad candidates:
  - $n_{1,amp}$ is never preponderant with respect to $n_{2,amp}$.
  - Periodic sawteeth occur even during high-β_N time window.
- Good candidates:
  - $n_{1,amp} \gg n_{2,amp}$ and no periodic sawteeth occur (or they disappear after few hundreds milliseconds that the high-β_N time window starts).
  - $n_{1,amp} \gg n_{2,amp}$ and isolated aperiodic sawteeth occur.

The labeling of the pulses in two classes revealed not to be exhaustive since several pulses presenting the high-β_N time window no clear features in, such us $n_{1,amp}$ not always much larger

than $n_{2,amp}$ or the sawteeth with an intermittent occurrence. Considering that the aim is to identify the best pulses to be simulated with TRANSP in order to find flux pumping evidence, a third class has been added, named possible candidate and the fishbones occurrence has been considered to better evaluate if the labeling. Indeed, when the $n_{1,amp}$ is not stable and always much larger than $n_{2,amp}$, the presence of the fishbones is considered as an index of flux-pumping presence. Fishbones can be detected by the fishbones shape on the core radiated power signal, visible by the central SXR channels. As an alternative they are visible on the spectral analysis of 2MHz fast magnetic acquisition system (see Figure 2.28) or from the spectral analysis of the SXR-ch10 (see Figure 2.25). Thus, an algorithm for SXR spectral analyses has been developed following the methodology described in [32], to take into account the fishbones occurrence during the labeling procedure. To check the sawteeth occurrence, the core temperature measured by the Radiometer channels, in a range of 0.4 m around the plasma barycenter radial position, has been chosen. In addition, since periodic sawteeth can be confused with temperature falls due to type 1 ELMs or giant ELMs (G-ELMs), the sawtooth presence has been confirmed by verifying that no ELMs occurred simultaneously. In the following an example of good, possible and bad candidates from ILW pulses are reported in Figures 2.24, 2.27 and 2.26 respectively, where on the upper subplots, together BTND and BTNM (red and green lines respectively), $n_{1,amp}$ (blue line) and $n_{2,amp}$ (brown line) are shown. In the middle subplots are reported the radiated power from the Soft-X-Ray core channel (SXR-ch5, blue line) and the D_α measurement (brown line). Finally, the bottom subplots report the core temperature measured by radiometer.

2.3.3.1 Good Candidate

Figure 2.24 reports the JET ILW pulse #83524 as an example of good candidate. The pulse presents $n_{1,amp} \gg n_{2,amp}$ (upper plot). The $n_{1,amp}$ collapse is concurrent with an isolated sawtooth (bottom plot) and with the fishbones interruption observable both from core radiated power signals, blue lines the middle subplot in Figure 2.24, and from the SXR-ch10 spectrum reported in Figure 2.25, right subplot. Figure 2.25 shows also AUG spectrum reported in [32] as reference of how fishbones should appear in radiated power spectrum representation. The absence of periodic saw-teeth in the high-β_N phase, $n_{1,amp} \gg n_{2,amp}$ and presence of fishbones are suggesting the flux pumping presence. Indeed, the JET ILW pulse #83524 has been labeled as a good candidate.

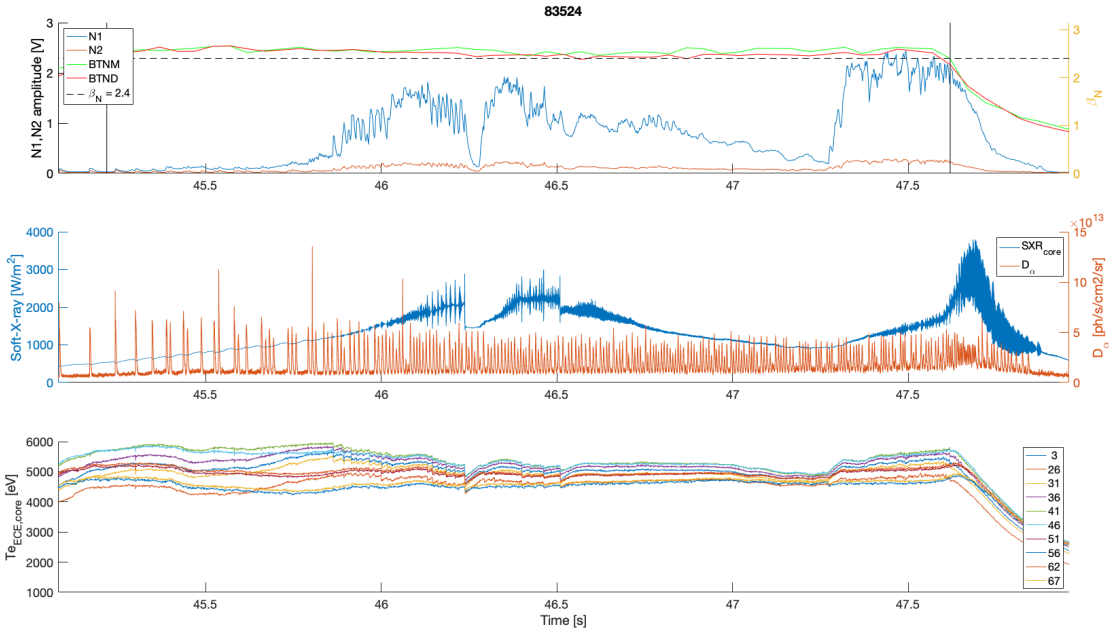

FIGURE 2.24: JET ILW #83524 - good candidate. Top plot: $n_{1,amp}$ and $n_{2,amp}$ on the left axis, respectively blue and brown lines, BTNM and BTND time traces on the right axis, respectively green and red line. Mid plot: core radiated power measured from the Soft-X-Ray (channel 5) on the left axis and D_α on the right axis, respectively blue and brown lines. Bottom plot: plasma core temperature measured from the radiometer.

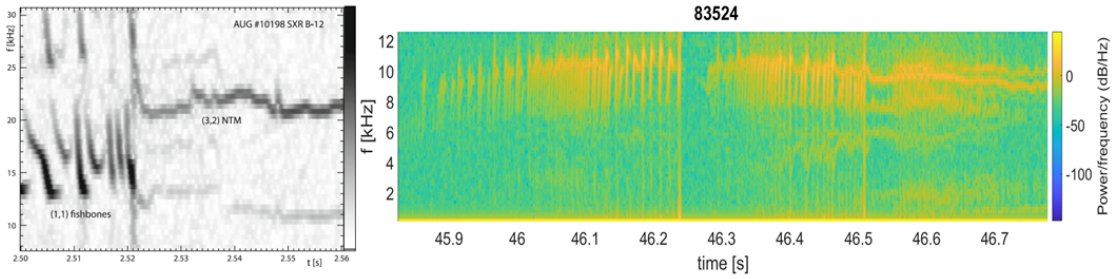

FIGURE 2.25: Spectral analyses on AUG SXR reported in [32] (left-plot), JET #83524 SXR-ch10 spectrum (right-plot)

2.3.3.2 Bad candidate

Figure 2.24 reports the JET ILW pulse #89293 as an example of bad candidate. The presence of periodic sawteeth, observable from the bottom subplot, during the high-β_N time window proves that the flux pumping is not occurring. Moreover, this is confirmed also from $n_{1,amp}$ that is not preponderant with respect to $n_{2,amp}$. Note that, to satisfy just one of the criteria for the bad candidate labeling (see section 2.3.3) it is sufficient for a shot to be labeled as a bad candidate. Thus, the JET ILW #89293 has been labeled as a bad candidate.

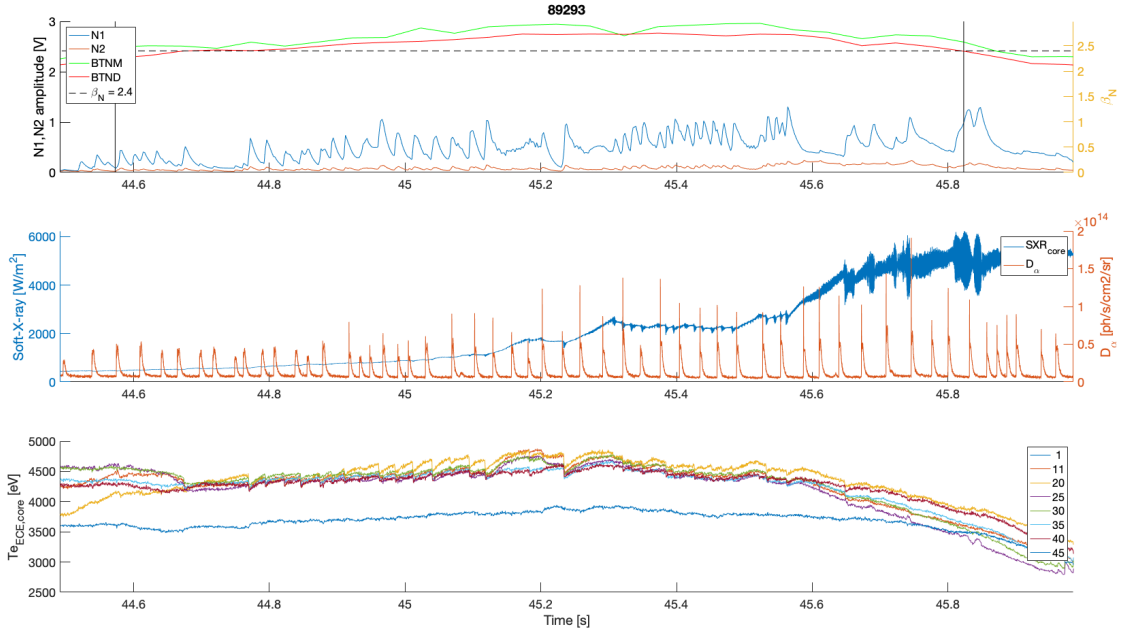

FIGURE 2.26: JET ILW #89293 - bad candidate. Top plot: $n_{1,amp}$ and $n_{2,amp}$ on the left axis, respectively blue and brown lines, BTNM and BTND time traces on the right axis, respectively green and red line. Mid plot: core radiated power measured from the Soft-X-Ray (channel 5) on the left axis and D_α on the right axis, respectively blue and brown lines. Bottom plot: plasma core temperature measured from the radiometer.

2.3.3.3 Possible candidate

Figure 2.27 reports the JET ILW pulse #83325 as an example of possible candidate. $n_{1,amp} \gg n_{2,amp}$ as for a good candidate and periodic sawteeth disappear at 46.4 s. Differently respect to the bad candidates, it is not possible to state that flux pumping is not present in this pulse. However, the core radiated power, blue line in the middle plot, doesn't present fishbones. Thus, this pulse has been labeled as possible candidate.

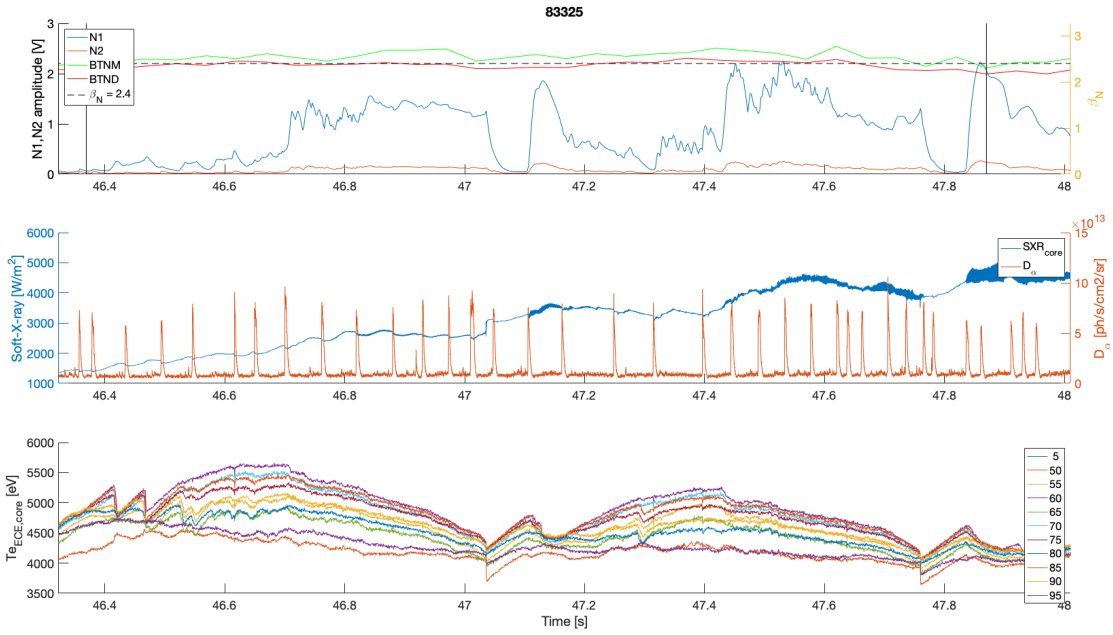

FIGURE 2.27: JET ILW #83325 - possible candidate. Top plot: $n_{1,amp}$ and $n_{2,amp}$ on the left axis, respectively blue and brown lines, BTNM and BTND time traces on the right axis, respectively green and red line. Mid plot: core radiated power measured from the Soft-X-Ray (channel 5) on the left axis and D_α on the right axis, respectively blue and brown lines. Bottom plot: plasma core temperature measured from the radiometer.

Following the same procedure CW pulses has been labeled. Note that, Soft-X-ray acquisition frequency for ILW pulses is in the range of 25 kHz while for CW list the available SXR signal has an acquisition frequency of 1 kHz. Thus, fishbones can't be observed from its measurements. However, they are visible also from the Mirnov coil spectrum as described in [55]. The Figure 2.28 shows two pulses from the CW list: the JET #68468 pulse (left plot) present an intermittent $n = 1$ mode without fishbones and it has been labeled as possible candidate, while in the JET pulse #68469 fish bones are clearly visible as spikes in the spectrum and the pulse has been labeled as good candidate.

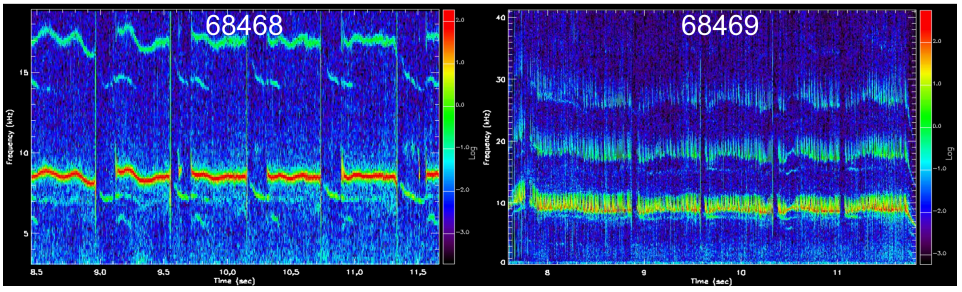

FIGURE 2.28: Mirnov coils spectral analyses for JET #68468 (left plot) and JET #68469

The table 2.6 reports the classification so conducted. For the ILW and CW good candidates two databases have been provided containing the following parameters:

- shot number
- Δt: length of the time window where C2 is respected
- q_0: mean value during Δt
- β_N: maximum mean value during Δt between BTND and BTNM
- $n_{1,mean}$ and $n_{2,mean}$ [V]: mean value during Δt
- B_T [T]: mean toroidal magnetic field during Δt
- $IPLA$ [A]: mean plasma current during Δt
- $P_{NBI}[W]$ mean Neutral Beam injected power during Δt

TABLE 2.6: Flux pumping candidates selection results.

	TOT	Good candidates	Possible candidates	Bad candidates
ILW	74	13	34	27
CW	77	15	21	41

Chapter 3

Manifold learning for MARFE key events detection at AUG

Disruptions represent a key issue for the operation of the next generation of tokamaks and in particular for ITER and EU-DEMO, for which they must be avoided, or at least adequately mitigated fro ITER. A disruption consists in a sudden loss of plasma confinement, which may lead to very harmful events. As first , a large heat load can be deposited on the first wall in a short-time interval. The following plasma current quench induces eddy currents on the surrounding metallic structures, leading to high electromagnetic forces [56, 57]. Some of the most relevant mechanisms that lead to a disruption are poorly understood or hardly detectable in real-time by a physics approach. In this context, machine learning algorithms are decisive since they can identify patterns and uncover complex relationships within high-dimensional data space, by using a large amount of data, that would be difficult to detect using traditional statistical methods or manual analysis. Indeed, Machine learning techniques have been successfully applied in disruption prediction task on the most relevant tokamaks such as JET [58–63], AUG [64–67], EAST [68] and DIII-D [68, 69]. In the last decade unsupervised manifold learning techniques, such as Self-organizing map (SOM) and its probabilistic counterpart, the generative topographic map (GTM), have been proposed to map the multidimensional plasma operational space JET towards disruption prediction and avoidance [57, 70, 71].

It should be noted that there are disruptions of different natures with different temporal scales,

therefore, the final goal of a predictor model would be to provide an early enough identification of a specific disruption type [72]. In this framework, the study developed in this chapter aims to obtain automatic warning times of density limit disruptions preceded by Multifaceted Asymmetric Radiation From the Edge (MARFE) at AUG, by tracking the different MARFE states, and to provide a real time trigger for the MARFE stabilization procedures. To this aim, a new database composed both of HDL and NO HDL pulses has been built by using the same algorithms for flat-top phase and disruptions detection presented in chapter 2.

3.1 H-mode Density Limit scenario at AUG

For typical ASDEX Upgrade (AUG) discharges, the H-mode density limit (HDL) is observed to be close to the Greenwald limit (see sec. 3.1.2). HDL experiments have three main goals. The first is to find operational scenarios which maximize the density, in particular the core one. The second is to investigate the physics which underlies the limit. Whereas, the third is to avoid the abrupt loss of energy confinement and to recover the plasma to the previous, high confinement, stable state. Understanding the density limit mechanism is crucial for extrapolating the machine performance into untested regimes and for developing avoidance and first wall protection strategies. In tokamaks, where the most extensive studies have been conducted, there is strong evidence linking the density limit to the plasma edge physics. Thus, it is possible to extend the operational range for line-averaged density by operating with peaked density profiles. Additional particles in the plasma core apparently have no effect on density limit physics. While there is not a widely accepted, first principle model for the density limit.

3.1.1 The H-mode

The high confinement mode (H-mode) is the foreseen operational regime for ITER and EU-DEMO. It is charac- terized by a particle and energy barrier at the edge of the confined plasma which increases the global plasma temperature and density and the energy confinement time. With respect to the low confinement mode (L-mode), the energy confinement time is improved by about a factor of 2. Despite its importance the physics of the H-mode, for example the transition from L-mode to H-mode, is not yet fully understood. The H-mode was discovered

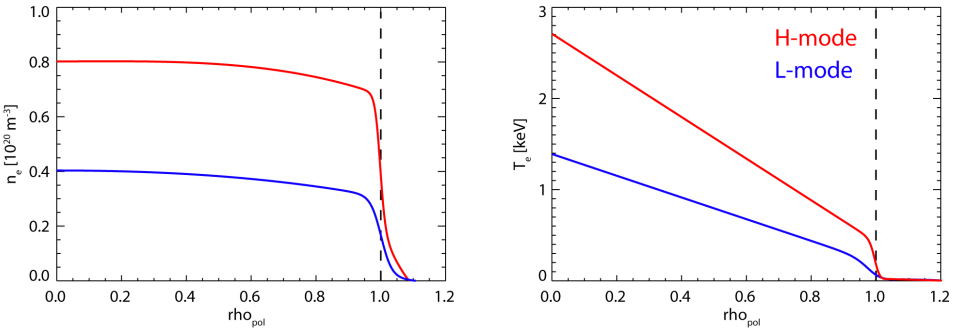

FIGURE 3.1: Electron density (left) and temperature (right) profiles over the normalized radius ρ_{pol} of (red) the H-mode and (blue) the L-mode phase of AUG #28730. The increased gradients close to the separatrix (dashed line) can be seen.[74]

at AUG, the predecessor of AUG, in 1982 by Prof. Friedrich Wagner [73]. It was achieved when applying sufficient heating power by Neutral Beam Injection (NBI) in a discharge with a poloidally diverted geometry. The H-mode exhibits strong gradients of the electron and ion density and temperature inside the separatrix (see Figure 3.1 [74]), the so-called pedestal (dashed line). These strong density and temperature gradients at the edge form an edge transport barrier (ETB), which suppresses the turbulence in this region. The central density and temperature are determined largely by their edge values and, thus, such increased edge values lead to a higher confinement. The widely accepted picture of the turbulence suppression, which stabilizes the H-mode and causes the strong gradients at the edge, is based on sheared plasma flows at the edge.

3.1.2 The Greenwald limit

It is desired to run future experiments and power plants at the highest plasma densities possible to increase their performance. However, magnetic confinement experiments cannot operate over an arbitrary range of plasma densities. Indeed, in addition to the operational limits imposed by MHD stability on plasma current and pressure, a limit on plasma density have been observed at the end of the 80s by Greenwald [10]. Each machine typically finds lower and upper density limits. Since the fusion reaction rate scales with n_e^2 the upper density limit is important to the goal of reaching high fusion power. The most common empirical scaling to the density limit is the Greenwald limit reported in equation (3.1) where Ip is the toroidal plasma

TABLE 3.1: Phenoma which occur at high denisty and often associated with the density limit are shown along with the range of normalized density at which they are observed. [75]

Phenomena	Range of normalized densities ($f_{GRW} = n_e/n_G$)
MARFEs	0.4-1
Divertor detachment	0.3-1
Drop in H-mode confinement	0.3-1
H/L Transition	0.8-1
Change in ELM activy	0.3-0.9
Poloidal detachment	0.7-1 (for clean plasma)
MHD and disruptions	~ 1

current and a is the minor radius.

$$n_G = \frac{I_P}{\pi a^2} \cdot 10^{13} \tag{3.1}$$

In a tokamak, several effects related to the density limit are observed to trigger a disruption. As the density is raised toward the limit, a wide variety of phenomena is encountered in sequence. Summarized in table 3.1, these phenomena include the appearance of MARFEs, divertor detachment, a drop in H-mode confinement, changes in ELM activity, the H/L transition, poloidal detachment, current channel shrinkage, a rise in MHD activity, and finally major disruptions. ASDEX Upgrade reports density limits with the P_{RAD}/P_{IN} between 60% and 80%, where P_{RAD} is the radiated power and P_{IN} is the input power. At ASDEX lower radiated power fraction, with respect to AUG, was observed at the density limit, in the range of 30-40% from the main chamber, and not exceeding 60-70% when the radiation from the divertor was included.

3.1.3 The H-mode density limit (HDL)

H-mode discharges which approach the Greenwald limit have a back transition in L-mode, before reaching the Greenwald limit. For several machines, the back transition has been observed for Greenwald fraction (f_{GRW}) between 0.8 and 1 (see Table 3.1). Where f_{GRW} is defined as the electron density fraction of the Greenwald limit (n_e/n_G). This H-mode density limit (HDL) defines a soft limit, as the back transition to L-mode allows to continue the plasma operation at lower confinement. Figure 3.2 shows the 2-D operational space of the H-mode at AUG with carbon Plasma Facing Components (PFCs), described by the power across the separatrix (P_{SEP})

and the electron density n_e, where the red line represents the H-mode density limit, the black dashed line the Greenwald limit. The orange and the blue traces represent the evolution of typical high-density discharges and pure L-mode discharges respectively. One can see that an H-mode discharge, which reaches the density of the HDL, turns into L-mode, at which point its density can increase further up to the Greenwald limit. In accordance with this, an H-mode plasma with a flat density profile has not yet been observed to reach the Greenwald limit. However, the exceedance of the Greenwald density limit for H-modes with largely elevated core density profiles but featuring typical edge densities is well discussed in [74]. The HDL has also to be distinguished from H- to L-mode back transition, which occurs due to a reduction of the heating power instead of an increase of the electron density, time trace downward movement in Figure 3.2 instead of a movement to the right. Moreover, a second transition into H-mode is in principle possible by lowering the density or increasing the heating power [76].

During the experimental campaigns in full-W ASDEX Upgrade between 2011 and 2013, several dedicated gas ramp discharges for the H-mode density limit studies were made. The gas ramp

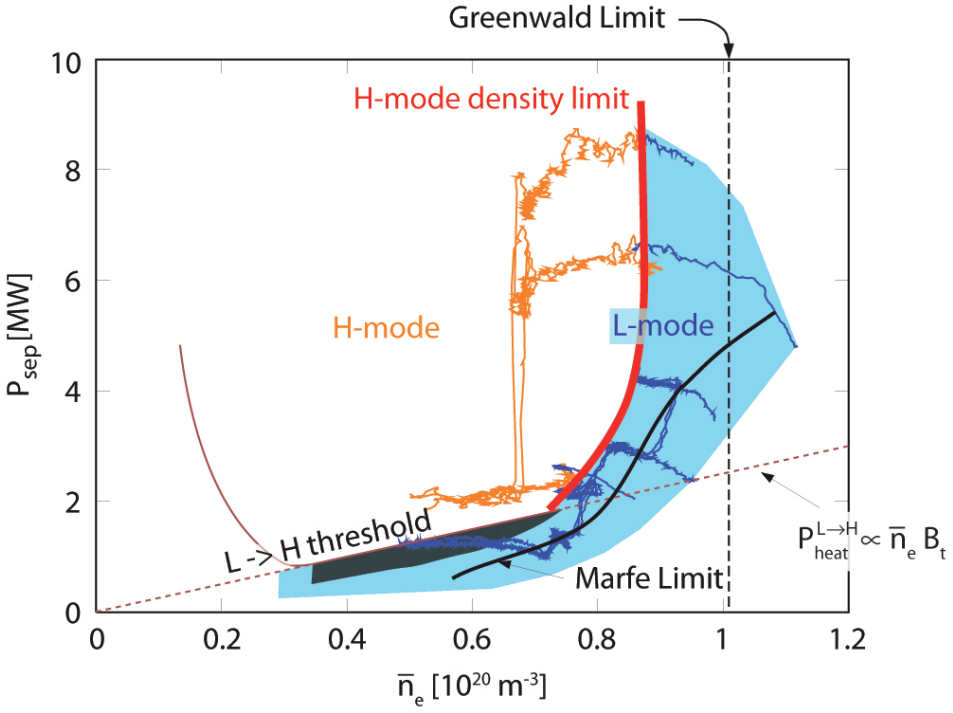

FIGURE 3.2: Operational space of the H-mode for high densities in AUG with carbon PFCs. The H-mode density limit is indicated by the solid red line, the Greenwald limit by the dashed line. The orange and blue lines represent the evolution of typical high-density discharges in H-mode with back transitions to L-mode and pure L-mode discharges.[76]

for the discharges is realized by injecting deuterium gas into the vacuum vessel. The neutral gas enters the plasma, is ionized and in this way increases the plasma density. Transport plus ionization and recombination mechanisms balance the plasma electron density with the neutral gas available in the vacuum vessel. For gas puffing several gas valves are installed below the divertor and on the low field side of the torus. The location and the rate of the gas puffing is programmed by the discharge control system before the discharge. The neutral pressure required for the HDL studies are up to 6 Pa in the divertor and 0.06 Pa in the main chamber. This is more than twice that in a standard H-mode discharge (about 2 Pa in the divertor and 0.004 Pa in the main chamber). Figure 3.3 shows on the left-side the time-traces of the stored energy (upper plot) and the line integrated density (bottom plot) at the plasma core (red line) and the plasma edge (blue line) of AUG #28728. In the right-side of Figure 3.3 the stored energy versus the the edge line integrated density is reported. The temporal evolution of the stored energy and the line integrated density exhibit four different phases [77] as indicated by the background colors in Figure 3.3. These phases are differentiated in the time derivative of density and stored energy and have for example an impact on the ELM behaviour or the divertor detachment. They become evident when the stored energy is plotted versus the edge line integrated density as reported in Figure 3.3(right-side).

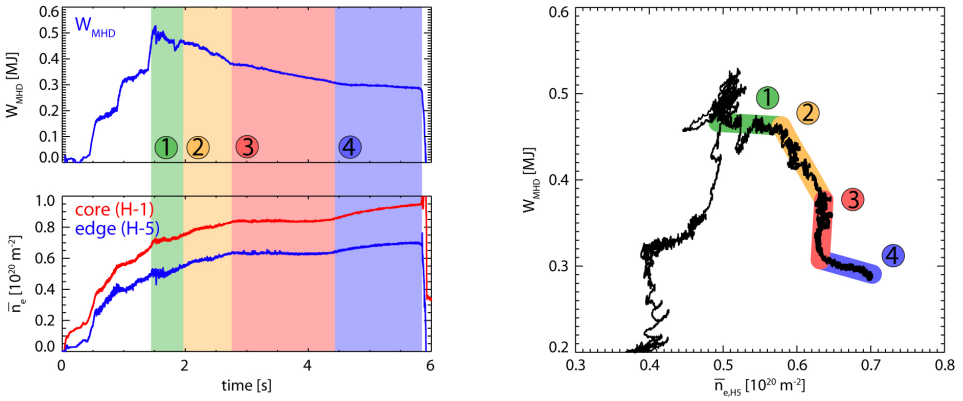

FIGURE 3.3: Time traces of stored energy and line integrated density of AUG #28728 (left side). Stored energy plotted versus the edge line integrated density. The background color highlights four distinct HDL phase. 1. Stable H-mode (green), 2. degrading H-mode (orange), 3. breakdown of H-mode (red) and 4. L-mode (blue) (right side).[77]

The 4 phases of an HDL discharge are deeply described in [74] and briefly reported here:

- 1. Stable H-mode: the stored energy stays flat and the density increase (see Figure 3.3 - green phase).
- 2. Degrading H-mode: a decreasing of the stored energy occurs at slightly increasing density (see Figure 3.3 - orange phase)
- 3. Breakdown of the H-mode: a sharp drop of the stored energy occurs at a constant density (see Figure 3.3 - red phase)
- 4. L-mode: the density increases again during a slight decrease of the stored energy. During this phase, a MARFE (see section 3.1.4) could develop in the X_{point} region

In [78], a 2D plasma-state boundary (see Figure 3.4) is proposed to detect the break-down of the H-mode as an early sensor for avoiding H-mode density limit (HDL) disruptions and recovering them to full performance. Furthermore, in HDL disruptions the plasma is strongly cooled from the edge, and this is typically accompanied by a MARFE.

3.1.4 Multifaceted Asymmetric Radiation From the Edge - MARFE

The multifaced asymmetric radiation from the edge (MARFE) is a toroidally symmetric, poloidally localized (tipically at minor radii) radiation instability [79]. It is a SOL effect and appears for divertor experiments mostly around the X_{point}. A MARFE generates a cold, dense plasma region, which, at AUG, radiates up to several MW of power. If a MARFE develops at the X_{point}, it reduces the power flux into the divertor and thus initiates detachment. If this cold and dense plasma region is close or inside the confined plasma, it can cool the pedestal and lead to an HDL. Typically, it is observed that a stable X_{point} MARFE starts to move upwards along the high field side SOL. This movement could generate the onset of an internal tearing mode, which leads finally to a disruption typically with a locking (2,1) mode [80]. The MARFE evolution is characterized by greatly increased radiation, high ion densities and density fluctuations, and relatively low electron temperature. MARFEs tend to occur in most tokamaks at similar values of f_{GRW} (MARFE threshold). [81]. Figure 3.5 shows the MARFE radiation evolution (time on the abscissa) around the X_{point} as measured by the diode horizontal camera of the absolute

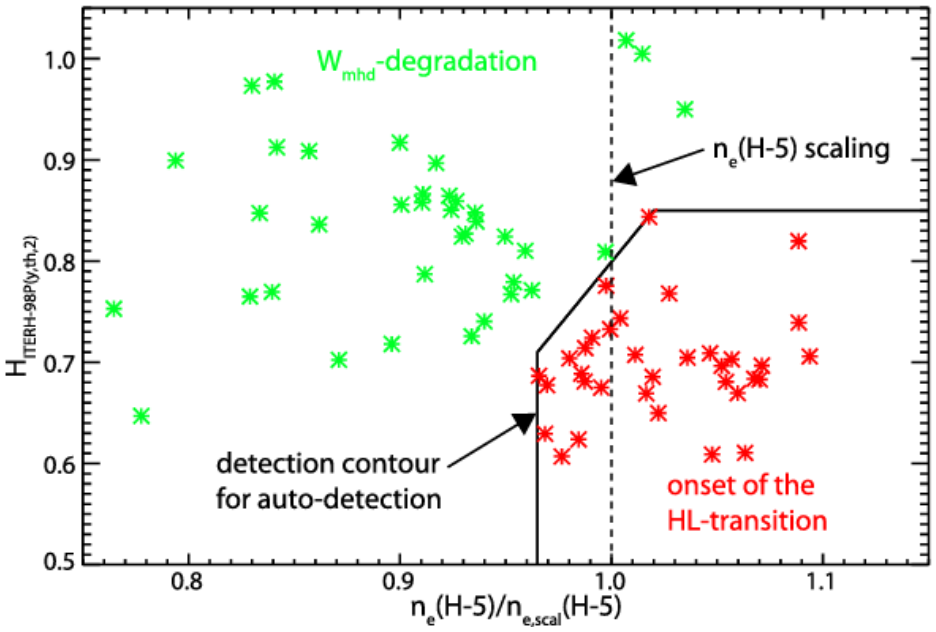

FIGURE 3.4: Operation diagram in terms of $n_e(H-5)/n_{e,scal}(H-5)$ versus $H_{ITERH-98(y,th,2)}$. The green points represent the times when the discharge performance was already degrading in terms of $H_{ITERH-98(y,th,2)}$ (phase 2), the red points show the time of the start of the H-L transition (begging of breakdown, phase 3). The solid black curve represents the suggested operation boundary at which the disruption handler should be activated.

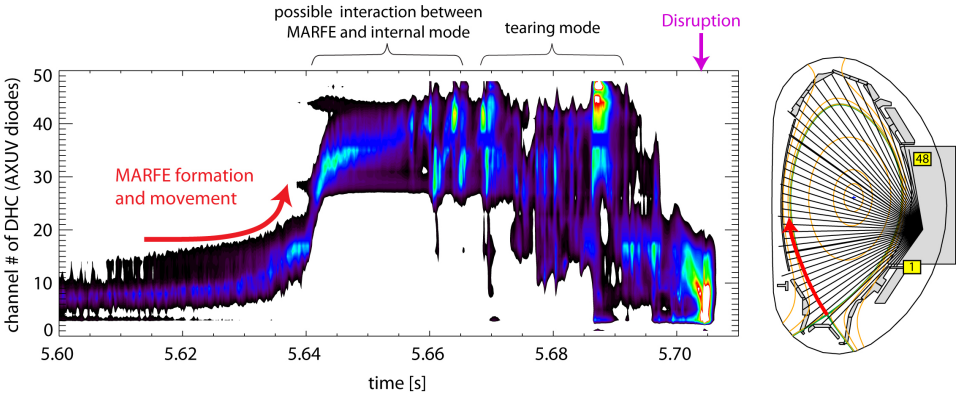

FIGURE 3.5: Left, development of a MARFE around the X_{point} and its upwards movement as measured by the DHC camera of the AXUV bolometry in discharge #26902 (contour plot of the measured radiation). Finally, the MARFE is initiating a disruption. Right, position and channel number of the DHC camera and direction of the MARFE movement.[74]

extreme ultraviolet (AXUV) bolometry and its movement upwards on the high-field side can be observed. The MARFE starts with a strongly fluctuating radiation localized around the X_{point}, then it moves upward. When the MARFE starts to move upwards, the outer divertor detaches completely. The movement of the MARFE coincides with the onset of an internal 2-1 tearing mode, which finally leads to the disruption as it was observed in ASDEX [82] and FTU [83]

plasmas. The MARFE threshold, as discussed earlier, is close to the density limit. In addition, when AUG plasmas are heated with NBI, the MARFE threshold and density limit are both increased [81].

3.1.4.1 MARFE Evolution Time (MET) and MARFE Evolution States(MES)

Understanding the mechanisms behind MARFEs and developing methods to mitigate their effects are essential for the development of sustainable fusion power. In this thesis the evolution of the MARFE is characterized by four MARFE Evolution Times (MET) initially defined by a manual investigation performed by expert physicist of the ASDEX Upgrade team, defined as in the following:

- MARFE formation (t_{MF}), it is the time when the bright region appear just above the X_{point}.
- high MARFE time (t_{MH}), it is the time when the vertical distance between the MARFE position and X_{point} becomes equal to 5 cm.
- low MARFE time (t_{ML}), it is the time when the vertical distance between the MARFE position and X_{point} comes back to be lower than 5 cm.
- MARFE stabilization time (t_{MS}), it is the time when the MARFE is stabilized and mostly the bright region disappear.

The definition of the METs allows to distinguish between three MARFE Evolution States (MES), defined as in the following:

- SAFE, when $t_i < t < t_{MF}$ & $t_{MS} < t < t_f$ where t_i is the starting of the flat-top and t_f its ending, no MARFE is present (green region in Figure 3.6).
- MARFE<5cm, when $t_{MF} < t < t_{MH}$ & $t_{ML} < t < t_{MS}$ a MARFE is present and it is far from X_{point} less than 5 centimeter (blue region in Figure 3.6).
- MARFE>5cm, when $t_{MH} < t < t_{ML}$ a MARFE is present and it is far from X_{point} more than 5 centimeter(red region in Figure 3.6).

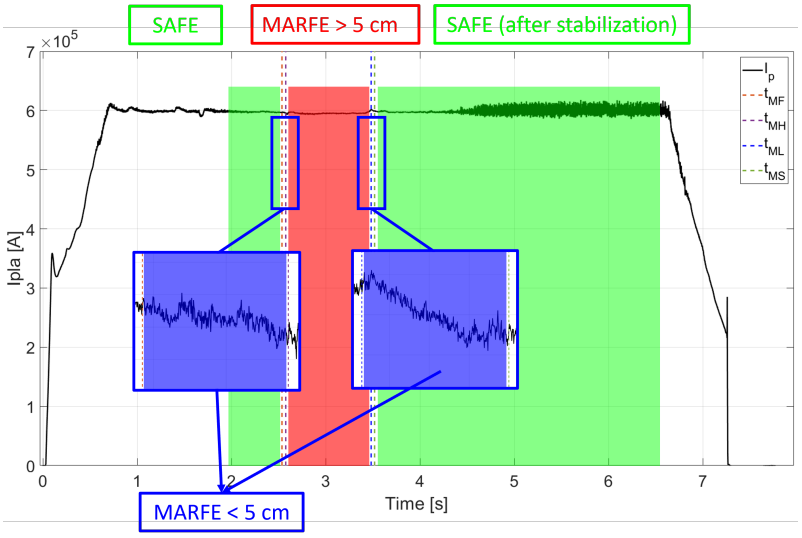

FIGURE 3.6: MET and MES for AUG pulse #33681. SAFE(green region), MARFE<5cm (blue region), MARFE>5 cm (red region).

As an example, MET and MES manually identified for the AUG pulse #33681, are reported in Figure 3.6 over the plasma current. This thesis aims to develop an automatic real-time MES detector, based on machine learning algorithm. To this purpose a database representing HDL scenarios, in which the MARFE is the most clear and identifiable event, and scenarios free from MARFE (simply indicated as NO HDL) has been built. The database consists in 110 discharges from the following pulse sets:

- 26 HDL pulses from 2011-2016 campaign (#26xxx-#33xxx). These pulses are characterized by a gas fluxes behaviour mainly ramped during the flat-top phase. Figure 3.7a) shows the plasma current and the overall D2 gas-fluxes rate (D_{tot}) time traces for a pulse extracted from this pulse set.
- 42 HDL pulses from 2017-2020 campaign (#34xxx-#37xxx). This list is mainly populated by pulses with a fast ramping of the D_{tot} followed by a flat trend. Figure 3.7b) shows the plasma current and D_{tot} time traces for a pulse extracted from this pulse set.
- 36 no HDL pulses from 2011-2017 campaign (#26xxx-#34xxx)
- 6 no HDL pulses from 2021-2022 campaign (#39xxx-#41xxx), characterized by the presence of high modes

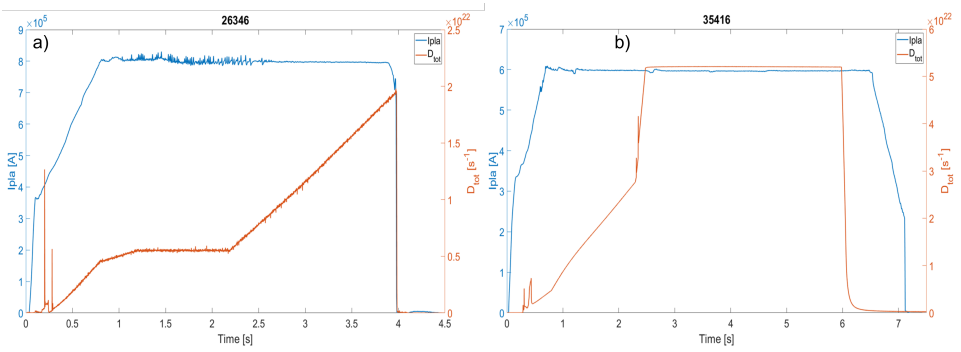

FIGURE 3.7: Subplot a) AUG pulse #26346, plasma current $Ipla$ (blue line) and the overall D2 gas-fluxes rate D_{tot} (light brown line). AUG pulses from 2011 to 2016 mainly present a ramped D_{tot} during the flat-top phase. Subplot b) AUG pulse #35416, $Ipla$ (blue line) and D_{tot} (light brown line). AUG pulses after 2017 present a fast ramping of D_{tot} followed by a flat trend.

3.2 ISOmetric feature MAPping algorithm for manifold learning

Scientists often deal with problems involving high-dimensional data and the most obvious issue is visualization. Indeed when the data dimension is greater than three, they cannot be visualized and it becomes harder to perceive similarities and dissimilarities between different variables. Algorithms that operate on high-dimensional data face with the 'curse of dimensionality' and the associated issues, resulting in a very high complexity. For example, organizing and searching data relies on detecting areas where objects form groups with similar properties. However, in high-dimensional data all objects appear to be sparse and dissimilar, which prevents common data organization strategies from being efficient. One approach to visualize the data of interest is to assume that they lie on a low-dimensional manifold, embedded in the high-dimensional space. Thus, data reduced to a small enough number of dimensions can be visualized in the low dimensional embedding space. Attempting to uncover this manifold structure in a data set is referred as manifold learning. It is noteworthy to mention that identifying the right manifold would also allow us to better model the relevant physics. Therefore, manifold learning has the potential not only to improve the visualization and the intuitive estimation of problems but also to qualitatively increase the understanding of the relevant physics embedded in the data. In the last few years, many manifold learning techniques have been developed for dimensionality reduction. Several supervised and unsupervised linear dimensionality reduction frameworks have been proposed, which define specific procedures to choose interesting linear

projections of the data, such as PCA [84] and Grand Tour [85]. These linear methods can be powerful, but often miss important nonlinear structures in the data. Recently, different algorithms have been developed to perform nonlinear dimensionality reduction. Among them, there are powerful methods such as Self Organizing Map (SOM) [86], Generative Topographic Mapping (GTM) [87], and ISOmetric feature MAPping (ISOMAP) [88] and Locally Linear Embedding [89]

3.2.1 Introduction to manifold learning

Manifold learning (ML) is a brach of machine learning. Within the field of machine learning, two different types of training approaches can be distinguished, supervised and unsupervised. Supervised learning is done using prior knowledge of the output values. Therefore, the goal of supervised learning is to learn a function that best approximates the relationship between observable input and output data features. Unsupervised learning techniques work by comparing data and looking for similarities or differences. It learns the high-dimensional structure of the data from the data itself, without the use of prior classifications or labeling of the examples. Though supervised variants exist, the typical manifold learning problem is unsupervised. Machine Learning can review large volumes of data and discover specific trends and patterns offering a low-dimensional space representation obtained through a dimensionality reduction process. The dimensionality reduction essentially projects data from a high-dimensional feature space into a low-dimensional feature one, called latent space, preserving the original data metric. The dimensionality reduction is commonly used in data visualization to understand and interpret the data behavior. The latent space often referred to intrinsic variables, which can be assumed as the features from which the data are produced. In addition, dimensionality reduction can be used as a general pre-processing technique to raise the classification accuracy [90]. The most common techniques for dimensionality reduction, like PCA, Multi-Dimensional Scaling, Independent Component Analysis and others, perform linear projections of the data in a latent space. They are simple to implement, efficiently computable, and guaranteed to discover the true structure of data lying on or near a linear subspace of the original high-dimensional input space. These methods can be powerful, but often miss important non-linear structure in the data. The ML can be thought of as an attempt to generalize linear projection frameworks, to be sensitive also to non-linear structure in data. ML is a modern innovation that has

enhanced many research fields such as pattern recognition, classification problems and feature extraction. Unlike classical dimensionality reduction techniques, the non-linear ML algorithms are able to discover the nonlinear degrees of freedom that underlie complex natural observations (manifold), such as ISOMAP, LLE and others. In the pattern recognition field, ML algorithms, performing both clustering and dimensionality reduction task, can be employed to obtained, in a completely unsupervised way, a 2-D or 3-D maps containing clusters populated by samples of similar points (close to each other in the high-dimensional manifold), such as SOM and GTM. These maps provide a way of visualizing the structure of the high-dimensional and allow discrimination between regions with different characteristics. Figure 3.8 shows the results of a SOM application to visualize and analyze the structure of a ten-dimensional JET operational space conducted in [71]. Safe or disruptive labels were associated to each sample of the considered database, depending on the experiment they came from, regularly terminated or disrupted discharges respectively. After the SOM training, label associated with each sample allows to identify four main categories of clusters depending on their composition: empty clusters, which contain no samples; disruptive clusters, which contain disruptive samples; safe clusters, which contain safe samples; mixed clusters, which contain both safe and disruptive samples. A color is associated with each cluster type: safe clusters are blue; disruptive clusters are red, mixed clusters are gray and empty clusters are white. A different disruption risk can be associated to each cluster type, safe clusters (blue) have low risk of disruption, disruptive cluster (red) have high risk of disruption, while mixed and empty cluster have no defined risk. Thus, Figure 3.8 is a 2D representation of the JET operational space in terms of disruption risk. In addition, following the trajectory of a new pulse in the 2D map, it is possible to eventually recognize the proximity of the disruptions depending on the location of the operating point. Indeed, the trajectories of a safe discharge (#78000, cyan trajectory) and of a disruptive discharge (#73851, magenta trajectory) are reported. As can be noted, the disrupted discharge starts in a safe cluster, evolves among safe, mixed clusters and white regions, and terminates in a disruptive region. The regularly terminated discharge starts in a safe cluster and evolves with the time moving into the safe region never going in the disruptive ones.

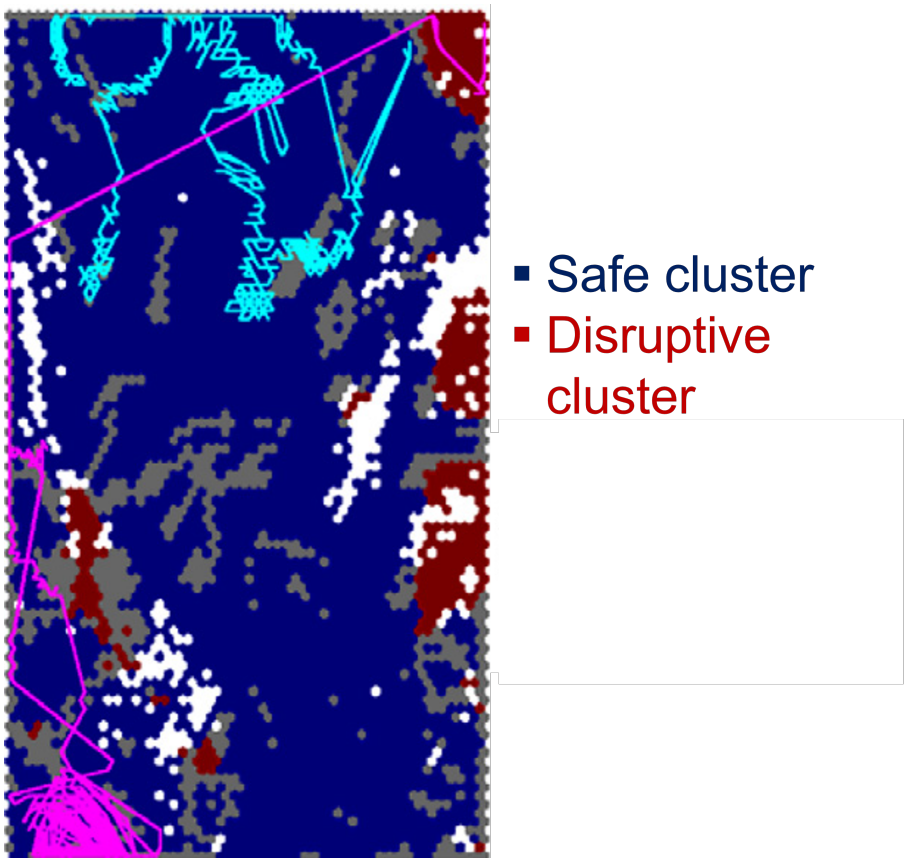

FIGURE 3.8: SOM of the 10D JET operational space. Safe clusters (blue), disruptive clusters (red), mixed clusters (gray), empty clusters (white), tracks of the disruptive pulse #73851 (magenta) and of the safe pulse #78000 (cyan).

3.2.2 ISOmetric feature MAPping - ISOMAP

ISOMAP is a nonlinear unsupervised dimensionality reduction technique based on the idea that similarity between points on a high dimension manifold can be preserved on a lower dimensional latent space through their geodesic distance, presented by Joshua B. Tenenbaum in [88]. A geodesic is the shortest path between two points on a surface, the geodesic distance is the length of the path. The geodesic distance evaluates the distance between two points following the surface of the data manifold, allowing to overcome shortcuts errors create by Euclidean distances that does not properly represent the shape of the manifold. Indeed, geodesic distance is able to discover nonlinear degrees of freedom that underlie complex natural observations, such as human handwriting or images of a face under different viewing conditions [88]. To easily display the ability of the ISOMAP, Figure 3.9A illustrates the challenge of interpreting

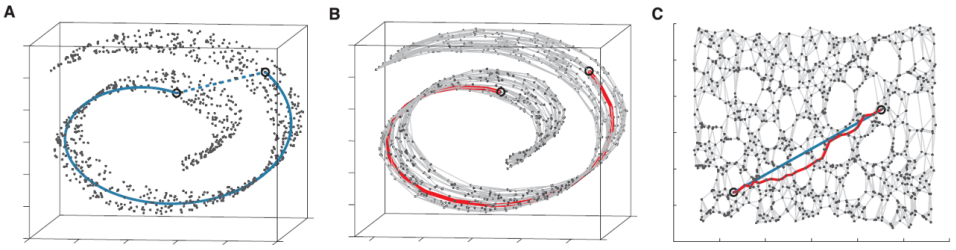

FIGURE 3.9: "Swiss roll" data set. (A) For two arbitrary points (black circles) on a nonlinear manifold, their Euclidean distance in the high-dimensional input space (length of dashed line) may not accurately reflect their intrinsic similarity, as measured by geodesic distance along the low-dimensional manifold (length of the solid curve). (B) The neighborhood graph G constructed in step one of ISOMAP algorithm (k = 7, N = 1000 data points) allows an approximation of the true geodesic path computed in the step two as the shortest path (red segments). (C) The two-dimensional embedding recovered by ISOMAP algorithm in step three. The shortest path (red segments) provides an accurate estimation of the true geodesic distance (blue line).

nonlinear structure in the data with data lying on a 3D swiss roll. Points far apart on the underlying manifold, as measured by their geodesic distance (blue line), may appear deceptively close in the high-dimensional input space if the adopted metrics is their straight-line Euclidean distance, blue dashed line. Only the ISOMAP can reflect the true manifold geometry in a 2D latent space, while linear projection such as PCA and MDS can see just the Euclidean structure. The idea behind the ISOMAP is that the Euclidan distance can be used only to quantify distance between close samples (the neighbors). Thus, a neighborhood can be computed, by meaning of the Euclidean distance, to define a graph on which geodesic distance matrix can be computed, as shown in Figure 3.9B. Finally, applying MDS techniques, a 2-D (or 3-D) space, which preserves the structure of the original manifold, can be obtained as illustrate in Figure 3.9C.

3.2.2.1 ISOMAP steps

The key point of the ISOMAP is estimating the geodesic distance between faraway points considering the input- space pairwise distances (Euclidean distances). For neighboring points, the pairwise distance provides a good approximation to geodesic distance. For faraway points, geodesic distance can be approximated by adding up a sequence of "short hops" between neighboring points. These approximations are computed efficiently by finding shortest paths in a graph with edges connecting neighboring data points. The complete ISOMAP algorithm has three steps, which are described in the following:

1. The first step determines which points are neighbors on the manifold M, based on the Euclidean distances $d_E(i,j)$ between pairs of points i,j in the input space (Figure 3.9A). Let n be the dimensionality of the input space and N the number of samples (or point), the high-dimensional input points is $X = \{x_1, x_2, ..., x_N\}$ with x_i and $x_j \in \Re^n$, $d_E(i,j)$ is defined by equation (3.2)

$$d_E(i,j) = |x_i - x_j| \tag{3.2}$$

   Two simple methods can be adopted to define the neighbors of each point, the first considers all points within some fixed radius ε (giving an ε-ISOMAP), the second assumes the k nearest neighbors (giving a k-ISOMAP). These neighborhood relations generates a weighted graph G into the input space, where $d_E(i,j)$ is the weight of the edges between the i^{th} and j^{th} neighboring points (see Figure 3.9B).

2. The second step, estimates the geodesic distances between all pairs of points on the manifold by computing their shortest path distances $d_G(i,j)$ in the graph G, and it creates the geodesic distance matrix $D_G = \{dG(i,j)\}^{N \times N}$ (see red line in Figure 3.9B).

3. The final step applies classical MDS to the matrix of geodesic distances D_G, by constructing an embedding of the data in a low-dimensional space that best preserves the manifold's estimated intrinsic geometry (see Figure 3.9C).

The ISOMAP algorithm provides among the outputs the geodesic distances matrix D_G, which preserves the original dimension of the input space. Thus, the geodesic distance of a new operating point from a region of interest can be valuated exploiting the original manifold, without any lack of information. Therefore, in this thesis a tool to determine the geodesic distances of test samples from the different MARFE Evolution States represented in a training input space has been developed, with the aim of providing the automatic alarms of the MARFE Evolution Times. In addition, both 2D and 3D ISOMAP representation of the high dimensional manifold (computed by step 3, see section 3.2.2.1) have been performed to track the plasma state evolution of a test pulse among the different MESs. The database for training and testing the developed tool is described in the section 3.4.

3.3 Database

The database is built considering a set of physical and engineering parameters recorded by several diagnostics for the 110 pulses described in section 3.1.4.1

3.3.1 Plasma parameter selection and data pre-processing

In this section the features selected to describe the plasma state and the pre-processing procedure applied to define the ISOMAP input features is presented. Plasma parameters have been selected among those available in real-time from AUG database, considering their capability to describe the plasma state (i.e. plasma internal parameters) and taking also as reference those used from various authors for MARFE and the HDL studies [77, 78]. The following 0D and 1D signals have been selected:

1. Safety factor at 95% flux surface ($q95$)
2. Internal Inductance (li)
3. Plasma energy ($Wmhd$)
4. Sum of D2 gas-fluxes (D_{tot})
5. Electron density from a peripheral interferometer line of sight (Ne_{edge})
6. Greenwald fraction (f_{GRW})
7. Total applied power (P_{TOT})
8. Plasma elongation (k)
9. Radiated power profile from the foil bolometer horizontal camera ($P_{rad,FHC}$)
10. Electron temperature from the ECE radiometer (Te_{ECE})

For each selected pulse, only the time window of the plasma current flat-top has been selected to be used for the ISOMAP training and test. Thus, as first step, initial and final flat-top time (t_0 and t_f respectively) have been automatically detected using the algorithm for the automatic

flat-top detection described in [9]. Then, to avoid unrealistic values of the features that occur near the disruption, such as negative values of Ne_{edge}, the final time of each pulse has been usually set equal to $t_{cut} = t_f - 200$ ms. Since a MARFE could lead to a disruption, t_{MF} and t_{HF} can occur in the window $t_f - 200$ ms, for the pulses with a MARFE near to the disruption, the t_{cut} has been manually optimized in order to obtain $t_{cut} > t_{HF}$ when the signals have no unreliable value, otherwise the last MARFE has been removed and considered as undetectable. To avoid improper jump both in the ISOMAP graph G and in evaluation geodesic distance of an operating point from a region of interest during a test pulse projection due to outliers, a Gaussian filter has been applied to smooth li, $Wmhd$, Ne_{edge}, P_{TOT} and k behaviors. To be applied in real time the filter needs to be causal, thus it takes into account a time window of 50 samples preceding the operating one. As last pre-processing step, each feature has been linearly interpolated on the plasma current time-base (in the time window between t_0 and t_{cut}) and then down-sampled at 200 Hz. The down sampling was necessary to find a compromise between the number of samples needed to properly represent the AUG manifold and the RAM limit of the UNICA cluster-computer (RAM = 100 Gb), used for the ISOMAP training. Figure 3.10 shows the time traces of the 0-D signals from 1 to 8 listed above, in the window t_0 to t_{cut}, for pulse #35416. The radiated power and the temperature profiles consist of 49 and 61 time series respectively, retrieving the measures from different Line of Sight (LoS). When defining the data input space, an overblown number of features must be avoided because big data yields more sparsity. Machine learning models trained on sparse data performed poorly in the test dataset [91]. Indeed, the computational complexity increases and the ML models during the training learn noise and they are not able to generalize; hence they overfit. Thus, to limit the dimensionality of the input space and to be independent by the quality measure of each LoS, 7 features (four radiated powers and three electron temperatures) have been processed from 110 time series, as reported in the following subsections. These features describe the parameter behavior in different plasma section regions, thus maintaining the spatial information without excessively increasing the input space dimensionality.

3.3.1.1 Radiated power features from Foil Bolometer measures

The radiated power measured by the foil bolometer P_{rad}, Line of Sights (LoSs) of the horizontal camera, have been subdivided to compute 4 different features to represent in the

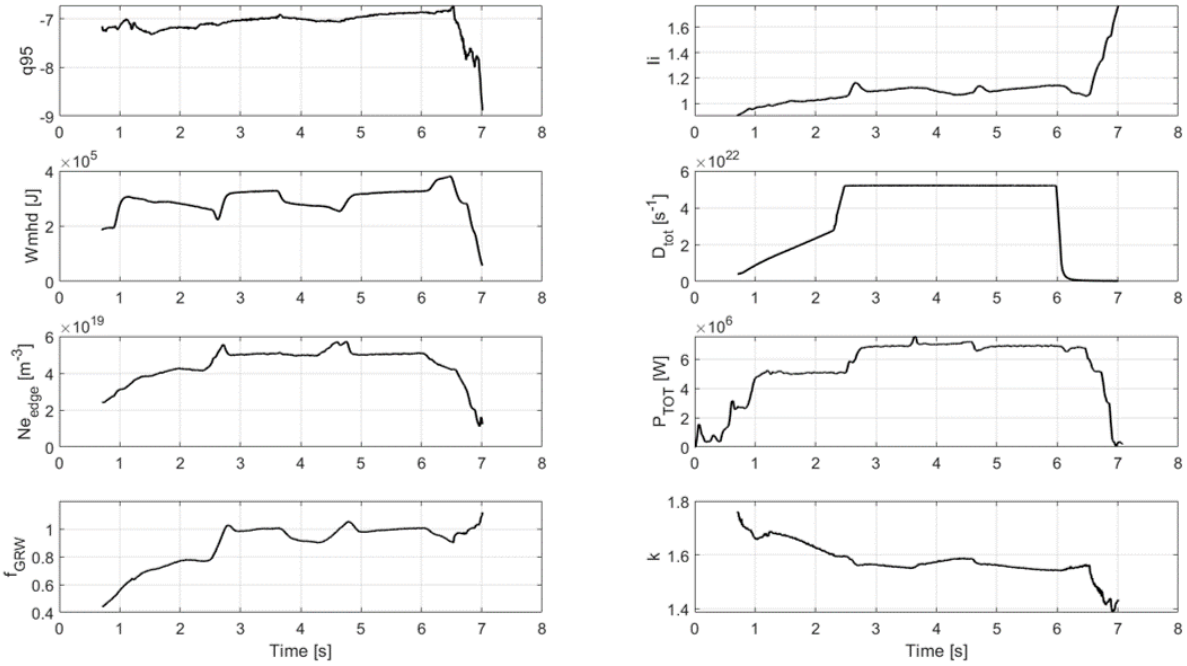

FIGURE 3.10: 8 features of AUG pulse #35416. Left column, from top to bottom: safety factor ($q95$), plasma energy ($Wmhd$), plasma density at the edge (Ne_{edge}), Greenwald fraction (f_{GRW}). Right column, from top to bottom: internal inductance (li), sum of D2 gas-fluxes (D_{tot}), total applied power (P_{TOT}), elongation (k).

ML input space the radiated power from different region of the poloidal plasma section. A P_{rad} signal version, available in real-time, has been provided by the ASDEX Upgrade team. To avoid unreliable values and outliers, a preprocessing procedure has been applied to each LoS measure. As first step, all available measurements have been smoothed considering a Gaussian causal filter on a time window of 500 ms. Then, only the ones having a mean value greater than 10^4, in the time window from $t_0 + 0.3$ s to t_{cut} are considered, (during the time window from $t_0 - 0.3\ s \div t_{cut}$). After the pre-processing step, the following four features have been computed, performing sample by sample the arithmetic mean through selected LoSs:

1. $P_{rad,DIV}$: mean of the radiated powers from divertor LoS
2. $P_{rad,UPPER}$: mean of radiated powers from upper LoS
3. $P_{rad,CORE}$: mean of radiated powers from core LoS
4. $P_{rad,MAIN}$: mean of radiated powers from upper and core LoS

The LoSs looking at the divertor region are reported in Figure 3.11a), those selected for defining the core region are reported in Figure 3.11b) and the ones selected for defining the upper region are reported in Figure 3.11c). In particular, $P_{rad,DIV}$ takes into account only LoSs from 1 to 12, $P_{rad,UPPER}$ takes into account LoSs from 13 to 33, $P_{rad,CORE}$ considers LoSs from 34 to 49, while $P_{rad,MAIN}$ considers both LoSs from 13 to 49. The four subplots in Figure 3.12 show the different time traces of the $P_{rad,FHC}$ and the four P_{rad} features for AUG #35416. The radiated power from divertor region (colored lines) and $P_{rad,DIV}$ (black line) are reported in the upper-left plot, the radiated power from the plasma core region (colored lines) and $P_{rad,CORE}$ (black line) are reported in the upper-right plot, the radiated power from the upper plasma region (colored lines) and $P_{rad,UPPER}$ (black line) are reported in the bottom-left plot and the radiated power from the main (core and upper) region (colored lines) and $P_{rad,MAIN}$ (black line) are reported in the bottom-right plot.

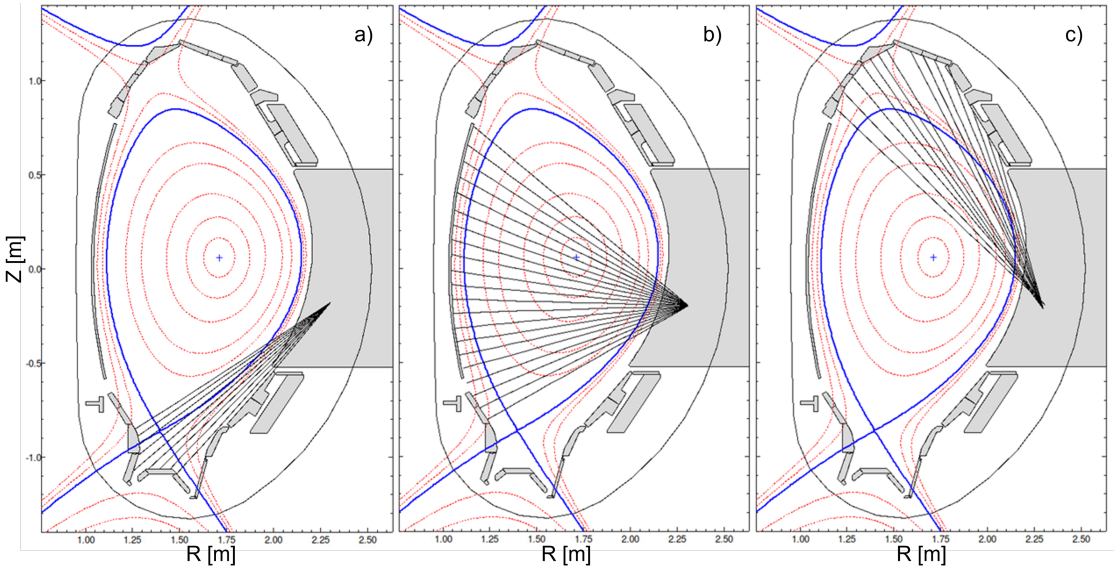

FIGURE 3.11: Foil bolometer horizontal cameras. a) LoS that look at the divertor region, b) LoS that look at the plasma core region, c) LoS that look at plasma upper region.

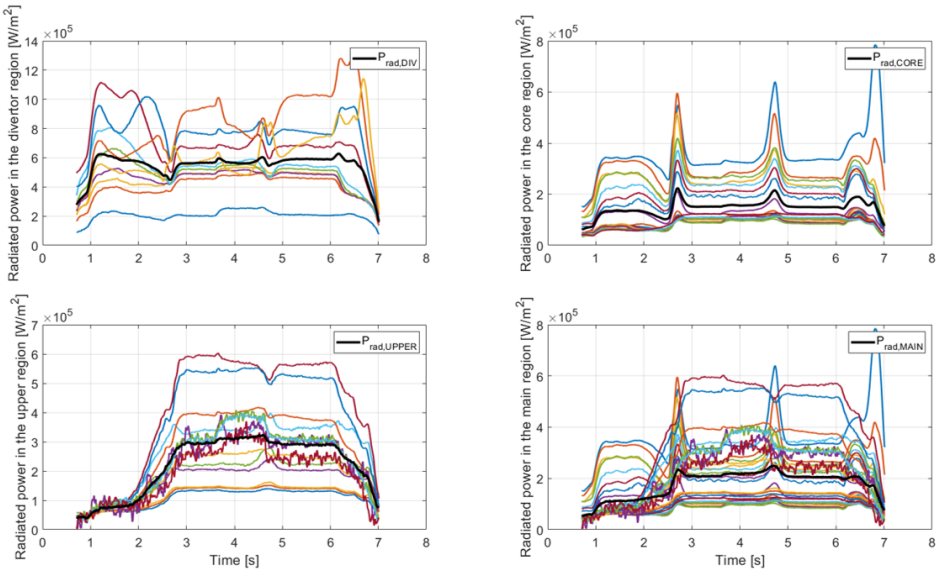

FIGURE 3.12: Radiated power and P_{rad} features for AUG #35416. Upper-left plot, radiated power from divertor region (colored lines) and $P_{rad,DIV}$ (black line). Upper right plot, radiated power from the plasma core region (colored lines) and $P_{rad,CORE}$ (black line). Bottom-left plot, radiated power from the upper plasma region (colored lines) and $P_{rad,UPPER}$ (black line). Bottom-right plot, radiated power from the main (core and upper) region (colored lines) and $P_{rad,MAIN}$ (black line).

3.3.1.2 Electron temperature features derived from the ECE radiometer

The electron temperature measured by the ECE radiometer LoSs have been subdivided to compute three different features to represent in the input data space the electron temperature from different region of the poloidal plasma section. To avoid unreliable values due to cut-off and outliers, a preprocessing procedure has been applied to each LoS measure consisting in a Gaussian causal filtering on a time window of 150 ms. In addition, the LoSs which temperatures verify at least one of the following condition in the flat-top time window have been excluded: mean value lower than 30 eV, maximum value greater than 6000 eV, minimum value lower than -200 eV, and a pairwise linear correlation coefficient lower than 0.3 (all these parameters have been tuned with an euristic procedure). To divide the ECE LoSs into the three different groups their radial position time traces (R_ECE [m]) have been considered and compared with the radial position time trace of the last closed surface (R_{out} [m]). The adopted radial ranges are: $1.02 < R_{ECE}(t) < 1.8$ m for defining the inner channels, $1.8 < R_{ECE}(t) < 2.02$ m for defining the intermediate channels, and $2.02 < R_{ECE}(t) < R_{out}(t)$ for the outer ones. Three electron

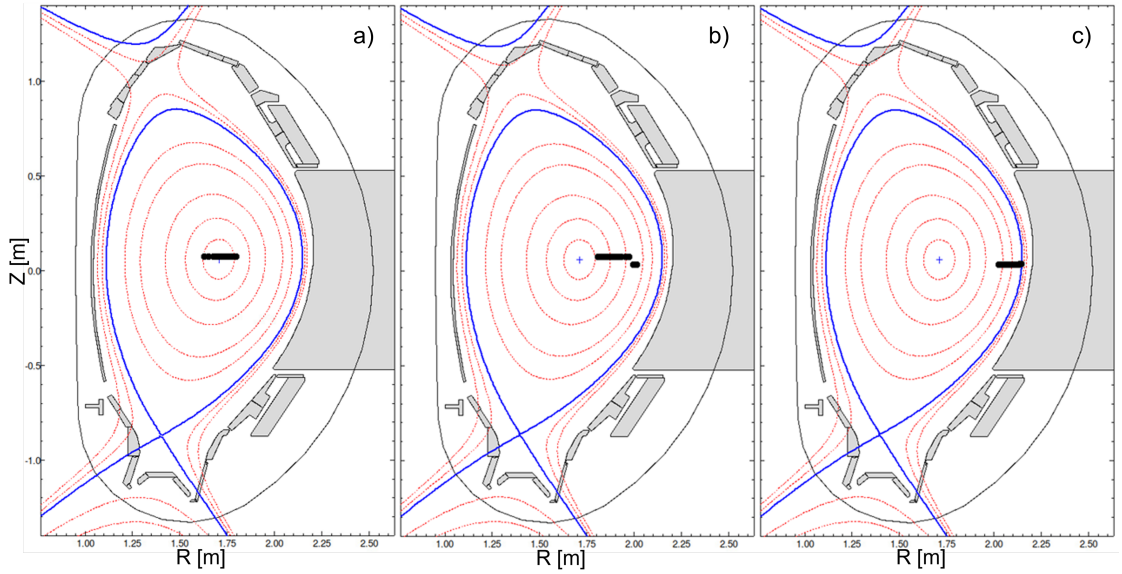

FIGURE 3.13: ECE radiometers LoS selected for defining: a)plasma core region, b)plasma ex-core region, c)plasma edge.

temperature features have been computed through arithmetic mean on the three different channel groups:

1. $Te_{mean,CORE}$: electron temperature average of the inner channels
2. $Te_{mean,EX-CORE}$: electron temperature average of the intermediate channels
3. $Te_{mean,EDGE}$: electron temperature average of the outer channels

The Figure 3.13 shows the LoSs partitioning for AUG #35416, subplot a) reports the inner LoS used to define the plasma core temperature, subplot b) reports the intermediate LoSs used to define the external core temperature, and subplot c) reports the outer LoSs used to define edge temperature. Figure 3.14 shows the Electron temperature time traces for AUG #35416 as measured by every ECE LoS. The colored tiny lines are the pre-processed ECE measurements and the bold lines represent $Te_{mean,CORE}$ (black line), $Te_{mean,EX-CORE}$ (magenta line), $Te_{mean,EDGE}$ (green line).

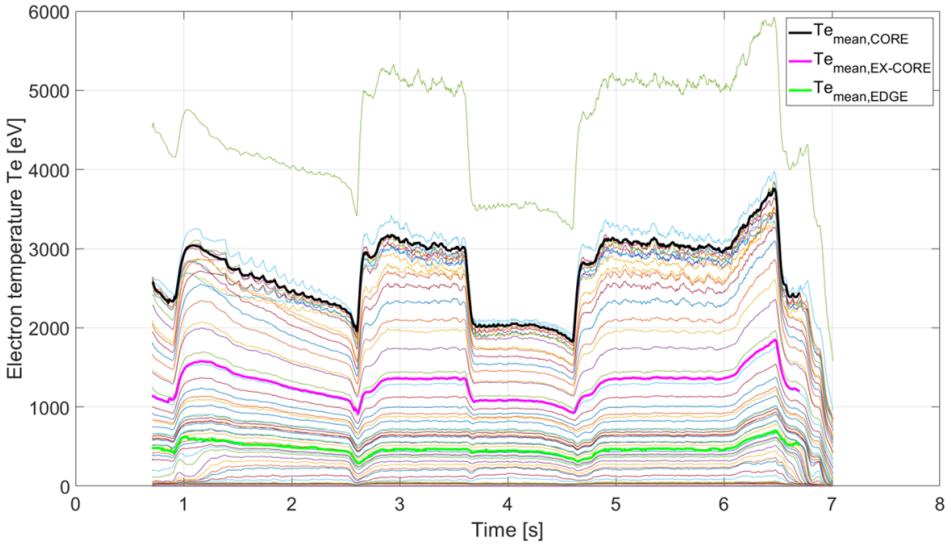

FIGURE 3.14: Electron temperature and Te features for AUG #35416. Te_{ECE} (colored lines), $Te_{mean,CORE}$ (black line), $Te_{mean,EX-CORE}$ (magenta line) and $Te_{mean,EDGE}$ (green line).

3.4 ISOMAP algorithm for AUG HDL manifold learning

A Dimensionality Reduction (DR) toolbox for Matlab has been developed by Laurens van der Maaten [92]. The toolbox allows the execution of more than 30 different DR techniques among which the ISOMAP. In the next sections it will be described how to the toolbox has been modified to be applied for the AUG MES predictor.

3.4.1 ISOMAP application and implementation

ISOMAP has never been applied to study a manifold representing tokamak operative conditions. Thus, a lot of attempts have been conducted to find the best algorithm settings (i.e. neighbors definition, algorithms for shortest path calculation, features selection). A "Swiss roll" test problem has been used as benchmark to proof the validity of each selected setting and to compare them in term of computational effort. Considering the dataset presented in 3.1.4.1, the input space used to train the ISOMAP, consists of 37231 samples and 15 input features. With such a big dataset the step 1 and 2 of the ISOMAP algorithm (see section 3.2.2.1) were very time consuming using traditional computing techniques. The computational time has been drastically reduced implementing an algorithm to conduct both the steps 1 and 2 using parallel computing technique on a UNICA server with a 100 GB RAM and 50 processor units.

3.4.1.1 Neighborhood definition

The neighborhood definition is the most crucial step of the ISOMAP training, indeed it strongly impacts the graph structure, which in turn affects the path between pairs of points and thus both the geodesic distance matrix D_G and the results of the MDS. As highlighted in section 3.2.2, two basic training methods can be used depending on neighborhood definition, the ε-ISOMAP and the k-ISOMAP. The ε-ISOMAP requires a priori knowledge of the manifold or an iterative optimization is needed to set the ε value. A more complex definition of the k neighbors can be adopted, the *kadaptive*-ISOMAP. It is suggested for manifolds with strong variating curvature and nodes density, and it is based on the idea to calculate an adaptive k for each sample, which takes into account the local values of curvature and density of the manifold. The neighborhood definition fails if data lies on disconnected manifolds. Indeed, the input space can lie on different batches instead of a connected graph. This means that at least two different batches of samples exist. As an example, Figure 3.15(left-side) shows two different batches A and B for $k = 2$ where each point of the batch A has not a neighbor in the batch B. Thus, there is no connection allowing a path definition from any point in A to any point in B. In this case $d_G(a, b) = \infty$, where a and b are samples of A and B respectively. This problem can be overcome by creating edges between the two batches, as shown in Figure 3.15, right side. Since k-ISOMAP, ε-ISOMAP and *kadaptive*-ISOMAP are all included in the *DR toolbox*, they have been investigated to define which is the best method for our application. Both ε-ISOMAP (considering the range $\varepsilon = 0.05 \div 0.5$) and *kadaptive*-ISOMAP failed to create a connected graph and the reasons of the disconnections were hard to understand. The k-ISOMAP is much

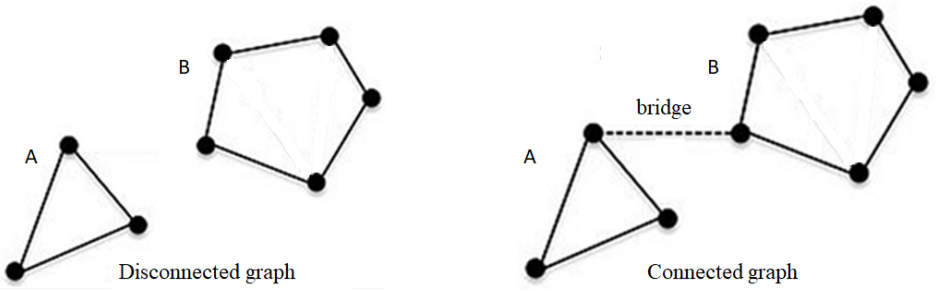

FIGURE 3.15: Batching during neighborhood definition. Left-side: a disconnected graph composed by two batches A and B, it is not possible to define a path to go from A to B ($d_G(a, b) = \infty$). Rigth-side: batches A and B can be connected creating a edge that allows the path definition between each pair of points.

simpler and more stable, suggested values of k can be find in literature [93, 94] and causes of disconnections were easily individuated. Thus, the k-ISOMAP method has been used in this thesis, opportunely implemented to overcome graph disconnections.

The considered database presents two different sources of batching, both related to the specific behaviors. The first one has been initially observed training the ISOMAP on a single shot, and it persists also training on large number of pulses. During a tokamak discharge the modulation of the neutral beam injected power causes a rapid and large variation of the P_{TOT} and others features (i.e. $Wmhd$), selected in this thesis to describe the HDL operational space. Because of these strong variations of the input features a disconnection of the manifold occurs from the neighborhood definition. This effect is clearly represented in Figure 3.16 where the plasma current ($Ipla$) and the and NBI total input power (P_{NBI}) for AUG #26592 are reported in the upper plot, blue and red line respectively. Whereas, in the bottom plot the number of connected samples for each batch is reported, the 4 colored boxes help to visualize that the batching of the pulse is due to the P_{NBI} variations. This subplot highlights the presence of different batches. The four batches are unaffected by different values of k (i.e. 5, 8, 12, 20). As solution of this problem, it has been chosen to create an edge between subsequent samples belonging to the same pulse, thus i^{th} sample will be always connected to sample $i^{th}+1$ even if an NBI variation occurs between them. This solutions is consistent with the intrinsic nature of data since successive samples represent successive operative conditions. To not increase the overall number of edges, for each sample this forced edge replaces the one with the farthest neighbor. The label $k+1$-ISOMAP is used to refer to the ISOMAP trained adopting this neighborhood definition. The other source of batching is related to the database topology, indeed since it is composed by pulses, each pulse can potentially generate a disconnection of the graph. Whereas, applying the $k+1$-ISOMAP, the graph could be again made of different batches, where each batch contains pulses that are close to each other (i.e. same session, similar q_{95}). This is because the $k+1$-ISOMAP allows to select as neighbors samples that belong to the same pulse. Therefore, to avoid the batching of the graph due to the pulse ending, edges ensuring the connection between samples belonging to different pulses are necessary, without modifying the manifold behavior. This aim can be reached in different ways, in this thesis the following three different solutions have been exploited:

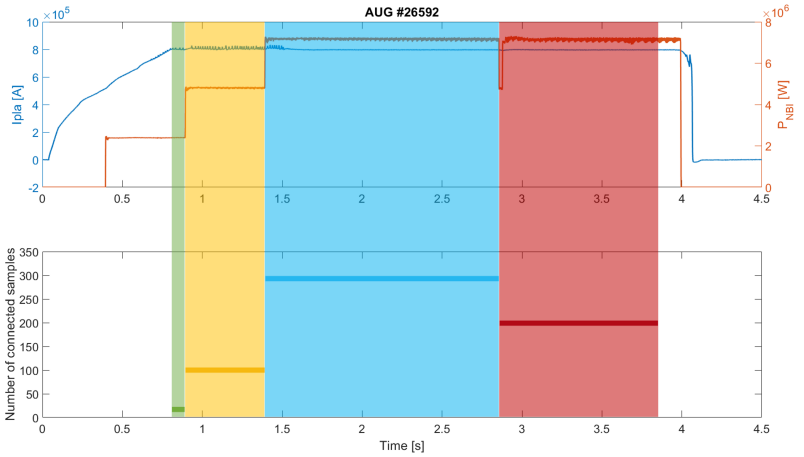

FIGURE 3.16: AUG pulses #26592. *Ipla* (blue line), P_{NBI} (brown line), SoF (black dasehd lines), EoP (black line), the colored boxes represent the batches created using a standard k-ISOMAP.

1. Creating m additional edges for each sample. Each sample is additionally connected to the nearest sample from m different pulses. The label $12 + m$-ISOMAP marks this solution.

2. Creating $M - 1$ additional edges for each samples, where M is the number of pulses in the dataset. These $M - 1$ connect each sample to nearest sample of each other pulse. The label $12 + (M - 1)$-ISOMAP marks this solution.

3. Augmenting the number of natural neighbors up to K, until a connected graph is obtained. The label K-ISOMAP marks this solution

Since the ISOMAP training is time consuming, and it depends by the number of samples in the database, the neighbor value k has been optimized on a train subset of 60 pulses, down-sampled at 100 Hz (resulting in 23000 samples), in order to quickly provide the required ML outputs. For the considered dataset, $m = 5$ is the minimum value that allows to get a connected graph. Thus, the option 1 results in $k = 17$ for each sample. The option 2 results in 71 edges for each sample, while $K = 50$ has been obtained adopting the option 3, resulting in 62 edges for each sample. Figure 3.17 shows the 3D representations (3D-ISOMAP), obtained applying the PCA on the geodesic distance matrix D_G evaluated setting the k value with three different options. From left to right, $12 + (m)$-ISOMAP, $12 + (M - 1)$-ISOMAP with $M = 60$, K-ISOMAP. In the 3D-ISOMAP A_1, A_2 and A_3 are the first three eigen-values of D_G. In these maps the green samples represent the SAFE state, the blues samples the MARFE< 5cm state and the

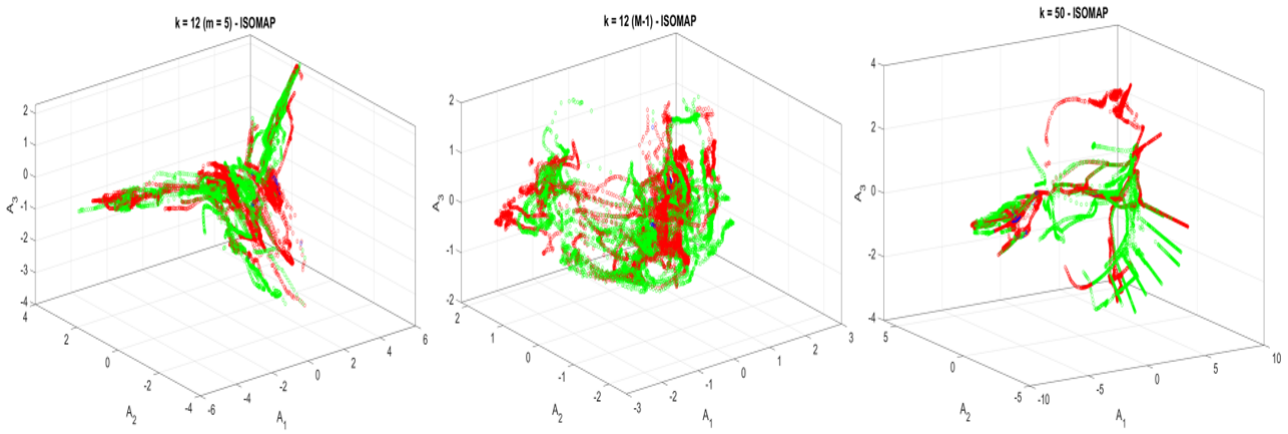

FIGURE 3.17: 3D-ISOMAP. From left to right: k = *12(M)*-ISOMAP, k = *12 (M-1)*-ISOMAP, k = *50*-ISOMAP. A_1, A_2 and A_3 are the first three eigen-values of D_G. MES: SAFE (green), MARFE<5cm (blue), MARFE>5 cm (red).

red samples the MARFE> 5cm state. The 3D-ISOMAP on the right side presents the lowest overlapping of samples belonging to different MESs, while the overlapping is more evident for the $12+(M-1)$-ISOMAP. An excessive creation of forced edges could create shortcut errors due to connections between samples far both in terms of manifold structure and Euclidean distance, resulting in an excessive map overlapping. Thus, option 1 has been adopted to construct the connected graph, since it results to be one that best preserves the intrinsic structure of the data and allows to save computational efforts. Indeed, it is important to underline that for the ISOMAP training the most time-consuming task is to create the adjacency matrix representing the graph G (step 1, section 3.2.2.1), which is a sparse matrix storing the weight of the graph edges.

3.4.1.2 Shortest path calculation

To find the shortest path between graph nodes (step 2, section 3.2.2.1), two different approaches can be used, the Dijkstra's and Floyd-Marshall's algorithms. Dijkstra's algorithm solves a single-source shortest path problem, aiming to find the shortest path from a single source node to all destination nodes. It makes locally optimal choices at each step leading to a globally optimal solution on termination. Floyd-Marshall's algorithms solves the All-Pairs Shortest Paths problem, meaning it computes the shortest paths between all pairs of nodes in the graph. Dijkstra's algorithm computes the shortest path from a given source node to all the others

in time $O(N^2)$, where N is the number of the nodes, with $O(N)$ extra memory. To compute D_G, it has to be repeated N times, thus $O(N^2 \cdot N) = O(N^3)$ time is needed. On the other hand, Floyd-Marshall' algorithm computes the shortest path between every pair of nodes in time $O(N^3)$ with $O(N^2)$ extra memory. In principle the Dijkstra's algorithms is recommended to compute all the shortest paths from a given source node and the Floyd-Marshall is recommended when the shortest paths have to be computed for all the source nodes. In practice, Floyd-Marshall is useful for small graphs ($10^2 < N < 10^3$ nodes), that is not our case ($N > 10^4$), as it uses a lot of memory to compute D_G with a single iteration. Instead, the Dijkstra's algorithm is recommended to compute the D_G for a sparse matrix of weighted edge between nodes, which is precisely our output after the neighbor definition. In addition, it is suitable for a parallel computing application. The Dijkstra algorithms computes, for each node the minimum path tree $dG(i,1), dG(i,2), ..., dG(i,N)$ from the i^{th} source node to all $N-1$ destination nodes and it works through the following steps:

1. Set the path tree distances to infinity except for the source node itself to 0, $\{0, INF, ..., INF\}$; and set all nodes as non-visited node.
2. Assume as current node C the non-visited node with the smallest current distance; at the 1st iteration C is the source node, since $dG(i,1) = 0$.
3. Compute the distance of each j^{th} neighbor of C from the source node i, excluding those already marked as visited, by adding to the $d(i,C)$ distance value the weight of the edge between i and C ($dG(i,j) = d(i,C) + w_{C,j}$). Store the distance $dG(i,j)$ in path tree only when it is smaller than a previously stored one.
4. Mark C as visited
5. Repeat step 2, 3 and 4 until all nodes are marked as visited.

This procedure must be repeated N times, assuming each node as the source node and the remaining ones the destination ones.

3.4.1.3 Multi-Dimensional Scaling

Two different methods can be used in the *DR toolbox* to compute the MDS. The classic single value decomposition is suggested for manifold with $n < 1000$ samples, while for $n > 10\,000$ the Schur decomposition is suggested, thus it has been adopted in this thesis. The Schur decomposition or Schur triangulation, which takes the name from Issai Schur, is a matrix decomposition. Giving A as an $n \times n$ square matrix with eigenvalues $\lambda_1, ..., \lambda_n$, the Schur triangularization theorem states that there is an unitary matrix U such that:

$$U^* A U = T \tag{3.3}$$

where T is an upper triangular matrix with diagonal entries $t_{ii} = \lambda_i$ for $i = 1, ..., n$. More specific details about the Schur theorem can be founded in [95]

3.5 Train & Test

The features presented in section 3.3, related to the dataset presented in 3.1.4.1, has been used for the ISOMAP training and test. The partitioning in train and test has been conducted mainly considering the experimental sessions at which the pulses belong to. Indeed, since the pulse sets, listed in section 3.1.4.1, represent different operational space behavior, pulses coming from the same set would be present both in the train and in the test. As usual in the ML field, for each pulse set two-thirds are used for the ISOMAP training and the third part as test set. Table 3.2 reports the final combination of train and test sets in terms of pulse range and operational behavior. Considering this division our manifold consists in 71 training pulses. As

TABLE 3.2: Final subdivision of the database in train and test sets

HDL			
42 pulses 2017-2020 34xxx-37xxx		26 pulses 2011-2016 26xxx-33xxx	
Train	Test	Train	Test
28	14	17	9
NO HDL			
6 pulses 2021-2022 39xxx-41xxx		36 pulses 2011-2016 26xxx-34xxx	
Train	Test	Train	Test
24	12	4	2

described in the section 3.3.1, all signals used to describe the manifold have been down sampled to 200 Hz (1 sample each 5 ms). Moreover, in order to reduce the training samples without losing information related to the MARFE evolution, every t_0 has been set equal to 2 s, since no MARFE occurs before that time and the majority of SAFE samples is however presents in the manifold. The pulse selection and pre-processing result in 37231 samples available for the ISOMAP training.

Figure 3.18 shows the normalized distributions of the features describing the ISOMAP input space for samples belonging both to HDL pulses (blue bars) and to NO HDL pulses (orange bars). Note that, for several features, HDL and NO HDL pulses present noticeable differences in terms of the distribution. NO HDL distribution is characterized by lower values with respect to HDL one for the following features: $Wmhd$, Ne_{edge}, f_{GRW}, $P_{rad,UPPER}$, $P_{rad,CORE}$, $P_{rad,DIV}$, and $P_{rad,MAIN}$, and P_{TOT}. Instead li, $Te_{mean,CORE}$, $Te_{mean,EX-CORE}$ and $Te_{mean,OUT}$ distributions present higher value for NO HDL pulses with respect to HDL ones. Since the features present different order of magnitude, they must be normalized, which means to report feature on a

smiliar scale. This processo improves the stability of the model giving the same numerical relevance to each feature. Thus, a normalization from 0 to 1 has been applied to each feature. Since ISOMAP is an unsupervised ML algorithm, no pulse labels are assigned to the samples during the training phase.

3.5.1 3D-ISOMAP and 2D-ISOMAP Clustering

The final step of the ISOMAP applies classical MDS to the geodesic distances matrix D_G, constructing an embedding of the data in a low-dimensional space (d) preserving the intrinsic manifold geometry. This procedure computes d eigen-values of the geodesic distance matrix. Choosing the first two or the first three eigen-values a 2D or 3D representation of the manifolds can be obtained, respectively. Note that, the ISOMAP is an unsupervised algorithm, this means that no label has been used to compute the geodesic distance matrix and the MDS. A label or a color can be assigned to each sample, depending on the phase or state at which the sample belongs to, straight on the resulting low dimensional mapping. In this thesis the adopted color code depends on the MESs, and it is the same reported in Figure 3.6, green for SAFE samples, blue for sample belonging to MARFE<5cm and red for MARFE>5 cm. In terms of MES

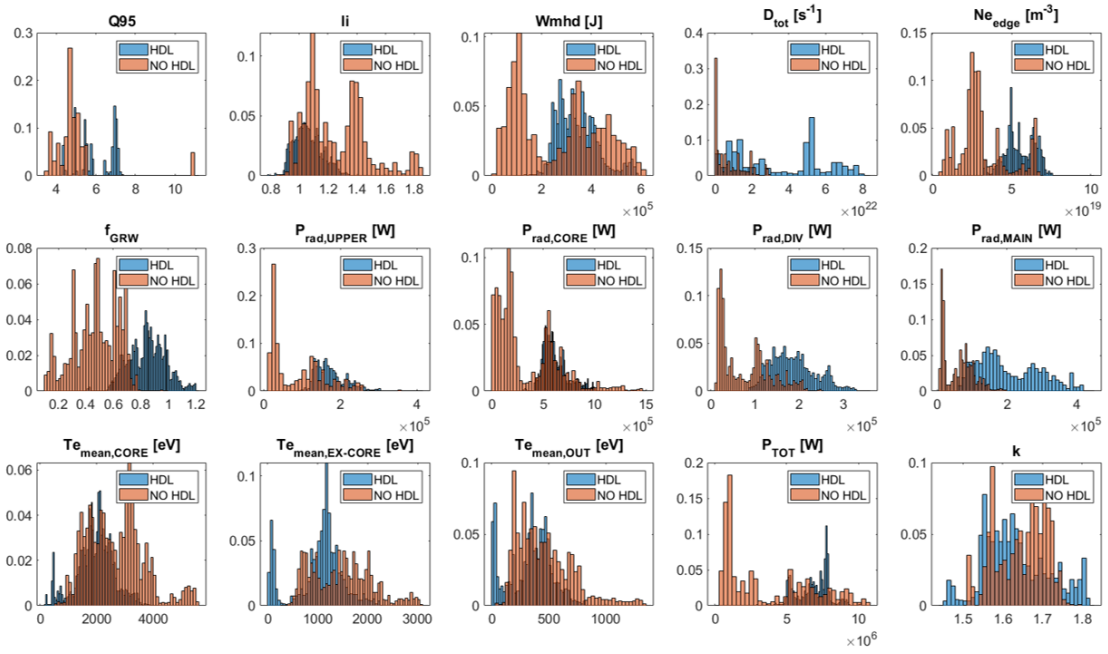

FIGURE 3.18: Feature distributions of the input space for samples belonging both to HDL pulses (blue bars) and NO HDL pulses (orange bars).

Type	**Definition**	**% of clusters**	**Number of samples**
Green	containg only SAFE samples	41.8	23529
Blue	containg only MARFE<5 cm samples	0.66	215
Red	containg only MARFE>5 cm samples	0.52	566
RGB	depending on red, blue and green samples fraction	4.21	12919
Black	do not contain any sample	52.81	0

TABLE 3.3: 2D-ISOMAP Clustering composition. Clusters type (1^{st} column), cluster definition (2_{nd} column), number of clusters (3_{rd} column, number of samples).

the manifold is divided as follows: 31632 SAFE samples, 1697 MARFE<5cm samples, 3902 MARFE>5 cm samples. The Figure 3.19a) shows the monochromatic 3D projection of the manifold, instead Figure 3.19b) reports the colored mapping. The latter allows to preliminary evaluate the goodness of the low-dimensional embedding by estimating the overlapping among the different MESs. Indeed, a qualitative evaluation of the overlapping can be done by rotating the 3D-ISOMAP view. This allow to understand if samples are truly overlapped and when it's only a matter of prospective from a specific point of view. In addition, a clustering of the latent space is shown in Figure 3.20a), where a grid on the A_1A_2-plane has been obtained by uniformly partitioning A_1 and A_2. A linear interpolating surface of the 3D embedded manifold is depicted, where the surface shading depends on the A_3 mean value in the squares. The number of squares (clusters) composing the grid depends on the number of intervals chosen to divide the A_1 and A_2 ranges, set equal to 50 for each direction, resulting in 2401 squares. Among them, 1354 are necessary to preserve the input data manifold in the 2D-ISOMAP Clustering, while 1047 are out of input data manifold. The 2D-ISOMAP Clustering is reported in Figure 3.20b) where a RGB scale has been used to color the cluster depending on the cluster composition in terms of MESs. Therefore, five cluster types can be defined as reported in Table 3.3 among with the 2D-ISOMAP Clustering composition. Note that the paucity of blue and red clusters is due to the limited number of samples representing the corresponding MES.

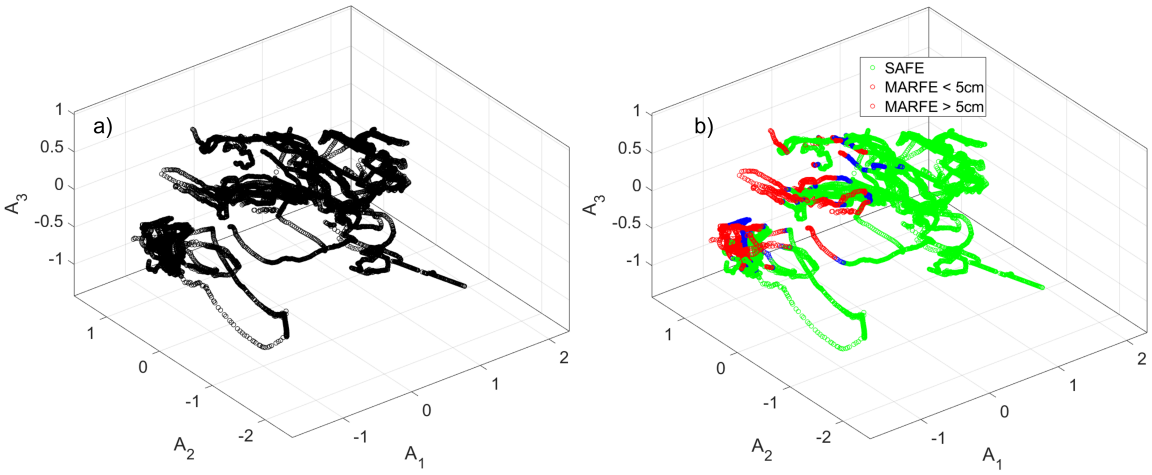

FIGURE 3.19: 3D-ISOMAP. A_1, A_2 and A_3 are the first three eigen-values of D_G. a) monochromatic 3D embedding, b) 3D embedding colored using the MESs color code: SAFE samples in green, MARFE<5cm samples in blue, MARFE>5 cm samples in red.

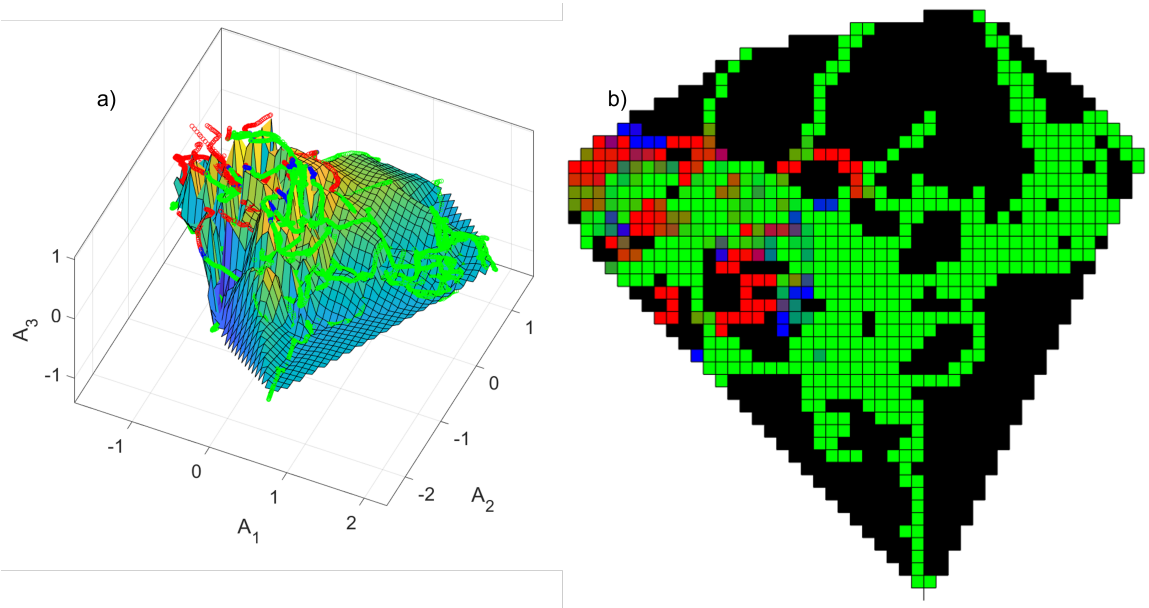

FIGURE 3.20: 2D-ISOMAP Clustering. A_1, A_2 and A_3 are the first three eigen-values of D_G. a) linear interpolating surface of the 3D embedded manifold obtained by partitioning the A_1A_2-plane in 20401 squares. The surface shading is computed by averaging A_3. b) 2D-ISOMAP Clustering on A_1A_2-plane, the cluster colors depends on the cluster composition in terms of MESs.

3.5.2 Test projection

As described in section 3.2.2.1 the main application of the ISOMAP is not only to visualize the HDL manifold by a 2D-ISOMAP Clustering or 3D-ISOMAP, but also to exploit it for tracking the evolution of the HDL pulses towards the disruption through the MESs. In the framework of the disruption avoidance, this application allows to develop a procedure for triggering an alarm able to activate a MARFE stabilization procedure. This aim can be pursued by evaluating the geodesic distance of each new operating point from the different MESs represented in the input space. Note that, this approach allows us to preserve the original manifold information, since the geodesic distance is evaluated on the high-dimensional input space. Thus, in this thesis a tool to compute the geodesic distance for test pulses has been developed. When a test pulse is projected into the ISOMAP, the geodesic distance (*Geo*) from each MES is evaluated for each operating point (sample or time instant), as described in the following taking as reference the SAFE state. Let be the i^{th} operating point represented by the orange circle in the Figure 3.21:

- **Point Projection**: the i^{th} operating is added to original high-dimensional manifold by normalizing its features with respect to the maximum and minimum values used to normalize the input space for the ISOMAP training.

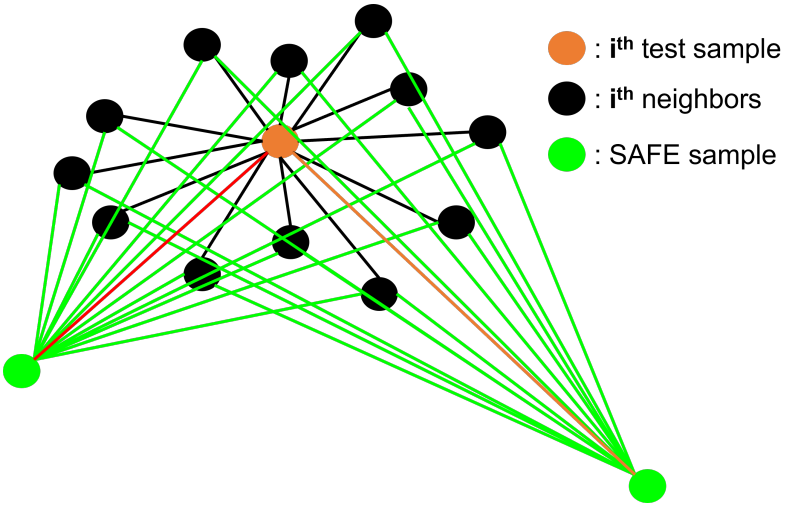

FIGURE 3.21: Operating point projection into the ISOMAP. i^{th} operating point (orange circle), k-neighbors of i^{th} (black circles), SAFE samples (green circles), Euclidean distance of the i^{th} operating point from neighbors (black lines), geodesic distance of the i^{th} operating point neighbors from SAFE samples (green lines), averaged geodesic distances of the i^{th} operating neighbors from the SAFE samples (red and orange lines). The red line is assumed as the geodesic distance of the i^{th} operating point from the SAFE state.

- **Neighborhood definition**: the i^{th} operating point neighbors are the k nearest samples (black circle in Figure 3.21), evaluated in the input space in terms of Euclidean distances (black lines in Figure 3.21)

- **Geodesic distance evaluation**: for each j^{th} map samples belonging to the SAFE state the geodesic distance average $Geo_{mean,j}$ from the k neighbors of the i_{th} operating point is evaluated. Let be S the safe samples in the input space, $Geo_{mean}(i) = Geo_{mean,1}, Geo_{mean,2}, ..., Geo_{mean,S}$. In Figure 3.21, the green lines represent the neighbor's geodesic distances from SAFE samples, while the orange and red lines are the averaged distance of the SAFE samples from the k neighbors. Thus, let be S the number of the SAFE samples in the inpute space $Geo_{mean,j} = \text{mean}(Geo_{j,1}, ...Geo_{j,k})$ with $j \in 1, ..., S$ is the mean value of the green line lengths. The minimum of the averaged geodesic distances $Geo_{mean} = Geo_{mean,1}, Geo_{mean,2}, ..., Geo_{mean,S}$ is assumed as the i^{th} geodesic distance $Geo_{SAFE}(i)$(3.4) of the i_{th} operating from the SAFE state (red line in Figure 3.21)

$$Geo_{SAFE} = \min(Geo_{mean}) = \min(G_{mean,1}, G_{mean,2}, ..., G_{mean,S}) \tag{3.4}$$

The procedure above, repeated for each operating point belonging of the test pulse from the SAFE state. A low value of the fuctions suggest the membership of the operating point to the considered state, on the contrary, an high function value suggests its foreigness. Applying the same procedure with respect to the M samples belonging to the MARFE<5cm state and the M' samples belonging to the MARFE>5 cm state, three different time series are computed:

1. $Geo_{SAFE}(t)$: geodesic distance of the projected samples from the SAFE state
2. $Geo_{MARFE}(t)$: geodesic distance of the projected sample from the MARFE state
3. $Geo_{MARFE@5}(t)$: geodesic distance of the projected sample from the MARFE above 5 cm state

Note that, when a pulse sample will be projected on red clusters indicating a $MARFE > 5$ cm state, $Geo_{MARFE}(t)$ and $Geo_{MARFE}(t)$ will be mathematically equal since their definition.
As for SOM and GTM, the trajectory of a test pulse never used in the training can be depicted on both 3D-ISOMAP and 2D-ISOMAP Clustering. To visualize the evolution in time of a new

pulse on the trained map the nearest neighbor of each operating sample is highlighted. Figure 3.23 shows the projection of the AUG pulse #33681 into the 2D-ISOMAP Clustering. The colored circles are the nearest neighbor of each test sample and the color shade, from cyan to magenta, is linked to the growing of $Geo_{SAFE}(t)$ value. Thus, the cyan samples in Figure 3.23a) are characterized by low $Geo_{SAFE}(t)$ values, indicating the similarity to the SAFE phase, indeed they falls in green clusters. The magenta samples are characterized by high $Geo_{SAFE}(t)$ values, suggesting the MARFE formation, indeed they mainly belong to red clusters. Instead, in Figure 3.23b) the $Geo_{MARFE}(t)$ amplitude has been used to color the samples, the color shade, from cyan to magenta, is linked to the growing of $Geo_{MARFE}(t)$ amplitude. The color shade results to be reversed with respect to Figure 3.23a), the cyan samples, characterized by low $Geo_{MARFE}(t)$, suggest the presence of a MARFE, instead the magenta samples, characterized by high $Geo_{MARFE}(t)$ values, suggest a safe condition. In agreement, the cyan samples fall in the red clusters whereas the magenta samples in the green ones. The behavior of the pulse trajectories depicted on the 2D-ISOMAP Clustering seems to well refer the information on the MESs. Figure 3.23 shows the potentiality of the 2D-ISOMAP Clustering in tracking the trajectory of a pulse thorught the MARFE states. Thus, it would be employed for disruption avoidance purposes by MARFE stabilization procedure.

Another meaningful representation of the pulse behavior is gotten by plotting $Geo_{SAFE}(t)$, $Geo_{MARFE}(t)$ and $Geo_{MARFE@5}(t)$ time traces. Figure 3.22 shows the evolution in time of the geodesic distance functions from each MES for each sample of the test pulse #33681. $Geo_{SAFE}(t)$ in green, $Geo_{MARFE}(t)$ in blue line and $Geo_{MARFE@5}(t)$ in red. The dashed vertical lines indicate the manual detected METs: MARFE formation time (t_{MF}, orange line), the time at which the distance between the MARFE and the X_{point} becomes equal to 5 cm (t_{MH}, magenta line), the time at which the vertical distance between the MARFE and X_{point} comes back to be lower than 5 cm (t_{ML}, blue line), MARFE stabilization time (t_{MS} green line). The behavior of $Geo_{SAFE}(t)$, $Geo_{MARFE}(t)$ and $Geo_{MARFE@5}(t)$ confirms the manually detected MARFE evolution. Indeed, the geodesic distance from the SAFE state is very low until the t_{MF}. The absence of MARFE is confirmed also by the high values of geodesic distances from the states presenting MARFE, $Geo_{MARFE}(t)$ and $Geo_{MARFE@5}(t)$, which start to decrease just few hundred milliseconds before the MARFE formation. When the MARFE is formed, at around 2.5 s, a trend inversion of the three geodesic distance functions is observed, $Geo_{SAFE}(t)$

becomes larger than both $Geo_{MARFE}(t)$ and $Geo_{MARFE@5}(t)$. When the MARFE is stabilized (around 3.5 s), by an avoidance procedure, a second inversions of the three geodesic distance functions trend is observed, and $Geo_{SAFE}(t)$ come back to being lower than $Geo_{MARFE}(t)$ and $Geo_{MARFE@5}(t)$. In addition, looking between t_{MF} (dashed orange line) and t_{MH} (magenta line), $Geo_{MARFE}(t)$ is lower than $Geo_{MARFE@5}(t)$, meaning that the distance between the MARFE and X_{point} is increasing. Thus, in this time window the automatically detected MES is MARFE<5cm, but evolving toward MARFE>5cm since $Geo_{MARFE@5}$(t) is decreasing. In the time window between t_{MH} and t_{ML} (magenta and blue lines , respectively), $Geo_{MARFE}(t)$ and $Geo_{MARFE@5}$(t) are completely overlapped. This recursive behavior has been assumed as condition for automatically distinguishing between MARFE<5cm and MARFE<5cm states. Finally, between the t_{ML} (dashed blue line) and the t_{MS} (dashed green line) $Geo_{MARFE}(t)$ becomes again lower than $Geo_{MARFE@5}(t)$, meaning that the distance between the MARFE and X_{point} is decreasing, thus the MES goes back to MARFE<5cm, latter evolving in a stable state. Thus, the behavior of the three geodesic distance functions well refer the information on the MESs. This suggest us to compare the dissimilarity functions, $Geo_{SAFE}(t)$, $Geo_{MARFE}(t)$ and $Geo_{MARFE}(t)$, to define a criterion for developing an automatic detector of the MESs, to be employed as a trigger for applying MARFE stabilization procedures in HDL pulses. In the next section the optimized criterion to automatically detect the MESs, and the corresponding METs, is described.

3.5.3 Alarm Criteria

Projecting on the ISOMAP the training pulses, a recurring behavior of the three geodesic distance functions has been observed, such as the one observable in Figure 3.22. When no MARFE is developed, Geo_{SAFE} is much lower than Geo_{MARFE} and $Geo_{MARFE@5}$. When the MARFE distance from X_{point} is lower than 5 cm, Geo_{MARFE} is greater than $Geo_{MARFE@5}$, and both are lower than Geo_{SAFE}. While, when the MARFE distance from X_{point} is larger than 5 cm, Geo_{MARFE} overlaps $Geo_{MARFE@5}$, and both are much lower than Geo_{SAFE}. Therefore, different thresholds on $Geo_{SAFE}(t)$, $Geo_{MARFE}(t)$ and $Geo_{MARFE@5}(t)$ amplitudes have been optimized to provide automatic alarms of the METs, by establishing for each operating point the MES membership among SAFE, MARFE < 5 and MARFE>5. An algorithm for the real-time detection of the current MES and providing an alarm when a state change occurs has been

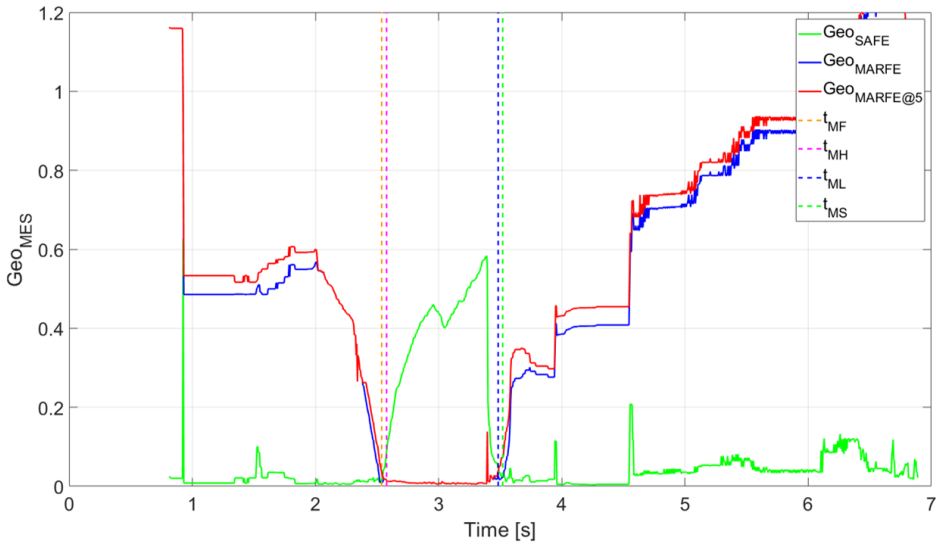

FIGURE 3.22: Geodesic distance function for AUG pulse #33681. Geo_{SAFE} green time trace, Geo_{MARFE} blue time trace, $Geo_{MARFE@5}$ red time trace. Manual times (dashed vertical lines): t_{MF} in orange, t_{MH} in magenta, t_{ML} in blue, t_{MS} in green. When no MARFE is developed, before t_{MF} and after t_{MS}, Geo_{SAFE} is much lower than Geo_{MARFE} and $Geo_{MARFE@5}$. When the MARFE distance from X_{point} is lower than 5 cm, between t_{MF} and t_{MH} and between t_{ML} and t_{MS}, Geo_{MARFE} is greater than $Geo_{MARFE@5}$, and both are lower than Geo_{SAFE}. When the MARFE distance from X_{point} is larger than 5 cm, between t_{MH} and t_{ML}, Geo_{MARFE} overlaps $Geo_{MARFE@5}$, and both are much lower than Geo_{SAFE}.

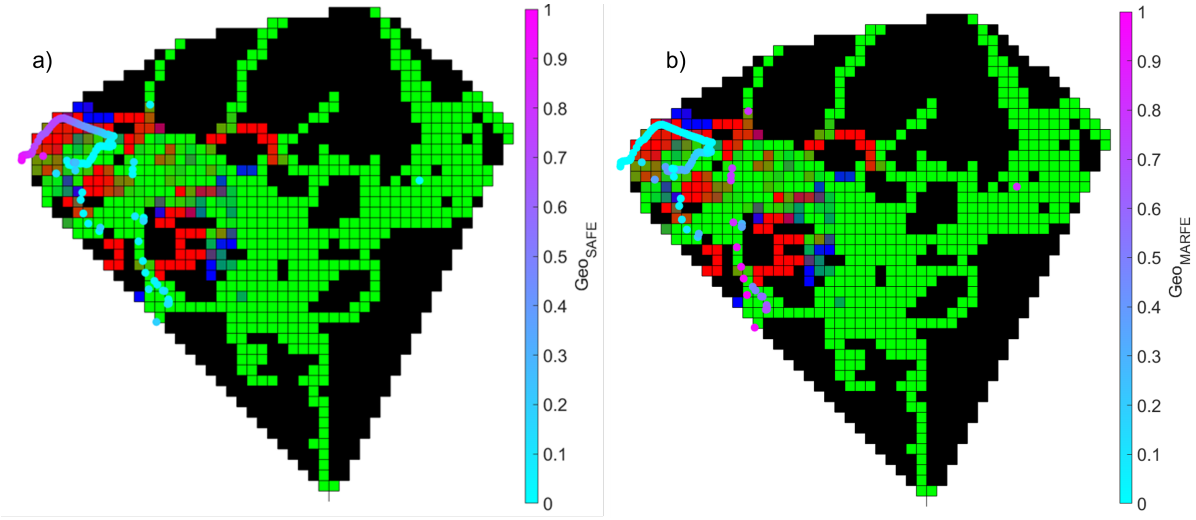

FIGURE 3.23: AUG pulses #33681 projected in the 2D-ISOMAP Clustering. a) color shade, from cyan to magenta, is linked to $Geo_{SAFE}(t)$ growing values, cyan samples falling in green clusters suggest a SAFE state, magenta samples falling in red clusters suggest a MARFE>5cm state. b) color shade, from cyan to magenta, is linked to $Geo_{MARFE@5}(t)$ growing values. The magenta samples falling in the green clusters suggest a SAFE state, while the cyan samples falling in the red clusters suggest the presence of the MARFE.

developed. Two toggles, have been defined to describe the MES in a programming environment, as in the following:

- **MARFE**
  - **0**: a MARFE is not present ($Geo_{SAFE}(t_i) < Geo_{MARFE}(t_i)$)
  - **1**: a MARFE is present

- **MARFE@5cm**
  - **0**: the MARFE is below the 5 cm
  - **1**: the MARFE is abow the 5 cm

Both toggles are set to 0 for $t = 0$ when $Geo_{SAFE}(t_i) < (Geo_{MARFE}(t_i),\ Geo_{MARFE@5}(t_i))$ assuming a SAFE state. The Table 3.4 reports the MES definitions for $t > 0$ depending on the status of the toggles. The combination of the two toggles in column one defines the MES reported in column two.

TABLE 3.4: MES definition (column 2) depending on the toggle combination (column 1).

Toggles	MES
MARFE = 0 and MARFE@5cm = 0	SAFE
MARFE = 1 and MARFE@5cm = 0	MARFE<5cm
MARFE = 1 and MARFE@5cm = 1	MARFE>5cm

As described above, four thresholds have been optimized to trigger the automatic alarms:

- $\Delta SAFE_{thr}$ is the minimum difference between $Geo_{MARFEE}(t_i)$ and $Geo_{SAFE}(t_i)$ required to define a SAFE state. If $Geo_{MARFE}(t_i) - Geo_{SAFE}(t_i)$ becomes lower than $\Delta SAFE_{thr}$ the $t_{MF,auto}$ alarm is triggered.

TABLE 3.5: Alarm criteria for the MES automatic alarm triggers. 1^{st} column, prerequisite to trigger the alarm. 2^{nd}column, conditions of geodesic distances that trigger the alarm. 3^{rd} column, triggered alarm. 4^{th} column, switching of the toggles following the automatic detection.

Pre-requisite	Trigger Condition	Alarm	Toggle $t > t_i$
MARFE = 0 **and** MARFE@5cm = 0	$Geo_{MARFE}(t_i) - Geo_{SAFE}(t_i) < \Delta SAFE_{thr}$	$t_i = t_{MF,auto}$	MARFE = 1 **and** MARFE@5cm = 0
MARFE = 1 **and** MARFE@5cm = 0	$Geo_{MARFE@5}(t_i) - Geo_{MARFE}(t_i) < \Delta 5cm_{thr}$	$t_i = t_{MH,auto}$	MARFE = 1 **and** MARFE@5cm = 1
MARFE = 1 **and** MARFE@5cm = 1 **and** $t_i > t_{MH,auto} + 50ms$	$Geo_{MARFE}(t_i - 25ms \div t_{i-1}) = Geo_{MARFE@5}(t_i - 25ms \div t_{i-1})$ **and** $Geo_{MARFE}(t_i) < Geo_{MARFE@5}(t_i)$	$t_i = t_{ML,auto}$	MARFE = 1 **and** MARFE@5cm = 0
MARFE = 1 **and** MARFE@5cm = 0	$Geo_{SAFE}(t_i) < Geo_{MARFE}(t_i)$ **and** $Geo_{SAFE} < SAFE_{thr}$ **and** $Geo_{MARFE} > MARFE_{thr}$	$t_i = t_{MS,auto}$	MARFE = 0 **and** MARFE@5cm = 0

- $\Delta 5cm_{thr}$ is the minimum difference between $Geo_{MARFE@5}(t_i)$ and $Geo_{MARFE}(t_i)$ required to define a MARFE>5 MES. If $Geo_{MARFE@5}(t_i) - Geo_{MARFE}(t_i)$ becomes lower than $\Delta 5cm_{thr}$ the $t_{MH,auto}$ alarm is triggered.

- $SAFE_{thr}$ is the maximum value of $Geo_{SAFE}(t_i)$ required to define a returning to a SAFE state after a MARFE formation. If $Geo_{SAFE}(t_i)$ is lower than $SAFE_{thr}$, the $t_{MS,auto}$ alarm is triggered, meaning that the operative condition at t_i is geodesically close enough to the SAFE state.

- $MARFE_{thr}$ is the minimum value of $Geo_{MARFE}(t_i)$ required to define a returning to a SAFE state after a MARFE formation. If $Geo_{MARFE}(t_i)$ is greater than $MARFE_{thr}$ the $t_{MS,auto}$ alarm is triggered, meaning that the operative condition at t_i is geodesically far enough the MARFE<5cm state.

Table 3.5 shows the Toggles prerequisite and the conditions on $Geo_{SAFE}(t)$, $Geo_{MARFE}(t)$ and $Geo_{MARFE@5}(t)$ amplititued, column 1 and 2 respectively, to be verified at $t = t_i$ to detect each MET. $t_{MF,auto}$, $t_{MH,auto}$, $t_{ML,auto}$ and $t_{MS,auto}$ automatic alarms are triggered when passing from SAFE to MARFE<5cm, from MARFE<cm5 to MARFE>5cm, from MARFE>5cm to MARFE<5cm and from MARFE< 5cm to SAFE states respectively. This would allows the operator to undertake suitable avoidance actions. When the automatic detection of the METs is conducted the following scenarios may arise:

- Detected: a manual identified MET is automatically detected. A Detected MET is characterized by $\Delta t = t_{man} - t_{auto}$; a positive Δt indicates an earlier automatic detection, while a negative Δt means a later automatic detection.
- Undetectable: undetectable MET for lack of data because $t_f < t_{MF}$ or $t_f < t_{MH}$ (see section 3.3.1).
- Missed Detection (MD): undetected MET due to criteria failure.
- False Detection (FD): a MET is detected by ISOMAP but not identified during the manual analysis.

The four thresholds have been optimized by means an heuristic procedure, minimizing the anticipation time on both t_{MF} and t_{MH}(up to 100 ms), the number of later automatic alarms on t_{MF} and t_{MH}, FDs and MDs of each MET, on the training pulses. Since t_{ML} and t_{MS} represent a returning to a safe condition, later automatic alarms of these METs can be accepted. On the contrary, more attention must be dedicated to the t_{MF} and t_{MH} detection, since they should trigger an active control to suppress the MARFE a large anticipation time can be unreliable and unsuitable, and no late detections are wished. Note that to correctly detect both t_{MF} and t_{MH} is not an easy task even during the manual investigation.

3.5.4 Training Performance

Table 3.6 summarizes the ISOMAP performance as MET automatic detector on the train pulses. The table reports the number of detected, undetectable, MD and FD for each MET defined in section 3.1.4. Note that the training set does not present any FDs and MDs. The train performance, in terms of difference between the manual and the automatically detected METs are shown in Figure 3.24, where the bar lengths are the fractions of detectable events for different time windows. From Figure 3.24, upper plot, it can be seen that maximum anticipation times are: $\Delta t_{MF} = t_{MF,man} - t_{MF,auto} < 0.8$ s, and $\Delta t_{MF} = t_{MH,man} - t_{MH,auto} < 0.7$ s. Moreover, it can be observed that 70% of both t_{MF} and t_{MH} are automatically detected within 200 ms from the manual time. Instead, less than 5% of the t_{MF}, auto and 20% of the t_{MH},auto are late detected. From the Figure 3.24, bottom plot, it can be observed that $|t_{ML,man} - t_{ML,auto}| < 0.01$

s and $|t_{MS,man} - t_{MS,auto}| < 0.03$, as pointed out in section 3.5.3 later automatic alarms on t_{ML} and t_{MS} can be accepted.

TABLE 3.6: Training performance for MET automatic detection, in terms of Detected, Undetectable, MDs and FDs for HDL pulses and FD performance not HDL pulses.

Total	Detected	Undetectables	MDs	FDs
t_{MF}				
49	48	1	0	0
t_{MH}				
49	44	5	0	0
t_{ML}				
9	9	0	0	0
t_{MS}				
9	9	0	0	0
NO HDL				
Pulses			FDs	
28			0	

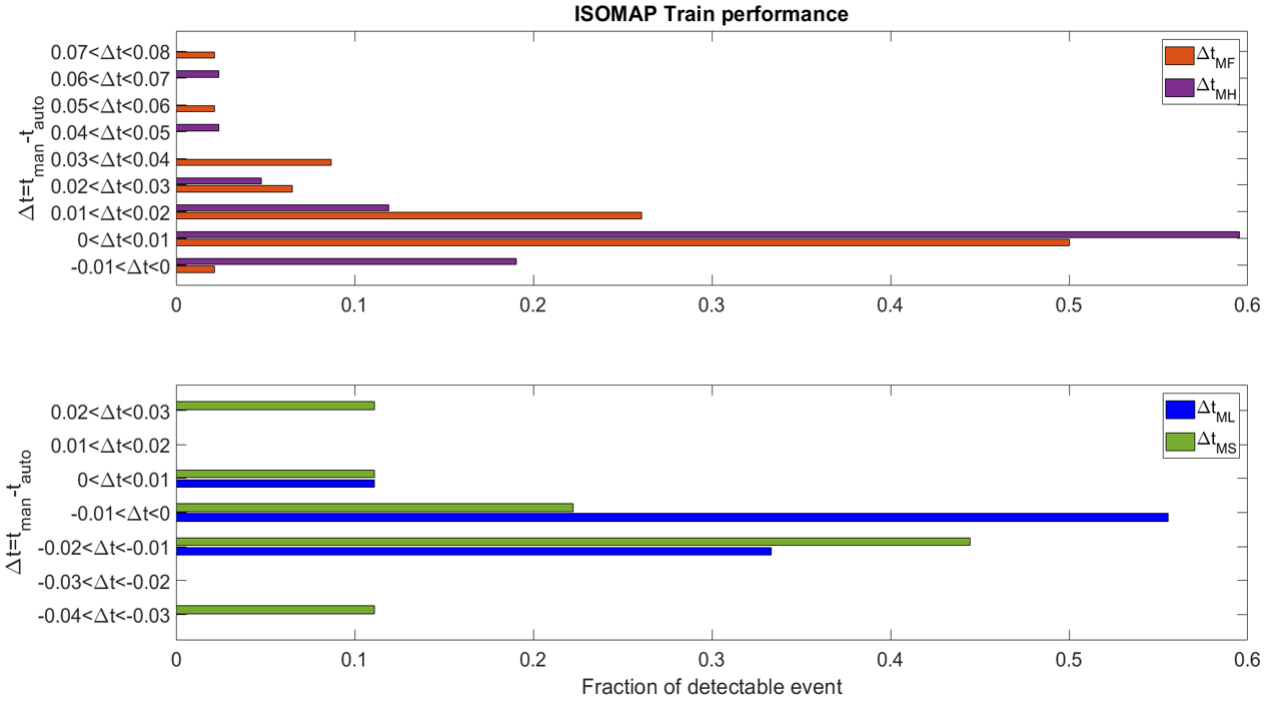

FIGURE 3.24: Training performance in terms of fraction of detectable event for different time window. Upper-plot: $\Delta t_{MF} = t_{MF,man} - t_{MF,auto}$ (orange bars) and $\Delta t_{MH} = t_{MH,man} - t_{MH,auto}$ (purple bars). Bottom-plot: $\Delta t_{ML} = t_{ML,man} - t_{ML,auto}$ (blue bars) and $\Delta t_{MS} = t_{M,man} - t_{MS,auto}$ (green bars).

3.5.5 Testing performance

Table 3.7 summarizes the ISOMAP performance as MET automatic detector on the test pulses. Table 3.7 reports the number of detected, undetectable, MD and FD for each MET. Note that, except for the t_{MH}, each MES presents 5 FDs. These pulses present a behavior of the geodesic distances that describes a complete MARFE evolution, including all the MESs. Moreover, the 3 FDs from NO HDL pulses, 2021-2022 experiments (#39xxx-#41xxx), have high-modes number. In these pulses, the FD could be caused by the presence of high-modes numbers, which usually are activated by MARFEs. Instead, t_{MS} presents 2 MDs, this happens in those pulses where the manual investigation detects two MARFEs in the same pulse, where a first MARFE stabilization is followed by a second MARFE formation. In these two cases the optimized criterion for automatic detection does not reveal the first stabilization, since Geo_{SAFE} does not become lower of Geo_{MARFE}, thus, no prerequisite condition is verified for detecting a new formation. This means that, the ISOMAP see the evolution of one MARFE lasting for a time window covering the two MARFEs. Thus, the missed detection of t_{MS} MDs bring the missed detections of t_{MF}. The test performance, in terms of the difference between the manual and the automatically detected METs is summarized in Figure 3.25, where the bar length represent the fractions of detectable events for different time windows. From Figure 3.25, upper-plot, it can be seen that 60% of t_{MF} and t_{MH} are earlier detected, and 45% of Δt_{MF} and Δt_{MH} are lower than 120 ms, while for two events $t_{MF,auto}$ is detected more than 0.5 s in advance. Moreover, it can be observed that, for late detection, the $\Delta t_{MF,max} < 0.09$ s and the $\Delta t_{MH,max} < 0.06$ s. Figure 3.25, bottom-plot, shows both t_{ML} and t_{MS}, it can be seen that earlier detections present a maximum in the range $0.06 \div 0.08$ s while, a maximum in the range $0.8 \div 1$ is recorded for later detection since. Such a large value of late detection is due to the fact that thresholds for the automatic detection of t_{ML} and t_{MS} have not been optimized to provides anticipated detection, as described in the section 3.5.3. In addition, just 9 cases, both for t_{ML} and t_{MS}, are present among the train examples, this does not allow a suitable threshold optimization for discriminating the transition between the MARFE>5 cm and MARFE<5 cm and between the MARFE<5 cm and SAFE.

TABLE 3.7: Testing performance in terms of Detected, Undetectable, MDs and FDs for HDL pulses and FDs performance for not HDL pulses.

Total	Detected	Undetectables	MDs	FDs
t_{MF}				
28	23	2	3	5
t_{MH}				
28	24	3	1	6
t_{ML}				
11	11	0	0	5
t_{MS}				
10	8	0	2	5
NO HDL				
Pulses			FDs	
14			3	

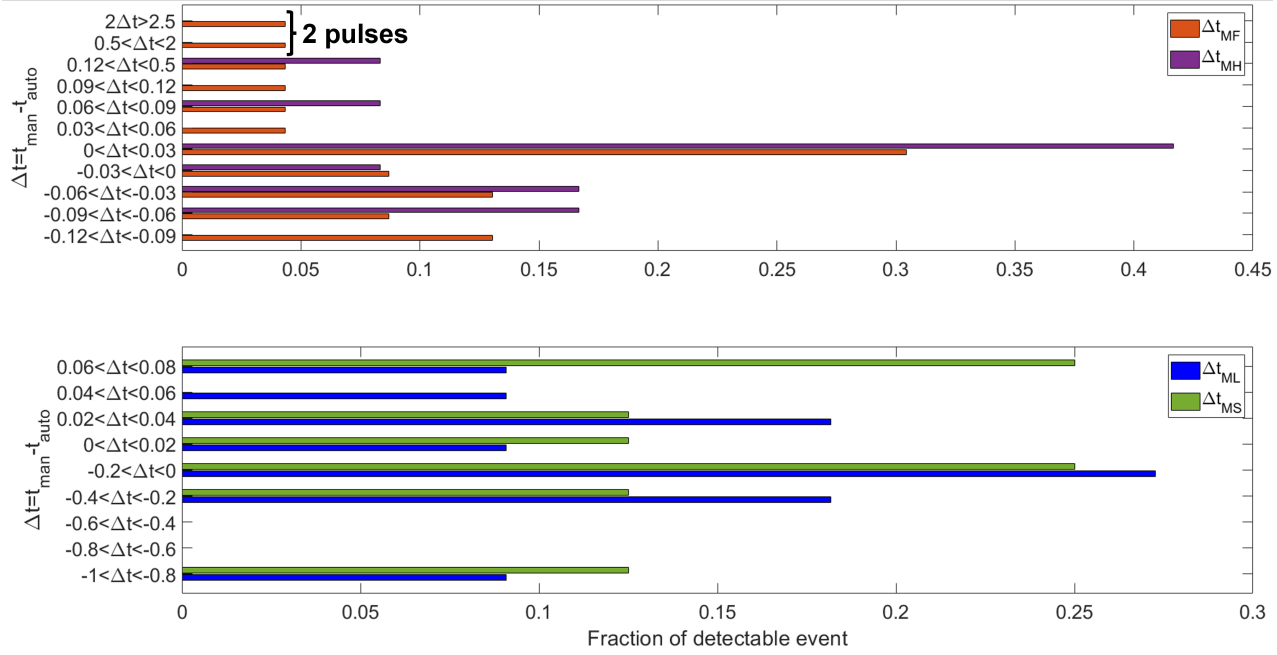

FIGURE 3.25: Testing performance for METs automatic detection in terms of fraction of detectable event for different time windows. Upper-plot: Δt_{MF} (orange bars) and Δt_{MH} (purple bars). Bottom-plot: Δt_{ML} (blue bars) and Δt_{MS} (green bars).

3.5.6 Results discussion

Summarizing the results presented in 3.5.4 and 3.5.5, the training set consists in 116 events among with 6 are not detectable and the remaining are all well detected. Whereas, the test set is made of 77 events, among these 66 are detected, 5 are undetectables and 6 are undetected. In the following, several test examples are presented to discuss strengths and weakness of the ISOMAP detector and to show the different scenarios presented in test set. In particular, the following test cases are discussed:

Correct detections

- Accurate METs detection AUG#33681.
- Detected MARFE formation with large anticipation time (AUG#37538 and AUG#29810).
- No FD for NO HDL pulse (AUG#33294).
- Avoided FD for HDL pulse (AUG#28140).

Incorrect detections

- MD for MARFE formation for AUG#28331
- Undetectable MARFE formation for AUG#28729
- FD for HDL pulse (AUG#37458)
- FD for NO HDL (AUG#41098)

3.5.6.1 Accurate METs detection

For the AUG test pulse #33681, the behavior of the geodesic distances properly describes the MARFE evolution states, allowing a good detection of the METs, as already described in section 3.5.2. Figure 3.26 shows that every MET has been well detected by the proposed algorithm, with earlier detection of t_{MF} and t_{MH} within 22 ms and later detection of t_{ML} and t_{MS} within 15 ms. The subplot a) shows the geodesic distances: Geo_{SAFE} (green time trace), Geo_{MARFE} blue time trace and $Geo_{MARFE@5}$ (red time trace). The METs are highlighted by

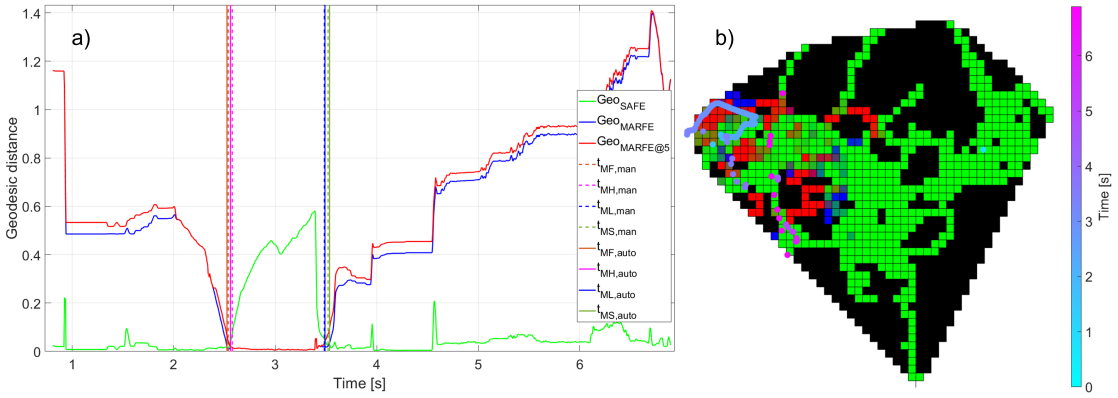

FIGURE 3.26: AUG test pulse #33681. Subplot a), geodesic distance functions time traces: Geo_{SAFE} in green, Geo_{MARFE} in blue, $Geo_{MARFE@5}$ in red. Manual times (dashed vertical lines): $t_{MF,man}$ in orange, $t_{MH,man}$ in magenta, $t_{ML,man}$ in blue, $t_{MS,man}$ in green. Automatic times (continuous vertical lines): $t_{MF,auto}$ in orange, $t_{MH,auto}$ in magenta, $t_{ML,auto}$ in blue, $t_{MS,auto}$ in green. Subplot b), pulse projection into the 2D-ISOMAP Clustering, the color shade of the samples, from cyan to magenta, is linked to the growing of the time, for $t_i = t_0$ the sample is cyan and for $t_i = t_{cut}$ the sample is magenta. It can be observed that the projection starts on green clusters in the upper left region and proceeds to red cluster also in the upper left region. Following, after the MARFE stabilization, from $t_i = t_{MF} \approx 3.5$ s to $t_i = t_{cut}$, the samples falls in green cluster (from indigo to magenta samples) in agreement with the pulse behavior that ends in SAFE state.

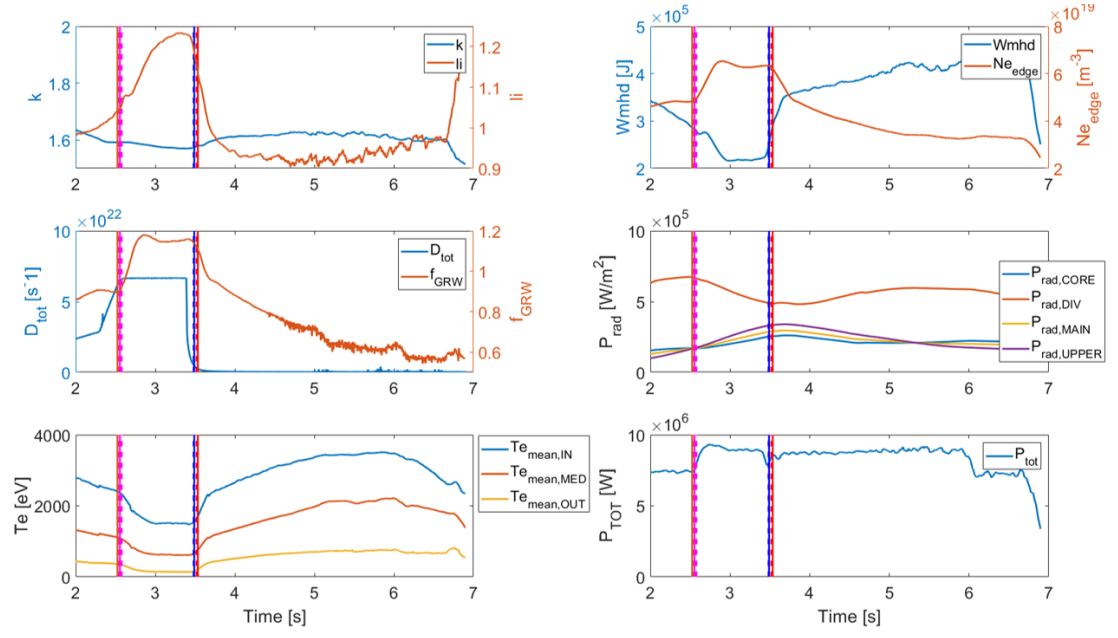

FIGURE 3.27: AUG test pulse #33681 features. 1^{st} column from top to bottom: elongation (k) and internal inductance (li), sum of D2 gas-fluxes (D_{tot}) and Greenwald fraction (f_{GRW}), electron temperature features ($Te_{mean,CORE}$, $Te_{mean,EX-CORE}$, $Te_{mean,EDGE}$). 2^{nd} column from top to bottom: plasma energy ($Wmhd$) and electron density at the plasma edge (Ne_{edge}), radiated power features ($P_{rad,CORE}$, $P_{rad,DIV}$,$P_{rad,MAIN}$, $P_{rad,UPPER}$), total applied power (P_{TOT}). During the MARFE evolution, between t_{MF} and t_{MS}, li, Ne_{edge} and f_{GRW} are increasing, while the electron temperature features are decreasing.

vertical lines: t_{MF} in orange, t_{MH} in magenta, t_{ML} in blue, t_{MS} in green. The manual times are indicated by dashed lines, and the automatically detected times by continuous lines. The dashed and continuous line having the same color are almost overlapped, meaning accurate detections. The subplot b) reports the test AUG#33681 projection into the 2D-ISOMAP Clustering, the trajectory is in agreement with the MARFE evolution described by the geodesic distances. Indeed, it starts from green cluster (cyan samples), go through red clusters (indigo samples) and ends on green cluster (magenta sample), where the color shade, from cyan to magenta, is linked to growing of the time, from t_0 to t_{cut}. The trajectory behavior is already described in section 3.5.2. Figure 3.27 reports the behavior of the 15 features defining the high dimensional input space parameter. Note that, the MARFE occurence is well represented by the features. Indeed, between t_{MF} and t_{MF} and t_{MS}, li, Ne_{edge} and f_{GRW} (brown lines in upper-left, upper-right, and middle-left subplot respectively) are mostly increasing, while electron temperature features are decreasing (bottom-left plot). The middle-right subplot, where the radiated power features are reported, shows a behavior observed in most of the test pulses. $P_{rad,DIV}$ (orange line) is the highest radiated power features for all the HDL pulses, moreover an inversion of $P_{rad,UPPER}$ (purple line) and $P_{rad,CORE}$ (blue line), with respect to $P_{rad,MAIN}$ (yellow line) takes place during the MARFE evolution, at t_{MF}. It is clear that, the ISOMAP is able to encode the different MESs well described by the input space features.

3.5.6.2 Detected MARFE formation with large anticipation time (AUG #37538)

As previously highlighted in the section 3.5.5, two test pulses present a detection error of the MARFE formation time ($\Delta t_{MF} = t_{MF,man} - t_{MF,auto}$) greater than 0.5 s (note that $\Delta t_{MF} > 0$ indicates an early detection). These test pulses have been analyzed with an off-line IDL routine, available by IPP, for a post pulse offline MARFE tracking. This routine allows the tracking of the MARFE position by following the position of the maximum radiation region, visible by the diode bolometer divertor camera (see Figure 3.30). The procedure to evaluate the MARFE vertical position will be now shortly presented. Figure 3.30 reports both the thirteen lines of sight of the bolometer divertor cameras (left side) and their calibrated measurements (right side), for the AUG pulse #37538. From the calibrated measurements, a radiation contouring plot can be obtained (see Figure 3.31a)) reporting the evolution in time of the radiated power per square meter as function of the camera angle. Starting from top to

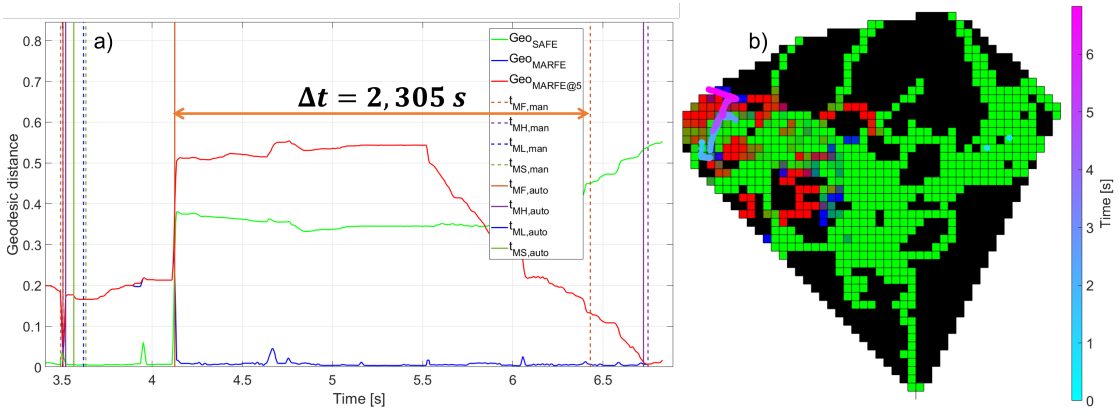

FIGURE 3.28: AUG test pulse #37538, detection of MARFE formation with $t_{MF,man} - t_{MF,auto} = 2.305$ s. Subplot a), geodesic distance functions time traces: Geo_{SAFE} in green, Geo_{MARFE} in blue, $Geo_{MARFE@5}$ in red. Manual times (dashed vertical lines): $t_{MF,man}$ in orange, $t_{MH,man}$ in magenta, $t_{ML,man}$ in blue, $t_{MS,man}$ in green. Automatic times (continuous vertical lines): $t_{MF,auto}$ in orange, $t_{MH,auto}$ in magenta, $t_{ML,auto}$ in blue, $t_{MS,auto}$ in green. After a MARFE evolution, well automatically detected and suppressed around 3.7 s, a second MARFE is observed at 6.43 s ($t_{MF,man}$). This second MARFE is automatically detected at $t_{MF,auto} = 4.13$ s. Subplot b) Pulse projection into the 2D-ISOMAP Clustering, the color shade of the samples, from cyan to magenta, is linked to the growing of the time, for $t_i = t_0$ the sample is cyan and for $t_i = t_{cut}$ the sample is magenta. The pulse projection is in agreement with the behavior observable from the geodesic distance time traces. Indeed, the first MARFE formation occurs at 3.5 s with its stabilization at 3.7 s and the projected samples corresponding to this time window (indigo samples) fall on a mixed green-red clusters region just below the red clusters region in the upper-left corner. Moreover, in the time window $4.13 \div 6.75$ the MES described by the behavior of the geodesic distances is MARFE<5cm and samples belonging to this time window (from purple to magenta samples) fall on a mixed blue-red clusters and blue cluster.

bottom, the red dashed lines represent the X_{point} position and the positions 5 cm and 10 cm above the X_{point}, along the z-axis of the machine. A Gaussian filtering and a calibration of the bolometer measurements, considering a time window between -0.1 s and 0.05 s, is performed on the bolometer data. The R and Z coordinates of X_{point} position, loaded from the equilibrium code, are projected on the contouring plot (with respect to the camera pinhole angles), to be compared with the position of the maximum radiation region. When the maximum of the radiation is above the X_{point} (below the upper red dashed line) a MARFE is inside the plasma region, indicating a MARFE formation. From the Figure 3.31a) the evolution of the first MARFE can be seen by the white arrow in Figure 3.31a)). However, from the radiation map in subplot a), it's not easy to evaluate the MARFE position and to state with a good precision when the MARFE is formed. To overcome this limit, two different approaches can be adopted to evaluate the vertical position of the MARFE (Z_{MARFE}), as reported in the following:

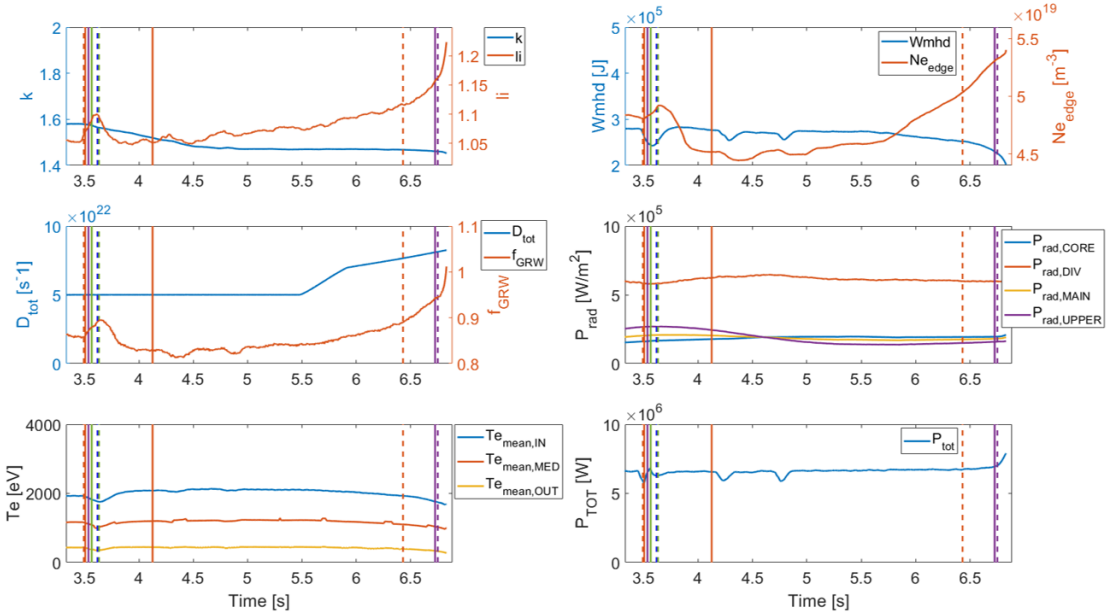

FIGURE 3.29: AUG test pulse #33681 features. 1^{st} column from top to bottom: elongation (k) and internal inductance (li), sum of D2 gas-fluxes (D_{tot}) and Greenwald fraction (f_{GRW}), electron temperature features ($Te_{mean,CORE}$, $Te_{mean,EX-CORE}$, $Te_{mean,EDGE}$). 2^{nd} column from top to bottom: plasma energy ($Wmhd$) and electron density at the plasma edge (Ne_{edge}), radiated power features ($P_{rad,CORE}$, $P_{rad,DIV}$,$P_{rad,MAIN}$, $P_{rad,UPPER}$), total applied power (P_{TOT}). During the MARFE evolution, between t_{MF} and t_{MS}, li, Ne_{edge} and f_{GRW} are increasing, while the electron temperature features are decreasing.

- Defining $Z_{MARFE,max}$ as the intersection point between the LoS having the maximum radiation and the line $Z = Z_{X_{point}}$. The position of the MARFE with respect to the X_{point} postion is obtained subtracting from $Z_{MARFE,max}$ the Z-coordinate of the X_{point} ($\Delta Z_{MARFE,max} = Z_{MARFE,max} - Z_{X_{point}}$, cyan line in Figure 3.31 right-side).

- Defining $Z_{MARFE,Gauss}$ as the intersection point of the locally calculated line of sight under which the radiation maximum is observed with a vertical line with $Z = Z_{X_{point}}$. Then, $\Delta Z_{MARFE,Gauss}$ is obtained subtracting from $Z_{MARFE,Gauss}$ the Z-coordinate of the X_{point} ($\Delta Z_{MARFE,Gauss} = Z_{MARFE,Gauss} - Z_{X_{point}}$, blue line in Figure 3.31 right-side).

In Figure 3.31b) in addition to $\Delta Z_{MARFE,max}$ (cyan line) and $\Delta Z_{MARFE,Gauss}$ (blue line), the X_{point} and $X_{point} + 5$ cm positions are reported by the black and blue dashed lines respectively. $\Delta Z_{MARFE,Gauss}$ has been considered to verify the MARFE evolution described by the behaviour of the geodesic distance functions for that cases presenting high values of anticipation time, MD and/or FD. The MES can be depicted by $\Delta Z_{MARFE,Gauss}$ considering the following criteria:

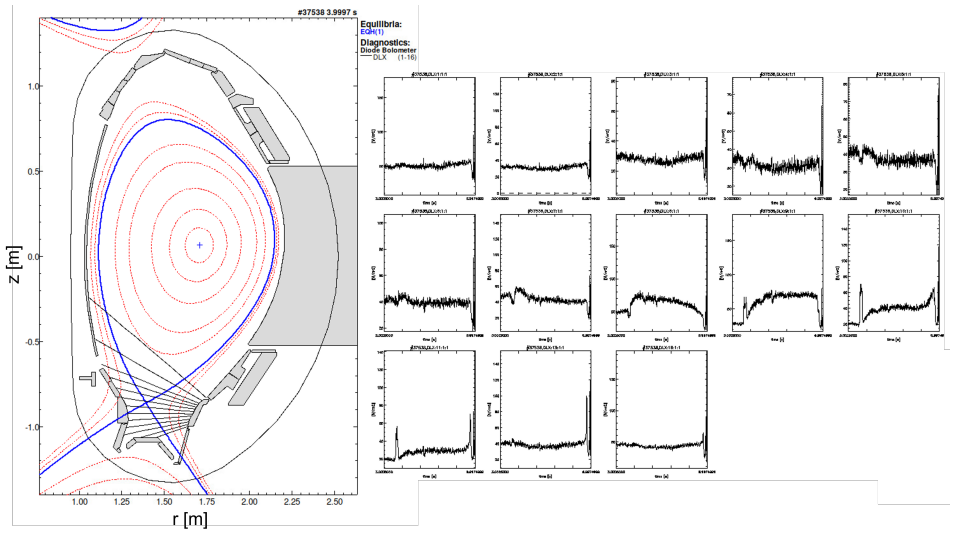

FIGURE 3.30: AUG test pulse #37538. Right side: lines of sight of the diode bolometer divertor camera (DLX). Left side: time traces of radiation measured by each line of sight in W/m^2

- $\Delta Z_{MARFE,Gauss} < 0$: the maximum radiation is outside the plasma region and the MES is SAFE.
- $\Delta Z_{MARFE,Gauss} > 0$: the maximum radiation is inside the plasma and above the X_{point}, thus a MARFE is present and the MES is MARFE<5 cm
- $\Delta Z_{MARFE,Gauss} > 5$ the maximum radiation is 5 cm above the X_{point} and the MES is MARFE>5 cm.

The METs evaluated during the $\Delta Z_{MARFE,Gauss}$ post pulse offline analysis will be indicated as t^*_{MF}, t^*_{MH}, t^*_{ML} and t^*_{MS}. For AUG #37538, $\Delta Z_{MARFE,Gauss}$ (blue line in Figure 3.31) describes the following MARFE evolution:

- MARFE formation: $\Delta Z_{MARFE,Gauss}$ goes above the zero (X_{point} position - black dashed lines) at $t^*_{MF,1} = 3.49$ s.
- MARFE>5cm: $\Delta Z_{MARFE,Gauss}$ overcomes 5 cm at $t^*_{MH,1} = 3.52$ s.
- MARFE<5cm: $\Delta Z_{MARFE,Gauss}$ drops down during the MARFE suppression becoming lower than 5 cm at $t^*_{ML,1} = 3.62$ s.
- MARFE stabilization: $\Delta Z_{MARFE,Gauss}$ goes below the zero at $t^*_{MS,1} = 3.64$ s.

- 2nd MARFE formation: $\Delta Z_{MARFE,Gauss} = 0$ cm at $t^*_{MF,2} = 4$ s.
- MARFE>5 cm ($t^*_{MH,2}$): $\Delta Z_{MARFE,Gauss} > 5$ at $t^*_{MH,2} = 6.69$ s.

The post pulse offline analysis confirms the evolution of the first MARFE provided in the database for AUG pulse #37538 and also well automatically detected. Indeed, in Figure 3.28, Geo_{SAFE} presents a sharp increase near $t_{MF,man}$, while Geo_{MARFE} and $Geo_{MARFE@5}$ are decreasing, and a decrease 70 ms before $t_{MF,man,1}$, while Geo_{MARFE} and $Geo_{MARFE@5}$ are increasing. Thus, $t_{MF,auto,1}$ and $t_{MH,auto,1}$ (orange and purple continuous lines respectively) are mostly overlapped with $t_{MF,man,1}$ and $t_{MH,man,1}$ with a later detection smaller than 30 ms, $t_{ML,auto,1}$ and $t_{MS,auto,1}$ have been early detected within 70 ms from $t_{ML,man,1}$ and $t_{ML,auto,1}$ respectively. Note that, for AUG#37538 a second MARFE evolution has been manually detected at $t_{MF,man,2} = 6.43$ s (second dashed orange line in Figure 3.28), and automatically detected in advance by the ISOMAP, at $t_{MF,auto,2} = 4.13$ s (second continuous orange line in Figure 3.28), with a $\Delta t_{MF} = 2.3$ s. However, the automatic detection is confirmed by the offline analysis, since $t^*_{MF,2} = 4$. Later, in the time window between $t^*_{MF,2}$ and $t^*_{MH,2}$, Geo_{MARFE} is the lowest geodesic distance function, until the MES becomes MARFE>5cm at $t^*_{MH,2}$ when $Geo_{MARFE5cm}$ has decreased enough to satisfy the condition describe in section 3.5.3. Both the manual and the automatic times, $t_{MH}, man = 6.75$ and $t_{MH,auto} = 6.73$ respectively, are confirmed by $t^*_{MH,2}$. Note that, $Geo_{MARFE@5}$ starts decreasing at 5.5 s when $\Delta Z_{MARFE,Gauss}$ starts to slightly increase. Figure 3.29 reports the behavior of the 15 features, from which there is not a strong evidence of the MARFE formation at $t = 4$s, except for the $P_{rad,UPPER}$ and $P_{rad,CORE}$ inversion, as the one mentioned in the previous example. However, this test example highlights the potentiality of the geodesic distances in describing the MARFE evolution through its characteristic states even when not clearly evidence can be gotten from the features of the high-dimensional input space.

3.5.6.3 Detected MARFE formation with large anticipation (AUG pulse #29810)

The AUG #29810 is the second test case for which the MARFE formation is detected more than 0.5 s in advance. Indeed, Figure 3.32 shows that a $t_{MF,man,1} = 5.31$ s was provided, while a MARFE formation is automatically detected around $t_{MF,auto,1} = 3.59$ s, with a $\Delta t_{MF} \approx 1.72$ s in

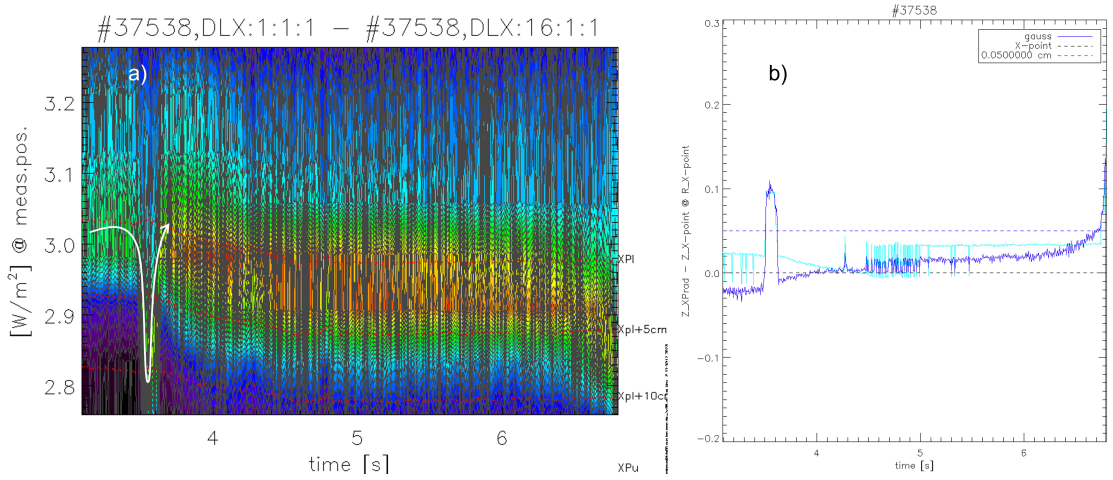

FIGURE 3.31: AUG test pulse #37538. Left side: radiation map in the divertor region by the DLX cameras, X_{point} position (upper red dashed line), 5 cm above the X_{point} (middle red dashed line), 10 cm above the X_{point} (bottom red dashed line). The green-red region allows to localize the maximum radiation. The white arrow highlights the first MARFE evolution. Indeed, the radiation maximum moves far from the X_{point} which means that the MARFE is formed. After the trajectory described by the white arrow it can be observed that the red region stays below the upper red dashed lines meaning that the maximum radiation is above the X_{point} and a second MARFE is formed. Right side: vertical distance of the maximum radiation from the X_point, $\Delta Z_{MARFE,max}$(cyan line) $\Delta Z_{MARFE,Gauss}$ (blue line). The blue line is considered as the MARFE vertical position with respect to the $Z_{X_{point}}$.

advance. Moreover, a MARFE stabilization with $t_{ML,man,1} = 5.42$ s and $t_{MS,man,1} = 5.43$ s and a second MARFE formation at $t_{MF,man,2} = 6.79$ s were provided. Differently, the ISOMAP never detected a MARFE stabilization, but provides alarms indicating a MARFE wobbling around $Z_{X_{point}} + 5$ cm. Once again, the offline analysis, conducted with the IDL tool, has been used to deeply investigate the MARFE evolution and to evaluate the goodness of the ISOMAP outputs. Figure 3.34 right-side shows the diode bolometer contouring in the time window between 3 s and 7 s, where both the regions inside the white boxes are characterized by radiated power reflected by the plasma facing components, highlighted in green in the Figure 3.34 left-side. These region have to be excluded opportunely selecting the camera angle ranges, otherwise the calculation of $Z_{MARFE,max}$ and $Z_{MARFE,Gauss}$ are affected by the radiated power reflected by the plasma facing components. Thus, the radiation map has been restricted as shown in the Figure 3.35 (left-side) where the reflection from the plasma facing components is totally excluded, while some reflected power from the limiter is still present since it is measured from LoS looking at X_{point}. Finally, the $\Delta Z_{MARFE,MAX}$ and $\Delta Z_{MARFE,Gauss}$ time traces can be computed (see Figure 3.35 right-side, cyan and blue line respectively) and observing $\Delta Z_{MARFE,Gauss}$ the following MARFE

evolution has been depicted:

- MARFE formation: $\Delta Z_{MARFE,Gauss}$ overcomes zero (black dashed line) at $t_{MF,1}* = 1.67$ s.
- MARFE wobbling: $\Delta Z_{MARFE,Gauss}$ oscillates between 0 and 5 cm until $t_{MH,1}* = 5.31$ s. Later, the MARFE starts wobbling around $Z_{X_{point}} + 5$ cm (blue dashed line), thus $t_{ML,1}* = 5.33$ s, $t_{MH,2}* = 5.38$ s, $t_{ML,2}* = 5.43$ s and $t_{MH,3} = 6.78$ s can be identified, followed by a disruption

Considering that the times define by the post pulse offline analysis the most reliable times, the ISOMAP error on $t_{MF,auto,1}$ it's not an early detection with respect to the provided $t_{MF,man,1}$ but a late detection with respect to $t^*_{MF,1}$. The MESs described by $\Delta Z_{MARFE,Gauss}$ represent a single MARFE evolving from $t^*_{MF,1}$ and leading to disruption. The MARFE start wobbling at $t^*_{MH,1}$, in agreement both with $t_{MH,auto} = 5.32$ s and with $t_{MH,man} = 5.33$ s. Later, the manual analysis detect a $t_{ML,man,1} = 5.42$, in agreement with $t_{ML,2}* = 5.43$, followed by $t_{MS,man,1}$ and by a second MARFE evolution characterized by $t_{MF,man,2} = 6.80$ and $t_{MH,man,2} = 6.81$ s.

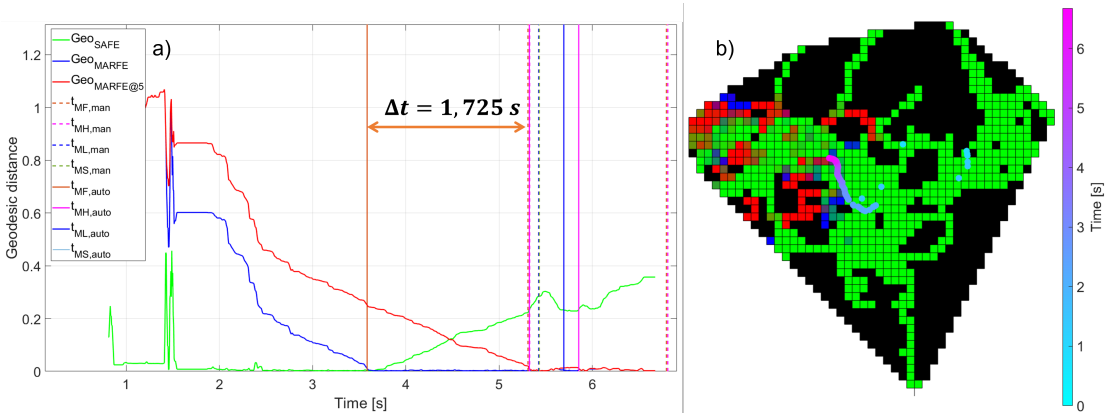

FIGURE 3.32: AUG test pulse#29810. MARFE formation detection with $\Delta t_{MF} = 1.725$ s. Subplot a), geodesic distance functions time traces: Geo_{SAFE} in green, Geo_{MARFE} in blue, $Geo_{MARFE@5}$ in red. Manual times (dashed vertical lines): $t_{MF,man}$ in orange, $t_{MH,man}$ in magenta, $t_{ML,man}$ in blue, $t_{MS,man}$ in green. Automatic times (continuous vertical lines): $t_{MF,auto}$ in orange, $t_{MH,auto}$ in magenta, $t_{ML,auto}$ in blue, $t_{MS,auto}$ in green. $t_{MF,man} \approx 5.3$ s and $t_{MF,auto \approx 3.6}$ with a $\Delta t \approx 1.7$. The automatic t_{MH} and t_{ML} times state a wobbling of the MARFE around $Z_{X_{point}} + 5$ cm. Subplot b) Pulse projection into the 2D-ISOMAP Clustering, the color shade of the samples, from cyan to magenta, is linked to the growing of the time, for $t_i = t_0$ the sample is cyan and for $t_i = t_{cut}$ the sample is magenta. The pulse projection starts with cyan samples falling on green clusters in the right side region in agreement with the SAFE state. Then, indigo samples fall on mixed green-blue clusters in agreement with the MARFE<5cm state automatically detected at $t_{MF,auto}$. The pulse end in a MARFE>5cm state confirmed by the magenta samples falling on mixed blue-red clusters.

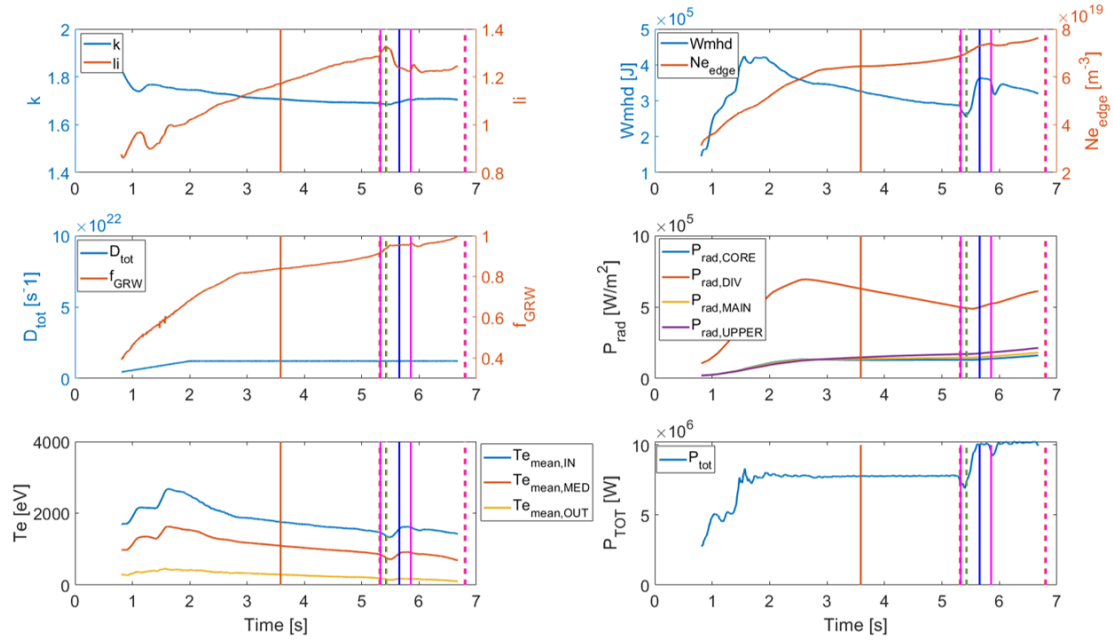

FIGURE 3.33: AUG test pulse #29810 features. 1^{st} column from top to bottom: elongation k and internal inductance (li), sum of D2 gas-fluxes (D_{tot}) and Greenwald fraction (f_{GRW}), electron temperature features ($Te_{mean,CORE}$, $Te_{mean,EX-CORE}$, $Te_{mean,EDGE}$). 2^{nd} column from top to bottom: plasma energy ($Wmhd$) and electron density at the plasma edge (Ne_{edge}), radiated power features ($P_{rad,CORE}$, $P_{rad,DIV}$,$P_{rad,MAIN}$, $P_{rad,UPPER}$), total applied power (P_{TOT}). In the time window across $t_{MF,auto} = 3.5$ s, the li, Ne_{edge} and f_{GRW} increasing is an indicator of the MARFE formation, as the decreasing both of the $Wmhd$ (blue line in upper-right plot) and of the electron temperature features (bottom-left plot).

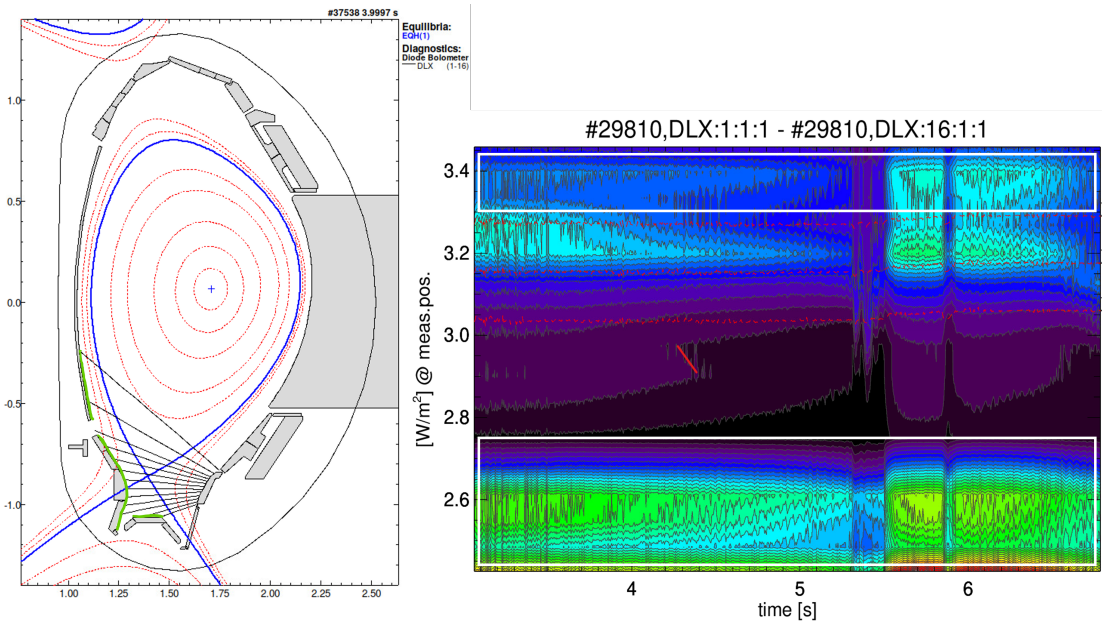

FIGURE 3.34: AUG test pulse #29810. Left side: diode bolometer LoS. Surfaces of the plasma facing components responsible for the radiated power reflection are highlighted in green. Right side: radiation map as measured from all the LoS. The white boxes indicates the regions where the measures are afflicted by the reflection

Instead, $t_{MS,auto,1} = 5.65$ and $t_{MH,auto,2} = 5.85$ have been automatically detected, defining a MARFE>5 cm that lasts until $t_{cut} < t^*_{MH,3}$. This example shows the capability of the ISOMAP to monitoring and correctly detect also small displacements of the MARFE, as its wobbling around $Z_{X_{point}} + 5$ cm, by analyzing the geodesic distances. Moreover, in Figure 3.32b), also the pulse trajectory on the 2D-ISOMAP Clustering provides a good tool for the MARFE evolution monitoring. Indeed, the trajectory overlaps blue clusters at $t_i = t_{MF,auto}$ indicating the MARFE formation, crosses mixed blue-green cluster suggesting that the MARFE is still present and ends on mixed blue-red clusters in agreement with the wobbling described above. Figure 3.33 reports the 15 features of the high-dimensional input space. The li, Ne_{edge} and f_{GRW} increasing is an indicator of the MARFE formation, as the decreasing both of the $Wmhd$ (blue line in upper-right plot) and of the electron temperature features (bottom-left plot). Moreover, from the middle-right plot, it can be observed that the $P_{rad,UPPER}$ and $P_{rad,CORE}$ inversion takes place during the MARFE evolution after t^*_{MF}. The train and test performance, reported in the sections 3.5.4 and 3.5.5, have been evaluated referring to the provided MET manual database. Thus, after this second investigation a t_{MH} FD (second magenta vertical line in Figure 3.32) and a t_{MS} MD have to be excluded from the ISOMAP errors on the test set.

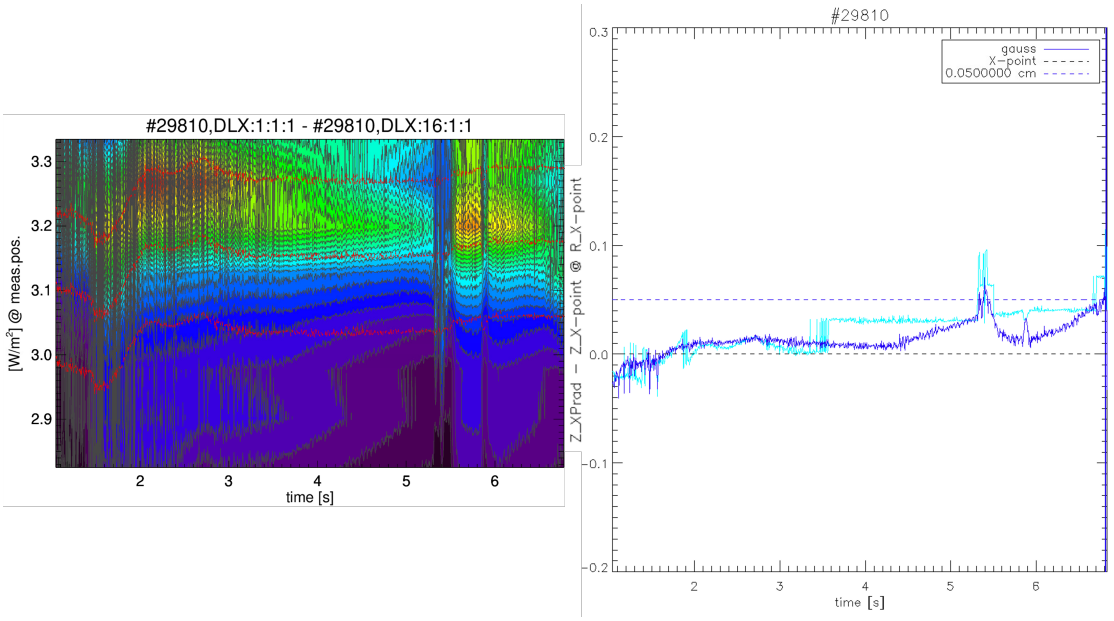

FIGURE 3.35: AUG test pulse #29810. Left side: radiation map excluding the region afflicted by radiated power reflection. Right side: vertical distance of the maximum radiation from the X_point, $\Delta Z_{MARFE,max}$(cyan line) $\Delta Z_{MARFE,Gauss}$ (blue line). The blue line is considered as the MARFE vertical position with respect to the $Z_{X_{point}}$.

3.5.6.4 No FD for NO HDL pulse (AUG#33294)

The ISOMAP performance have been evaluated also in terms on FD on both HDL and NO HDL pulses, for which no MARFE formations have been provided by the MET manual database. From the distribution of the input features, provided in Figure3.18, it can be seen that HDL pulses and NO HDL pulses, used for the ISOMAP training, present quite different distribution of several features, as described in section 3.2. Indeed, in the 2D-ISOMAP Clustering (see Figure 3.36), the NO HDL samples populate the green clusters in the upper-right corner, which is the farthest region from the red, blue and mixed clusters describing the MARFE development on the left side. Note that, among the NO HDL there are 12 disrupted in L-mode discharges. Since these disruptions doesn't present a MARFE, which is the disruption precursor of interest for this thesis, all samples have been labeled as SAFE state.

Figure 3.36 shows the geodesic distances times traces and the projection on the 2D-ISOMAP Clustering for NO HDL pulse AUG#33294 (disrupted in L-mode). Note that, Geo_{MARFE} and $Geo_{MARFE@5}$ are always much larger than Geo_{SAFE}, thus no MARFE formation is detected. Moreover, both Geo_{MARFE} and $Geo_{MARFE@5}$ evolve around values much larger than those of HDL pulses. This trend is verified in all tested NO HDL pulses. Usually, HDL pulses present

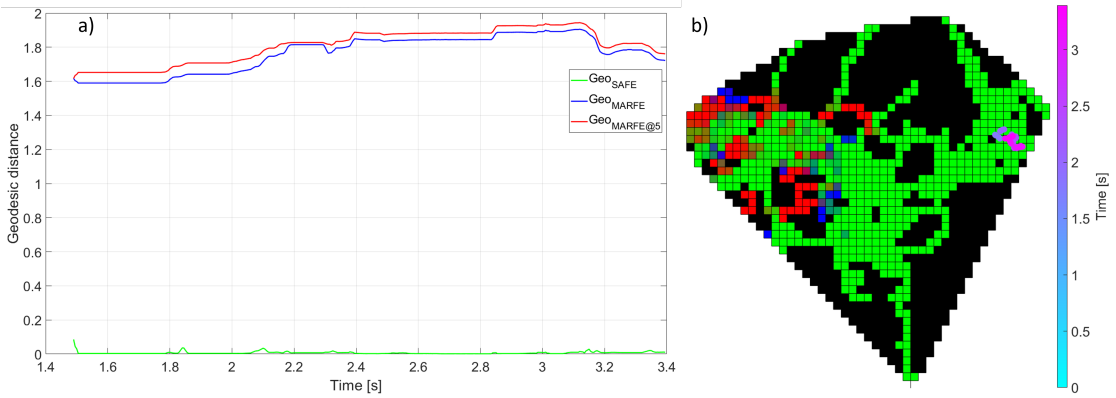

FIGURE 3.36: AUG test pulse #33294, no FD. Subplot a), geodesic distance functions time traces: Geo_{SAFE} in green, Geo_{MARFE} in blue, $Geo_{MARFE@5}$ in red. Manual times (dashed vertical lines): $t_{MF,man}$ in orange, $t_{MH,man}$ in magenta, $t_{ML,man}$ in blue, $t_{MS,man}$ in green. Automatic times (continuous vertical lines): $t_{MF,auto}$ in orange, $t_{MH,auto}$ in magenta, $t_{ML,auto}$ in blue, $t_{MS,auto}$ in green. For a NO HDL pulse Geo_{MARFE} and $Geo_{MARFE@5}$ values are much higher than those of HDL pulses. Subplot b), pulse projection into the 2D-ISOMAP Clustering, the color shade of the samples, from cyan to magenta, is linked to the growing of the time, for $t_i = t_0$ the sample is cyan and for $t_i = t_{cut}$ the sample is magenta. The pulse remains for the whole time in a safe region on the right side of the map

Geo_{MARFE} lower than 1, while NO HDL pulses present Geo_{MARFE} larger than 1. Thus, the geodesic distance functions well represent the considered manifold. The much lower values of Geo_{SAFE} (see Figure 3.36, green line), with respect to Geo_{MARFE}, indicates that the plasma is in a $SAFE$ state, in addition the larger values of Geo_{MARFE}, with respect to HDL pulses, highlight that NO HDL pulses are far away from the region characterized by MARFEs. Indeed, the AUG#33294 projection (see Figure 3.36 right-side) belongs to the green clusters in the upper right corner. The Figure 3.37 shows the times-traces of the input features. The mid-right subplot shows that both f_{GRW} and D_{tot} are in a very different range with respect to a HDL pulse. From this preliminary analysis, it seemed that the Geo_{MARFE} value alone could be used to distinguish between HDL and NO HDL pulses. Figure 3.38 shows the distribution of Geo_{MARFE} values for both HDL (magenta bars) and NO HDL (black bar) test samples. Even if poor, an overlapping between the two distributions is present. This is confirmed by the time trace trends reported in Figure 3.39, where the time trace of Geo_{MARFE} for all HDL pulses have been reported in magenta, and those of the NO HDL ones in black. These two plots highlight that only a simple threshold criterion on Geo_{MARFE} does not allow to distinguish between HDL and NO HDL pulses without any FD. Some condition about the Geo_{MARFE} time derivative needed to be optimized.

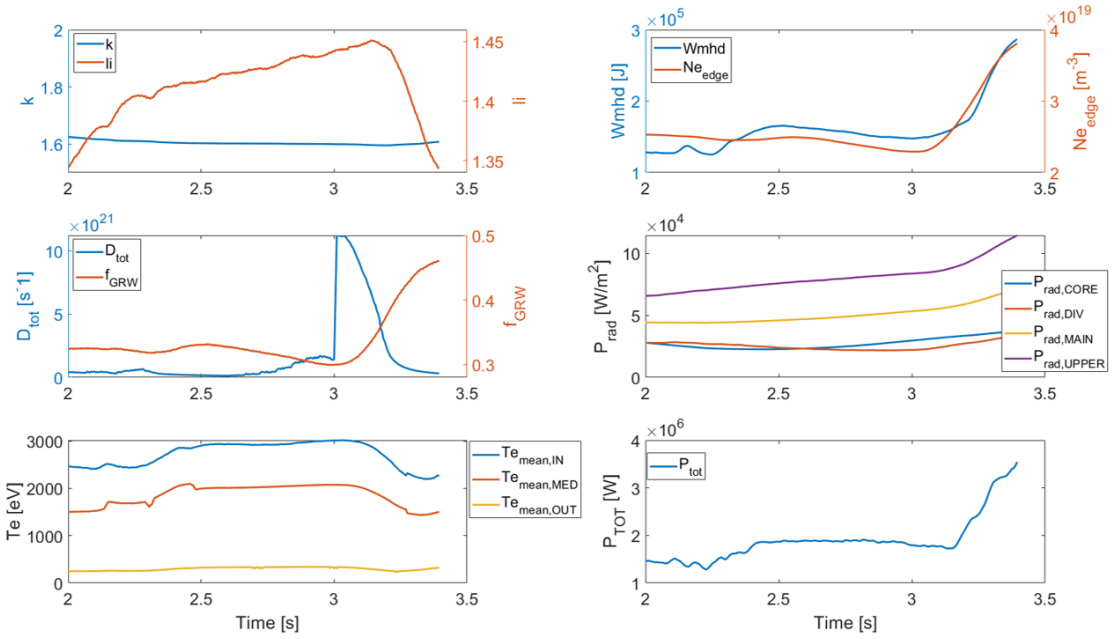

FIGURE 3.37: AUG test pulse#33294 feature. 1^{st} column from top to bottom: elongation k and internal inductance (li), sum of D2 gas-fluxes (D_{tot}) and Greenwald fraction (f_{GRW}), electron temperature features ($Te_{mean,CORE}$, $Te_{mean,EX-CORE}$, $Te_{mean,EDGE}$). 2^{nd} column from top to bottom: plasma energy ($Wmhd$) and electron density at the plasma edge (Ne_{edge}), radiated power features ($P_{rad,CORE}$, $P_{rad,DIV}$,$P_{rad,MAIN}$, $P_{rad,UPPER}$), total applied power (P_{TOT}). The mid-right subplot shows that both f_{GRW} and D_{tot} are in a very different range with respect to a HDL pulse.

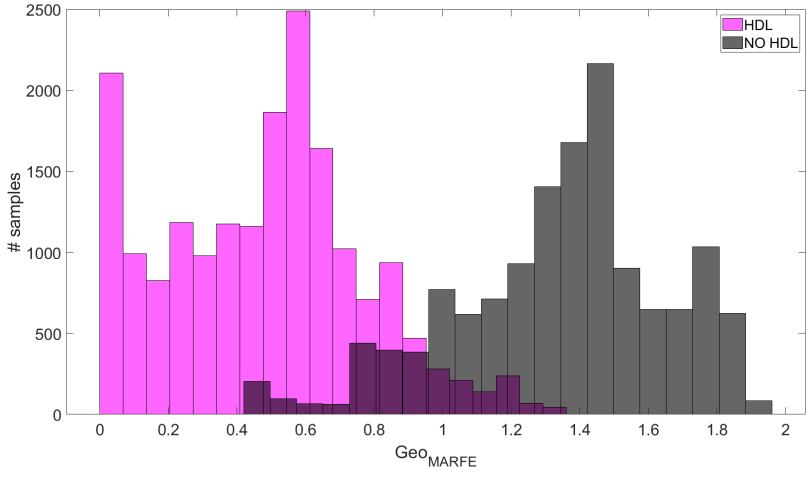

FIGURE 3.38: Geo_{MARFE} values histogram for test samples. HDL samples (magenta bars), NO HDL samples (black bars).

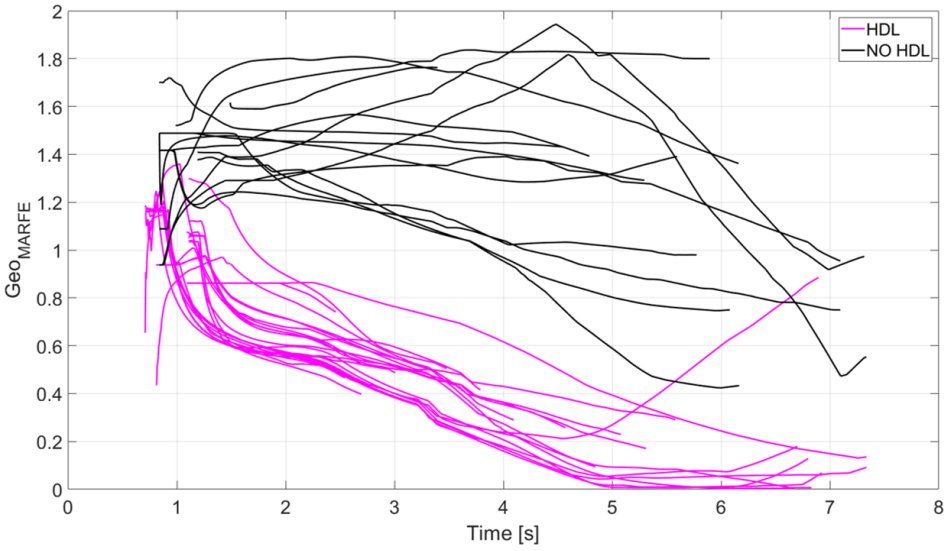

FIGURE 3.39: Geo_{MARFE} time traces of test pulses. HDL pulses (magenta lines), NO HDL pulses (black line). For this plot, Geo_{MARFE} have been smoothed considering a median filter on back-forward time window of 500 ms.

3.5.6.5 Avoided FD for HDL AUG pulse #28140

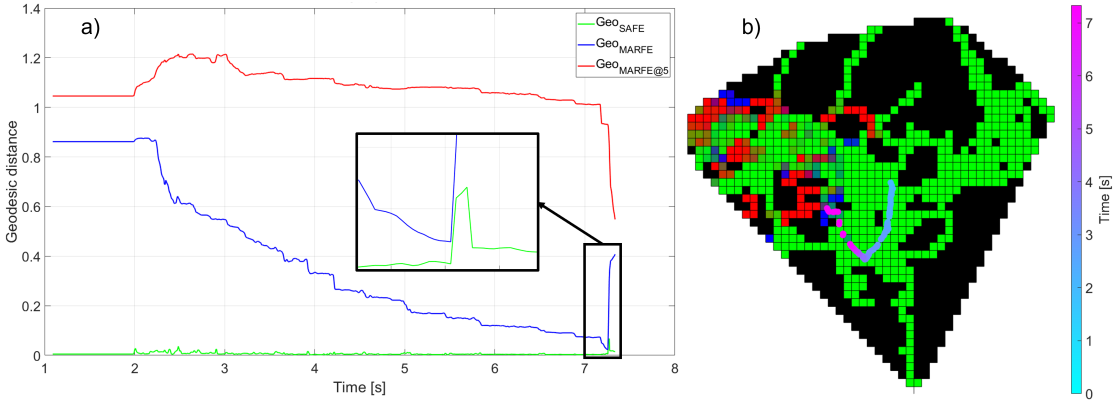

FIGURE 3.40: AUG test pulse #28140. Undetected MARFE. Subplot a), geodesic distance functions time traces: Geo_{SAFE} in green, Geo_{MARFE} in blue, $Geo_{MARFE@5}$ in red. Manual times (dashed vertical lines): $t_{MF,man}$ in orange, $t_{MH,man}$ in magenta, $t_{ML,man}$ in blue, $t_{MS,man}$ in green. Automatic times (continuous vertical lines): $t_{MF,auto}$ in orange, $t_{MH,auto}$ in magenta, $t_{ML,auto}$ in blue, $t_{MS,auto}$ in green. No MARFE formation alarm is triggered for this shot since Geo_{MARFE} always remains greater than Geo_{SAFE} as it can be clearly observed in the black box. Subplot b), pulse projection into the 2D-ISOMAP Clustering, the color shade of the samples, from cyan to magenta, is linked to the growing of the time, for $t_i = t_0$ the sample is cyan and for $t_i = t_{cut}$ the sample is magenta. The pulse approaches mixed blue-green clusters for t slightly before t_f.

To avoid a FD for HDL pulses is more crucial and challenging aspect with respect to NO HDL pulses. The AUG pulse #28140 is an HDL test pulse for which no METs were provided in the manual reference database. It has been selected to test ISOMAP False Detection. Indeed, it is geodesically close to HDL train pulses but no MARFE was developed. From Figure 3.40a), it can be observed that Geo_{MARFE} (blue line) is monotonically decreasing, it evolves in the characteristic range of HDL pulses, approaching the conditions for the automatic alarm just before t_f. However, Geo_{MARFE} always remains greater than Geo_{SAFE}, as it can be clearly observed in the black box. The Figure 3.40b) shows that for $t \approx t_f$ the test samples neighbors belong mainly to green-blue mixed clusters suggesting that the pulse is close to a MARFE formation, as happening at about 7.2 s. Indicators of the MARFE formation, at about 7.2 s, can be seen among features describing the high dimensional input space (see Figure 3.41), as the increasing of li, f_{GRW} and the decreasing of T_e, as validation of the geodesic distance functions. However, the $P_{rad,CORE}$ and $P_{rad,UPPER}$ inversion is not present.

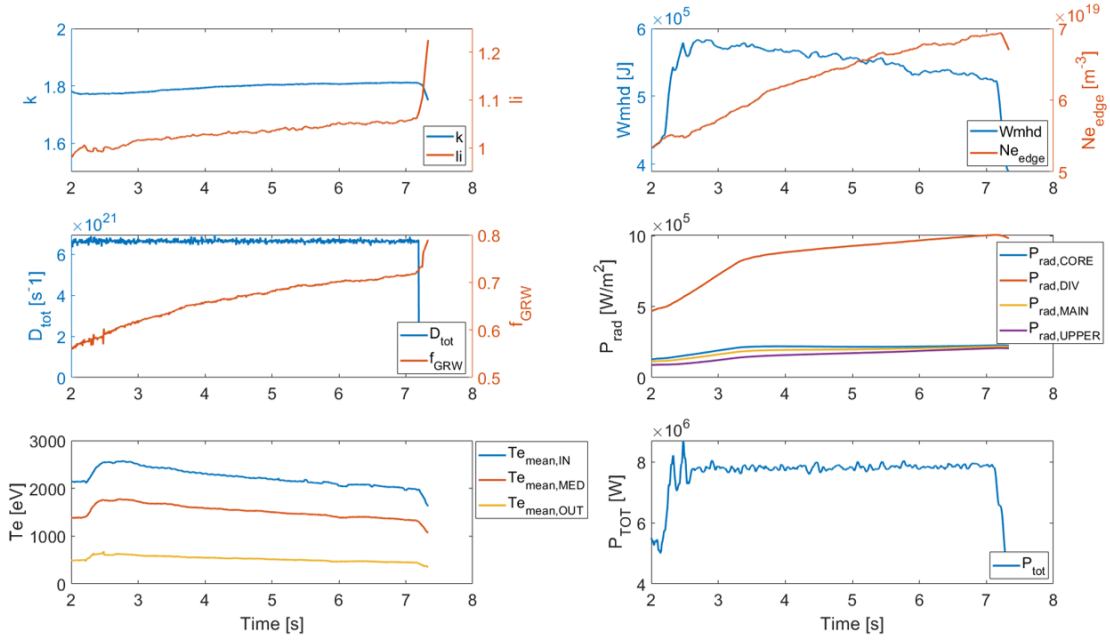

FIGURE 3.41: AUG test pulses #28140 features. 1^{st} column from top to bottom: elongation k and internal inductance (li), sum of D2 gas-fluxes (D_{tot}) and Greenwald fraction (f_{GRW}), electron temperature features ($Te_{mean,CORE}$, $Te_{mean,EX-CORE}$, $Te_{mean,EDGE}$). 2^{nd} column from top to bottom: plasma energy ($Wmhd$) and electron density at the plasma edge (Ne_{edge}), radiated power features ($P_{rad,CORE}$, $P_{rad,DIV}$,$P_{rad,MAIN}$, $P_{rad,UPPER}$), total applied power (P_{TOT}). The increasing of li, f_{GRW} and decreasing of T_e, at about 7.2 s, are indicators of a MARFE formation.

3.5.6.6 Undetected MARFE formation (AUG pulse #28331)

For the test pulse AUG#28331, whose geodesic distance functions are reported in Figure 3.42a), the ISOMAP misses both the MARFE formation and its upward motion. Geo_{MARFE} does not indicate the presence of a MARFE, indeed it is always above both Geo_{SAFE}. In addition, it is above 0.3, which is much higher than the characteristics values indicating a MARFE evolution. In the considered dataset, this pulse is the only case where the MD is not only due to the alarm criteria failure, but also it is due to the wrong behavior of the Geo_{MARFE} time trace. In terms of ISOMAP algorithm this happens because all neighbors of the projected samples are safe samples, meaning that for the pulses in similar operative conditions used in the train set, no MARFE formation has been provided. This is confirmed by observing Figure 3.42b) where all the test samples neighbors are projected in the SAFE region (green clusters). In Figure 3.43, reporting the time-traces of the 15 features, the increasing li, Ne_{edge} and $Wmhd$ (brown line in upper-right, upper-left e mid-right plot respectively) suggests a MARFE evolution not clearly detectable from the electron temperature features and neither described by the radiated power features since no $P_{rad,CORE}$ and $P_{rad,UPPER}$ inversion takes place.

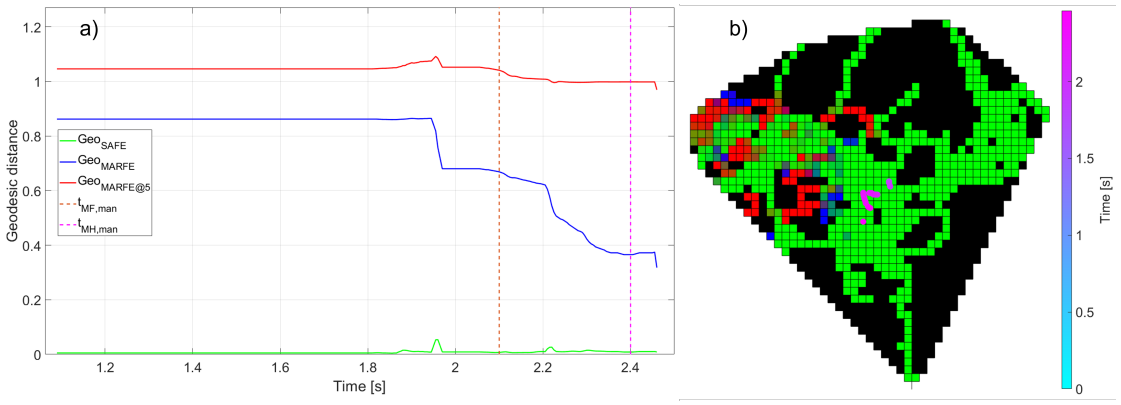

FIGURE 3.42: Test pulse #28331. Undetected MARFE. Subplot a), geodesic distance functions time traces: Geo_{SAFE} in green, Geo_{MARFE} in blue, $Geo_{MARFE@5}$ in red. Manual times (dashed vertical lines): $t_{MF,man}$ in orange, $t_{MH,man}$ in magenta, $t_{ML,man}$ in blue, $t_{MS,man}$ in green. Automatic times (continuous vertical lines): $t_{MF,auto}$ in orange, $t_{MH,auto}$ in magenta, $t_{ML,auto}$ in blue, $t_{MS,auto}$ in green. No automatic detection is possible for this pulse due to the different Geo_{MARFE} values with respect to those of the train pulses. Subplot b), pulse projection into the 2D-ISOMAP Clustering, the color shade of the samples, from cyan to magenta, is linked to the growing of the time, for $t_i = t_0$ the sample is cyan and for $t_i = t_{cut}$ the sample is magenta. The pulse remains for the whole time in a safe region.

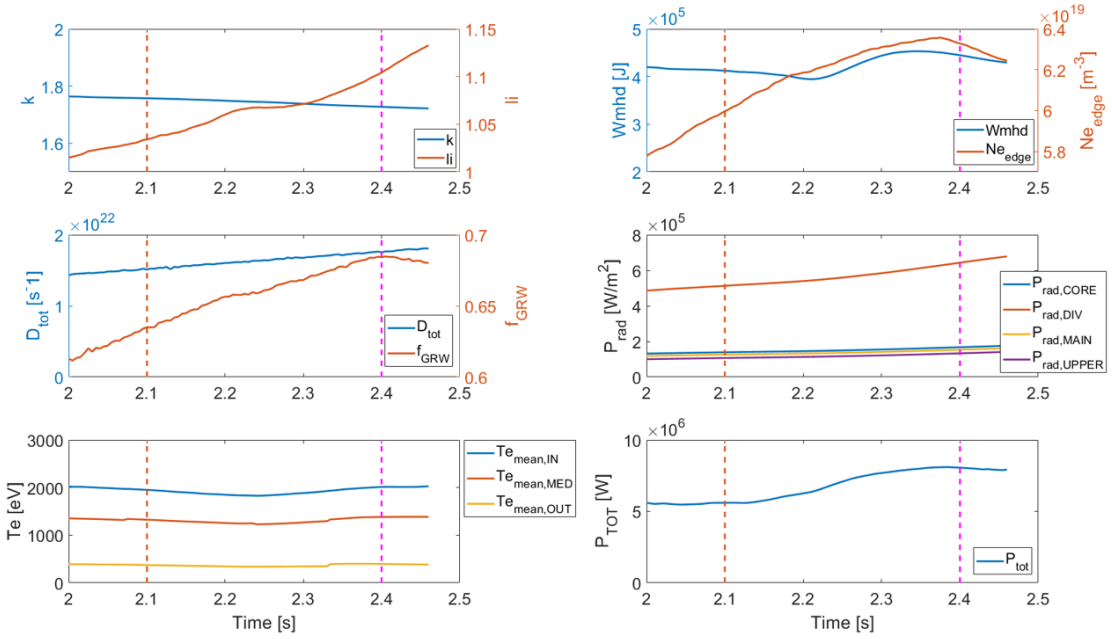

FIGURE 3.43: AUG pulses #28331 features. 1^{st} column from top to bottom: elongation (k) and internal inductance (li), sum of D2 gas-fluxes (D_{tot}) and Greenwald fraction (f_{GRW}), electron temperature features ($Te_{mean,CORE}$, $Te_{mean,EX-CORE}$, $Te_{mean,EDGE}$). 2^{nd} column from top to bottom: plasma energy ($Wmhd$) and electron density at the plasma edge (Ne_{edge}), radiated power features ($P_{rad,CORE}$, $P_{rad,DIV}$,$P_{rad,MAIN}$, $P_{rad,UPPER}$), total applied power (P_{TOT}). The increasing li, Ne_{edge} and $Wmhd$ (brown line in upper-right, upper-left e mid-right plot respectively) suggests a MARFE evolution not clearly detectable from the electron temperature features and neither described by the radiated power features since no $P_{rad,CORE}$ and $P_{rad,UPPER}$ inversion takes place.

3.5.6.7 Undetectable MARFE for AUG pulse #28729

Figure 3.44 shows an example of an undetectable MARFE evolution. As describe in the section 3.3 the end of the flat-top (t_{cut}) has been optimized in order to collect as most as possible MESs near the disruption, avoiding the inclusion of some unrealistic feature values. Therefore, most of the t_f has been set to exclude negative values both of electron temperature and electron density. In this way, for two test pulses t_{MF} is later than t_{cut}, in three test pulses t_{MH} is later than t_{cut} and these METs can't be automatically detected. The manually detected MESs for AUG pulse #28729 both occur after the end of the available time base. In Figure 3.44 the geodesic distance functions for the test pulse AUG #28729 are reported, Geo_{MARFE} ramps down, reaching values lower than 0.2 at $t = t_f$, suggesting that a MARFE is going to be formed before the pulse disruption. In addition, in Figure 3.44b) it can be seen that, in the last part of the projection (magenta points) the samples neighbors are getting closer to MARFE clusters, as

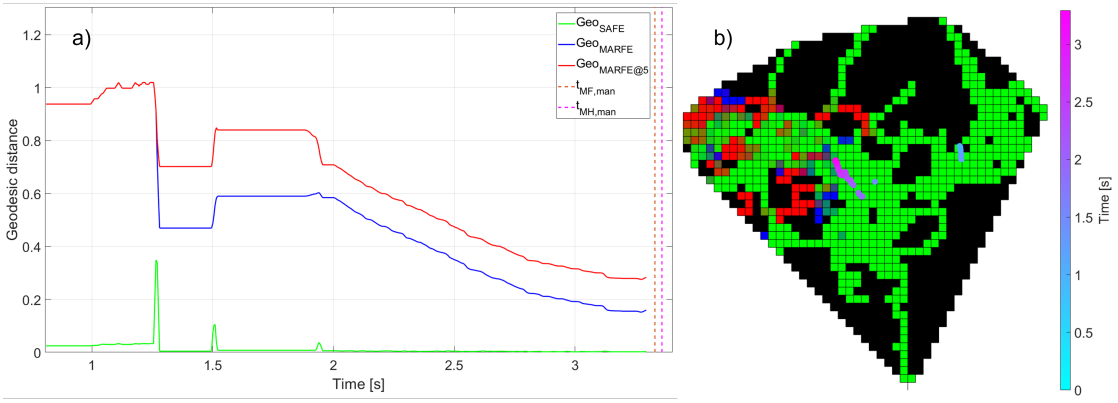

FIGURE 3.44: AUG test pulse #28729. Undetected MARFE. Subplot a), geodesic distance functions time traces: Geo_{SAFE} in green, Geo_{MARFE} in blue, $Geo_{MARFE@5}$ in red. Manual times (dashed vertical lines): $t_{MF,man}$ in orange, $t_{MH,man}$ in magenta, $t_{ML,man}$ in blue, $t_{MS,man}$ in green. Automatic times (continuous vertical lines): $t_{MF,auto}$ in orange, $t_{MH,auto}$ in magenta, $t_{ML,auto}$ in blue, $t_{MS,auto}$ in green. The manually detected MES both occur after the end of the available time base for this shot. Subplot b), pulse projection into the 2D-ISOMAP Clustering, the color shade of the samples, from cyan to magenta, is linked to the growing of the time, for $t_i = t_0$ the sample is cyan and for $t_i = t_{cut}$ the sample is magenta. The pulse projection starts on safe (green) cluster (cyan and indigo sample in the left and central region of the map) confirming the SAFE state and ends on mixed blue-red cluster in agreement with the undetectable subsequent MARFE formation.

they belong to mixed green-blue clusters, evolving from the safe (green) ones. The Figure 3.45 shows the li, Ne_{edge} and f_{GRW} increasing as MARFE indicators before $t = t_f$, the inversion between $P_{rad,UPPER}$ and $P_{rad,CORE}$ is going to occur. The electron temperature in the MED and OUT region (orange and yellow line in bottom-left subplot respectively) are very low with respect to other HDL pulses belonging to the training set.

3.5.6.8 FD for HDL pulse #37458

As describe is section 3.5.5, FDs never occur isolated, indeed when a false t_{MF} is detected, also subsequents t_{MH}, t_{ML} and t_{MS} are always detected. Figure 3.46 shows the behavior of geodesic distance functions in case of a false detected MARFE, highlighted by the red box. The time traces of the input features (see Figure 3.47) can be observed to understand the reason of this FD. Most of them suggests a MARFE formation between 2.6 s and 2.9 s, such as the increasing of both li and plasma density, observable both at the edge (by Ne_{edge}) and at the core (by f_{GRW}), and the temperature decreasing, observable by the three temperature features reported in the bottom-left plot. However, this behavior should not affect the algorithm, since

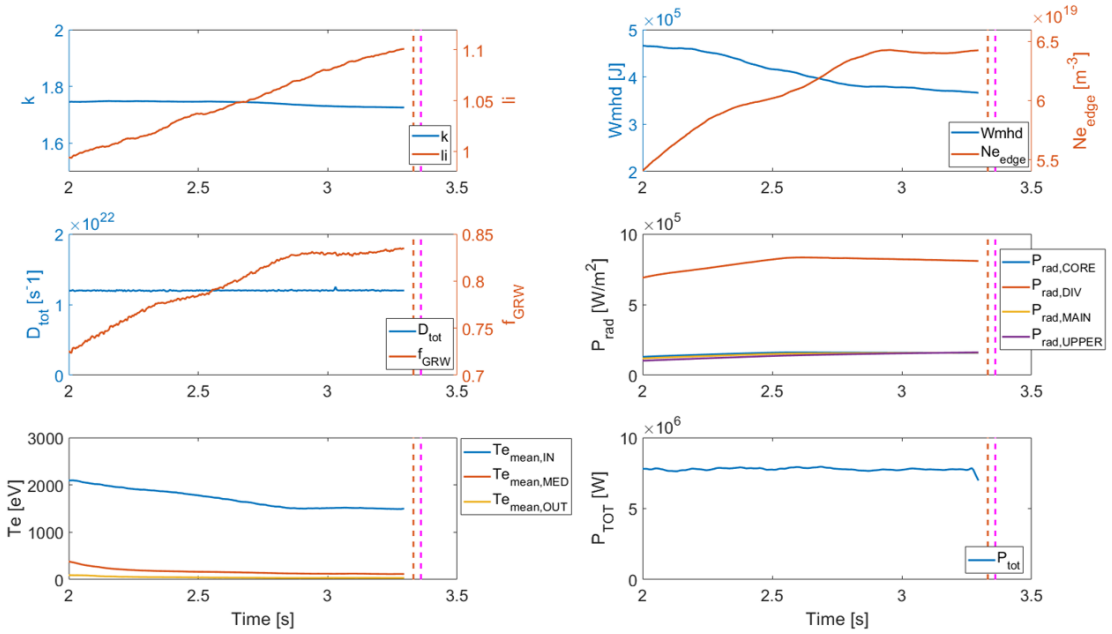

FIGURE 3.45: AUG test pulse #28729 features: 1^{st} column from top to bottom: elongation (k) and internal inductance (li), sum of D2 gas-fluxes (D_{tot}) and Greenwald fraction (f_{GRW}), electron temperature features ($Te_{mean,CORE}$, $Te_{mean,EX-CORE}$, $Te_{mean,EDGE}$). 2^{nd} column from top to bottom: plasma energy ($Wmhd$) and electron density at the plasma edge (Ne_{edge}), radiated power features ($P_{rad,CORE}$, $P_{rad,DIV}$,$P_{rad,MAIN}$, $P_{rad,UPPER}$), total applied power (P_{TOT}). The time traces show the li, Ne_{edge} and f_{GRW} increasing as MARFE indicators before $t = t_f$, the inversion between $P_{rad,UPPER}$ and $P_{rad,CORE}$ is going to occur. The electron temperature in the MED and OUT region (orange and yellow line in bottom-left subplot respectively) are very low with respect to other HDL pulses belonging to the training set.

no time derivative is taken into account as inputs, but the features values and their combination drive the pulse path into the different manifold regions. In this case, the pulse is projected into regions mainly populated by MARFE states. Indeed, the algorithm failure can be better understood by observing the pulse projection on the 2D-ISOMAP Clustering. Indeed, in Figure 3.46 the trajectory at about 2 s is projected on mixed (green-blue, blue) clusters. This means that sample neighbors (in the FD time window) present at least a MARFE a formation state. Indeed, comparing Figure 3.46b) with Figure 3.32b), it can be noticed that the clusters overlapped by the AUG pulse #37458 trajectory, between 2.6 s and 2.9 s, fall on the same cluster with respect to the AUG pulse #29810 trajectory at about 6 s, when a good MARFE evolution detection is provided.

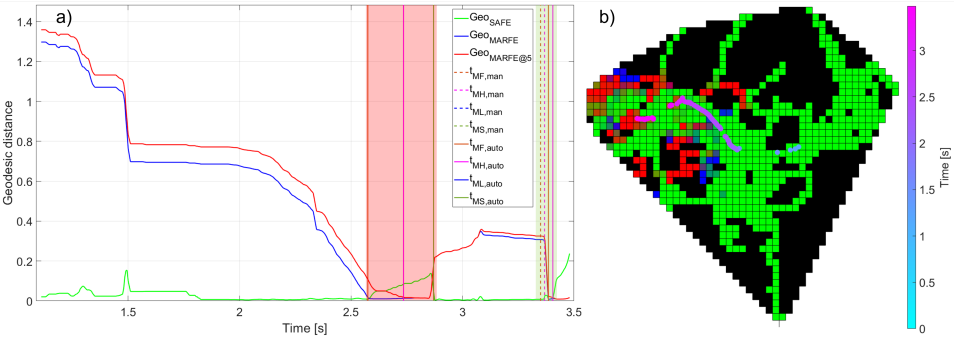

FIGURE 3.46: AUG test pulse #37458. MARFE evolution FD. Subplot a), geodesic distance functions time traces: Geo_{SAFE} in green, Geo_{MARFE} in blue, $Geo_{MARFE@5}$ in red. Manual times (dashed vertical lines): $t_{MF,man}$ in orange, $t_{MH,man}$ in magenta, $t_{ML,man}$ in blue, $t_{MS,man}$ in green. Automatic times (continuous vertical lines): $t_{MF,auto}$ in orange, $t_{MH,auto}$ in magenta, $t_{ML,auto}$ in blue, $t_{MS,auto}$ in green. The alarm criteria detect a complete MARFE evolution not provided in reference manual database (highlighted by the red box). Subplot b), pulse projection into the 2D-ISOMAP Clustering, the color shade of the samples, from cyan to magenta, is linked to the growing of the time, for $t_i = t_0$ the sample is cyan and for $t_i = t_{cut}$ the sample is magenta. The pulse projection starts from safe (green) clusters in the central region. Following, purple and magenta samples falls in green-blue mixed clusters first, where the FD is provided. Finally, magenta samples fall on mixed blue-red and green-red cluster and a good MARFE evolution automatic detection is provided.

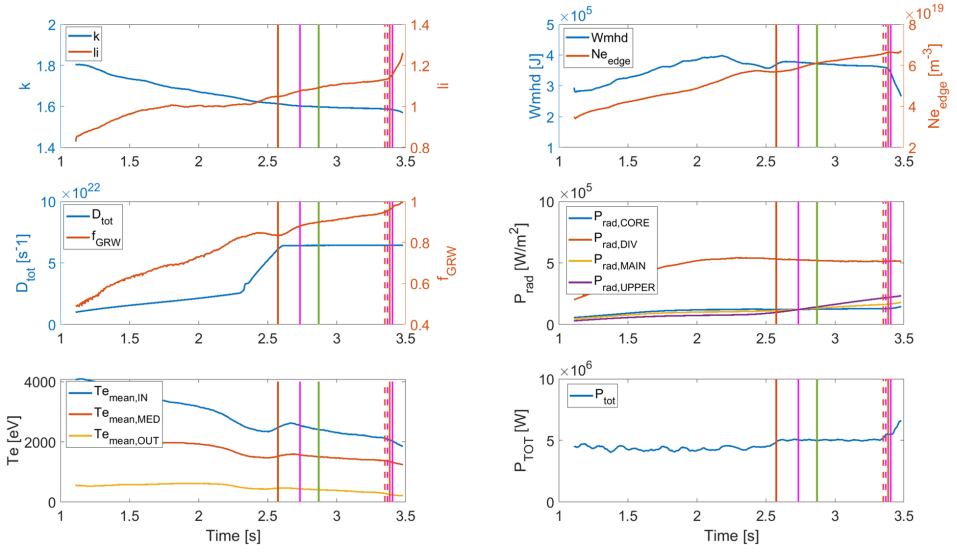

FIGURE 3.47: AUG test pulses #37458 features. 1^{st} column from top to bottom: elongation (k) and internal inductance (li), sum of D2 gas-fluxes (D_{tot}) and Greenwald fraction (f_{GRW}), electron temperature features ($Te_{mean,CORE}$, $Te_{mean,EX-CORE}$, $Te_{mean,EDGE}$). 2^{nd} column from top to bottom: plasma energy ($Wmhd$) and electron density at the plasma edge (Ne_{edge}), radiated power features ($P_{rad,CORE}$, $P_{rad,DIV}$,$P_{rad,MAIN}$, $P_{rad,UPPER}$), total applied power (P_{TOT}). Most of the features suggests a MARFE formation between 2.6 s and 2.9 s, such as the increasing of both li and plasma density, observable both at the edge (by Ne_{edge}) and at the core (by f_{GRW}), and the temperature decreasing.

3.5.6.9 FD for NO HDL pulse #41100

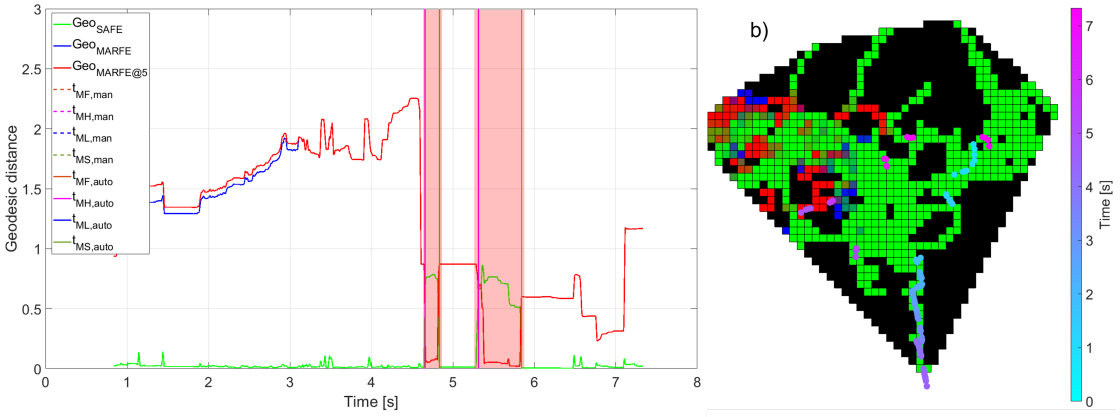

FIGURE 3.48: Test pulse #41100. MARFE evolution FD. ubplot a), geodesic distance functions time traces: Geo_{SAFE} in green, Geo_{MARFE} in blue, $Geo_{MARFE@5}$ in red. Manual times (dashed vertical lines): $t_{MF,man}$ in orange, $t_{MH,man}$ in magenta, $t_{ML,man}$ in blue, $t_{MS,man}$ in green. Automatic times (continuous vertical lines): $t_{MF,auto}$ in orange, $t_{MH,auto}$ in magenta, $t_{ML,auto}$ in blue, $t_{MS,auto}$ in green. The alarm criteria detect two complete MARFE evolution not provided by manual analysis (red boxes). Subplot b), pulse projection into the 2D-ISOMAP Clustering, the color shade of the samples, from cyan to magenta, is linked to the growing of the time, for $t_i = t_0$ the sample is cyan and for $t_i = t_{cut}$ the sample is magenta.

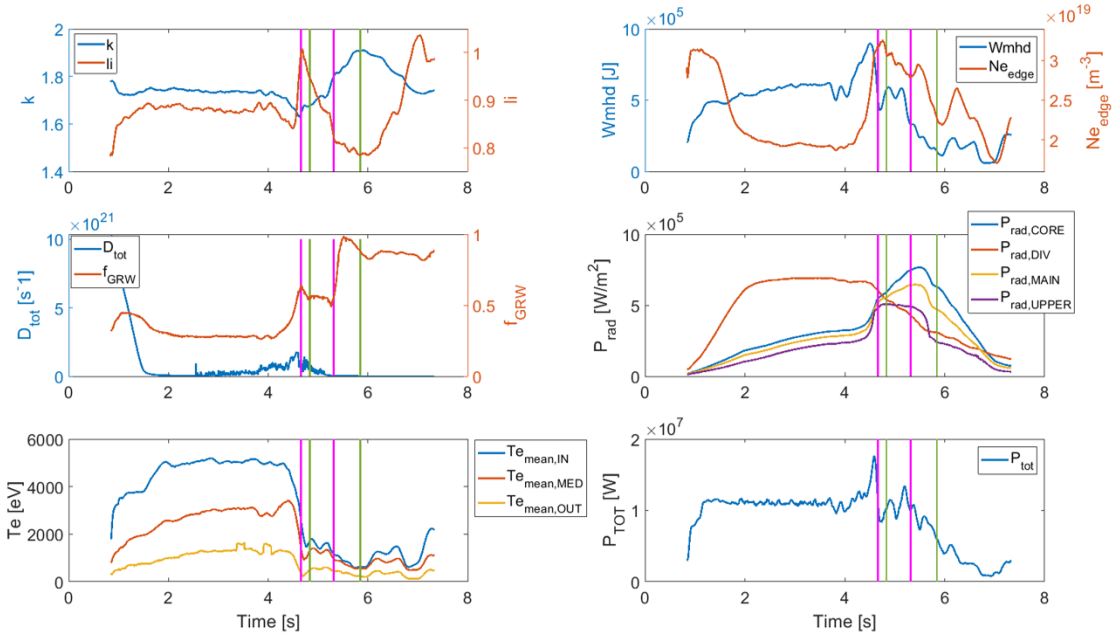

FIGURE 3.49: AUG pulses #41100 features. 1^{st} column from top to bottom: elongation (k) and internal inductance (li), sum of D2 gas-fluxes (D_{tot}) and Greenwald fraction (f_{GRW}), electron temperature features ($Te_{mean,CORE}$, $Te_{mean,EX-CORE}$, $Te_{mean,EDGE}$). 2^{nd} column from top to bottom: plasma energy ($Wmhd$) and electron density at the plasma edge (Ne_{edge}), radiated power features ($P_{rad,CORE}$, $P_{rad,DIV}$,$P_{rad,MAIN}$, $P_{rad,UPPER}$), total applied power (P_{TOT}).

The FDs for the NO HDL test pulses belong to the ones characterized by high mode numbers. As it can be observed in Figure 3.49 for pulses #41100, the features are characterized by large and quick changes, this behavior is mainly due to the presence of modes with high number. These changes lead to strong and sudden variations if the geodesic distance functions that trigger FDs, as highlighted by the red boxes (see Figure 3.48a)). The effects of the strong and sudden geodesic distance function variations can be observed also on the pulse projection on the 2D-ISOMAP Clustering (see Figure 3.48b)), indeed the trajectory is fragmented, between 4.5 s and 6 s, and it skips through clusters including the red ones. This closeness between NO HDL test samples and MARFE train samples could be justified considering that, as described in the section 3.1.4, during the MARFE the presence of high number modes is observed.

Chapter 4

White noise characterization of DTT pick-up coils

Magnetic diagnostics plays a key role in the understanding of plasma physics, machine protection, plasma control, and equilibrium reconstruction. The magnetic diagnostics system includes measurements of fields fluxes, plasma current, and diamagnetic flux made inside and outside the vacuum vessel [96]. Among the other, the local magnetic field measurements addressed by the pick-up coils play a crucial role in determining the MHD behavior of a plasma by detecting the amplitude fluctuations in the magnetic field as the plasma rotates inside the torus, in retrieving the plasma boundary, the plasma current and shape descriptors by means the equilibrium reconstruction. The characterization of white noise, affecting the pick-up coil measurements, is a key design driving requirement. The Last Closed Magnetic Surface (LCMS) determination in fusion reactors is a critical task in several applications, including plasma control and several off-line studies of the plasma configurations. The determination of the LCMS requires an accurate description of the magnetic field in the region of the plasma border. Given the centrality of this issue in the plasma control toward a safe operation in the developing of EU-DEMO, this thesis develops the characterization of the systematic error in the framework of the inverse boundary reconstruction due to white noise for DTT, referring to 2021 probe configuration [97]. In particular, section 4.1 shortly introduces the DTT scope, its main characteristics, and its main magnetic diagnostics. Section 4.2 describes the pick-up measurement rationalities and its role in feed-back plasma control scheme. Section 4.3 introduces the Inverse

plasma boundary reconstruction and the algorithm developed to perform it, reporting the magnetic reference configuration and highlighting the steps improved in this thesis. The section 4.3.4 reports the optimization of the pseudo-inverse reconstruction tolerance conducted in this thesis. Finally, in Section 4.4 the effect of noise on the measurements is presented in terms of ME, MSE, and variance on the gaps evaluation, and in terms of maximum and mean error in percentages on the plasma current value and the plasma barycenter position.

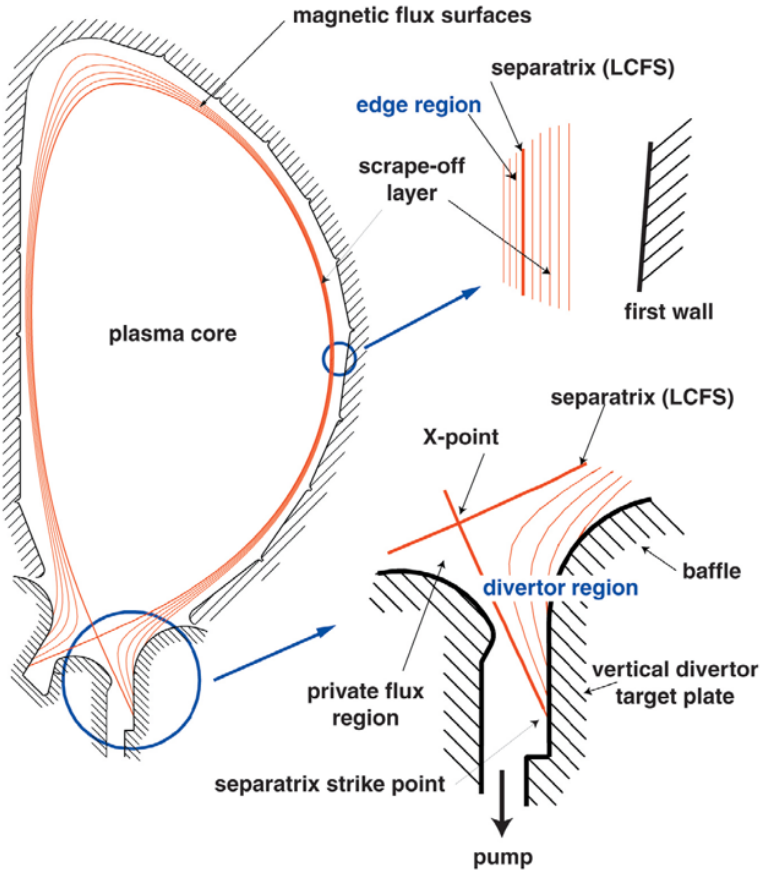

FIGURE 4.1: Poloidal cross-section of a tokamak plasma for EU-DEMO with a single magnetic null divertor configuration, illustrating the regions of the plasma and the boundary walls where important Plasma-Material interface and atomic physics processes take place. The characteristic regions are: the plasma core, the edge region just inside the separatrix, the scrape-off-layer (SOL) plasma outside the separatrix, and the divertor plasma region, which is an extension of the SOL plasma along field lines into the divertor chamber. The baffle structure is designed to prevent neutrals from leaving the divertor. In the private flux region below the X_{point}, the magnetic field surfaces are isolated from the rest of the plasma.[17]

4.1 DTT in EUROfusion roadmap

In a steady state magnetically confined fusion plasma the power which is injected into the plasma through auxiliary heating systems plus that produced by fusion reactions needs to be extracted from the device. The EUROfusion roadmap, presented in section 1.3, elaborates eight critical missions to the goal of nuclear electricity. In particular, the mission n. 2 - **Heat exhaust systems** - is aimed at identify solutions to the problem of the heat load disposal. The plasma confinement in a tokamak reactor is achieved with magnetic field lines forming a set of closed, nested magnetic surfaces. The edge of the plasma presents a thin region, with a

width in order of few millimeters, where open field lines appear, this is called Scrape-Off Layer (SOL - see Figure 4.1[17]). Charged particles (and their related energy) flowing out from the core plasma through the SOL are directed to the divertor plates towards the separatrix (the last closed magnetic surface in Figure 4.1). The heat flux at which the divertor will be exposed to is expected to be greater than that on the Sun's surface. Divertor geometry and magnetic flux map have to be designed with the aim to the reduce the normal heat flux on the target distributing the heat over a larger surface.

At present days, several alternatives, such as the cooled liquid Li limiter in FTU [98], the Snowflake divertor in TCV [99] or the Super-X divertor in MAST-U [100] are being investigated, however their extrapolation is not considered reliable for EU-DEMO. DTT's role is precisely to bridge the gap between present tokamaks and EU-DEMO bringing such solutions to a sufficient level of maturity and integration from both physics and technology perspective. The main DTT's objectives, as state in [6], are related both to test divertor solutions and improve experimental knowledge. Indeed, advanced divertor configurations or liquid metal, will be tested to understand if these solutions will be able to sustain strong thermal load if the fraction of radiated power is lower than expected. In addition, DTT will extend the bounds of available experiments grating a more suitable extrapolation to EU-DEMO, enlarge the power exhaust parameter range.

4.1.1 Main parameters

DTT will operate at relatively high toroidal field ($B_T = 6$ T) reaching plasma performance (mostly characterized by ratio between power and major radius) of about 15 MW/m, not far from those of EU-DEMO. The main parameters foreseen for DTT are reported in Table 4.1 for a Single-Null configuration:

TABLE 4.1: Main DTT parameters for a Single Null configuration

Parameter	**Value**
Major radius R [m]	2.11
Minor radius a [m]	0.64
R/a	3.3
Volume [m^3]	29
$q95$	3
$Ipla$ [MA]	5.5
B_T [T]	6.0
$H98$	1.0
Pulse length @EOF [s]	90

Other standard and advanced plasma configurations, such as negative Triangularity and Double Super-X, will be explored with a dedicated divertor [101].The DTT program foresees machine upgrades during its lifetime. In its first operating phase 23 MW of ICRH, 14.5 MW of ECRH and 7.5 of NBI will be available, following, additional power will be installed for total of 45 MW.

4.1.2 Main DTT magnetic probes

In DTT, magnetic probes inside the vessel must withstand a large temperature excursion being located between the first wall and VV. Similarly, the ones outside the vessel will face a hostile environment being place between the external VV suface ($T = 200$ °C) and the thermal shield ($T = -200$ °C), where the available radial distance is about 2 cm. Recent developments for ITER [103, 104] and RFX-mod2 [105] provide a guideline for the design and manufacturing of magnetic sensors for DTT. Several technologies are foreseen for the magnetic field, internal biaxial pick-up (Mirnov) coils of Mineral Insulated Cables (MIC) on Macor former appear to be suitable to fit the narrow space between first wall and vessel on the high field side, while ex-vessel pick-up coils shall be based on coated Cu wire on a Torlon plastic former. In addition, Low-Temperature co-fired Ceramics (LTCC) will be adopted to measure dB/dt fluctuations, granting a more compact design and higher bandwidth. Radiation Hard Hall and optic fiber are

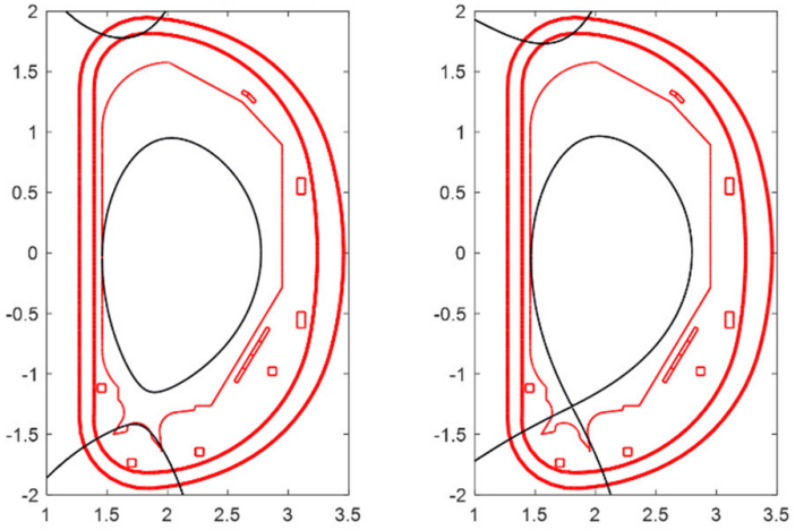

FIGURE 4.2: Magnetic diagnostics. All of these sensors operate on the same basic principle, the Faraday-Lenz law, namely, changing flux induces a voltage in a coil of wire. This voltage is integrated to determine the flux through the coil [102].

TABLE 4.2: Main magnetic diagnostics of DTT (in red those necessary for the first plasma)

MEASUREMENT	**DIAGNOSTIC**	ΔT
Magnetic flux	Flux saddle and diamagnetic loop	0.1 ms
Magnetic Field and dB/dt	Pick-up coils, Hall probes	0.1 ms, 0.5 μs for fluctuations
Halo/Eddy Currents	Rogowski coils	0.1 ms

also foreseen as non-integrated magnetic field and current measurements to calibrate standard probes. Rogosky coils with equi-spaced arrays in toroidal direction will diagnose the halo and eddy currents in the vessel and the first wall. The Table 4.2 reports the main magnetic diagnostics required for the first plasma, together with the measurements and the temporal resolution [101].

4.2 Pick-up coils

The simplest way to measure the magnetic field on a certain point along a specific direction is to use the Faraday-Lenz law (4.1) with a small coil of wire [106]. Indeed, in a varying with time magnetic field $B(t)$, the voltage induced in the coil is the (4.2), where N is the number of turn in the coil of area A, so NA is the so called *equivalent area* of the coil, and $\dot{B}$ is the time derivative of the magnetic field. Since one is normally interested in B rather than $\dot{B}$, an analog

integrating circuit is generally used to apply the (4.3).

$$\epsilon = -\frac{\partial \Psi(B)}{\partial t} \tag{4.1}$$

$$V = -NA\dot{B} \tag{4.2}$$

$$B(t) = -\frac{1}{NA}\int_{t_0}^{t} V(t)dt + B(t_0) \tag{4.3}$$

The Figure 4.3 shows on the left side a pick-up placed in $\mathbf{r}(r, z)$ where $\mathbf{r}$ is a vector in a cylindrical system of coordinates that individuate a point (r, z) and θ is the angle between the radial axis (r) of the machine and axes of the coil. The equation (4.3) can be written as the (4.4):

$$B(\mathbf{r}, t) = -\frac{1}{NA}\int_{t_0}^{t} V(t)dt + B(\mathbf{r}, t_0) \tag{4.4}$$

In DTT, a preliminary analysis [97] has established that redundant sets of around 40 biaxial pick-up coils poloidally distributed inside the vessel (see Figure 4.3), in six toroidal positions, can estimate the plasma current and its radial and vertical position reconstruction with less than 1 % and 1 cm error respectively. The same set is replicated by ex-vessel pick-up coils. The ratio of outer to inner equivalent area (NA) between external and internal pick-up coils should be about 3. In the section 4.1.2, Mirnov coils have been presented as bi-axial pick-up coils, indeed, in the Figure 4.3, the red arrows show the two axes of a pick-up placed in $\mathbf{r}$ which are in radial and tangential directions with respect to VV wall.

4.2.1 Pick-up coils in plasma control

The pick-up coils play an important role for the real time control, indeed the Table 4.3 shows how pick-up coils are involved in a feedback proportional–integral–derivative (PID) controller. The Figure 4.4 shows the eXtrema Shape Control (XSC) feedback control scheme integrated with the plasma current control and the vertical stabilization. The XSC is a MIMO (Multiple-Input, Multiple-Output) strategy control well tested on JET [107] and EAST [108] and it is proposed as reference control strategy for ITER [109]. As it can be seen from the Figure 4.4, the plasma current and shape descriptors (i.e. X_{point} position, gaps, etc) reconstructed by means of the pick-up coils measurements are used as the feedback in the control scheme. Plasma

current, density, equilibrium, MHD control, Neoclassical Tearing Modes (NTM), Resistive Wall Modes (RWM), ELMs frequency and amplitude and power exhaust control are some of the areas where feedback is to be applied.

TABLE 4.3: Real time control role of pick-up coils

Measurement	**Diagnostics**	**Actuators**	**Control Scheme**
Plasma current	Pick-up coils	Magnetic Flux	PID
Axissymmetric equilibrium	Pick-up coils, loops	PF coils	PID, Physics Model based
MHD, NTM, RWM	Pick-up coil,	Saddle coils	PID, Physic Model based

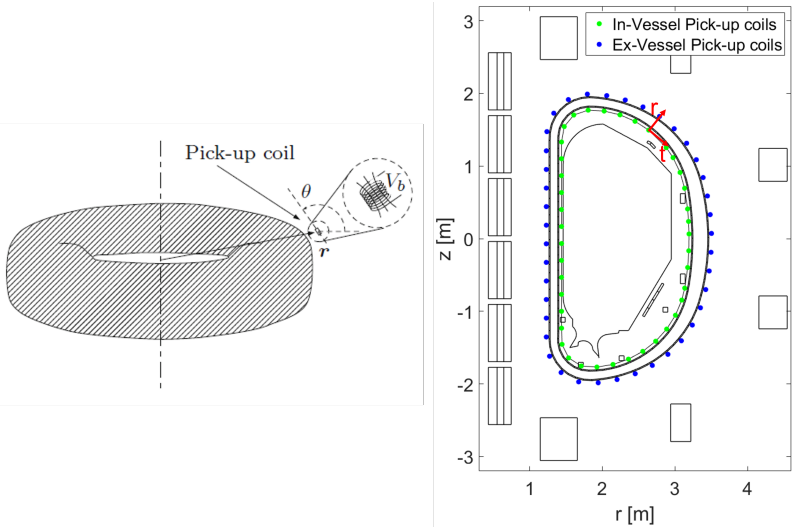

FIGURE 4.3: Right Side: schematic pick-up coil place in **r** near a torus. Left side: DTT poloidal cross section (black lines), In-Vessel pick-up Coils (green dots) and Ex-Vessel pick-up coil

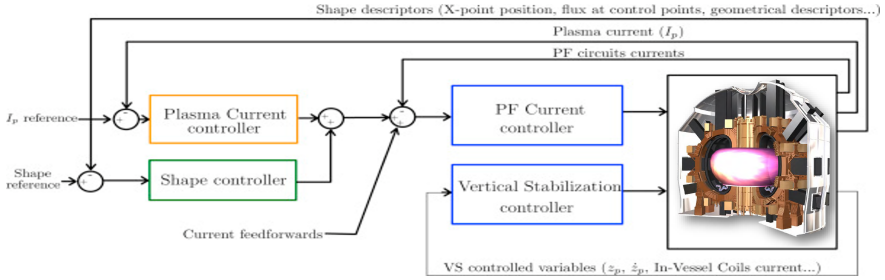

FIGURE 4.4: Scheme of the shape, current and VS control plasma scenarios in DTT [101]

4.3 Inverse plasma boundary reconstruction

The LCMS is widely accepted as the plasma boundary (PB) within the VV (see red line in Figure 4.5). Considering a plasma equilibrium approach, the PB should be determined by solving the Magneto-Hydro-Dynamic (MHD) equation, this implies solving a numerical computations problem not compatible with the limit of a real time response, also in axisymmetric geometry. Therefore, to overcome this limit different simplified purely electromagnetic approaches for reconstructing the PB have been proposed, such as the one fitting the magnetic measurements. In this thesis, a procedure allowing the PB reconstruction considering the poloidal magnetic field measurement from internal bi-axial pick-up coils has been adopted. The procedure aims to reconstruct the magnetic flux map on the poloidal plane assuming a filamentary representation of the plasma current density [110, 111]. Let be r and $\tilde{r}$ the vectors identify two specific points in the poloidal plane, by means (r, z) coordinates, the poloidal magnetic field and the poloidal magnetic flux $\mathbf{B}(\mathbf{r})$ and $\psi(\mathbf{r})$ respectively, are defined by equations (4.5) and (4.6)

$$\mathbf{B}(\mathbf{r}) = \int_{R^2} G_{0B}(\mathbf{r}, \tilde{\mathbf{r}}) \mathbf{J}_{\varphi}(\tilde{\mathbf{r}}) d\tilde{S} \tag{4.5}$$

$$\psi(\mathbf{r}) = \int_{R^2} G_{0\psi}(\mathbf{r}, \tilde{\mathbf{r}}) \mathbf{J}_{\varphi}(\tilde{\mathbf{r}}) d\tilde{S} \tag{4.6}$$

where G_{0B} and $G_{0\psi}$ are the Free-Space Green's Functions and $\mathbf{J}(\tilde{\mathbf{r}})_{\varphi}$ is the current density at the $(\tilde{r}, \tilde{z})$ point. In the equation (4.5) G_{0B} [T/A] represents the magnetic field in $\mathbf{r}$ due to a filament in $\tilde{\mathbf{r}}$ carrying a unitary current. Whereas in the equation (4.6), $G_{0\psi}$ [H] is the magnetic field flux in $\mathbf{r}$ due a filament in $\tilde{\mathbf{r}}$ carrying a unitary current. The procedure adopted in this thesis determines the poloidal magnetic flux map fitting the magnetic measurements by solving an inverse problem. In fact, the density current $\mathbf{J}(\tilde{\mathbf{r}})$, fitting the magnetic field $\mathbf{B}(\mathbf{r})$, is retrieved by equation (4.5) and then it is used in equation 4.6 for determining the magnetic flux map$\psi(\mathbf{r})$ in the poloidal section. To numerically solve both equations 4.5 and 4.6 the continuum models must be discretized. The Free-Space Green's Functions can be calculated as shown in [110], they depend on problem geometry, and they need solution of elliptic integral of the first and second. In this thesis a discrete algorithm for the inverse boundary reconstruction is proposed which allows the wished numerically solution of both 4.5 and 4.6 equation on a 2D domain with a Finite Element Method (FEM) analysis, by exploiting a tool for the Free-Space Green's

Functions evaluation provided by the CREATE group [110]. The Figure 4.5 reports the 2D domain under study, where the black lines draw the DTT poloidal section, the central solenoid and the outer poloidal field coils, while the light blue outlines the mesh grid. The green dots are the In-Vessel pick-up coils, the magenta squares, located on an ellipse (magenta line) inside the plasma region (red line), are the plasma current filaments. Let be n the number of the mesh nodes in the whole domain, n_{coil} the number of the active current filaments i_{coil}, located at the mesh element barycentre inside the poloidal field coil domains (black boxes in Figure 4.5), and n_{el} the number of fictitious current filaments i_{el} (magenta star), the integral equation (4.6) can be replaced by the linear equation system (4.7).

$$[\psi]^{n\times 1} = [G_{0\psi}]^{n\times(n_{coil}+n_{el})} \cdot [i]^{(n_{coil}+n_{el})\times 1} \tag{4.7}$$

Among the current filaments i_k, with $k = 1, ..., n_{coil} + n_{el}$, those from the active coils are provided as inputs, whereas both the values and the number of the fictitious plasma current filaments need to be evaluated by an optimization procedure. This implies that the linear equation system corresponding to the equation 4.5 is employed to determine the optimum fictitious set of filamentary currents ($i_{el,k}$), with $k = 1, ..., n_{el}$, fitting the poloidal magnetic field measures (B_{pol}) from In-Vessel pick-up coils.
The input available for retrieving the poloidal flux map by Inverse Reconstruction (IR) procedure are:

- The active currents from the inner (central solenoid) and outer poloidal field coils (black boxes in Figure 4.5) currents ($I_{coils,i}$) with $i = 1, ..., n_{coil}$.
- Poloidal magnetic field measures (B_{pol}) from n_{probes} In-Vessel pick-up coils placed inside the VV, for a total of $n_m = 2n_{probes}$ measures, half in radial direction ($\vec{\mathbf{r}}$) and half in tangential direction ($\vec{\mathbf{t}}$) with respect to the VV.
- Position and orientation of the In-Vessel pick-up coils (green dots in Figure 4.5).
- DTT geometry and mesh (black lines and light blue grid in Figure 4.5)

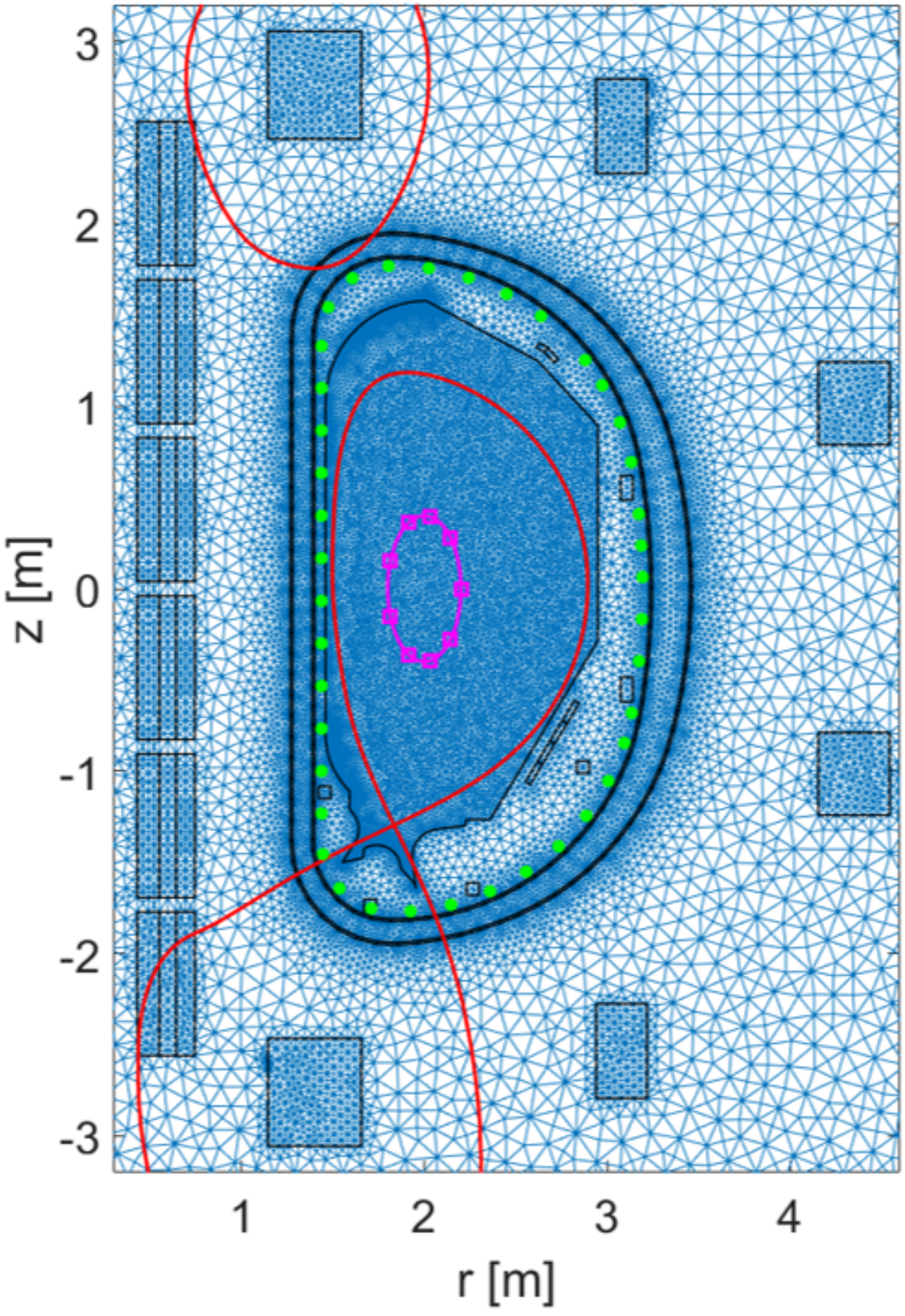

FIGURE 4.5: DTT poloidal section (black lines), In-Vessel pick-up coils (green dots), reconstructed plasma boundary (red line), i_{el} filaments (magenta squares) located on an ellipse (magenta line) inside the plasma region, DTT PDE tool mesh (light blue grid)

The procedure can be summarized in two main steps, the first consists in evaluating the contribute of the plasma current to the magnetic poloidal field $\mathbf{B}_{pol}$. Indeed, at each probes position, $\mathbf{B}_{pol}$ can be written as the sum of the poloidal magnetic field $\mathbf{B}_{coils}$ due to the coil currents $mathbfi_{coil}$ and the magnetic field B_{plasma} due to the plasma current, see equation (4.8).

$$\mathbf{B}_{pol} = \mathbf{B}_{plasma} + \mathbf{B}_{coils} \tag{4.8}$$

Since the poloidal field coils have a not negligible dimensions with respect to their distances from the probes, for each coil was considered a multitude of filaments, one for each mesh element barycenter inside the coil. This results in ncoils filaments. Thus, the n_m values of $\mathbf{B}coils$ (n_{probes} along radial and n_{probes} along tangential directions) evaluated at probe positions are calculated by solving the system of equations ((4.9))

$$[B_{coils}]^{n_m \times 1} = [G_{0B}]^{n_m \times n_{coils}} \cdot [i_{coils}]^{n_{coils} \times 1} \tag{4.9}$$

Once the n_m components of $\mathbf{B}_{coils}$ are evaluated, the n_m components of B_{plasma} are computed by means of the (4.10):

$$[B_{plasma}]^{n_m \times 1} = [B_{pol}]^{n_m \times 1} - [B_{coils}]^{n_m \times 1} \tag{4.10}$$

The second main step of the procedure is to compute a of fictitious currents $i_{el,k}$, with $k = 1, ..., n_{el}$, related to n_el filaments (magenta star) arranged on ellipse (magenta curve) located inside the plasma region, that fit the $\mathbf{B}_plasma$ got by equation (4.10). This is step is accomplished by inverting equation 4.11, see equation (4.12), which allow to evaluate the n_{el} filamentary currents i_el.

$$[B_{plasma}]^{n_m \times 1} = [G_{0B,el}]^{n_m \times n_{el}} \cdot [i_{el}]^{n_{el} \times 1} \tag{4.11}$$

$$[i_{el}]^{n_{el} \times 1} = \left(\text{pinv}\,[G_{0B,el}]^{n_m \times n_el}\right) \cdot [B_{plasma}]^{n_m \times 1} \tag{4.12}$$

The n_{el} number of filaments, in equation (4.12), is determined according to the pseudo-inverse operation tolerance (as it will be describe better in Section 4.3.4), it must be $n_{el} < n_m$. The

filamentary currents $[i_{el,k}]$ are fictitious because they have no physical meaning considered individually, even if their sum is the plasma current (Ip), see equation 4.13. The plasma current centroid position (r_0, z_0) is assumed as the weighted average of the filament positions using the filament currents as weight, see equation (4.14) and (4.15) for r and z coordinate respectively.

$$\mathbf{Ip} = \sum \mathbf{i}_{el} \tag{4.13}$$

$$r_0 = \sqrt{\frac{\sum i_{el} \cdot r_{el}^2}{Ip}} \tag{4.14}$$

$$z_0 = \frac{\sum i_{el} \cdot z_{el}}{Ip} \tag{4.15}$$

After step two, all the currents $[i_k]$ involved in the problem are known, thus the poloidal magnetic flux distribution is computed in all the mesh nodes (29589) throughout the system of equations (4.7). As an example, the isocurves in Figure 4.6(left-side), shaded lines from magenta to blue, are the final flux map output obtained applying the procedure described above, while in the Figure 4.6(right-side) the flux map obtained with the Non-Linear CREATE equilibrium reconstruction (CREATE-NL) is reported, starting from a referece DTT plasma scenario in SN

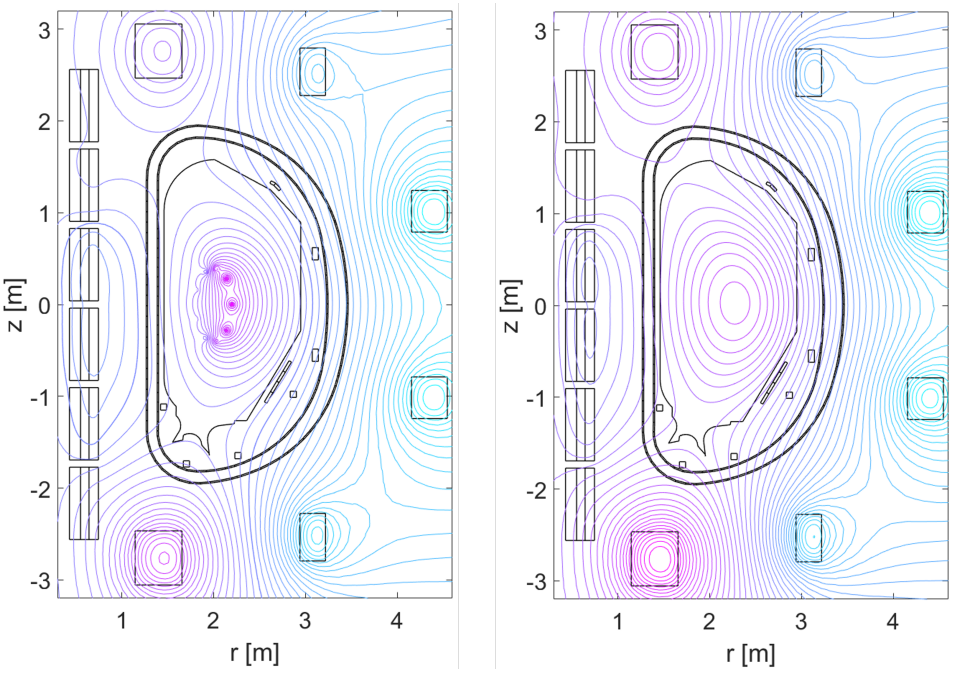

FIGURE 4.6: DTT flux map, computed with the inverse boundary reconstruction (left side) and with the CREATE-NL code

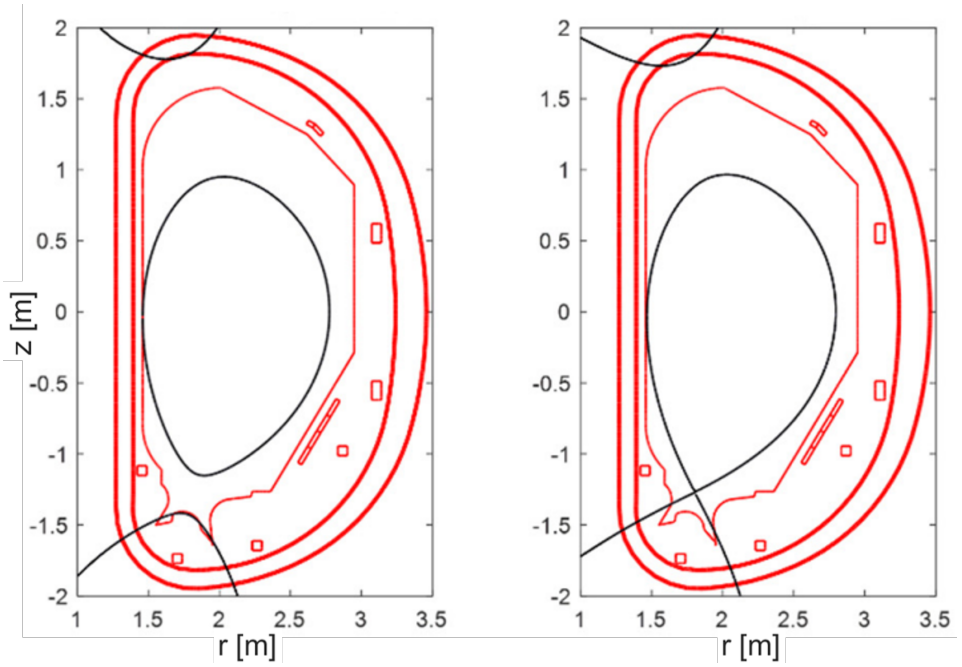

FIGURE 4.7: DTT plasma configurations: limiter plasma (left-side), diverted plasma (right-side)[112]

configuration. Note that, the flux map obtained with IR presents flux map aberrations in the region where the ellipse was located, this is due to the fact that the $[i_{el,k}]$ placed on the ellipse are fictitious and they have no physical meaning. However, aberration reported in Figure 4.6 afflict ψ value much larger than ψ such that ψ_{bound} isocurve will not be aberrated.

Finally, the plasma configuration, diverted o limiter, have to be determined to identify the PB as the LCMS. When the plasma is in a SN diverted configuration, it presents the X_{point} where the poloidal magnetic field is minimum. If the poloidal magnetic flux in this point (ψ_{X_p}) is greater than the maximum flux on the limiter (ψ_L, max), the plasma is in "diverted" configuration (as in Figure 4.7(right-side)), and the plasma boundary is assumed as the isocurve having the flux value ψ_{X_p}. Otherwise, the configuration is "limiter" (as in Figure 4.7(left-side)), and the plasma boundary is assumed as the isocurve having the flux $\psi_{L,max}$. Once the configuration is known and the plasma boundary flux value identified, the PB can be represented in the poloidal plane such as has been done in the Figure 4.8 where the IR (red line) and the CREATE-NL (blue line) have been drawn. In the next subsections the IR of the PB is presented for a given DTT magnetic reference configuration, described in 4.3.1. The section 4.3.2 presents the procedure used to determine the currents $\mathbf{i}_{coils}$ use to represent the active currents of the CS and PFC. The section 4.3.3 describes how the gaps between the PB and first wall are computed. Finally, since

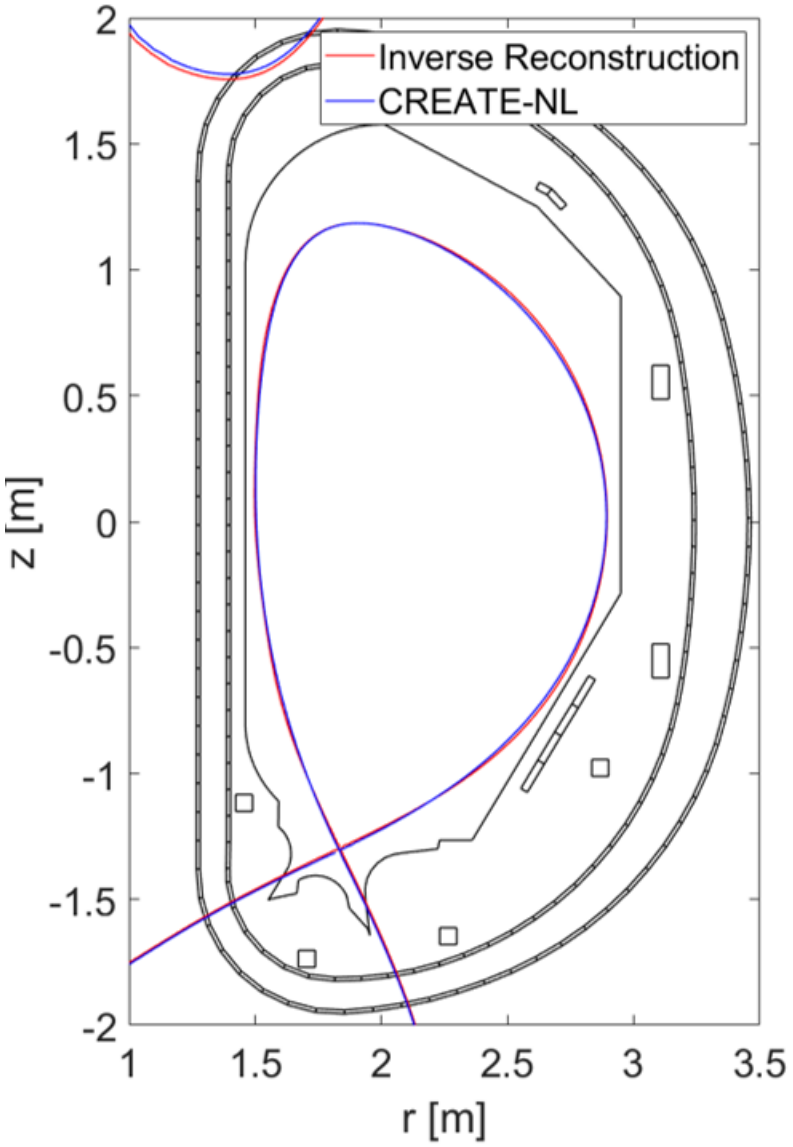

FIGURE 4.8: DTT plasma boundary. Inverse plasma boundary reconstruction (red line), CREATE-NL equilibrium reconstruction (blue line)

the both number of measurements ($n_m = 2n_{probes}$) and if fictious filaments strongly influence the pseudo inverse operation required to apply the (4.12), in the section 4.3.4 the optimization of the pseudo-inverse parameters will be here presented.

4.3.1 Magnetic reference configuration

The provided magnetic configuration [97] contains the input data for the inverse reconstruction algorithm:

- DTT geometry;
- 24 active currents ($\mathbf{I}_{turn}$) from poloidal field coils and central solenoid and their number of turns n_{turns};
- 80 poloidal magnetic field ($\mathbf{B}_{pol}$) measures from 40 pick-up coils (40 in radial direction and 40 in tangential direction);
- mount positions and orientations (with respect to the VV) of the 40 pick-up coils;
- mesh nodes: n = 29589.

4.3.2 Active coils filamentary current calculation

As previously said, the poloidal active coils sections are too much big, respect to the distance from to the probes, to make affordable the calculation of their poloidal magnetic field in the probe positions considering a coil as a single filament placed in the coil barycenter. To avoid this problem, a filament for each mesh element barycenter falling inside the coil was considered, then the current circulating in each filament must be computed. To do this the total current of the coil ($\mathbf{I}_{coil}$) is calculated as the current in the single turn ($\mathbf{I}_{turn}$) multiplied for the number of the turns (n_{turns}):

$$\mathbf{I}_{coil} = \mathbf{I}_{turn} \cdot n_{turns} \tag{4.16}$$

The current density in the coil ($\mathbf{J}_{coil}$) can now be calculated as $\mathbf{I}_{coil}/A_{coil}$ where A_{coil} is the coil poloidal section [m^2]. The sections (s_{coils}) and the barycenters of all the mesh element inside the coil are calculated and the filament current set of the coil can be known as:

$$\mathbf{i}_{coils} = \mathbf{J}_{coil} \cdot s_{coils} \tag{4.17}$$

This results in a vector of $n_{coils} = 5118$ currents placed in the mesh element barycenters of the coils.

4.3.3 Gaps evaluation

Once the plasma boundary flux is gained, the gaps must be determined as shape descriptors for the plasma shape and position feedback control. In this thesis, the gaps have been used to evaluate the IR errors in the presence of pick-up coils measurements afflicted by white noise. The gaps are the distances between the determined plasma boundary and the limiter (or the divertor) evaluated on several limiter point in orthogonal direction to the limiter itself. The strike points are the intersection between the plasma boundary and divertor in the region of the heat flux. To this aim a chord set needs to be defined. Each chord length is 1.5 m. The number and the position of chords are randomly chosen. Figure 4.9 reports the set of possible chords that has been chosen for the gap evaluation. As first attempt an iterative procedure was applied (provided by the CREATE), which allows the gap evaluation for chords having the outer points P_1 and P_2 on the limiter and inside the plasma respectively. The procedure implements the following steps:

1. For each chord the value of the poloidal fluxes ψ_1, ψ_2 and ψ_C, respectively on P_1 and P_2 and on the middle chord point P_c, are evaluated

2. Considering that the poloidal flux decreases going from the plasma center to the limiter, to determine the boundary position, the three fluxes values are compared and the definition of the points P_1, P_2 and P_C are updated by following the algorithm:

   - if $\text{sign}(\psi_2 - \psi_{bound}) = \text{sign}(\psi_c - \psi_{bound})$, meaning that P_2 and P_C are inside the boundary, P_C is assumed as the new P_2
   - else if $\text{sign}(\psi_1 - \psi_{bound}) = \text{sign}(\psi_c - \psi_{bound})$, meaning that P_1 and P_C are outside the boundary, P_C is assumed as the new P_1

3. The distance between P_1 and P_2 is evaluated, if it is lower than 0.01 mm, P_1 is assumed as belonging to the plasma boundary, otherwise the procedure is repeated from step 1 for the new point configuration.

This procedure does not allow the gap evaluation in the private flux region (divertor region wet by the plasma, see Figure 4.1), where the poloidal flux is greater than the one of the plasma boundary. Indeed, considering a chord length of 1.5 m both P_1 and P_2 fall inside the LCMS,

meaning that $\psi_1 > \psi_{bound}$ and $\psi_2 > \psi_{bound}$, then any condition of the step 2 can't be verified. To overcome this limit, in this thesis, the chord length in the private flux region is set equal to 0.2 m in order to intersect the plasma boundary just once (see Figure 4.9 in the private flux region).

In addition, the procedure fails also when both P_1 and P_2 fall outside the plasma region at the first iteration (the chord cross the whole plasma section). Indeed, in this case $\psi_1 < \psi_{bound}$

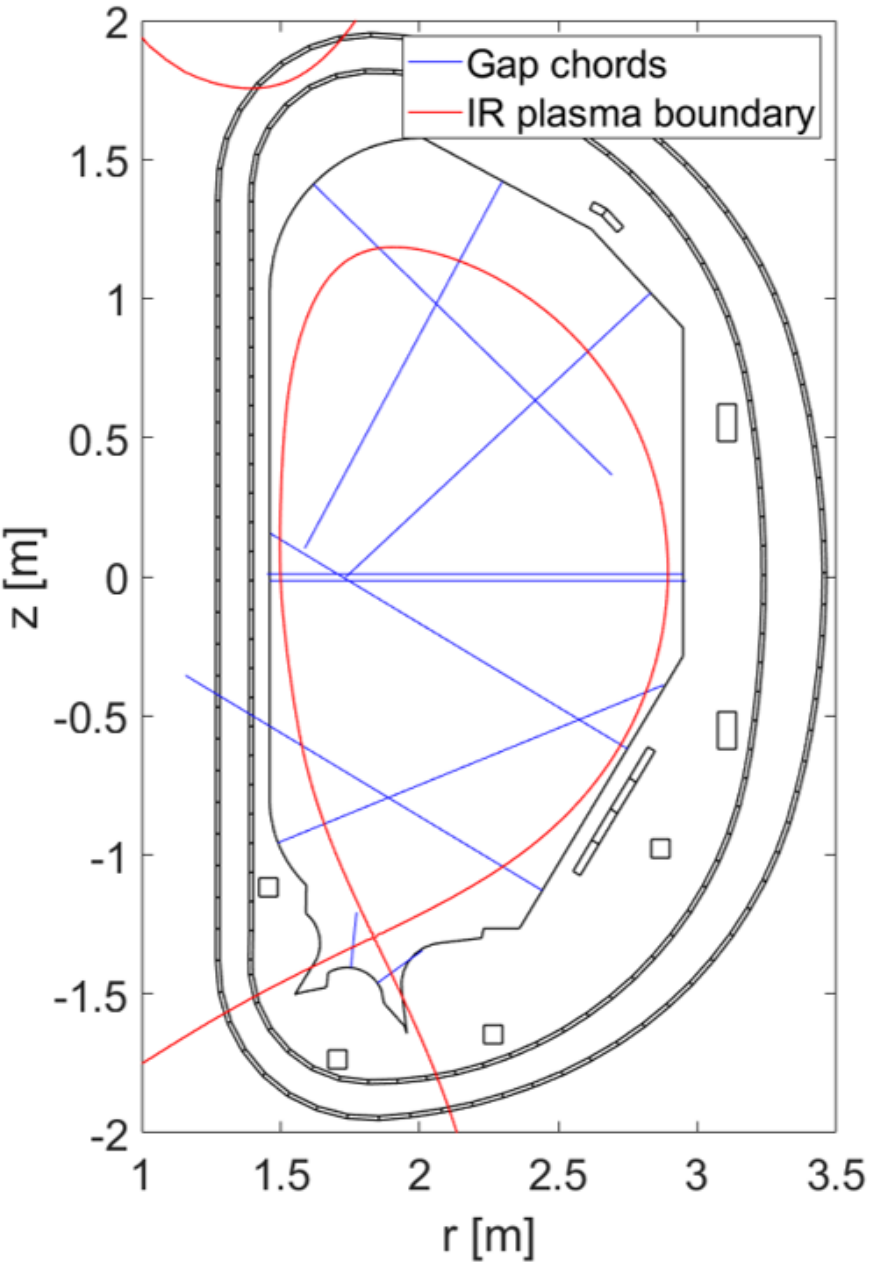

FIGURE 4.9: Set of chords considered for the gaps evaluation (blu lines)

(P_1 does not belong to the private flux region) and $\psi_2 < \psi_{bound}$ while $\psi_C > \psi_{bound}$, thus any condition of the step 2 is not verified and P_C can not be updated. Thus, in this thesis, the following condition has been added as third to the step 2:

- else if $\text{sign}(\psi_2 - \psi_{bound}) = \text{sign}(\psi_1 - \psi_{bound})$ P_C is assume as the new P_2

When the interactive procedure stops and for each chord the final point P_1 is given, the gaps are evaluated as the distance between P_1 and the limiter or the divertor. The additional knowledge of the gaps in the private flux region makes possible an approximated estimation of the strike point positions, which are defined as the points in which the plasma boundary intersects the divertor. In this thesis, they are assumed as the intersection points between the divertor and the line passing through the X_{point} and P_1 set on the 20 cm gaps chords.

4.3.4 Optimization of pseudo-inverse parameters

As described in section 4.3 the i_{el} fictitious currents are evaluated by equation (4.12) here reported:

$$|i_{el}|^{n_{el}\times 1} = (\text{pinv}|\text{G}_{0\text{B,el}}|)^{n_{el}\times n_m} \cdot |B_{plasma}|^{n_{el}\times 1}$$

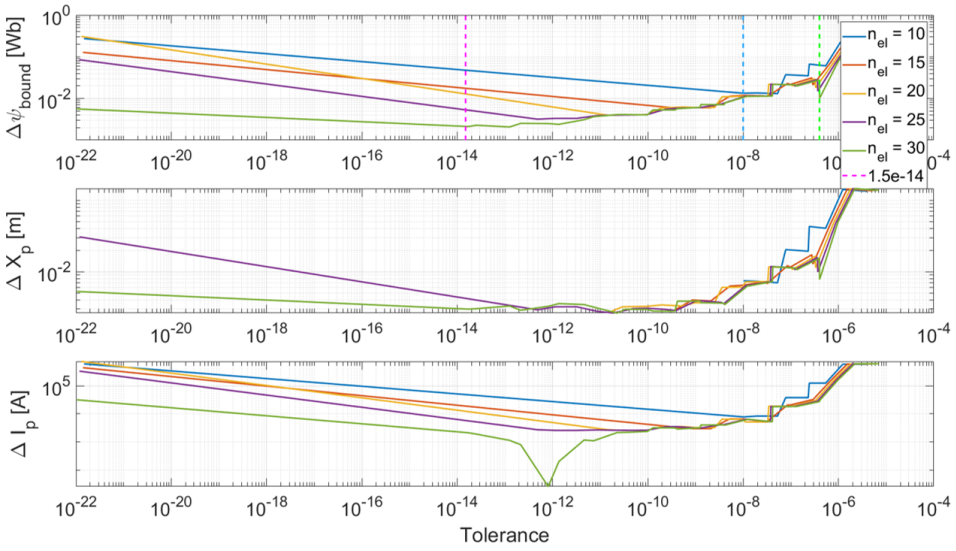

FIGURE 4.10: The trend of the difference of the plasma boundary flux values (upper subplot), distance between X_{point}s (middle subplot) and difference of the plasma currents (bottom subplot), between the inverse reconstruction and the direct reconstruction, for n_{el} in range 10×30, at varying tolerance.

where B_{plasma} is obtained by the (4.10) and $G_{0B,el}$ is a no-square matrix of the Free-Space Green's Functions. The function pinv indicates the pseudo inverse operation carried out through the Singolar Value Decomposition (SVD) technique [113]. In the pseudo-inverse operation, a tolerance, which defines the lowest singular value to be considered in the truncated SVD, needed to be defined. In addition to the tolerance value, the performance of pseudo-inversion also depends on the number of fictitious current filaments n_{el}, which must be much lower than n_m. In fact, the higher the number n_{el}, the more the problem is ill-posed, and the larger must be the tolerance to avoid flux map aberration. Thus, a good compromise between the tolerance and n_{el} values needs to be found to guarantee a reliable and correct boundary reconstruction. To this purpose, an optimization procedure has been developed that minimizes the difference between the inverse reconstruction and the direct one performed by the equilibrium solver CREATE-NL in terms of the plasma boundary flux values. The number n_{el} has been varied in the range $10 \div 30$ (with a step resolution equal to 5) and, for each n_{el} value, the size of the singular value vector is optimized in the range $1 \div n_{el}$ (with a step resolution equal to 1) by changing the tolerance of the pseudo inverse operation. Figure 4.10 shows the errors of the inverse reconstruction with respect to the direct one, assumed as the reference one, in terms of difference of the plasma boundary flux values ($\Delta\psi_{bound}$ - upper subplot), distance between X_{points} (ΔX_P - middle subplot) and difference of the plasma currents (ΔIp - bottom subplot), in the n_{el} range $10 \div 30$. For n_{el}=30, the magenta vertical line highlights the tolerance that minimizes $\Delta\psi_bound$, instead the green line indicates the tolerance required to avoid flux map aberration. The light blue vertical line corresponds to the tolerance that minimizes $\Delta\psi_bound$ without any flux map aberrations for $n_{el} = 10$.

Figure 4.11 shows, on the left plot, the reconstructed boundary with $n_{el} = 30$ and a tolerance value corresponding to the magenta vertical line in Figure 4.10. This unsuitable combination of n_{el} and tolerance values leads to flux map aberration in the plasma center region, even if the PBs got by direct and inverse reconstruction procedures are fully overlapped, blue and magenta line respectively. In the middle plot of the same Figure 4.11, the reconstructed boundary with $n_{el} = 30$ and a tolerance value corresponding to the green line in Figure 4.10 is reported. In this case, using a higher tolerance, the flux map aberration is avoided, but $\Delta\psi_bound$ increases, and the reconstructed boundary (green line) does not overlap the reference one (red line). Finally, the right plot reports the boundary reconstruction for the optimum tolerance value (light blue

vertical line in Fig 4.10) with $n_{el} = 10$. By reducing both n_{el} and the tolerance the numerical error is slightly reduced still avoiding the flux map aberration. The reconstructed boundary (light blue line) overlaps the reference one (black line). This reconstructed boundary is used for the white noise characterization of the pick-up coil measurements, described in the subsection 4.4.

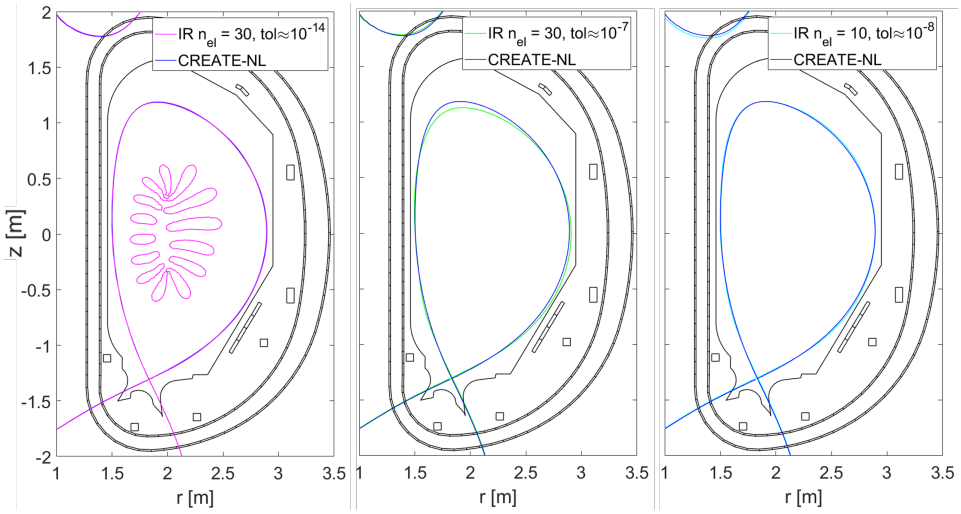

FIGURE 4.11: Inverse boundary reconstruction for different combinations of n_{el} and tolerance values. Left plot: a flux map aberration in the plasma centre is obtained with $n_{el} = 30$ and a tolerance value of about 10^{-14} (magenta vertical line in Fig 4.10). Middle plot: the flux map aberration is avoided with a tolerance value of about 10^{-7} (green line Fig 4.10). Right plot: optimum flux map reconstruction achieved with $n_{el} = 10$ and a tolerance value of about 10^{-8} (light blue vertical line in Figure 4.10).

4.4 White noise analysis

The aim of the study faced in this section is to characterize the systematic error on the poloidal field measurements, conducted by bi-axial In-Vessel pick-up coils, due to white noise. The presence of white noise on the probes outputs has been simulated adding a small random contribute to B_{pol} [14]. A parametric study, increasing values of probe noise variance (σ^2_{WN}), i.e., 2 mT, 4 mT and 8 mT, has been performed. For each variance value, the inverse reconstruction, optimized as described in section 4.3.4, was repeated a thousand times to better simulate the noise random effect on the inverse reconstruction. The noise effect is characterized evaluating the mean error (ME), the mean square error (MSE) and the variance (σ^2_{GAP}) on the gap difference between the noisy optimized inverse reconstruction and the ideal one (optimized in section 4.3.4). These gaps are evaluated on the most meaningful chords, reported in Figure 4.9. The ME, MSE andσ^2_{GAP} values, for the different noise variance, are reported in Table 4.4. Moreover, Table 2 reports, on columns two and three, the maximum and the mean values of the percentage error on the plasma current value, respectively, normalized with to the plasma current of the ideal IR evaluated by equation ((4.13)). Whereas, the mean errors between the plasma barycenter position (r_0,z_0) of the noisy IR and the ideal one, evaluated by equations (4.14) and (4.15) are reported in column four and five, respectively.

TABLE 4.4: Gap errors: ME, MSE and σ^2_{GAP} of noisy inverse reconstruction (reported as mean values) with respect to the ideal one

σ^2_{WN} [mT]	**ME** [mm]	**MSE** [mm]	σ^2_{GAP} [mm]
2	$-6 \cdot 10^{-1}$	$1.3 \cdot 10^{-3}$	$7.5 \cdot 10^{-4}$
4	-7	$5.8 \cdot 10^{-3}$	$3 \cdot 10^{-3}$
8	-7	$2.4 \cdot 10^{-2}$	$1 \cdot 10^{-2}$

TABLE 4.5: Maximum and minimum percentual error on plasma current value and mean error of the plasma current barycenter position (r and z coordinates) of noisy IR with respect to the ideal one

σ^2_{WN} [mT]	$\%Ip_{err,max}$	$\%Ip_{err,mean}$	$\Delta r_{0,mean}$ [mm]	$\Delta z_{0,mean}0$ [mm]
2	0.147	0.027	0.4	0.35
4	0.244	0.055	0.8	0.7
8	0.56	0.108	1.6	1.5

These results show that errors on the gaps evaluation due to the white noise effect is quite negligible since, for the noise variance values considered, the ME, MSE and σ^2_{GAP} results to be in order of magnitude of a few millimeters or lower. Instead, the $\%Ip_{err,max}$ (> 0.1 %) appears to be not negligible for all the considered conditions.

Chapter 5

Conclusions

EU-DEMO, ITER and future tokamak devices will face much more challenging conditions with respect to present day devices. The operating scenarios foreseen for future tokamaks require to control with enough precision and reliability highly unstable and strongly shaped plasmas. Nevertheless, accessible operative conditions of tokamaks are highly restricted by disruptive events. The disruption are a greater concern for the overall EU-DEMO integrity, this thesis has the aim to support the EU-DEMO R&D activities by developing several algorithms serving both the kinetic and electromagnetic control of the plasma as disruption avoidance strategies.
In the first chapter of this thesis an inter-machine database of EU-DEMOrelevant pulses has been presented. Dedicated algorithms have been developed to collect discharges affected by the considered plasma perturbations and to support the database construction. The settled database is divided in three main parts:

1. Plasma Perturbations from JET and AUG. The plasma vertical stability is one of the most challenging aspects in the EU-DEMO design, in this context an inter-machine database of EU-DEMOrelevant plasma perturbations has been built. The database allows to develop analysis about the implication of the plasma perturbations followed by VDEs on the plasma vertical stability from physical and engineering standpoints. A physical characterization of the vertical stability during ELMs and L-H/H-L transitions reveals the correlation of the plasma centroid vertical displacement with respect to the li and β_pol variations in a good agreement with previous studies. In the framework of the EU-DEMO limiter design,

predictive analyses to foreseen the plasma position and the EM loads, during the evolution of VDE recede by plasma perturbations, has been developed, starting from experimental behaviours, and properly scaled to EU-DEMO.

2. Disrupted experiment due to tungsten accumulation in the core. The tungsten alloys will be the primary materials for the plasma-facing surface in EU-DEMO [114]. Experiments in AUG [28] and JET [29] have been conducted to study the effect of W accumulation in the core on the plasma performance and to quantify the mechanisms that determine the W concentration in the plasma. Thus, a dataset of JET and AUG experiments in EU-DEMOrelevant conditions and presenting W accumulation in the plasma core has been collected.

3. Flux pumping possible candidate at JET. The flux pumping mechanism has shown very interesting properties in terms of plasma stabilization during AUG dedicated experiments, while no evidence has been gained up to now at JET. The FP mechanism has been observed in hybrid scenario which is a robust and high performance scenario, candidate for ITER and EU-DEMO scenarios. A dataset of JET Hybryd Scenario, both in ILW and CW has been analyzed to select those pulses presenting the flux pumping features. Those having good flux pumping characteristics are candidates for the TRANSP simulations needed to prove the presence of the flux pumping. The simulations conducted until now are unable to provide such confirmation due to poor quality of the EFIT equilibrium used both as in input for the reconstruction and as q_0 experimental evaluation. EFTF and EFTM equilibrium reconstruction will be employed in the next step on this time-consuming analysis.

The H-mode is the foreseen operational regime for EU-DEMO since it is desired to run future experiments at highest plasma densities at possible to increase their performance. However, when approaching the density limit a MARFE evolution can occur which can finally lead to a disruption. Indeed, a major aspect of this work involved the application of a new methodology based on machine learning techniques to address the automatic tracking of the MARFE evolution in real-time for disruption avoidance, in the framework of the kinetic control of the plasma. To better understand the MARFE evolution, four MARFE Evolution Times (METs) has been introduced: MARFE formation (t_{MF}), high MARFE time (t_{MH}), low MARFE time (t_{ML}), and MARFE stabilization time (t_{MS}). A database of 110 pulses containing both HDL

scenarios, enriched with manually selected METs, and scenarios devoid of MARFE, has been used to train and test the Isometric Mapping algorithm to provides automatic alarms of the METs. The developed procedure presents good performance in the real-time detection of all the METs. The most relevant for disruptions avoidance strategies, t_{MF} and t_{MH}, are detected with an anticipation lower than 120 ms for the 45% of the detectable event, while later detection present a maximum error lower than 9 ms. While false detections from NO HDL pulses belongs to the ones characterized by high number modes, which are observed during the MARFE evolution before the disruption. This study, developed by using AUG data, is the first step in view of an cross-machine algorithm, involving JET and WEST data, to be extended for the MARFE detection in ITER and EU-DEMO for which a manifold learning algorithm training is not feasible.

The feedback control of the plasma shape and position plays a key role in the plasma vertical stability fr any machine. The plasma shape and position is known by computing an inverse reconstruction of the plasma boundary. In this thesis, in the context of supporting the electromagnetic control of the plasma as disruption avoidance strategy, an algorithm for the inverse boundary reconstruction has been developed and optimized to characterize the white noise effect of in-vessel pick-up coils on the inverse boundary reconstruction. The work has been conducted considering DTT as reference machine. The noise effect has been evaluated in terms of mean error, mean square error and variance on the gap difference between the noisy optimized inverse reconstruction and the ideal one. The results show that errors on the gaps evaluation due to the white noise effect is quite negligible since, for the noise variance values considered, the ME, MSE and σ^2_{GAP} results to be in order of magnitude of a few millimeters or lower. Instead, the $\%Ip_{err,max} > 0.1\%$ appears to be not negligible for all the considered conditions.

Bibliography

[1] S Vaclav. *Energy Transitions - Global and National Perspectives*. Praeger, Dec. 2016.

[2] C. Meure et al. "Law dome CO2, CH4 and N2O ice core records extended to 2000 years BP". In: *Geophysical Research Letters - GEOPHYS RES LETT* 331 (July 2006). DOI: 10.1029/2006GL026152.

[3] P.A. Arias et al. "Technical Summary". In: (2021). Ed. by V. Masson-Delmotte et al., 33144. DOI: 10.1017/9781009157896.002.

[4] John Sheffield. "The physics of magnetic fusion reactors". In: *Rev. Mod. Phys.* 66 (3 July 1994), pp. 1015–1103. DOI: 10.1103/RevModPhys.66.1015. URL: https://link.aps.org/doi/10.1103/RevModPhys.66.1015.

[5] EUROfusion. *Fusion Electricity - A roadmap to the realisation of fusion energy*. Nov. 2012.

[6] EUROfusion. "European Research Roadmap to the Realisation of Fusion Energy". In: (Nov. 2018). URL: https://euro-fusion.org/wp-content/uploads/2022/10/2018_Research_roadmap_long_version_01.pdf.

[7] G. Pautasso et al. "On-line prediction and mitigation of disruptions in ASDEX Upgrade". In: *Nuclear Fusion* 42.1 (Jan. 2002), p. 100. DOI: 10.1088/0029-5515/42/1/314. URL: https://dx.doi.org/10.1088/0029-5515/42/1/314.

[8] F Wagner. "A quarter-century of H-mode studies". In: *Plasma Physics and Controlled Fusion* 49.12B (Nov. 2007), B1. DOI: 10.1088/0741-3335/49/12B/S01. URL: https://dx.doi.org/10.1088/0741-3335/49/12B/S01.

[9] G. Sias et al. "Inter-machine plasma perturbation studies in EU-DEMO-relevant scenarios: lessons learnt for prediction of EM forces during VDEs". In: *Nuclear Fusion* 62.7 (May 2022), p. 076004. DOI: 10.1088/1741-4326/ac544b. URL: https://dx.doi.org/10.1088/1741-4326/ac544b.

[10] Alessandro Pau. "Latest Developments in Data Analysis Tools for Disruption Prediction and for the Exploration of Multimachine Operational Spaces". In: *Proc. of 24th Fusion Energy Conference* (Oct. 2012).

[11] P C de Vries et al. "The impact of the ITER-like wall at JET on disruptions". In: *Plasma Physics and Controlled Fusion* 54.12 (Nov. 2012), p. 124032. DOI: 10.1088/0741-3335/54/12/124032. URL: https://dx.doi.org/10.1088/0741-3335/54/12/124032.

[12] M. Lacquaniti et al. "Machine learning approach for operational phases identification in H-mode Density Limit disruptions". In: *47th EPS Conference on Plasma Physics*. 2021.

[13] M. Lacquaniti et al. "Identification of H-mode Density Limit key events by ISOMAP at AUG". In: *32nd Symposium on Fusion Technology*. 2021.

[14] M. Lacquaniti et al. "White noise characterization and thermo-mechanical analysis of DTT pick-up coils". In: *Fusion Engineering and Design* 192 (2023), p. 113775. ISSN: 0920-3796. DOI: https://doi.org/10.1016/j.fusengdes.2023.113775. URL: https://www.sciencedirect.com/science/article/pii/S0920379623003575.

[15] Francesco Romanelli et al. *Fusion Electricity: A roadmap to the realization of fusion energy*. Efda, 2012.

[16] Ivan Alessio Maione et al. "Electromagnetic analysis activities in support of the Breeding Blanket during the DEMO Pre-Conceptual Design Phase: Methodology and main results". In: *Fusion Engineering and Design* 166 (2021), p. 112285. ISSN: 0920-3796. DOI: https://doi.org/10.1016/j.fusengdes.2021.112285. URL: https://www.sciencedirect.com/science/article/pii/S0920379621000612.

[17] G. Federici et al. "European DEMO design strategy and consequences for materials". In: *Nuclear Fusion* 57.9 (June 2017), p. 092002. DOI: 10.1088/1741-4326/57/9/092002. URL: https://dx.doi.org/10.1088/1741-4326/57/9/092002.

[18] MA Abdou et al. "Requirements and design envelope for a volumetric neutron source (VNS) fusion facility for fusion nuclear technology development". In: *Proceedings of the 15th IAEA Conf. on Plasma Phys. and Contr. Nucl. Fusion Res., Seville, Spain*. Vol. 26. Citeseer. 2025.

[19] R. Albanese et al. "Overview of modelling activities for Plasma Control Upgrade in JET". In: *Fusion Engineering and Design* 86.6 (2011). Proceedings of the 26th Symposium of Fusion Technology (SOFT-26), pp. 1030–1033. ISSN: 0920-3796. DOI: https://doi.org/10.1016/j.fusengdes.2011.01.146. URL: https://www.sciencedirect.com/science/article/pii/S092037961100158X.

[20] ITER Physics Expert Group on Confinement et al. "Chapter 2: Plasma confinement and transport". In: *Nuclear Fusion* 39.12 (Dec. 1999), p. 2175. DOI: 10.1088/0029-5515/39/12/302. URL: https://dx.doi.org/10.1088/0029-5515/39/12/302.

[21] "Disruptions". In: (2014), pp. 159–174. DOI: https://doi.org/10.1002/9783527677375.ch10. eprint: https://onlinelibrary.wiley.com/doi/pdf/10.1002/9783527677375.ch10. URL: https://onlinelibrary.wiley.com/doi/abs/10.1002/9783527677375.ch10.

[22] D.A. Humphreys et al. "Experimental vertical stability studies for ITER performance and design guidance". In: *Nuclear Fusion* 49.11 (Sept. 2009), p. 115003. DOI: 10.1088/0029-5515/49/11/115003. URL: https://dx.doi.org/10.1088/0029-5515/49/11/115003.

[23] Francesco Maviglia et al. "Impact of plasma thermal transients on the design of the EU DEMO first wall protection". In: *Fusion Engineering and Design* 158 (2020), p. 111713. ISSN: 0920-3796. DOI: https://doi.org/10.1016/j.fusengdes.2020.111713. URL: https://www.sciencedirect.com/science/article/pii/S0920379620302611.

[24] Raffaele Albanese et al. "Electromagnetic analyses of single and double null configurations in DEMO device". In: *Fusion Engineering and Design* 146 (2019). SI:SOFT-30, pp. 1468–1472. ISSN: 0920-3796. DOI: https://doi.org/10.1016/j.fusengdes.2019.02.107. URL: https://www.sciencedirect.com/science/article/pii/S0920379619302893.

[25] R. Albanese, R. Ambrosino, and M. Mattei. "CREATE-NL+: A robust control-oriented free boundary dynamic plasma equilibrium solver". In: *Fusion Engineering and Design* 96-97 (2015). Proceedings of the 28th Symposium On Fusion Technology (SOFT-28), pp. 664–667. ISSN: 0920-3796. DOI: https://doi.org/10.1016/j.fusengdes.2015.06.162. URL: https://www.sciencedirect.com/science/article/pii/S0920379615302167.

[26] F Villone et al. "Coupling of nonlinear axisymmetric plasma evolution with three-dimensional volumetric conductors". In: *Plasma Physics and Controlled Fusion* 55.9 (July 2013), p. 095008. DOI: 10.1088/0741-3335/55/9/095008. URL: https://dx.doi.org/10.1088/0741-3335/55/9/095008.

[27] V. Philipps. "Tungsten as material for plasma-facing components in fusion devices". In: *Journal of Nuclear Materials* 415.1, Supplement (2011). Proceedings of the 19th International Conference on Plasma-Surface Interactions in Controlled Fusion, S2–S9. ISSN: 0022-3115. DOI: https://doi.org/10.1016/j.jnucmat.2011.01.110. URL: https://www.sciencedirect.com/science/article/pii/S0022311511001589.

[28] K. Krieger et al. "Experiments on transient melting of tungsten by ELMs in ASDEX Upgrade". In: *Nuclear Fusion* 58.2 (Jan. 2018), p. 026024. DOI: 10.1088/1741-4326/aa9a05. URL: https://dx.doi.org/10.1088/1741-4326/aa9a05.

[29] F. Romanelli and JET EFDA Contributors. "Overview of the JET results with the ITER-like wall". In: *Nuclear Fusion* 53.10 (Sept. 2013), p. 104002. DOI: 10.1088/0029-5515/53/10/104002. URL: https://dx.doi.org/10.1088/0029-5515/53/10/104002.

[30] S. Di Genova et al. "Modelling of tungsten contamination and screening in WEST plasma discharges". In: 61.10 (Sept. 2021), p. 106019. DOI: 10.1088/1741-4326/ac2026. URL: https://dx.doi.org/10.1088/1741-4326/ac2026.

[31] L.-G. Eriksson et al. "Destabilization of Fast-Ion-Induced Long Sawteeth by Localized Current Drive in the JET Tokamak". In: *Phys. Rev. Lett.* 92 (23 June 2004), p. 235004. DOI: 10.1103/PhysRevLett.92.235004. URL: https://link.aps.org/doi/10.1103/PhysRevLett.92.235004.

[32] Valentin Igochine et al. "Conversion of the dominantly ideal perturbations into a tearing mode after a sawtooth crash". In: *Physics of Plasmas* 21 (Nov. 2014), p. 110702. DOI: 10.1063/1.4902106.

[33] H. Meyer et al. "Overview of physics studies on ASDEX Upgrade". In: *Nuclear Fusion* 59.11 (July 2019), p. 112014. DOI: 10.1088/1741-4326/ab18b8. URL: https://dx.doi.org/10.1088/1741-4326/ab18b8.

[34] C. C. Petty et al. "Magnetic-Flux Pumping in High-Performance, Stationary Plasmas with Tearing Modes". In: *Phys. Rev. Lett.* 102 (4 Jan. 2009), p. 045005. DOI: 10.1103/PhysRevLett.102.045005. URL: https://link.aps.org/doi/10.1103/PhysRevLett.102.045005.

[35] J. Stober et al. "The role of the current profile in the improved H-mode scenario in ASDEX Upgrade". In: *Nuclear Fusion* 47.8 (July 2007), p. 728. DOI: 10.1088/0029-5515/47/8/002. URL: https://dx.doi.org/10.1088/0029-5515/47/8/002.

[36] A. Burckhart et al. "Experimental evidence of magnetic flux pumping in ASDEX upgrade". In: *Nuclear Fusion* 63.12 (Nov. 2023), p. 126056. DOI: 10.1088/1741-4326/ad067b. URL: https://dx.doi.org/10.1088/1741-4326/ad067b.

[37] C.F. Maggi et al. "L–H power threshold studies in JET with Be/W and C wall". In: *Nuclear Fusion* 54.2 (Jan. 2014), p. 023007. DOI: 10.1088/0029-5515/54/2/023007. URL: https://dx.doi.org/10.1088/0029-5515/54/2/023007.

[38] S Saarelma et al. "Integrated modelling of H-mode pedestal and confinement in JET-ILW". In: *Plasma Physics and Controlled Fusion* 60.1 (Nov. 2017), p. 014042. DOI: 10.1088/1361-6587/aa8d45. URL: https://dx.doi.org/10.1088/1361-6587/aa8d45.

[39] Delabie E. et al. "Overview and interpretation of L-H threshold experiments on JET with the ITER-like Wall". English. In: *25th IAEA Fusion Energy Conference*. Austria: International Atomic Energy Agency IAEA, 2014, EX/P5–24. URL: http://www-naweb.iaea.org/napc/physics/FEC/FEC2014/fec_sourcebook_online.pdf.

[40] G. Saibene et al. "Characterization of small ELM experiments in highly shaped single null and quasi-double-null plasmas in JET". In: *Nuclear Fusion* 45 (Apr. 2005), p. 297. DOI: 10.1088/0029-5515/45/5/001.

[41] A. Pau et al. "A tool to support the construction of reliable disruption databases". In: *Fusion Engineering and Design* 125 (2017), pp. 139–153. ISSN: 0920-3796. DOI: https://doi.org/10.1016/j.fusengdes.2017.10.003. URL: https://www.sciencedirect.com/science/article/pii/S0920379617308207.

[42] H Zohm. "Edge localized modes (ELMs)". In: *Plasma Physics and Controlled Fusion* 38.2 (Feb. 1996), p. 105. DOI: 10.1088/0741-3335/38/2/001. URL: https://dx.doi.org/10.1088/0741-3335/38/2/001.

[43] X. Litaudon et al. "Progress towards steady-state operation and real-time control of internal transport barriers in JET". In: *Nuclear Fusion* 43 (June 2003), p. 565. DOI: 10.1088/0029-5515/43/7/309.

[44] E. Fable et al. "The role of the source versus the collisionality in predicting a reactor density profile as observed on ASDEX Upgrade discharges". In: *Nuclear Fusion* 59.7 (June 2019), p. 076042. DOI: 10.1088/1741-4326/ab1f28. URL: https://dx.doi.org/10.1088/1741-4326/ab1f28.

[45] Raffaele Albanese et al. "Plasma Current, Shape, and Position Control in ITER". In: *Fusion Technology* 30.2 (1996), pp. 167–183. DOI: 10.13182/FST96-A30749.

[46] C. Bachmann et al. "Initial definition of structural load conditions in DEMO". In: *Fusion Engineering and Design* 124 (2017). Proceedings of the 29th Symposium on Fusion Technology (SOFT-29) Prague, Czech Republic, September 5-9, 2016, pp. 633–637. ISSN: 0920-3796. DOI: https://doi.org/10.1016/j.fusengdes.2017.02.061. URL: https://www.sciencedirect.com/science/article/pii/S0920379617301540.

[47] Thomas Franke et al. "The EU DEMO equatorial outboard limiter — Design and port integration concept". In: *Fusion Engineering and Design* 158 (2020), p. 111647. ISSN: 0920-3796. DOI: https://doi.org/10.1016/j.fusengdes.2020.111647. URL: https://www.sciencedirect.com/science/article/pii/S0920379620301952.

[48] T Pütterich et al. "Modelling of measured tungsten spectra from ASDEXUpgrade and predictions for ITER". In: *Plasma Physics and Controlled Fusion* 50.8 (June 2008), p. 085016. DOI: 10.1088/0741-3335/50/8/085016. URL: https://dx.doi.org/10.1088/0741-3335/50/8/085016.

[49] J. Wesson and D.J. Campbell. *Tokamaks*. International Series of Monographs on Physics. OUP Oxford, 2011. ISBN: 9780199592234. URL: https://books.google.it/books?id=XJssMXjHUr0C.

[50] Francesca Turco et al. "The high-N hybrid scenario for ITER and FNSF steady-state missions". In: *Physics of Plasmas* 22 (May 2015), p. 056113. DOI: 10.1063/1.4921161.

[51] P. Piovesan et al. "Role of a continuous MHD dynamo in the formation of 3D equilibria in fusion plasmas". In: *Nuclear Fusion* 57.7 (May 2017), p. 076014. DOI: 10.1088/1741-4326/aa700b. URL: https://dx.doi.org/10.1088/1741-4326/aa700b.

[52] O. P. Ford et al. "Imaging motional Stark effect measurements at ASDEX Upgrade". In: *Review of Scientific Instruments* 87.11 (Aug. 2016), 11E537. ISSN: 0034-6748. DOI: 10.1063/1.4959873. eprint: https://pubs.aip.org/aip/rsi/article-pdf/doi/10.1063/1.4959873/15616174/11e537_1_online.pdf. URL: https://doi.org/10.1063/1.4959873.

[53] J Stober et al. "Exploring fusion-reactor physics with high-power electron cyclotron resonance heating on ASDEX Upgrade". In: *Plasma Physics and Controlled Fusion* 62.2 (Jan. 2020), p. 024012. DOI: 10.1088/1361-6587/ab512b. URL: https://dx.doi.org/10.1088/1361-6587/ab512b.

[54] I. Krebs et al. "Magnetic flux pumping in 3D nonlinear magnetohydrodynamic simulations". In: *Physics of Plasmas* 24.10 (Sept. 2017), p. 102511. ISSN: 1070-664X. DOI: 10.1063/1.4990704. eprint: https://pubs.aip.org/aip/pop/article-pdf/doi/10.1063/1.4990704/14895452/102511_1_online.pdf. URL: https://doi.org/10.1063/1.4990704.

[55] E. Joffrin et al. "The 'hybrid' scenario in JET: towards its validation for ITER". In: *Nuclear Fusion* 45.7 (June 2005), p. 626. DOI: 10.1088/0029-5515/45/7/010. URL: https://dx.doi.org/10.1088/0029-5515/45/7/010.

[56] B. Cannas et al. "Automatic disruption classification based on manifold learning for real-time applications on JET". In: *Nuclear Fusion* 53.9 (Aug. 2013), p. 093023. DOI: 10.1088/0029-5515/53/9/093023. URL: https://dx.doi.org/10.1088/0029-5515/53/9/093023.

[57] B Cannas et al. "Automatic disruption classification in JET with the ITER-like wall". In: *Plasma Physics and Controlled Fusion* 57.12 (Oct. 2015), p. 125003. DOI: 10.1088/0741-3335/57/12/125003. URL: https://dx.doi.org/10.1088/0741-3335/57/12/125003.

[58] A. Murari et al. "Prototype of an adaptive disruption predictor for JET based on fuzzy logic and regression trees". In: *Nuclear Fusion* 48.3 (Feb. 2008), p. 035010. DOI: 10.1088/0029-5515/48/3/035010. URL: https://dx.doi.org/10.1088/0029-5515/48/3/035010.

[59] S. Dormido-Canto et al. "Development of an efficient real-time disruption predictor from scratch on JET and implications for ITER". In: *Nuclear Fusion* 53.11 (Sept. 2013), p. 113001. DOI: 10.1088/0029-5515/53/11/113001. URL: https://dx.doi.org/10.1088/0029-5515/53/11/113001.

[60] G.A. Rattá et al. "An advanced disruption predictor for JET tested in a simulated real-time environment". In: *Nuclear Fusion* 50.2 (Jan. 2010), p. 025005. DOI: 10.1088/0029-5515/50/2/025005. URL: https://dx.doi.org/10.1088/0029-5515/50/2/025005.

[61] B Cannas et al. "Overview of manifold learning techniques for the investigation of disruptions on JET". In: *Plasma Physics and Controlled Fusion* 56.11 (Oct. 2014), p. 114005. DOI: 10.1088/0741-3335/56/11/114005. URL: https://dx.doi.org/10.1088/0741-3335/56/11/114005.

[62] A. Murari et al. "Adaptive predictors based on probabilistic SVM for real time disruption mitigation on JET". In: *Nuclear Fusion* 58.5 (Mar. 2018), p. 056002. DOI: 10.1088/1741-4326/aaaf9c. URL: https://dx.doi.org/10.1088/1741-4326/aaaf9c.

[63] A. Pau et al. "A machine learning approach based on generative topographic mapping for disruption prevention and avoidance at JET". In: *Nuclear Fusion* 59.10 (Aug. 2019), p. 106017. DOI: 10.1088/1741-4326/ab2ea9. URL: https://dx.doi.org/10.1088/1741-4326/ab2ea9.

[64] R. Aledda et al. "Adaptive mapping of the plasma operational space of ASDEX Upgrade for disruption prediction". In: *INTERNATIONAL JOURNAL OF APPLIED ELECTROMAGNETICS AND MECHANICS* 39 (2012), pp. 43–49. DOI: https://dx.doi.org/10.3233/JAE-2012-1441.

[65] R. Aledda et al. "Mapping of the ASDEX Upgrade operational space for disruption prediction". In: (2011), pp. 1–6. DOI: 10.1109/SOFE.2011.6052211.

[66] R. Aledda et al. "Improvements in disruption prediction at ASDEX Upgrade". In: *Fusion Engineering and Design* 96-97 (2015). Proceedings of the 28th Symposium On Fusion Technology (SOFT-28), pp. 698–702. ISSN: 0920-3796. DOI: https://doi.org/10.1016/j.fusengdes.2015.03.045. URL: https://www.sciencedirect.com/science/article/pii/S0920379615002148.

[67] B. Cannas et al. "Disruption prediction with adaptive neural networks for ASDEX Upgrade". In: *Fusion Engineering and Design* 86.6 (2011). Proceedings of the 26th Symposium of Fusion Technology (SOFT-26), pp. 1039–1044. ISSN: 0920-3796. DOI: https://doi.org/10.1016/j.fusengdes.2011.01.069. URL: https://www.sciencedirect.com/science/article/pii/S0920379611000810.

[68] K.J. Montes et al. "Machine learning for disruption warnings on Alcator C-Mod, DIII-D, and EAST". In: *Nuclear Fusion* 59.9 (July 2019), p. 096015. DOI: 10.1088/1741-4326/ab1df4. URL: https://dx.doi.org/10.1088/1741-4326/ab1df4.

[69] C Rea et al. "Disruption prediction investigations using Machine Learning tools on DIII-D and Alcator C-Mod". In: *Plasma Physics and Controlled Fusion* 60.8 (June 2018), p. 084004. DOI: 10.1088/1361-6587/aac7fe. URL: https://dx.doi.org/10.1088/1361-6587/aac7fe.

[70] Massimo Camplani et al. "Tracking of the Plasma States in a Nuclear Fusion Device Using SOMs". In: *Engineering Applications of Neural Networks*. Ed. by Palmer-Brown. Berlin, Heidelberg: Springer Berlin Heidelberg, 2009, pp. 430–437.

[71] B Cannas et al. "Manifold learning to interpret JET high-dimensional operational space". In: *Plasma Physics and Controlled Fusion* 55.4 (Mar. 2013), p. 045006. DOI: 10.1088/0741-3335/55/4/045006. URL: https://dx.doi.org/10.1088/0741-3335/55/4/045006.

[72] P.C. de Vries et al. "Survey of disruption causes at JET". In: *Nuclear Fusion* 51.5 (Apr. 2011), p. 053018. DOI: 10.1088/0029-5515/51/5/053018. URL: https://dx.doi.org/10.1088/0029-5515/51/5/053018.

[73] F. Wagner et al. "Regime of Improved Confinement and High Beta in Neutral-Beam-Heated Divertor Discharges of the ASDEX Tokamak". In: *Physical Review Letters - PHYS REV LETT* 49 (Nov. 1982), pp. 1408–1412. DOI: 10.1103/PhysRevLett.49.1408.

[74] Matthias Bernert. "Analysis of the H-mode density limit in the ASDEX Upgrade tokamak using bolometry". In: (2013).

[75] Martin Greenwald. "Density limits in toroidal plasmas". In: *Plasma Physics and Controlled Fusion* 44.8 (July 2002), R27. DOI: 10.1088/0741-3335/44/8/201. URL: https://dx.doi.org/10.1088/0741-3335/44/8/201.

[76] V. Mertens et al. "High density operation close to Greenwald limit and H mode limit in ASDEX upgrade". In: *Nuclear Fusion* 37.11 (Nov. 1997), p. 1607. DOI: 10.1088/0029-5515/37/11/I10. URL: https://dx.doi.org/10.1088/0029-5515/37/11/I10.

[77] M Bernert et al. "The H-mode density limit in the full tungsten ASDEX Upgrade tokamak". In: *Plasma Physics and Controlled Fusion* 57.1 (Nov. 2014), p. 014038. DOI: 10.1088/0741-3335/57/1/014038. URL: https://dx.doi.org/10.1088/0741-3335/57/1/014038.

[78] M Maraschek et al. "Path-oriented early reaction to approaching disruptions in ASDEX Upgrade and TCV in view of the future needs for ITER and DEMO". In: *Plasma Physics and Controlled Fusion* 60.1 (Nov. 2017), p. 014047. DOI: 10.1088/1361-6587/aa8d05. URL: https://dx.doi.org/10.1088/1361-6587/aa8d05.

[79] B. Lipschultz et al. "Marfe: an edge plasma phenomenon". In: *Nuclear Fusion* 24.8 (Aug. 1984), p. 977. DOI: 10.1088/0029-5515/24/8/002. URL: https://dx.doi.org/10.1088/0029-5515/24/8/002.

[80] Valentin Igochine. *Active Control of Magneto-hydrodynamic Instabilities in Hot Plasmas*. Vol. 83. Oct. 2014. ISBN: ISBN: 978-3-662-44221-0 (Print) 978-3-662-44222-7 (Online). DOI: 10.1007/978-3-662-44222-7.

[81] B. Lipschultz. "Review of MARFE phenomena in tokamaks". In: *Journal of Nuclear Materials* 145-147 (1987), pp. 15–25. ISSN: 0022-3115. DOI: https://doi.org/10.1016/0022-3115(87)90306-0. URL: https://www.sciencedirect.com/science/article/pii/0022311587903060.

[82] H. Niedermeyer et al. "Changes of plasma properties prior to high density disruption in ASDEX". In: (1983).

[83] "The regime of enhanced particle recycling in high density tokamak discharges in the Frascati torus". In: *Physics Letters A* 90.8 (1982), pp. 405–409. ISSN: 0375-9601. DOI: https://doi.org/10.1016/0375-9601(82)90796-4. URL: https://www.sciencedirect.com/science/article/pii/0375960182907964.

[84] I.T. Jolliffe. *Principal Component Analysis*. Springer Series in Statistics. Springer New York, 2013. ISBN: 9781475719048. URL: https://books.google.it/books?id=-ongBwAAQBAJ.

[85] Daniel Asimov. "The Grand Tour: A Tool for Viewing Multidimensional Data". In: *SIAM Journal on Scientific and Statistical Computing* 6.1 (1985), pp. 128–143. DOI: 10.1137/0906011. URL: https://doi.org/10.1137/0906011.

[86] T. Kohonen. "The self-organizing map". In: *Proceedings of the IEEE* 78.9 (1990), pp. 1464–1480. DOI: 10.1109/5.58325.

[87] Christopher M. Bishop, Markus Svensén, and Christopher K. I. Williams. "GTM: The Generative Topographic Mapping". In: *Neural Computation* 10.1 (1998), pp. 215–234. DOI: 10.1162/089976698300017953.

[88] Joshua B. Tenenbaum, Vin de Silva, and John C. Langford. "A Global Geometric Framework for Nonlinear Dimensionality Reduction". In: *Science* 290.5500 (2000), pp. 2319–2323. DOI: 10.1126/science.290.5500.2319. eprint: https://www.science.org/doi/pdf/10.1126/science.290.5500.2319. URL: https://www.science.org/doi/abs/10.1126/science.290.5500.2319.

[89] Sam T. Roweis and Lawrence K. Saul. "Nonlinear Dimensionality Reduction by Locally Linear Embedding". In: *Science* 290.5500 (2000), pp. 2323–2326. DOI: 10.1126/science.290.5500.2323. eprint: https://www.science.org/doi/pdf/10.1126/science.290.5500.2323. URL: https://www.science.org/doi/abs/10.1126/science.290.5500.2323.

[90] Changjie Tang et al. "Advanced Data Mining and Applications, 4th International Conference, ADMA 2008, Chengdu, China, October 8-10, 2008. Proceedings". In: (Jan. 2008).

[91] Oliver Kuss. "Global goodness-of-fit tests in logistic regression with sparse data". In: *Statistics in Medicine* 21.24 (2002), pp. 3789–3801. DOI: https://doi.org/10.1002/sim.1421. eprint: https://onlinelibrary.wiley.com/doi/pdf/10.1002/sim.1421. URL: https://onlinelibrary.wiley.com/doi/abs/10.1002/sim.1421.

[92] Laurens van der Maaten, Eric Postma, and H. Herik. "Dimensionality Reduction: A Comparative Review". In: *Journal of Machine Learning Research - JMLR* 10 (Jan. 2007).

[93] O. Samko, A.D. Marshall, and P.L. Rosin. "Selection of the optimal parameter value for the Isomap algorithm". In: *Pattern Recognition Letters* 27.9 (2006), pp. 968–979. ISSN: 0167-8655. DOI: https://doi.org/10.1016/j.patrec.2005.11.017. URL: https://www.sciencedirect.com/science/article/pii/S0167865505003648.

[94] Jukka Kortelainen, Eero Väyrynen, and Tapio Seppänen. "Isomap Approach to EEG-Based Assessment of Neurophysiological Changes During Anesthesia". In: *IEEE Transactions on Neural Systems and Rehabilitation Engineering* 19.2 (2011), pp. 113–120. DOI: 10.1109/TNSRE.2010.2098420.

[95] Johnson Horn. "Matrix Analysis". In: *Cambridge University Press* (1985).

[96] D. et al Testa. "The magnetic diagnostic set for ITER". In: *IEEE Transactions on Plasma Science* 38 (Mar. 2010). DOI: 10.1109/TPS.2009.2037226.

[97] M. et al Baruzzo. "Conceptual design of DTT magnetic diagnostics". In: (July 2019). DOI: 2-s2.0-85084018338.

[98] G. Mazzitelli et al. "FTU results with a liquid lithium limiter". In: *Nuclear Fusion* 51.7 (May 2011), p. 073006. DOI: 10.1088/0029-5515/51/7/073006. URL: https://dx.doi.org/10.1088/0029-5515/51/7/073006.

[99] B. Labit et al. "Experimental studies of the snowflake divertor in TCV". In: *Nuclear Materials and Energy* 12 (2017). Proceedings of the 22nd International Conference on Plasma Surface Interactions 2016, 22nd PSI, pp. 1015–1019. ISSN: 2352-1791. DOI: https://doi.org/10.1016/j.nme.2017.03.013. URL: https://www.sciencedirect.com/science/article/pii/S235217911630179X.

[100] A. Fil et al. "Comparison between MAST-U conventional and Super-X configurations through SOLPS-ITER modelling". In: *Nuclear Fusion* 62.9 (Aug. 2022), p. 096026. DOI: 10.1088/1741-4326/ac81d8. URL: https://dx.doi.org/10.1088/1741-4326/ac81d8.

[101] R. Bonifetto et al. "DTT - Divertor Tokamak Test facility - Interim Design Report (Green Book)". In: (Apr. 2019). DOI: ISBN978-88-8286-378-4.

[102] Alessandro Beghi and Angelo Cenedese. "Advances in real-time plasma boundary reconstruction - From gaps to snakes". In: *Control Systems, IEEE* 25 (Nov. 2005), pp. 44–64. DOI: 10.1109/MCS.2005.1512795.

[103] George Vayakis et al. "Nuclear technology aspects of ITER vessel-mounted diagnostics". In: *Journal of Nuclear Materials* 417.1 (2011). Proceedings of ICFRM-14, pp. 780–786. ISSN: 0022-3115. DOI: https://doi.org/10.1016/j.jnucmat.2011.01.081. URL: https://www.sciencedirect.com/science/article/pii/S0022311511001139.

[104] Simone Peruzzo et al. "R&D on ITER in-vessel magnetic sensors". In: *Fusion Engineering and Design* 88.6 (2013). Proceedings of the 27th Symposium On Fusion Technology (SOFT-27); Liège, Belgium, September 24-28, 2012, pp. 1302–1305. ISSN: 0920-3796. DOI: https://doi.org/10.1016/j.fusengdes.2013.02.018. URL: https://www.sciencedirect.com/science/article/pii/S0920379613001324.

[105] G. Marchiori et al. "Upgraded electromagnetic measurement system for RFX-mod". In: *Fusion Engineering and Design* 123 (2017). Proceedings of the 29th Symposium on Fusion Technology (SOFT-29) Prague, Czech Republic, September 5-9, 2016, pp. 892–896. ISSN: 0920-3796. DOI: https://doi.org/10.1016/j.fusengdes.2017.03.098. URL: https://www.sciencedirect.com/science/article/pii/S0920379617303204.

[106] P.E. Stott and J. S'anchez. "Plasma diagnostics for tokamaks and stellarators (Proceedings of the IV course and workshop on magnetic onfinement fusion. UIMP Santander (Spain), June 1992)". In: 739 (1994). URL: http://www-fusion.ciemat.es/InternalReport/IR739.pdf.

[107] R. Albanese et al. "Design, implementation and test of the XSC extreme shape controller in JET". In: *Fusion Engineering and Design* 74.1 (2005). Proceedings of the 23rd Symposium of Fusion Technology, pp. 627–632. ISSN: 0920-3796. DOI: https://doi.org/10.1016/j.fusengdes.2005.06.290. URL: https://www.sciencedirect.com/science/article/pii/S0920379605002772.

[108] A. Mele et al. "MIMO shape control at the EAST tokamak: Simulations and experiments". In: *Fusion Engineering and Design* 146 (2019). SI:SOFT-30, pp. 1282–1285. ISSN: 0920-3796. DOI: https://doi.org/10.1016/j.fusengdes.2019.02.058. URL: https://www.sciencedirect.com/science/article/pii/S0920379619302340.

[109] Raffaele Albanese et al. "ITER-like Vertical Stabilization system for the EAST tokamak". In: *Nuclear Fusion* 57 (June 2017). DOI: 10.1088/1741-4326/aa7a78.

[110] A. Pironti and M. Walker. "Control of tokamak plasmas: introduction to a special section". In: *IEEE Control Systems Magazine* 25.5 (2005), pp. 24–29. DOI: 10.1109/MCS.2005.1512793.

[111] Marco Ariola and Alfredo Pironti. "Plasma Magnetic Control Problem". In: *Magnetic Control of Tokamak Plasmas*. Cham: Springer International Publishing, 2016, pp. 77–90.

[112] Antonio Castaldo et al. "Plasma Scenarios for the DTT Tokamak with Optimized Poloidal Field Coil Current Waveforms". In: *Energies* 15.5 (2022). ISSN: 1996-1073. DOI: 10.3390/en15051702. URL: https://www.mdpi.com/1996-1073/15/5/1702.

[113] S.L. Brunton and J.N. Kutz. "Data-Driven Science and Engineering: Machine Learning, Dynamical Systems, and Control". In: (2019). URL: https://books.google.it/books?id=gNcRuQEACAAJ.

[114] Yuri Igitkhanov et al. "Design Strategy for the PFC in DEMO Reactor (KIT Scientific Reports ; 7637)". In: (2013). 31.10.01; LK 01. DOI: 10.5445/KSP/1000032116.